NASA TECHNICAL NOTE

NASA TN D-5512

NASA TN D-5512

INVESTIGATION OF LAMINAR AND TURBULENT BOUNDARY LAYERS INTERACTING WITH EXTERNALLY GENERATED SHOCK WAVES

by Earl C. Watson, John D. Murphy, and William C. Rose

Ames Research Center
Moffett Field, Calif.

NATIONAL AERONAUTICS AND SPACE ADMINISTRATION • WASHINGTON, D. C. • NOVEMBER 1969

TECHNICAL REPORT STANDARD TITLE PAGE

1. Report No. NASA TN D-5512	2. Government Accession No.	3. Recipient's Catalog No.
4. Title and Subtitle INVESTIGATION OF LAMINAR AND TURBULENT BOUNDARY LAYERS INTERACTING WITH EXTERNALLY GENERATED SHOCK WAVES		5. Report Date November 1969 6. Performing Organization Code
7. Author(s) Earl C. Watson, John D. Murphy, and William C. Rose		8. Performing Organization Report No. A-3204
9. Performing Organization Name and Address NASA Ames Research Center Moffett Field, Calif. 94035		10. Work Unit No. 722-03-00-01-00-21 11. Contract or Grant No.
12. Sponsoring Agency Name and Address National Aeronautics and Space Administration Washington, D.C. 20546		13. Type of Report and Period Covered Technical Note 14. Sponsoring Agency Code

15. Supplementary Notes

16. Abstract

This report presents the results of a study of the interactions of laminar and turbulent boundary layers with externally generated shock waves. The study included tests at nominal free-stream Mach numbers of 7.3 and 10.4, as well as a comprehensive review of previous work by others in related areas. The experimental studies considered interactions that occurred on two different models : a flat plate and a curved surface that provided isentropic compression of the flow. Each model had a sharp leading edge; the contour of the compression surface was representative of that for a hypersonic inlet. Data were examined to determine parameters that correlated significant features of the interactions. The data considered from the present and other investigations cover a range of free-stream Mach numbers from 2 to 15 and free-stream Reynolds numbers per foot from 2×10^5 to 1×10^7. It is concluded that further work needs to be done before details of the interactions, such as shock configuration, mass entrainment in the boundary layer, and changes in boundary-layer parameters across an interaction can be well defined.

17. Key Words Suggested by Author(s)	18. Distribution Statement
Interactions Laminar boundary layer Turbulent boundary layer	Unclassified - Unlimited

19. Security Classif. (of this report)	20. Security Classif. (of this page)	21. No. of Pages	22. Price*
Unclassified	Unclassified	132	$3.00

*For sale by the Clearinghouse for Federal Scientific and Technical Information
Springfield, Virginia 22151

INVESTIGATION OF LAMINAR AND TURBULENT BOUNDARY LAYERS INTERACTING WITH EXTERNALLY GENERATED SHOCK WAVES

By Earl C. Watson, John D. Murphy, and William C. Rose

Ames Research Center

SUMMARY

This report presents the results of a study of the interactions of laminar and turbulent boundary layers with externally generated shock waves. The investigation included an experimental study with tests conducted at nominal free-stream Mach numbers of 7.3 and 10.4, as well as a comprehensive review of previous interaction work by others in related areas. The interactions in the present experimental study occurred on two different models: a flat plate and a curved surface that provided isentropic compression of the flow. Each model had a sharp leading edge; the contour of the compression surface was representative of that for a hypersonic inlet. Data from the present and other studies, covering a range of free-stream Mach numbers from 2 to 15 and free-stream Reynolds numbers per foot from 2×10^5 to 1×10^7, were examined to determine parameters that correlated significant features of the interactions. These features included the pressure rise for incipient separation; the plateau pressure; and the free-interaction, plateau, and total-interaction lengths.

Study results indicate that semiempirical correlations are sufficient to predict the length of the free-interaction region for laminar flow, and the incipient separation and plateau pressures for both laminar and turbulent flows. For other interaction parameters, no correlations were found that were valid over the wide range of flow conditions considered.

Analytical methods have been considered from the viewpoint of their applicability and limitations for interactions between an oblique shock and laminar and turbulent boundary layers. Improved methods are needed for predicting such gross parameters as total-interaction length and, for separated flows, the lengths of the plateau and reattachment regions, particularly for interactions occurring on compression surfaces. An analytical method employing a two-layer concept is proposed for analyzing the interaction with a turbulent boundary layer. With the assumption of inviscid flow, and considering only the outer layer, the method predicted part of the shock-wave configuration and a good approximation to the surface pressure distribution. In considering the analytical methods in general, it is concluded that further work must be done to define the details of the interaction, such as the shock configuration, the mass entrainment into the boundary layer, and changes in other boundary-layer parameters across the interaction.

INTRODUCTION

The inlet in an air-breathing propulsion system provides high energy air to the engine at the required mass flow without excessive external drag or flow distortion at the entrance to the compressor or combustor. At hypersonic speeds, where the use of supersonic combustion engines is contemplated, boundary-layer control through mass removal may be impractical because of the high total temperature of the boundary-layer gases. Without boundary-layer removal, the flow entering the combustor will contain the cumulative effects of the boundary-layer development. Consequently, the design of the inlets for such engines must account for the boundary-layer development in detail throughout the inlet.

In the past, inlet designers have employed various approximations for the solution of the Prandtl boundary-layer equations (e.g., similarity assumptions, von Karman integral methods, etc.). However, even exact solutions to these basic equations fail to describe adequately the phenomena observed in certain flow regions of an inlet because these regions are characterized by large pressure gradients normal to the wall or by the existence of shock waves impinging on, and interacting with, the boundary layer. In computing programs used for predicting the inlet flow field, empirical techniques have been applied to account for such interactions, because adequate analytical methods have not been established. In reference 1, for example, empirical criteria are applied to determine whether separation occurs at an interaction, but details of the interaction, such as shock structure and boundary-layer profiles, are not determined.

Generally, simple model configurations have been employed in experiments to study the interaction of a boundary layer with the local inviscid flow. It should be recognized, therefore, that the empirical techniques developed for the treatment of an interaction are actually limited in their applicability to interactions that are relatively simple when compared with the complex interactions that may be encountered in hypersonic inlets. Nevertheless, simple processes must be studied and understood before the more complicated ones can be considered. Thus, with the model configurations used in the studies described in references 2 through 9, various interactions, such as those induced by steps, wedges, flares, and incident shocks impinging on a flat plate, were investigated. Various separated flows were considered, including those for which the boundary layer was laminar, transitional, and turbulent, and for which the stream velocity ranged from low supersonic to hypersonic. Most of the studies concerned those aspects of the interaction important to external flow over control surfaces or flared afterbodies; consequently, some details of the interactions that are important to internal flows have not been carefully studied. For example, in studies of control surfaces or flares, the major interest has been directed toward the determination of surface pressure and temperature, heat transfer, and skin friction. However, the inlet designer must also have a detailed knowledge of the changes occurring in the shock-wave structure and boundary-layer characteristics across an interaction.

The investigation reported herein consisted of two parts. One was an experimental study of interactions between an oblique shock and the boundary layer occurring on (1) a flat plate and (2) a representative compression surface for a hypersonic inlet. Data obtained with the flat-plate model provided a reference for comparison of the results obtained with the compression-surface model and those obtained from other investigations. The second part of the investigation consisted of a review of other work. The review was conducted to obtain results for inclusion with those of the present investigation to determine correlation parameters for certain features of an interaction. The interaction types considered include those in which the initial boundary layer is laminar or turbulent and interactions both with and without separation. Data were examined to determine parameters that correlate significant pressures and lengths, such as incipient separation and plateau pressures, and free-interaction, plateau, and total-interaction lengths.

Available analytical methods for the treatment of interactions were examined to determine their applicability to the interactions of this study. These methods are based on flow models, which, for the most part, were not duplicated in the experiments. For example, the methods described in references 10 and 11 are for weak interactions on flat plates in which the boundary layer is laminar at both the beginning and the end of the interaction. These methods provide such information as heat transfer, skin friction, and surface pressure distribution in the interaction region. It was found that no method is available for (1) treating interactions in which the boundary layer is initially laminar but is transitional or turbulent at the end of the interaction, (2) predicting details of the shock configuration associated with a laminar interaction, or (3) treating laminar interactions that occur on a curved surface providing an adverse pressure gradient. As another example, the method presented in reference 9 is for interactions on flat plates in which the boundary layer is initially turbulent. The empirical relations developed in reference 9 are not applicable to the range of Mach numbers and the wall-to-stagnation-temperature ratios of this investigation. In view of the shortcomings and limitations of present analytical methods, of which the above examples are representative, it is the intent here to accomplish the following: (1) to present experimental data for a variety of interaction conditions so that they may be used for verifying analytical methods that may be developed, and (2) to scrutinize the data for information that might provide a basis for the development of better analytical models. Every effort has been made to present all the necessary data in a form consistent with these goals.

The experimental part of the investigation was conducted at nominal free-stream Mach numbers of 7.3 and 10.4 for wind-tunnel stagnation conditions providing a range of free-stream Reynolds numbers per foot from 2.2×10^5 to 3.5×10^6. The data considered in the review of other related work cover a range of free-stream Mach numbers from 2 to 15 and free-stream Reynolds numbers per foot from 2×10^5 to 1×10^7.

NOTATION

C	Chapman-Rubesin constant
C_f	local skin-friction coefficient
C_p	pressure coefficient
CS FP	compression-surface model flat-plate model } Used with a numeral to designate the run number and model
l_P	plateau length, defined in sketch (a)
l_R	reattachment length, defined in sketch (a)
l_T	total length, defined in sketch (a)
l_U	upstream interaction length, defined in sketch (a)
l_1	length defined in figure 32
m	boundary-layer mass flow, $\int_0^\delta \rho u \, dy$
M	Mach number
N	velocity profile index for a turbulent boundary layer
p	local static pressures
p_o, p_P, p_F	surface static pressures identified in sketch (a)
p_t'	pitot pressure
p_t	total pressure
q	dynamic pressure
r	temperature recovery factor
Re	Reynolds number based on local flow conditions and a length indicated by a subscript
T	temperature
u	velocity
u_1	velocity at boundary-layer edge immediately upstream of impinging shock
u_2	velocity at boundary-layer edge immediately downstream of impinging shock

x distance along the model measured from leading edge (note: for the flat-plate model x is the distance along the surface (see fig. 2), while for the compression-surface model x is the distance measured horizontally (see fig. 4))

y distance normal to the wall

Y distance from wall to shock intercept (fig. 32) or surface coordinates of compression-surface model

α_L local flow deflection angle across the impinging shock

β $\sqrt{M_o^2 - 1}$

δ boundary-layer thickness

δ^* boundary-layer displacement thickness

θ boundary-layer momentum thickness

ν kinematic viscosity

ρ density

$\bar{\chi}_o$ viscous interaction parameter, $M_o^3 \sqrt{\frac{C}{Re_{x_o}}}$

Subscripts

i intercept of linear projection of incident shock and wall

INC incipient

o station at onset of pressure rise at beginning of interaction

P station at beginning of plateau

P_e station at end of plateau

t total conditions

w wall conditions

x distance along model measured from leading edge

x_o distance along model to onset of pressure rise at beginning of interaction

x_1 distance along model to station at intercept of impinging shock and edge of turbulent boundary layer

x_{eff} distance along the model, measured from the effective origin of the turbulent boundary layer

δ boundary-layer-edge condition or boundary-layer thickness

1 station at intercept of impinging shock and edge of turbulent boundary layer, or conditions upstream of impinging shock

2 conditions between an impinging shock and the reflected shock

3 conditions downstream of a reflected shock

∞ free stream

Superscript

$*$ evaluated at the Eckert reference enthalpy, except when used to denote displacement thickness, δ^*

APPARATUS

The experimental investigation was carried out in the Ames 3.5-Foot Hypersonic Wind Tunnel. A brief description of this facility may be found in reference 12.

Two large-scale models were employed in this study. The first was a flat-plate model, 18 inches wide by 48 inches long. A photograph of this model mounted in the wind tunnel with the shock generator in place is shown in figure 1. Figure 2 shows the planform dimensions of the model and the instrumentation locations. The second model was a curved surface that provided isentropic compression of the flow. A photograph of this model with the shock generator mounted is shown in figure 3, and surface coordinates and planform dimensions are shown in figure 4. Instrumentation locations for this model are shown in figure 5. The models were mounted in the tunnel so that the initial flat surface was inclined at 3° to the free stream to provide a small degree of compression. This was necessary since previous experience had shown that the boundary-layer flow was unstable on a flat plate at 0° incidence and that the instrumentation was not sensitive enough to measure the low static pressure at a Mach number of 10. Neither model had side plates. Both models had a nominally sharp (0.002-inch radius), internally water-cooled, leading-edge section fabricated from tool steel. The major portion of the models' surface was constructed of 7075 aluminum, and only a short section adjacent to the steel leading-edge section was water cooled. Because of the large heat capacity and limited test times (of the order of 3 minutes), the temperature of the uncooled portion of the model surface did not increase by more than 50° R during any run. However, a large unknown temperature gradient did exist near the leading edge. The magnitude of this gradient was determined by the temperature of the leading edge, which glowed a cherry-red color during a run, and the temperature of the water coolant

passage. It is believed that the effects of the hot leading edge were insignificant since calculations of the laminar boundary-layer development with a step wall-temperature profile showed that the temperature effects persisted downstream for only a few boundary-layer thicknesses.

Nominal test conditions for the experimental runs considered are presented in table I. It should be noted that, since the tunnel is of the blowdown type, it was not possible to hold the tunnel stagnation conditions absolutely constant during the course of a run. Variation in tunnel stagnation conditions was not, however, a cause for concern since the variation in total temperature never exceeded 5 percent and total pressure variations were negligible throughout any run.

Measurements were made of surface pressure and temperature. In addition, a small probe was employed to measure local pitot and static pressure and local total-temperature distributions through the boundary layer. A sketch of the probe assembly is presented in figure 6. The temperature-measuring component consisted of a singly-shielded, aspirating probe employing a platinum/rhodium thermocouple element. The locations of the probe measuring stations are shown in figures 2 and 4 and noted for each run in table I.

A discussion of certain inconsistencies in the measured surface pressures is presented in the appendix. Effects of errors in temperature measurement and calibration, as well as effects of uncertainties in boundary-layer thickness, on boundary-layer integral parameters are also discussed in the appendix.

PRESENTATION OF RESULTS

A large number of figures are used to present the results of this investigation. An index to the figures is presented in table II to accommodate the reader in locating specific data and/or particular analyses of the data.

Boundary-Layer Surveys

Both the flat-plate and compression-surface models were tested with a shock generator, which produced a shock wave that interacted with the boundary layer on the model. The type of data obtained for the interactions varied considerably. In some cases only surface pressures were measured; in others, schlieren photographs, static and pitot-pressure measurements, and total-temperature measurements upstream and downstream of the interactions were obtained. Because of the model construction no probe surveys could be obtained downstream of an interaction on the compression model. Pitot and static pressures and total-temperature data obtained upstream and downstream of the interactions that occurred on the flat-plate model for both initially laminar and turbulent boundary layers are presented in figures 7 through 10. When examining the profiles downstream of the interaction, consideration must

be given to the location of the probing station relative to the surface pressure distribution and the incident and reflected shock-wave system. To clarify the locations of the measured profiles, a sketch showing the probe location relative to the pressure distribution and the shock system has been included with each downstream set of probe data. In some instances, severe gradients or sharp discontinuities are evident in the data; generally, these are associated with the reflected shock structure. The symbols A and A' are used in figures 7 through 10 to relate the observed position of the shock structure to the probe data.

Boundary-Layer Development

Figures 11 through 14 show the variation of boundary-layer-edge properties and integral parameters along the models in the absence of an interaction. Pitot pressure, static pressure, and total-temperature profiles obtained from boundary-layer traverses were used to deduce the experimental boundary-layer thickness and associated integral properties at each of the three probe stations (see appendix). It is necessary to interpolate for the conditions between the probe stations when the flow characteristics immediately upstream of an interaction are required. Schlieren photographs and theoretical boundary-layer solutions (discussed below) were employed to obtain the predicted and estimated curves shown in these figures. These curves were used to interpolate the values of the above quantities at other stations.

For a laminar boundary layer, the experimental values of the integral parameters, as well as Mach number and total-temperature profiles, were compared with theoretical predictions. The theory employed the laminar boundary-layer-edge solutions of Kendall and Bartlett (ref. 13) in an iterative procedure with the inviscid solutions by the method of characteristics as described in reference 14. The predicted distribution of boundary-layer-edge conditions was obtained from the inviscid flow solution and a mass balance on the boundary-layer solutions. In this way the variation in edge total pressure due to leading-edge viscous interaction was accounted for. Since the predicted edge conditions were generally in good agreement with data at the probe stations, theoretical results were used to obtain the boundary-layer parameters between the probe stations. At a free-stream Mach number of 10.4 and for a low Reynolds number (laminar flow), the surface static-pressure data were inaccurate (see appendix); therefore, the theoretical and experimental edge Mach numbers differ. In the data analysis for these free-stream conditions, the theoretical static pressure was used; thus, theoretical curves (fig. 12(b)) were used to obtain edge conditions and integral properties.

For turbulent boundary-layer flow, the absolute value of the boundary-layer thickness and associated integral properties could not be reliably determined from available theoretical analyses. As a result, boundary-layer-edge conditions were inferred from a combination of experimental data and boundary-layer integral solutions (ref. 1) based on an assumed transition location. Integral solutions were employed to interpolate and extrapolate

the data, since they yield, in general, the correct growth rate of the boundary-layer parameters. Quantities obtained in this fashion are denoted "estimated" in figures 11 through 14 for turbulent boundary-layer flow.

Figure 11 presents the edge conditions and integral properties for the flat-plate model at a free-stream Mach number of 7.3 for laminar and turbulent flow. Figure 12 presents similar information at a free-stream Mach number of 10.4. Figure 13 presents edge conditions and integral properties for the compression-surface model at a free-stream Mach number of 7.3. Figure 14 presents similar information at a Mach number of 10.4; at this Mach number no laminar interaction data were obtained on the compression-surface model. For the compression-surface model, the experimentally determined static pressure gradient normal to surface and the surface static pressure were employed in determining the boundary-layer-edge conditions (see appendix).

Boundary-Layer Profiles

Figure 15 presents Mach number and total-temperature profiles typical of those upstream of an interaction on the flat-plate model for a free-stream Mach number of 7.3. The profiles were obtained in the absence of an interaction from data such as those presented in figures 7 through 10. The experimental data are compared (in fig. 15(a)) with results obtained from the theoretical laminar boundary-layer solutions previously noted (ref. 13). The departure of the experimental points from the theoretical curves in the lower portion of the boundary layer was attributed to flow interference between the probe and the model surface. In figure 15(b) the experimental profiles are presented for the same model and Mach number with a turbulent boundary layer. (Since existing analytical methods for predicting compressible turbulent boundary-layer parameters generally employ low-order integral methods, which do not provide the details of the flow, i.e., velocity and temperature profiles, theoretical profiles have not been included.) Figure 16 presents similar information for the compression-surface model.

Figures 17 and 18 present Mach number and total-temperature profiles for the flat-plate and compression-surface models, respectively, at a free-stream Mach number of 10.4. For the compression-surface model, only the turbulent results are presented, since, as noted earlier, no pure laminar interactions were obtained for this model and Mach number. The turbulent profiles presented show a region within the boundary layer in which the local total temperature exceeds the free-stream value. It could not be determined whether this excess above the free-stream temperature results from an error associated with the probe and its calibration characteristics (see appendix), or if a so-called temperature "overshoot" exists in the local stream. An overshoot in the physical flow should not be ruled out since the occurrence of an overshoot is in qualitative agreement, at least, with results obtained for laminar boundary-layer flow with nonunity Prandtl number, as presented by Crocco in reference 15.

Interaction Photographs and Surface Pressure Distributions

Figures 19 through 22 present the individual surface pressure distributions together with schlieren photographs of the interactions considered. These data, together with the boundary-layer-edge conditions, integral properties, and selected probe measurements presented earlier, constitute the primary data of this report.

DISCUSSION OF RESULTS

Classification of Interactions

It has been shown (ref. 2) that the character of the boundary-layer flow (i.e., whether it is laminar, transitional, or turbulent) throughout the interaction controls the mechanics of the mixing and reattachment processes and hence the characteristics of the interaction. The data obtained in the present investigation were assigned to one of the above categories (i.e., laminar, transitional, or turbulent) on the basis of an examination of the schlieren photographs and the velocity profiles upstream and downstream of the interaction. Details of this classification procedure are discussed below.

Upstream of an interaction the character of the boundary layer was determined by means of probe surveys and schlieren photographs. The measured laminar boundary-layer profiles on both models for free-stream Mach numbers of 7.3 and 10.4 agreed well with predicted profiles. When natural transition did not occur, turbulent boundary layers were obtained by the use of trips located as shown in figures 2 and 5. The trips were effective in producing the relatively full velocity and temperature profiles characteristic of turbulent flow.

Turbulent boundary-layer profiles are also characterized by their logarithmic form when plotted in "law-of-the-wall" coordinates. A convenient way to compare experimental results with profiles obtained from the law-of-the-wall representation is to use the parameters shown in figure 23. When plotted in this fashion the form of an experimentally determined profile can be compared readily with the logarithmic form obtained from the law-of-the-wall representation. In figure 23 the theoretical curves were obtained from the equation shown therein. The representative experimental profile shown in figure 23 has an extensive logarithmic portion, which has a slope that agrees closely with that for the theory. This agreement indicates that the boundary layer is turbulent.

Downstream of an interaction the character of the boundary-layer flow was more difficult to determine. The probe station aft of the interaction was generally located some distance downstream of the shock impingement point. As a result, a boundary layer that was laminar at reattachment could undergo transition between reattachment and the survey probe station. Since profile data in the immediate vicinity of reattachment were not available, schlieren photographs were relied on to judge whether the boundary layer was laminar or

turbulent in the reattachment region. In the interpretation of the data, interactions in which the entering boundary layer was laminar and the downstream boundary layer appeared to be laminar from schlieren photographs are presented herein as "laminar interactions." When the entering boundary layer was turbulent, the downstream boundary layer was always turbulent. These are presented herein as "turbulent interactions." When the entering boundary layer was laminar and schlieren photographs indicated transition upstream of or at reattachment, the interaction was considered to be transitional. Data in this latter category are not presented in this report. However, it should be noted that some data for which transition occurred downstream of the reattachment point are presented.

Definitions

In order to facilitate the following discussion, it is necessary to establish some pertinent definitions. Sketch (a) shows schematically the interaction between an incident, or impinging, shock and a laminar boundary

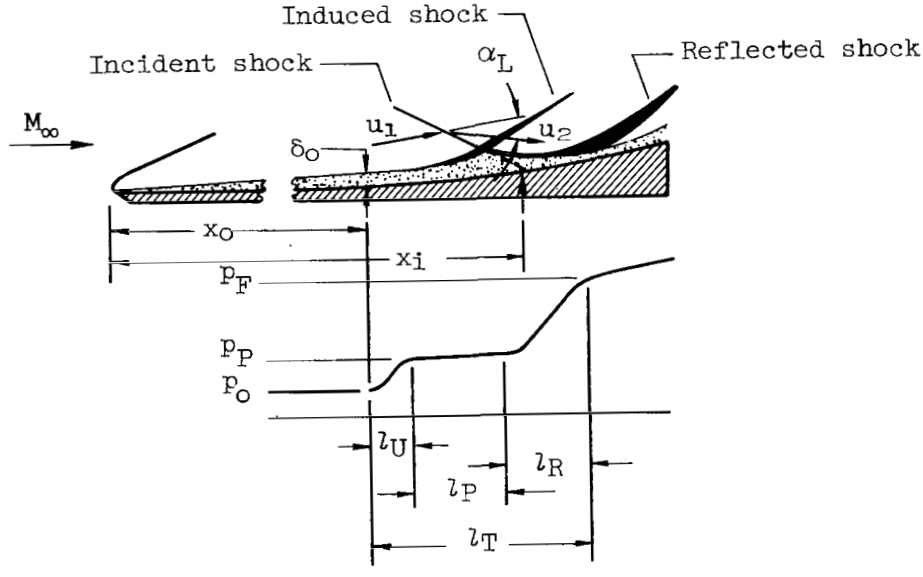

Sketch (a) Schematic of shock configuration and surface pressure distribution.

layer. It represents an interaction occurring on a compression surface where the shock strength is sufficient to cause local flow separation. The model alinement and flow direction are the same as they were in the tests, and a typical surface pressure distribution is shown. The impinging shock interacts with the laminar boundary layer and reflects into the flow field. The location of the interaction may be identified by the intercept at the wall of the linear extension of the impinging shock before it encounters any influence from the interaction. The pressures of interest are the upstream pressure, p_o, the plateau pressure, p_P, and final pressure, p_F. The incremental lengths, l_U, l_P, and l_R, define the free interaction, plateau, and reattachment regions, respectively, while l_T defines the overall interaction length. The strength of an interaction is represented by the quantity α_L. This

angle is the local flow-deflection angle across the incident shock at the edge of the boundary layer. Its value was deduced using the local edge Mach number immediately upstream of the interaction and the shock-wave angle of the incident shock measured from a schlieren photograph.

Composite Pressure Distributions

The effects of incident shock strength on surface pressure distribution are shown in the composite plots of figure 24 for the flat plate at a free-stream Mach number of 7.3; the data are shown for laminar and turbulent flow in figure 24.

For the laminar flow (fig. 24(a)), the individual pressure distributions have been plotted so that positions of the initial pressure rise coincide. When plotted in this fashion, it is evident that the shape of the pressure distribution in the free-interaction region is independent of shock strength. This is another example that supports the free-interaction hypothesis of Chapman et al. (ref. 2). This hypothesis states that the behavior of the flow is independent of the downstream mechanism causing the separation. In addition, it can be seen (fig. 24(a)) that for increasing shock strength (i.e., α_L increasing) both the length of the pressure plateau and the pressure gradient in the reattachment region increase. The presence of separation is indicated by a plateau, or nearly constant pressure region, in the surface pressure distribution.

The pressure rise for incipient separation can be obtained by cross plotting the plateau length, l_p, against the local flow-deflection angle, α_L, and extrapolating to zero plateau length. This method was employed herein and it yielded a pressure rise for incipient separation slightly higher than that shown for $\alpha_L = 2^\circ$. It also showed that the pressure rise for incipient separation is greater than the plateau pressure, in accordance with the findings of Chapman et al. (ref. 2) for supersonic speeds, and Needham (ref. 6) for hypersonic speeds.

The composite pressure distributions for turbulent boundary-layer flow were constructed so that the points of intercept of the linear extension of the impinging shock wave with the wall were coincident. When presented in this manner, the composite plot shows the increase in the extent of the upstream influence with increasing shock strength. For the shock strengths shown in figure 24(b), no evidence of flow separation, such as an inflection in the region of the rise in pressure, can be observed, but it should be noted that the orifice spacing was too large for a small inflection to be detected if one had occurred. It is believed that the presence of an inflection can be inferred from the trends evident in the fairing of data for increasingly stronger interactions. For example, in figure 24(b) the fairing for $\alpha_L = 10^\circ$ has been dashed to indicate that an inflection may be present for this stronger interaction. A comparison of the results for laminar and turbulent flow (fig. 24) shows, in agreement with previously established results, that the turbulent boundary layer can withstand a larger pressure rise without separation.

The composite pressure distributions in figure 25(a) were obtained on the compression-surface model with a laminar boundary layer. Again, it can be seen that the pressure distributions in the free-interaction region are coincident, and a pressure higher than the plateau pressure was obtained without separation for the 3° flow-deflection angle. These pressure distributions differ from those on the flat plate in the length of the plateau region and in the shape in the reattachment region. These differences will be discussed in the Correlations section. For local flow-deflection angles of 3° and 7°, the final pressure was found to agree with that expected from an inviscid pressure rise across the incident and reflected shock system. For stronger interactions, however, the final pressure is lower than expected. This discrepancy is believed due to the expansion fan emanating from the surface employed to generate the impinging shock wave. This problem did not occur on the flat-plate model, and the inviscid pressure rise was always attained. In addition to the expansion fan, it is possible that a loss of two-dimensionality may have occurred because of lateral spillage in these strong interactions. If this occurred it could contribute to the reduction in overall pressure rise across the interaction.

Figure 25(b) shows the composite pressure distributions for the compression-surface model with a turbulent boundary layer. For this case an obvious inflection in the region of the rise in the surface pressure distribution is apparent for the strongest shock considered, $\alpha_L = 17^{\circ}$. An inflection is not obvious for $\alpha_L = 14^{\circ}$, but the presence of one can be inferred from the trends in the data, as indicated by the fairing.

Composite pressure distributions for the Mach 10.4 flow conditions were also constructed. They are not presented here since they do not differ significantly from those obtained at Mach 7.3.

Correlations

The data presented in figures 19 through 22, together with similar data from other investigations, have been analyzed to obtain parameters that correlate significant features of an interaction. Data were considered for free-stream Mach numbers ranging from 2 to 14.8 and free-stream Reynolds numbers per foot from 2×10^5 to 1×10^7.

Pressure correlations.- Correlation of the pressure ratio for incipient separation of laminar boundary layers is presented in figure 26(a). The data of references 3 and 6 and the present study are presented in terms of the correlation parameters of reference 6. Accordingly, the parameters chosen are the pressure ratio and viscous interaction parameter, $\bar{\chi}_o$. It can be seen that more data are needed to fully substantiate the validity of these parameters for the correlation of the pressure rise for incipient separation. Therefore, caution should be exercised in applying these results for design purposes. In addition, it should be remembered that all available data are for single interactions. If two or more interactions occur in tandem, as may occur in hypersonic inlets, incipient separation may occur at different pressure ratios for interactions downstream of the first, depending on the

proximity of transition, the spacing between interactions, and the change in boundary-layer characteristics across the upstream interaction.

The pressure rise for incipient separation of turbulent boundary layers is presented in figure 26(b). In this figure the data of Kuehn (ref. 16), as given by Popinski and Ehrlich (ref. 8), and the data of the present study are compared. The open circle for the present study was obtained on the basis of the discussion of the pressure distribution data for the flat plate in figure 24(b). For the purposes here it is assumed that incipient separation is indicated by the first appearance of an inflection in the surface pressure distribution, for $\alpha_L = 10^\circ$ in this case. The line represents the relation proposed by Popinski (ref. 7). A fairly good correlation of the data is obtained for the limited data available with both flat-plate and compression-surface models. Again, due to the paucity of experimental data, caution should be exercised in employing these results for design purposes.

In figure 27(a) the plateau pressure for interactions with laminar boundary layers is presented. The correlation proposed by Needham (ref. 6) is used to compare the data of references 3, 6, and 17 with those of the present study. Excellent agreement is obtained for both flat-plate and compression-surface data. In addition, the data represent interactions occurring for a wide range of wall temperatures, varying from adiabatic for the data of reference 3 to cold-wall conditions for the data of reference 6 and the present study.

In figure 27(b) the plateau pressure for turbulent boundary layers is presented. The parameters used by Popinski and Ehrlich (ref. 8) are employed in figure 27(b) to compare the data of references 4, 9, and 16 with those of the present study. Again, the agreement is fairly good. It should be noted that the data are not sufficiently precise to provide complete support for the relation represented by the empirical equation of reference 8; this relation results in only a slightly better agreement than the relation proposed by Erdos and Pallone (ref. 5). Some uncertainty exists in defining the plateau pressure for interactions whose strength is near that for incipient separation, since, as noted previously, an inflection in the pressure distribution is generally observed for a turbulent boundary layer rather than a nearly constant plateau pressure as with a laminar boundary layer. In figure 27(b) the data points represent the mean value of the surface pressure over the separated region.

Figure 28(a) presents the dimensionless pressure distribution in the free-interaction region of a laminar boundary-layer shock-wave interaction. Erdos and Pallone (ref. 5) hypothesized that this distribution was "universal." As can be seen, the data obtained with a cold wall in the present study depart markedly from the universal distribution of reference 5. The universal distribution was derived from the data of reference 2 for adiabatic wall conditions.

Figure 28(b) presents the dimensionless pressure distribution for the reattachment region of a laminar boundary-layer shock-wave interaction. This distribution appears to be highly sensitive to Mach number and less sensitive

to shock strength. Also, it is evident from examination of the difference between distributions on the compression surface and flat plate (for approximately the same range of local flow-deflection angles) that model configuration affects the shape of these curves.

The pressure in the free-interaction and reattachment regions of the turbulent boundary-layer shock-wave interactions could not be resolved in detail in the present study because the spacing of the orifices was too large relative to the length of these regions.

The pressure distributions for unseparated interactions are given for the laminar boundary layer in figure 29(a) and for the turbulent boundary layer in figure 29(b). Again, a pronounced Mach number dependence is demonstrated for both the laminar and turbulent boundary layers.

The foregoing discussion has shown that the pressure distributions are affected by Mach number and local streamwise and/or normal pressure gradients. There may also be effects associated with wall cooling, but they have not been specifically investigated.

Length correlations.- Parameters used for correlating the free-interaction length are presented in figure 30 for interactions with laminar and turbulent boundary layers. The parameters used for the laminar boundary layer were developed during the present study, whereas those for the turbulent boundary layer were proposed by Popinski and Ehrlich (ref. 8). The equation in figure 30(a) represents the recommended relation for defining the free-interaction length for laminar flow as a function of the incremental pressure rise to the beginning of the plateau. For the laminar interactions, the reference data were obtained from references 2, 3, and 6; for the turbulent interactions, the data from references 16, 18, and 19 are shown as presented by Popinski and Ehrlich (ref. 8).

No simple parameters are available for describing the length of the plateau region for interactions with separation. Hakkinen et al. (ref. 3) applied a momentum balance to a separated region to determine the parameters involved in a laminar separation for adiabatic wall conditions. In an attempt to correlate data, the parameters evolved in that analysis are employed in figure 31 with data for plateau length. It is evident that all of the data do not collapse to single line, and that the data for the compression surface stand apart from the flat-plate data. However, considering the range of conditions represented by the data (i.e., Mach numbers between 2 and 8.4, and wall temperature ratios (T_w/T_{t_∞}) between 0.28 and 1.0), it appears that the flat-plate data collapse reasonably well for interactions whose strength is less than about 0.5 in terms of the abscissa parameter. Thus, while the parameters provided a basis for predicting the plateau length for weak interactions on a flat plate, they fail to do this for the stronger interactions on both surfaces. The laminar boundary-layer data from the present test have been analyzed also by Kutschenreuter et al. (ref. 20) with respect to the separation length parameters proposed in reference 5 by Erdos and Pallone. It should be noted that the separation length as defined in this reference is essentially the same as the plateau length discussed above. No

correlating relation was found; however, there was evidence of a strong Mach number dependence. For a turbulent boundary layer, no correlations are available for the plateau length.

A semiempirical method of analysis was developed by Pinckney (ref. 9) for turbulent boundary-layer shock-wave interactions. In this analysis special parameters were employed to define certain features of the interaction. Among these parameters is the height Y (see sketch in fig. 32), which is the height from the wall to the intercept of the impinging shock and the induced shock. The shock structure of the turbulent interactions of the present study has been examined to determine this parameter and the length parameter, l_1. Figure 32 presents the ratio of these two parameters as a function of the pressure coefficient across the interaction. Another ratio given in reference 9, the total-interaction length divided by entering boundary-layer thickness, is presented in figure 33 as a function of the shock strength. The variations of both of these ratios, as obtained in the present study, differ from those indicated by Pinckney for adiabatic wall conditions and for Mach numbers up to 5; the present results are for cold-wall conditions and a local Mach number of 6.5. An analysis by Kutschenreuter (ref. 20) has shown that for turbulent interactions wall temperature has an effect on the shock strength required for separation, and it is therefore believed that wall-temperature effects may be the underlying cause for the differences noted in the above parameters. It is concluded that further investigation of the general effects of wall cooling on boundary-layer shock-wave interactions is needed and that care should be exercised in extrapolating the Pinckney results.

For laminar interactions, correlation parameters obtained in the present study for the total-interaction length are shown in figure 34. In view of the lack of success in obtaining correlations for plateau and reattachment lengths, it is somewhat unexpected to find such good correlation for the total-interaction length. Whereas the data for the flat plate from the referenced and present studies agree reasonably well for the wide range of conditions represented, the data for the compression surface at the stronger interactions ($p_F - p_o/p_o > 2$) do not agree. This indicates a sensitivity of total-interaction length to local streamwise and/or normal pressure gradients.

Shock-Wave Configuration for Turbulent Interactions

The preceding sections have been concerned for the most part with those features of the interaction that can be determined from surface measurements and the location and strength of the impinging shock. It is also of interest to observe the actual shock configuration in an interaction region and to compare it with the structure assumed in empirical methods that are employed to represent the interaction. Figure 35 presents a schlieren photograph of a turbulent boundary-layer shock-wave interaction. Superimposed on the photograph is the shock configuration obtained by two different empirical methods. The impinging shock is assumed to be unaffected by the boundary layer; in one case, it is reflected from the displacement thickness (δ^*) and, in the other, from the solid wall. It is evident that these approximations poorly represent the actual interaction.

An analytical model for predicting the shock configuration, surface pressure distribution, and a large portion of boundary-layer profile downstream of the interaction has been developed during the present study for an interaction between a turbulent boundary layer and a shock wave. Details of the analysis are presented in reference 21. Some of the results presented therein are shown in figure 36.

Figure 36(a) compares the experimental and predicted shock-wave shape and surface pressure distribution for an interaction obtained on the flat-plate model at Mach 7.3 and $\alpha_L = 2^\circ$. Figure 36(b) presents the same quantities for a stronger impinging shock, $\alpha_L = 8^\circ$. As can be seen, good agreement is obtained in pressure distribution except for the discontinuous pressure rise across the shock system. Reasonable agreement in shock shape and location is also obtained except for the presence of an extra reflected shock termed the "induced shock," which can be clearly seen in figure 36(b). One explanation for the presence of the induced shock is that it is formed by the coalescence of weak compression waves generated by the outward deflection of the viscous sublayer upstream of the interaction. It is believed that this shock is evidence of the presence of a flow process that is similar to that involved in the free-interaction region of laminar flow. Additional analysis, including the effects of coupling the inner viscous and outer inviscid layers, will be required before detailed surface information such as skin friction and heat transfer can be predicted. It is believed that the success of the above comparisons indicates the strongly inviscid nature of these interactions.

CHANGES IN BOUNDARY-LAYER CHARACTERISTICS ACROSS AN INTERACTION

One of the objectives of the present investigation was to obtain boundary-layer data, both upstream and downstream of interactions, which can be used in the assessment of the accuracy of analytical models. Data obtained from measurements, such as those presented in figures 7 through 10, have been analyzed to determine the variation of boundary-layer displacement thickness, momentum thickness, and mass flow across interactions that occurred on the flat-plate model. These data were obtained for interactions for which the entering boundary layers were both laminar and turbulent. Figure 37 presents the values of the displacement and momentum thicknesses downstream of an interaction normalized with respect to the values obtained in the absence of an interaction. Figure 38 presents the corresponding mass-flow ratios. The profile measurements were made at fixed model stations, whereas the location of the interaction varied, depending on the location of the leading edge of the generator and the generator angle. Since the changes that occur in the boundary-layer characteristics in the nearly constant pressure regions upstream and downstream of the interaction are small, relative to the changes that occur in the region of pressure rise, the changes indicated by the data should be a good approximation to the changes that occur across the interaction alone.

For these interactions both the displacement and momentum-thickness ratios undergo a significant reduction with increasing shock strength, and

the greatest change occurs for pressure ratios between 1 and 6. With both the momentum and displacement thicknesses changing across an interaction, the degree to which the shape parameter (δ^*/θ) is affected will depend on the relative change between these two quantities. Even though there is considerable scatter in the momentum thickness data of figure 37(b), the data indicate a trend that depends on the nature of the boundary layer. For interactions in which the initial boundary layer is laminar and for pressure ratios below 8, a greater reduction in momentum thickness occurs than when the boundary layer is initially turbulent. It follows that, for a given strength of interaction, greater changes in shape parameter (δ^*/θ) occur across an interaction when the entering flow is laminar than when it is turbulent.

In some analytical models for a turbulent boundary-layer, shock-wave interaction, the assumption is made that there is no mass addition to the boundary layer throughout the interaction (ref. 20), or that there is significant mass addition downstream of the region of pressure rise (ref. 9). In addition, in the model employed in reference 20, it is assumed that the entire pressure rise associated with the interaction occurs between the points where the incident and reflected shocks intercept the edge of the boundary layer. Data obtained in the present study were examined to assess the validity of these assumptions.

In one interaction study at a Mach number of 10.4 and a flow deflection angle of 10°, a boundary-layer survey was made within the interaction region. The surface pressure distribution and a sketch of the principal observable features of this interaction, as obtained from a schlieren photograph, are shown to the same scale and properly alined in figure 39(a). The circled numbers shown on the sketch are employed in subsequent figures to relate specific locations on the shock structure to boundary-layer survey points. The distance from the surface corresponding to these numbers is indicated in figure 39(b), which presents the pitot-pressure, static-pressure, and total-temperature profiles obtained at the station indicated in figure 39(a). Figure 39(c) shows the relative value of boundary-layer mass flow that would be obtained if the boundary-layer edge were located at each of the noted distances from the surface. The estimated distribution of the mass-flow ratio, m/m_{start}, through the interaction is shown in figure 39(d). This estimate is based on an examination of the following data: survey measurements at stations 16.1, 26.1, and 35.0; a schlieren photograph of the interaction; and the surface pressure distribution, which is shown also in figure 39(d). The measured temperature profile data were employed to determine the edge of the boundary layers at station 26.1 (circled point 2). The above data show that the reflected shock is within the boundary layer at station 26.1. Therefore, the intercept of the reflected shock with the boundary-layer edge must be located farther downstream (probably in the region of the final pressure rise), since at station 26.1, the reflected shock is located at a height of about half the boundary-layer thickness, and the angle between the reflected shock and the surface is small.

On the basis of the above information, the following observations have been made. It appears that the entrainment of mass into the boundary layer occurs in the region of the pressure rise and that most of the pressure rise occurs between the intercepts of the impinging and reflected shocks with the

edge of the boundary layer. It is concluded that the assumption of no mass addition employed in the analytical models is not in conformity with the physically observed flow. Therefore, for hypersonic flows at least, the validity of methods employing such assumptions is questionable.

CONCLUDING REMARKS

This report on the interaction of a shock wave with a boundary layer on a flat plate and a compression surface presents new experimental data for free-stream Mach numbers of 7.3 and 10.4. Local flow and wall conditions are presented for the convenience of other investigators to evaluate and use the data. Data from both other sources and the present investigation have been examined to evaluate semiempirical correlation parameters for defining certain features of the interactions. For the wide range of local flow conditions considered, it was found that reasonably good correlations were obtained for the free-interaction length for laminar flow and for the incipient and plateau pressures for both laminar and turbulent flow. No parameters were found to correlate other features of an interaction, such as plateau length, the dimensionless surface pressure distributions, and the total-interaction length.

Some analytical models for the interactions have been considered qualitatively to point out the limitations of their applicability and the validity of the assumptions employed in their formulation:

1. For interactions in which the entering flow is laminar, it has been pointed out that present analytical methods apply for weak interactions that are laminar throughout. Whereas these methods provide boundary-layer profile information and surface information, such as pressure distribution, heat transfer, and skin friction, they do not provide the shock structure of the interaction. For a strong interaction with a long separated region and for which transition may occur, the methods are inadequate.

2. For interactions in which the entering boundary layer is turbulent, some of the present semiempirical analytical models for the interaction have been discussed with respect to the validity of the assumptions employed relative to the location of mass addition and the length of the interaction with respect to the length of the surface pressure distribution. It was concluded that, to be in conformity with the physical flow, the mass addition must occur over the region of the rise in surface pressure.

An inviscid analytical model was proposed for analyzing two of the turbulent interactions. This model assumes the boundary layer to consist of an inviscid outer layer and a viscous sublayer. The viscous sublayer was neglected in this preliminary model. Details of the shock configuration and a good approximation to the surface pressure distribution were predicted using the inviscid part of the model. However, this model does not provide

surface information, such as skin friction and heat transfer, nor has it been applied to resolve the questions about the location of mass addition.

Ames Research Center
National Aeronautics and Space Administration
Moffett Field, Calif., 94035, April 21, 1969

APPENDIX

ACCURACY AND REDUCTION OF DATA

SURFACE PRESSURE MEASUREMENTS

For the range of stagnation pressures used in the laminar boundary-layer studies of the present tests, the surface pressures ahead of, or in the absence of, an impinging shock were very low. When the measured surface pressure was lower than that which could be accurately resolved by the pressure transducers, theoretical surface pressures were employed to determine the boundary-layer properties.

In the experimental study, Statham (model PA 207 TC) unbonded strain gage pressure transducers with a range of 0 to 5.0 psia were used. The quoted accuracy of these transducers is ±0.75 percent of full scale, or ±0.0375 psia; however, each transducer was calibrated individually over the low pressure range, and the accuracy was found to be somewhat better than that quoted. For both the Mach number 7.3 and 10.4 laminar boundary-layer runs, the surface pressure levels were of the order of 0.04 psia. Consequently, considerable uncertainty is present in these surface pressure data. Figure 40 shows a typical experimental surface pressure distribution for the flat-plate model without a shock-wave impingement. The Mach number is 10.4 and the total pressure is 625 psia. Also shown are the surface pressures predicted by iteration with a method-of-characteristics solution and a boundary-layer solution, and the pressure as predicted by the weak interaction theory of Bertram and Blackstock (ref. 22). It can be seen that the two predictions agree very closely with each other but are of the order of 20 percent low when compared with experimental data.

To substantiate the use of theoretical surface pressures for the present study, the pitot-pressure distribution and total-temperature distribution were predicted from a coupled boundary-layer, method-of-characteristics solution. Results of these calculations are compared with experimental data at probe station 1, for Mach number 10.4, in figures 41 and 42. In view of the excellent agreement between data and theory, it is believed reasonable to employ predicted surface pressures for the reduction of experimental data when the pressures are too low for reliable measurement.

The problem of resolution of the surface pressures did not arise in the case of the turbulent boundary-layer tests since the tunnel stagnation pressures were from 4 to 10 times those for the laminar boundary-layer runs. Figure 43 shows a typical surface pressure distribution for test conditions representative of those employed for the turbulent boundary-layer runs. The Mach number is 7.3 and the stagnation pressure is 600 psia. Pressures on the surface are of the order of 0.2 psia. The largest possible error is then about ±18 percent of the observed reading. The data for this case compare well with the values from weak interaction theory, and, as can be seen, the data scatter is well within the 18-percent band.

Downstream of shock-wave impingement, the surface pressures are sufficiently high to give accurate measurements. All surface pressures quoted herein for a laminar boundary layer employed the weak interaction theoretical surface pressures upstream of shock impingement and the measured surface pressures elsewhere.

BOUNDARY-LAYER PRESSURE MEASUREMENTS

The data of the boundary-layer surveys consist of pitot pressure, static pressure, and total temperature. The accuracy of each of these quantities contributes to the overall accuracy of the boundary-layer integral parameters.

The pitot pressures were obtained through Statham pressure transducers. Two types of cells were used, a 0- to 10-psia cell ahead of the boundary-layer shock-wave interactions, and a 0- to 50-psia cell behind the interactions. The manufacturer's quoted accuracy was ±0.75 percent of the full-scale value. The transducers used for pitot measurements were individually calibrated over the range of operation. The resulting calibration curves indicated the cells to be far more accurate than the manufacturer's quoted accuracy. Thus, even for the low Reynolds number runs, confidence may be placed in the measured pitot pressures.

As previously noted, both the surface pressure and static pressure were measured throughout the boundary layer. In most cases, as is evident in figures 7 through 10, there was good agreement between the probe static pressure and surface pressure in regions that were "clean" (i.e., essentially zero streamwise pressure gradient and no shock-wave impingement influence). On the compression surface model, however, a gradient of static pressure through the boundary layer was observed near the rear of the model. The observed gradients were felt to be qualitatively correct, even though uncertainties similar to those in the surface pressures are present in the probe static pressure levels. The surface pressure was employed in conjunction with pitot pressures to obtain the Mach numbers in all cases except when large, normal, static-pressure gradients existed in the boundary layer. In this case, the observed static-pressure gradients were used to obtain the departure in static pressure in the boundary layer from the surface pressure level.

It should be noted that the errors in determining the absolute level of Mach number are related to the errors in static pressure. However, when mass and momentum profiles are normalized with respect to the edge condition, a slight error in static-pressure level does not significantly alter the dimensionless profiles. Thus, the inaccuracies in the boundary-layer pressure measurements will not significantly affect the boundary-layer integral parameters, δ^* and θ.

TOTAL-TEMPERATURE MEASUREMENTS

Boundary-layer total-temperature measurements were obtained with an aspirated thermocouple probe calibrated under wind-tunnel conditions similar

to those encountered in the clean, flat-plate portion of the present study. A typical thermocouple calibration curve is shown in figure 44. The parameters employed in this figure are those of reference 23. However, due to the flow conditions of the present study it was necessary to obtain the calibrations over a much larger range of parameters than that in reference 23. Generally, the probe was traversed from the wall into the stream, and it was positioned in the boundary layer and held stationary for a short period of time to allow the probe to reach a thermal steady state. At least three readings were taken at each boundary-layer point. (A typical temperature difference between the last two readings was 10° R.) The temperature data in figures 7 through 10 show that, in some cases, the total temperature obtained from the probe when it was outside the boundary layer agreed well with the tunnel stagnation temperature; in other cases, the temperature differed. This probe behavior was more prevalent in the data obtained at a free-stream Mach number of 10.4 and has not been explained. However, it is believed that this type of probe is valuable in detecting where temperature changes occur in the boundary layer. Experience with this type of probe in the flow environment of the present tests has shown that more detailed probe calibrations are required to determine the sensitivity of the calibration to local flow conditions. Specifically, it is not known whether the probe recovery factor is independent of pressure gradient. It has also been found that slightly different calibrations are obtained, depending on the calibration technique employed. Two techniques were examined in the present study. In one case, the probe was mounted above the surface of a flat plate outside of the boundary layer; tunnel stagnation conditions and Mach number were varied to provide a limited range of values for the calibration parameters. In the other case, the probe was traversed through a thick boundary layer on a wind-tunnel wall to provide a wider range of calibration parameters.

It is of interest to determine the magnitude of the uncertainty in the boundary-layer integral parameters due to an uncertainty in the total temperature. A comparison between the measured total temperature and the total temperature obtained from the Mach number profile by the relation between the unity Prandtl number and Crocco temperature shows the effect of temperature variation on boundary-layer integral parameters. The two total-temperature distributions for a typical laminar case are shown in figure 45. These two different temperature distributions were used to obtain the mass flux profile (fig. 46) and the momentum profile (fig. 47). It is seen that there is a negligible difference in these profiles as a result of the imposed temperature variation; hence, the values of δ^* and θ are essentially unaffected by this imposed variation of total temperature. When the boundary layer is turbulent, the measured temperature profiles deviate from the Crocco temperature profiles. Representative experimental and Crocco temperature profiles are shown in figure 48. The temperature differences are representative of the largest encountered. These two temperature distributions for turbulent flow were employed to convert the Mach number profiles to the mass-flux and momentum profiles shown in figures 49 and 50, respectively. The uncertainty in δ^* is ± 1 percent, and in θ it is ± 10 percent. In connection with this uncertainty in δ^* and θ, it should be noted that for a given dimensionless Mach number profile (M/M_δ), the dimensionless momentum profile $[\rho u^2/(\rho u^2)_\delta]$ is independent of the total temperature. In addition, for a given Mach number profile, it may be shown that small differences in the mass-flux profile

$[\rho u/(\rho u)_\delta]$ (i.e., δ^*) produce large differences in θ. Thus, the momentum profile shown in figure 50 is unaffected by total temperature. However, the uncertainty in θ for these conditions reflects the large effect of a small variation in the mass-flow profile of figure 49.

BOUNDARY-LAYER THICKNESS

Another source of error in the integral parameters is the uncertainty in the choice of boundary-layer thickness, δ. Several methods using pitot profiles, total-temperature profiles, and schlieren photographs were employed in an attempt to determine δ. The pitot-pressure profile was relied on most heavily. The uncertainty in the selection of δ arises from the finite gradient normal to the surface in velocity at the edge of the viscous layer. In these tests the velocity gradient at the boundary-layer edge was affected by two phenomena: (1) the bow shock wave was curved due to hypersonic viscous interaction; hence, a finite entropy gradient (expressible as a velocity gradient) exists in the region of the boundary-layer edge; (2) trips employed to produce turbulent flow introduce a loss that appears as a velocity gradient. Thus, the classical definition of the boundary-layer edge (i.e., $\partial u/\partial y = 0$) as used in the analysis of experimental data is not strictly applicable. A representative velocity profile for laminar flow, along with a range of δ that could be rationally chosen, is presented in figure 51. The upper and lower extremes of δ were used to obtain the mass and momentum profiles given in figures 52 and 53. These curves were integrated to determine δ^* and θ. It was found that the uncertainties arising from the variation in δ are ±1 percent in δ^* and ±20 percent in θ. Thus, the parameters used to correlate data that involve θ may be subject to considerable error due to the uncertainty in δ alone.

REFERENCES

1. Benson, J. L.; and Maslowe, S. A.: Bluntness and Boundary-Layer Displacement Effects on Hypersonic Inlet Flowfields. J. Spacecraft and Rockets, vol. 3, no. 9. Sept. 1966, pp. 1394-1401.

2. Chapman, Dean R.; Kuehn, Donald M.; and Larson, Howard K.: Investigation of Separated Flows in Supersonic and Subsonic Streams With Emphasis on the Effect of Transition. NACA Rep. 1356, 1958.

3. Hakkinen, R. J.; Greber, I.; Trilling, L.; and Abarbanel, S. S.: The Interaction of an Oblique Shock Wave With a Laminar Boundary Layer. NASA MEMO 2-18-59W, 1959.

4. Kuehn, Donald M.: Turbulent Boundary-Layer Separation Induced by Flares on Cylinders at Zero Angle of Attack. NASA TR R-117, 1961.

5. Erdos, John; and Pallone, Adrian: Shock-Boundary-Layer Interaction and Flow Separation. Proc. 1962 Heat Transfer and Fluid Mechanics Institute. F. E. Ehlers, J. J. Kauzlarich, C. A. Sleicher, and R. E. Street, eds. Stanford Univ. Press, 1962, pp. 239-254.

6. Needham, D. A.: Laminar Separation in Hypersonic Flow. Ph.D Thesis, Univ. of London, 1965.

7. Popinski, Z.: Shock-Wave Boundary-Layer Interaction. Rep. LR 18307, Lockheed California Co., 29 June 1965.

8. Popinski, Z.; and Ehrlich, C. F.: Development Design Methods for Predicting Hypersonic Aerodynamic Control Characteristics. Final Report, 2 June 1965-15 April 1966, AFFDL TR 66-85. LR-19460, Lockheed California Co., Sept. 1966.

9. Pinckney, S. Z.: Semiempirical Method for Predicting Effects of Incident-Reflecting Shocks on the Turbulent Boundary Layer. NASA TN D-3029, 1965.

10. Lees, Lester; and Reeves, Barry L.: Supersonic Separated and Reattaching Laminar Flows: I. General Theory and Application to Adiabatic Boundary-Layer/Shock-Wave Interactions. AIAA J., vol. 2, no. 11, Nov. 1964, pp. 1907-1920.

11. Nielsen, J. N.; Lynes, L. L.; and Goodwin, F. K.: Calculation of Laminar Separation With Free Interaction by the Method of Integral Relations. Part II. Two-Dimensional Supersonic Nonadiabatic Flow and Axisymmetric Supersonic Adiabatic and Non-Adiabatic Flows. AFFDL TR 65-107, pt. II, VIDYA Rep. 203, Itek Corp., Palo Alto, Calif., Jan. 1966.

12. Holdaway, George H.; Polek, Thomas E.; and Kemp, Joseph H., Jr.: Aerodynamic Characteristics of a Blunt Half-Cone Entry Configuration at Mach Numbers of 5.2, 7.4, and 10.4. NASA TM X-782, 1963.

13. Kendall, Robert M.; and Bartlett, Eugene P.: Nonsimilar Solution of the Multicomponent Laminar Boundary Layer by an Integral Matrix Method. AIAA Paper 67-218, 1967.

14. Sorensen, Virginia L.: Computer Program for Calculating Flow Fields in Supersonic Inlets. NASA TN D-2897, 1965.

15. Crocco, L.: The Laminar Boundary Layer in Gases. Monografie Scientifiche di Aeronautica, no. 3, Dec. 1946, translated by I. Hodes and J. Castelfranco. Rep. CF 1038, North American Aviation, July 1948.

16. Kuehn, Donald M.: Experimental Investigation of the Pressure Rise Required for the Incipient Separation of Turbulent Boundary Layers in Two-Dimensional Supersonic Flow. NASA MEMO 1-21-59A, 1959.

17. Sterrett, James R.; and Emery, James C.: Extension of Boundary-Layer Separation Criteria to a Mach Number of 6.5 by Utilizing Flat Plates With Forward-Facing Steps. NASA TN D-618, 1960.

18. Levin, V.; and Fabish, T. J.: Thermal Effects of Shockwave Turbulent Boundary Layer Interaction at Mach Numbers 3 and 5. Rep. NA-62H-795, North American Aviation, Nov. 1962.

19. Sayano, S.; Bauch, H. P.; and Donnelly, R. J.: Aerodynamic Heating Due to Shock Impingement on a Flat Plate, Model DM 20. Rep. SM 41331, Missile and Space Systems Division, Douglas Aircraft Co., Aug. 1962.

20. Kutschenreuter, Paul H., Jr.; Brown, David L.; and Hoelmer, Werner: Investigation of Hypersonic Inlet Shock-Wave Boundary Layer Interaction. Part II. Continuous Flow Test and Analysis. AFFDL TR 65-36, General Electric Co., Evendale, Ohio, April 1966.

21. Rose, William C.; Murphy, John D.; and Watson, Earl C.: Interaction of an Oblique Shock Wave With a Turbulent Boundary Layer. AIAA J., vol. 6, no. 9, Sept. 1968, pp. 1792-1793.

22. Bertram, M. H.; and Blackstock, T. A.: Some Simple Solutions to the Problem of Predicting Boundary-Layer Self-Induced Pressures. NASA TN D-798, 1961.

23. Winkler, E. M.: Stagnation Temperature Probes for Use at High Supersonic Speeds and Elevated Temperatures. NAVORD Rep. 3834, U. S. Naval Ordinance Lab., White Oak, Md., Oct. 1952.

TABLE I.- TEST CONDITIONS

(a) Flat-plate model

Run	M_∞	T_{t_∞}, °R	p_{t_∞}, psia	Probe station[a]	Probe location with respect to interaction	α_L	Boundary-layer condition upstream of interaction	Remarks
F.P. 11	10.40	1850	615	2	NI[b]	None	Laminar	---
F.P. 19	10.55	1950	1830	2	NI	None	Turbulent	Note 1
F.P. 23	10.40	1850	625	1	NI	None	Laminar	---
F.P. 35	10.40	1850	628	---	None	2° to 10°	Laminar	Note 2
F.P. 37	10.55	1850	1824	---	None	2° to 10°	Turbulent	Note 1, Note 2
F.P. 40	10.55	1900	1830	1	Ahead	5°	Turbulent	Note 1
F.P. 41	10.40	1850	625	1	Ahead	5°	Laminar	---
F.P. 46	10.55	1915	1830	2	Behind	10°	Turbulent	Note 1
F.P. 48	10.55	1950	1830	3	Behind	5°	Turbulent	Note 1
F.P. 49	10.55	1850	1830	3	Behind	10°	Turbulent	Note 1
F.P. 50	10.40	1850	630	3	Behind	1.5°	Laminar	---
F.P. 51	10.40	1900	630	3	Behind	5°	Laminar	---
F.P. 59	7.34	1400	620	---	None	2° to 10°	Turbulent	Note 2, Note 3
F.P. 60	7.30	1380	112	---	None	2° to 10°	Laminar	Note 2
F.P. 61	7.30	1380	111	2	Behind	2°	Laminar	---
F.P. 62	7.30	1360	109	2	Behind	8°	Laminar	---
F.P. 64	7.30	1380	113	1	Ahead	8°	Laminar	---
F.P. 66	7.34	1470	625	2	Behind	5°	Turbulent	Note 3
F.P. 67	7.30	1440	114	2	None	None	Laminar	---
F.P. 69	7.34	1435	625	1	NI	None	Turbulent	Note 3
F.P. 71	7.34	1431	601	1	NI	None	Turbulent	Natural transition

[a]Station 1 = 16.13 inches, Station 2 = 26.13 inches, Station 3 = 35.38 inches.
[b]No interaction.
Note 1 - Three rows of trips located as shown on figure 2.
Note 2 - Shock generator swept through $2^\circ \leq \alpha_L \leq 10^\circ$.
Note 3 - One row of trips (first row) shown on figure 2.

TABLE I.- TEST CONDITIONS - Concluded

(b) Compression-surface model

Run	M_∞	T_{t_∞}, ^oR	p_{t_∞}, psia	Probe station[a]	Probe location with respect to interaction	α_L	Boundary-layer condition upstream of interaction	Remarks
C.S. 18	10.55	1860	1850	---	None	3^o	Turbulent	Note 4
C.S. 25	10.55	1790	1830	---	None	7^o	Turbulent	Note 4
C.S. 38	10.55	1930	1840	3	Ahead	14^o	Turbulent	Note 4
C.S. 46	10.55	1950	1840	2	NI[b]	None	Turbulent	Note 4
C.S. 54	7.34	1810	626	2	NI	None	Turbulent	Natural transition
C.S. 62	7.34	1890	630	---	None	7^o	Turbulent	Natural transition
C.S. 69	7.34	1900	630	---	None	17^o	Turbulent	Natural transition
C.S. 75	7.30	1640	63	3	Ahead	14^o	Laminar	---
C.S. 76	7.34	1750	625	3	Ahead	14^o	Turbulent	Natural transition
C.S. 79	7.30	1500	60	3	Ahead	7^o	Laminar	---
C.S. 93	7.30	1500	60	2	NI	None	Laminar	---
C.S. 102	7.30	1520	60	3	Ahead	3^o	Laminar	---
C.S. 104	7.34	1740	630	---	None	2^o	Turbulent	Natural transition
C.S. 105	7.30	1520	50	---	None	10^o	Laminar	---

[a]Station 1 = 16.13 inches, Station 2 = 26.13 inches, Station 3 = 35.00 inches.
[b]No interaction.
Note 4 - Two rows of trips (first two rows) shown on figure 4.

TABLE II.- INDEX TO FIGURES

Figure No.	Title
1	Flat-plate model with shock generator installed.
2	Flat-plate model instrumentation locations.
3	Compression-surface model with shock generator installed.
4	Compression-surface model and shock generator configuration.
5	Compression-surface model instrumentation locations.
6	Boundary-layer probe assembly.
7	Pitot pressure, static pressure, and total-temperature measurements at $M_\infty = 7.3$ for an initially laminar boundary layer on flat-plate model. (a) Upstream of interaction, FP 64; $p_w/p_\infty = 2.2$; $T_w/T_{t_\infty} = 0.42$. (b) Downstream of interaction, FP 61; $p_F/p_o = 1.85$; $p_w/p_\infty = 3.6$; $T_w/T_{t_\infty} = 0.40$. (c) Downstream of interaction, FP 62; $p_F/p_o = 7.0$; $p_w/p_\infty = 13.8$; $T_w/T_{t_\infty} = 0.42$.
8	Pitot pressure, static pressure, and total-temperature measurements at $M_\infty = 7.3$ for an entering turbulent boundary layer on flat-plate model. (a) Upstream of interaction, FP 69; $p_w/p_\infty = 1.8$; $T_w/T_{t_\infty} = 0.43$. (b) Downstream of interaction, FP 66; $p_F/p_o = 4.3$; $p_w/p_\infty = 7.5$; $T_w/T_{t_\infty} = 0.46$.
9	Pitot pressure, static pressure, and total-temperature measurements at $M_\infty = 10.4$ for an entering laminar boundary layer on flat-plate model. (a) Upstream of interaction, FP 41; $p_w/p_\infty = 3.0$; $T_w/T_{t_\infty} = 0.32$. (b) Downstream of interaction, FP 50; $p_F/p_o = 2.1$; $p_w/p_\infty = 5.2$; $T_w/T_{t_\infty} = 0.31$. (c) Downstream of interaction, FP 51; $p_F/p_o = 7.0$; $p_w/p_\infty = 15.3$; $T_w/T_{t_\infty} = 0.31$.

TABLE II.- INDEX TO FIGURES - Continued

Figure No.	Title
10	Pitot pressure, static pressure, and total-temperature measurements at $M_\infty = 10.4$ for an entering turbulent boundary layer on flat-plate model. (a) Upstream of interaction, FP 40; $p_w/p_\infty = 2.7$; $T_w/T_{t_\infty} = 0.40$. (b) Downstream of interaction, FP 48; $p_F/p_o = 5.8$; $p_w/p_\infty = 16.4$; $T_w/T_{t_\infty} = 0.35$. (c) Downstream of interaction, FP 49; $p_F/p_o = 21.5$; $p_w/p_\infty = 52.0$; $T_w/T_{t_\infty} = 0.38$.
11	Boundary-layer-edge conditions and integral properties for flat-plate model at Mach number 7.3. (a) Laminar flow. (b) Turbulent flow (first row of trips).
12	Boundary-layer-edge conditions and integral properties for flat-plate model at Mach number 10.4. (a) Laminar flow. (b) Turbulent flow (three rows of trips).
13	Boundary-layer-edge conditions and integral properties for compression-surface model at Mach number 7.3. (a) Laminar flow. (b) Turbulent flow (natural transition).
14	Boundary-layer-edge conditions and integral properties for compression-surface model at Mach number 10.4 - turbulent flow (two rows of trips).
15	Typical Mach number and total-temperature profiles ahead of interactions on the flat-plate model; $M_\infty = 7.3$. (a) Laminar boundary layer; FP 67. (b) Turbulent boundary layer; FP 68.
16	Typical Mach number and total-temperature profiles ahead of interactions on the compression-surface model; $M_\infty = 7.3$. (a) Laminar boundary layer; CS 93. (b) Turbulent boundary layer; CS 54.

TABLE II.- INDEX TO FIGURES - Continued

Figure No.	Title
17	Typical Mach number and total-temperature profiles ahead of interactions on the flat-plate model; $M_\infty = 10.4$.
	(a) Laminar boundary layer; FP 11.
	(b) Turbulent boundary layer; FP 19.
18	Typical Mach number and total-temperature profiles ahead of interactions on the compression-surface model; CS 46, $M_\infty = 10.4$, turbulent boundary layer.
19	Schlieren photograph and experimental surface pressure distribution for interaction on flat-plate model; $M_\infty = 7.3$.
	(a) Laminar boundary layer; FP 60, $\alpha_L = 2^\circ$.
	(b) Laminar boundary layer; FP 60, $\alpha_L = 4^\circ$.
	(c) Laminar boundary layer; FP 60, $\alpha_L = 6^\circ$.
	(d) Laminar boundary layer; FP 60, $\alpha_L = 8^\circ$.
	(e) Laminar boundary layer; FP 60, $\alpha_L = 10^\circ$.
	(f) Turbulent boundary layer; FP 59, $\alpha_L = 2^\circ$.
	(g) Turbulent boundary layer; FP 59, $\alpha_L = 6^\circ$.
	(h) Turbulent boundary layer; FP 59, $\alpha_L = 8^\circ$.
	(i) Turbulent boundary layer; FP 59, $\alpha_L = 10^\circ$.
20	Shclieren photograph and experimental surface pressure distribution for interaction on compression-surface model; $M_\infty = 7.3$.
	(a) Laminar boundary layer; CS 102, $\alpha_L = 3^\circ$.
	(b) Laminar boundary layer; CS 79, $\alpha_L = 7^\circ$.
	(c) Laminar boundary layer; CS 105, $\alpha_L = 10^\circ$.
	(d) Laminar boundary layer; CS 75, $\alpha_L = 14^\circ$.
	(e) Turbulent boundary layer; CS 62, $\alpha_L = 7^\circ$.
	(f) Turbulent boundary layer; CS 76, $\alpha_L = 14^\circ$.
	(g) Turbulent boundary layer; CS 69, $\alpha_L = 17^\circ$.

TABLE II.- INDEX TO FIGURES - Continued

Figure No.	Title
21	Schlieren photograph and experimental surface pressure distribution for interaction on flat-plate model; $M_\infty = 10.4$. (a) Laminar boundary layer; FP 35, $\alpha_L = 3^\circ$. (b) Laminar boundary layer; FP 35, $\alpha_L = 5^\circ$. (c) Turbulent boundary layer; FP 37, $\alpha_L = 5^\circ$. (d) Turbulent boundary layer; FP 37, $\alpha_L = 8^\circ$. (e) Turbulent boundary layer; FP 37, $\alpha_L = 10^\circ$.
22	Schlieren photograph and experimental surface pressure distribution for interaction on compression-surface model; $M_\infty = 10.4$. (a) Turbulent boundary layer; CS 18, $\alpha_L = 3^\circ$. (b) Turbulent boundary layer; CS 25, $\alpha_L = 7^\circ$. (c) Turbulent boundary layer; CS 38, $\alpha_L = 14^\circ$.
23	Comparison of experimental velocity profile with "law-of-the-wall" profiles; FP 19, $M_\infty = 10.4$.
24	Composite pressure distribution for flat-plate model; $M_\infty = 7.3$. (a) Laminar boundary layer. (b) Turbulent boundary layer.
25	Composite pressure distribution for compression-surface model; $M_\infty = 7.3$. (a) Laminar boundary layer. (b) Turbulent boundary layer.
26	Correlation of incipient separation pressures. (a) Laminar boundary layer. (b) Turbulent boundary layer.
27	Correlation of plateau pressures. (a) Laminar boundary layer. (b) Turbulent boundary layer.
28	Dimensionless pressure distribution for separated laminar boundary layers. (a) Free interaction region. (b) Reattachment region.

TABLE II.- INDEX TO FIGURES - Continued

Figure No.	Title
29	Dimensionless pressure distribution for unseparated interactions. (a) Laminar boundary layer. (b) Turbulent boundary layer.
30	Correlation of free interaction length. (a) Laminar boundary layer. (b) Turbulent boundary layer.
31	Comparison of plateau length data using parameter of Hakkinen; laminar boundary layer.
32	Variation of Pinckney parameter, Y/l_1 with the pressure coefficient across the interaction; turbulent boundary layer.
33	Variation of total interaction length with impinging shock strength; turbulent boundary layer.
34	Correlation of total interaction length; laminar boundary layer.
35	Example of two simple interaction models superimposed on schlieren photograph; FP 66, $M_\infty = 7.3$, $\alpha_L = 5^\circ$, turbulent boundary layer.
36	Comparison of predicted and experimental shock-wave configuration and surface pressure distribution; FP 59, $M_\infty = 7.4$, turbulent boundary layer. (a) $\alpha_L = 2^\circ$ (b) $\alpha_L = 8^\circ$
37	Variation of downstream integral parameters with pressure rise. (a) Displacement thickness. (b) Momentum thickness.
38	Variation of downstream boundary-layer mass flow with pressure rise.
39	Details of a turbulent boundary-layer shock-wave interaction; $M_\infty = 10.4$, $\alpha_L = 10^\circ$. (a) Surface pressure and shock configuration, FP 49. (b) Probe surveys, FP 46. (c) Normalized mass-flow variation, FP 46 and FP 49. (d) Longitudinal distribution of mass flow and surface pressure, FP 46 and FP 49.

TABLE II.- INDEX TO FIGURES - Continued

Figure No.	Title
40	Comparison of pressure data for a typical low-pressure test condition with results obtained from weak interaction theory (ref. 22) and the method of characteristics; FP 23, $M_\infty = 10.4$.
41	Comparison of measured and predicted pitot pressure at probe station 1; FP 23, $M_\infty = 10.4$, laminar boundary layer.
42	Comparison of experimental and predicted total-temperature profiles; FP 23, $M_\infty = 10.4$, laminar boundary layer.
43	Comparison of pressure data for a typical high-pressure test condition with results obtained from weak interaction theory (ref. 22); FP 71, $M_\infty = 7.3$.
44	Typical total-temperature calibration curves for the probe temperature recovery factor.
45	Comparison of experimental total-temperature profile with results obtained by using the experimental Mach number distribution and the Crocco relationship (Prandtl number = 1.0); FP 23, $M_\infty = 10.4$, laminar boundary layer.
46	Mass-flux profile in the boundary layer computed using experimental and Crocco temperature distributions; FP 23, $M_\infty = 10.4$, laminar boundary layer.
47	Momentum-flux profile in the boundary layer computed using experimental and Crocco temperature distributions; FP 23, $M_\infty = 10.4$, laminar boundary layer.
48	Comparison of experimental total-temperature profile with results obtained using the experimental Mach number distribution and the Crocco relationship (Prandtl number = 1.0); FP 19, $M_\infty = 10.4$, turbulent boundary layer.
49	Mass-flux profile in the boundary layer computed using experimental and Crocco temperature distributions; FP 19, $M_\infty = 10.4$, turbulent boundary layer.
50	Momentum-flux profile in the boundary layer computed using experimental and Crocco temperature distributions; FP 19, $M_\infty = 10.4$, turbulent boundary layer.
51	Typical velocity distribution showing uncertainty in boundary-layer thickness; FP 23, $M_\infty = 10.4$, laminar boundary layer.

TABLE II.- INDEX TO FIGURES - Concluded

Figure No.	Title
52	The effect of the choice of boundary-layer thickness on the mass-flux profile; FP 23, M_∞ = 10.4, laminar boundary layer.
53	The effect of the choice of boundary-layer thickness on the momentum-flux profile; FP 23, M_∞ = 10.4, laminar boundary layer.

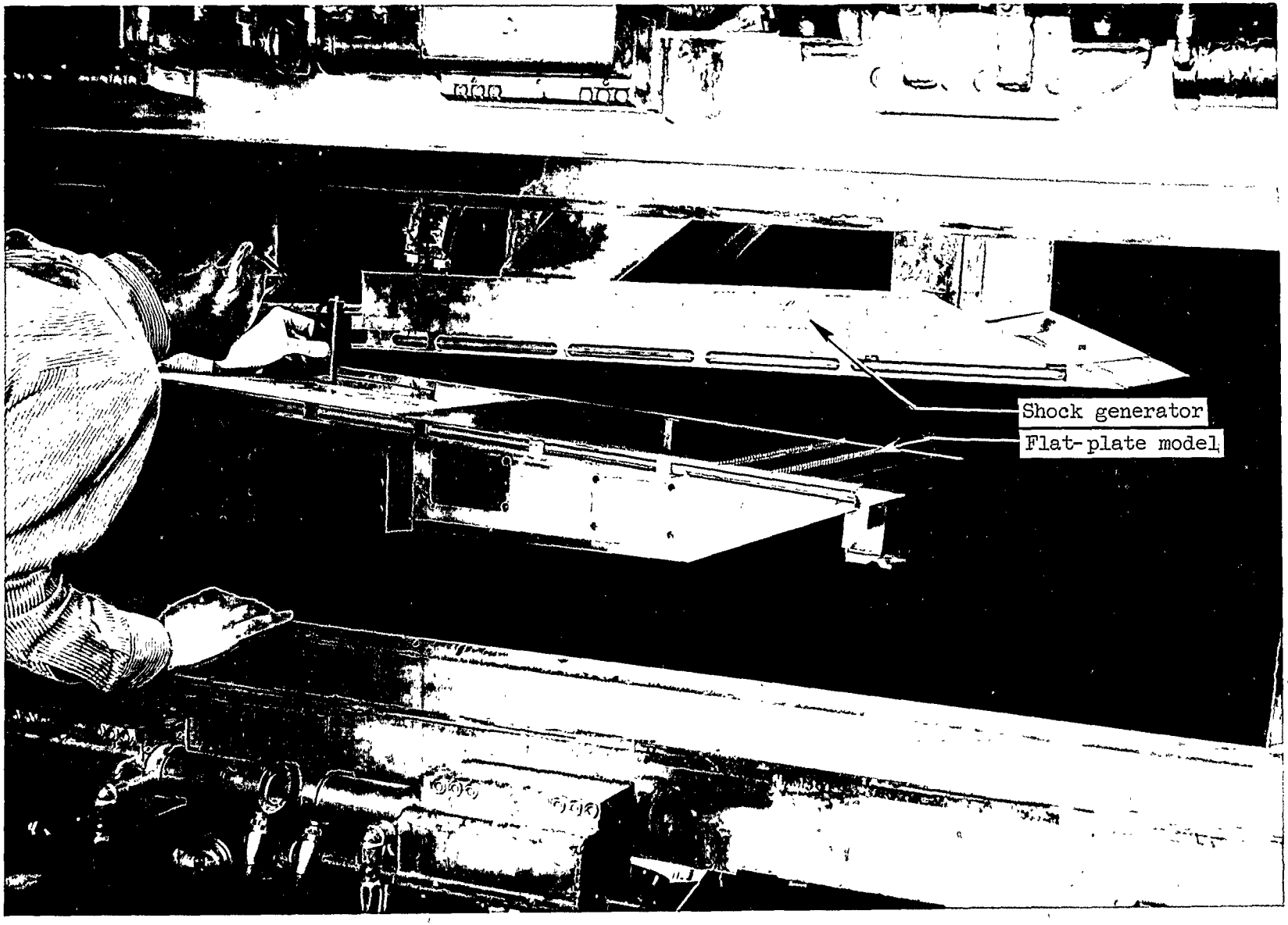

A-34045

Figure 1.- Flat-plate model with shock generator installed.

Surface Pressure Orifice Locations			
x (inches)	Offset (inches)	x (inches)	Offset (inches)
1.50	0	26.56	-0.875
4.00	0	27.06	-0.875
6.06	0	27.50	-0.875
8.00	0	27.94	0
10.00	0	28.44	0
12.00	0	28.94	0
13.75	0	29.44	-0.875
14.38	-0.875	29.94	-0.875
15.00	0	30.50	-0.875
15.56	0	31.00	0
16.13	0.500	31.50	0
16.13	0	32.00	0
16.13	-0.500	32.50	0
16.63	-0.875	33.00	0
17.13	-0.875	33.62	-0.875
17.56	-0.875	34.25	0
18.00	0	34.81	0
18.50	0	35.38	0.500
19.00	0	35.38	0
19.50	-0.875	35.38	-0.500
20.00	-0.875	35.38	-0.875
20.50	-0.875	36.38	-0.875
21.00	0	36.88	-0.875
21.50	0	37.19	0
22.00	0	37.69	0
22.50	0	38.19	0
23.00	0	38.75	-0.875
23.38	0	39.25	-0.875
23.75	0	42.00	0
24.32	-0.875	43.00	0
24.94	0	44.00	0
25.50	0	45.00	0
26.06	0.500	46.00	0
26.06	0	47.00	0
26.06	-0.500		

Thermocouple Locations											
T	1	2	3	4	5	6	7	8	9	10	11
x (inches)	2.44	5.25	9.50	16.50	21.00	24.00	27.00	30.00	33.00	36.00	39.00

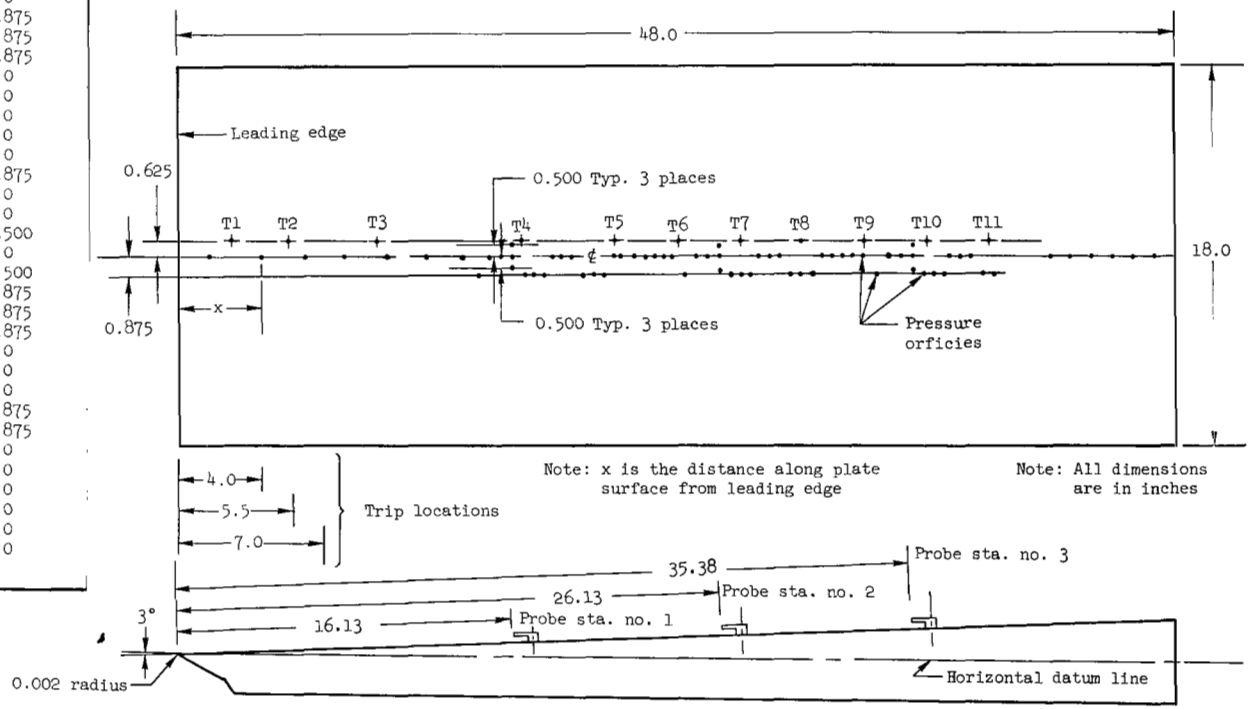

Figure 2.- Flat-plate model instrumentation locations.

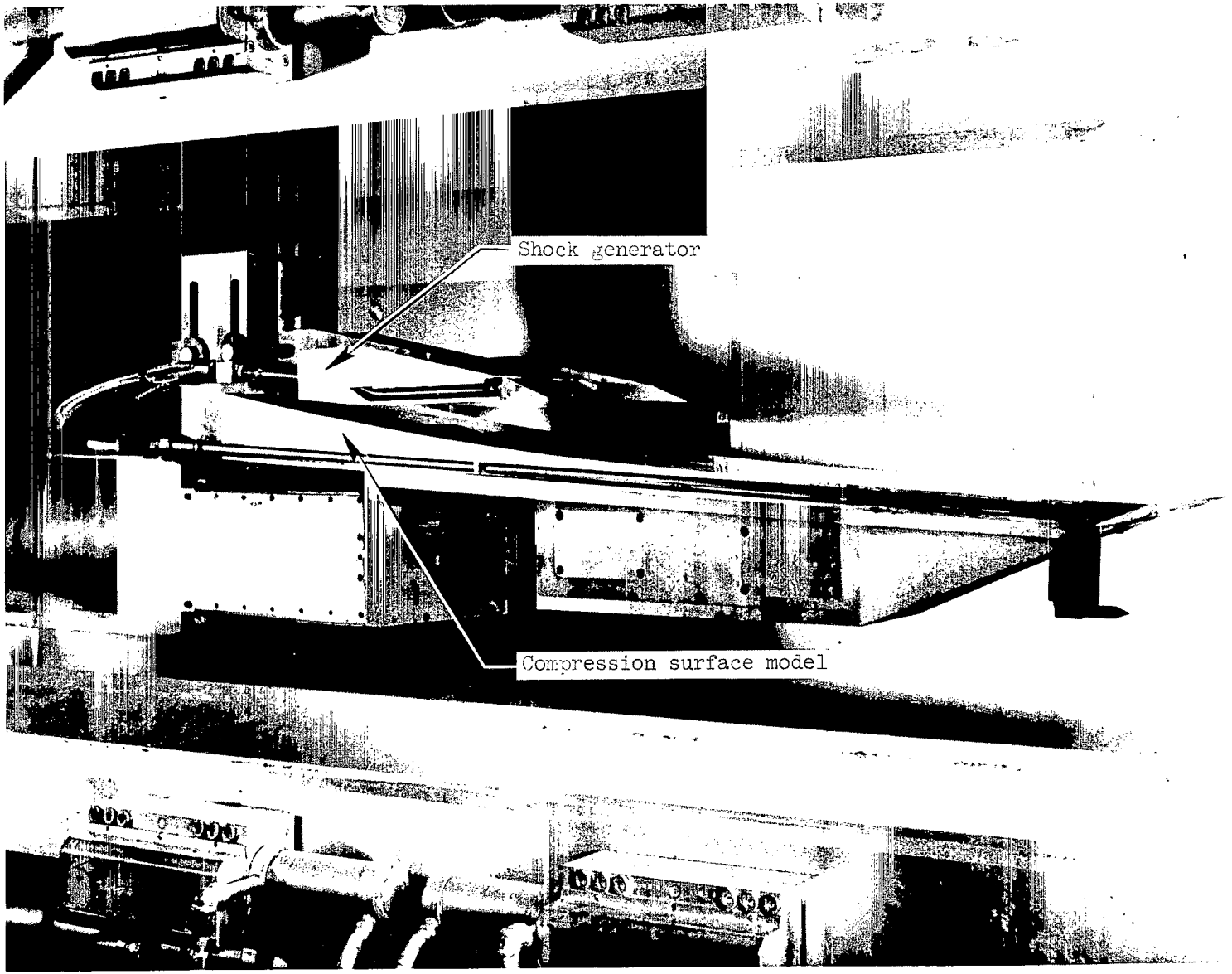

A-34803

Figure 3.- Compression-surface model with shock generator installed.

Ramp Surface Coordinates	
x (inches)	Y (inches)
0	0
10	0.524
11	0.578
12	0.634
13	0.692
14	0.813
15	0.813
16	0.874
17	0.936
18	1.000
19	1.066
20	1.136
21	1.210
22	1.286
23	1.366
24	1.450
25	1.536
26	1.626
27	1.720
28	1.820
29	1.926
30	2.038
31	2.156
32	2.280
33	2.408
34	2.540
35	2.676
36	2.816
37	2.960
38	3.108
39	3.260
40	3.414
41	3.572
42	3.734
43	3.900
44	4.070
45	4.244
46	4.422
47	4.604
48	4.790

Shock Generator Coordinates	
x (inches)	Y (inches)
28	4.188
29	4.198
30	4.208
31	4.218
32	4.228
33	4.238
34	4.250
35	4.266
36	4.288
37	4.318
38	4.360
39	4.418
40	4.494
41	4.586
42	4.690
43	4.802

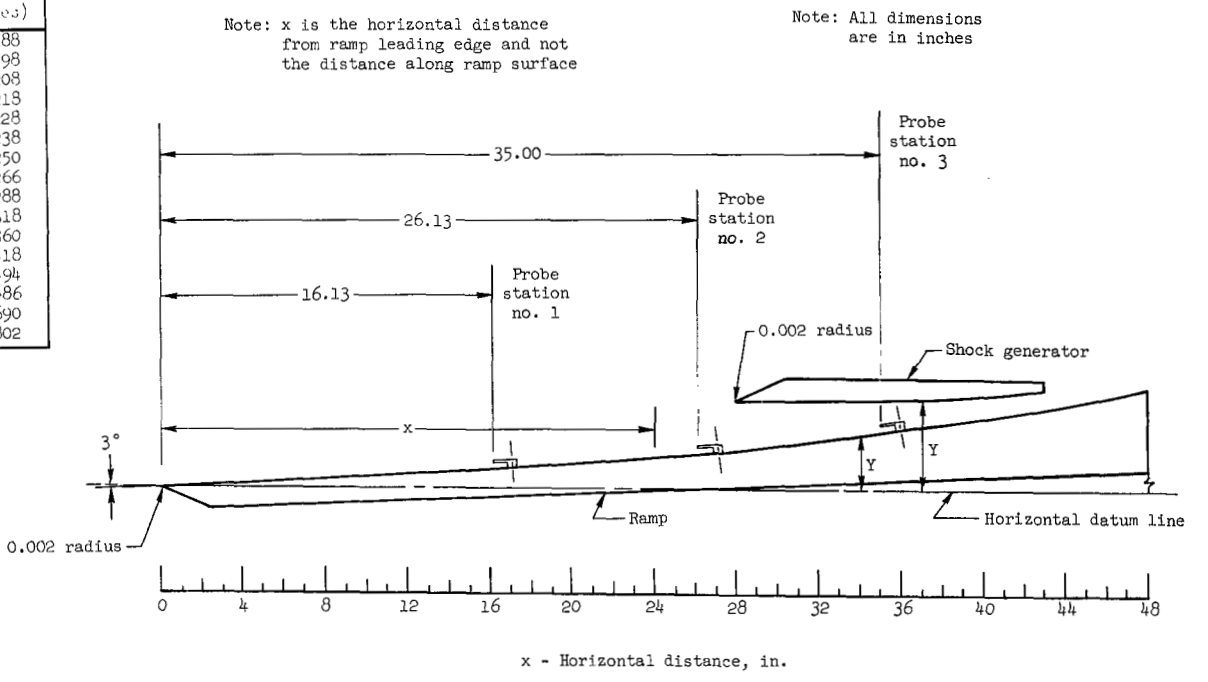

Figure 4.- Compression-surface model and shock generator configuration.

Surface Pressure Orifice Locations			
x (inches)	Offset (inches)	x (inches)	Offset (inches)
1.50	0	29.00	0
3.75	0	29.50	-0.875
6.00	0	30.00	-0.875
8.00	0	30.50	-0.875
10.00	0	31.00	0
12.00	0	31.50	0
14.00	-0.875	32.00	0
14.50	-0.875	32.50	0
15.00	0	33.00	-0.875
15.50	0	33.50	-0.875
16.13	0.500	34.00	0
16.13	0	34.50	0
16.13	-0.500	35.00	0.500
16.63	-0.875	35.00	0
17.13	-0.875	35.00	-0.500
17.76	-0.875	35.50	-0.875
18.00	0	36.00	-0.875
18.50	0	36.50	-0.875
19.00	0	37.00	0
19.50	-0.875	37.50	0
20.00	-0.875	38.00	0
20.50	-0.875	38.50	-0.875
21.00	0	39.00	-0.875
21.50	0	42.00	0
22.00	0	43.00	0
22.50	0	44.00	0
23.00	0	45.00	0
23.50	0	46.00	0
24.00	-0.875	47.00	0
24.50	-0.875	39.50	-0.875
25.00	0	40.00	0
25.50	0	40.50	0
26.13	0.500	41.00	0
26.13	0	41.50	0
26.13	-0.500	42.50	0
26.63	-0.875	43.50	0
27.13	0.875	44.50	0
27.56	-0.875	45.50	0
28.00	0	46.50	0
28.50	0	47.50	0

Thermocouple Locations											
T	1	2	3	4	5	6	7	8	9	10	11
x (inches)	2.44	5.25	9.50	16.00	20.50	23.50	26.50	29.50	32.50	35.50	38.50

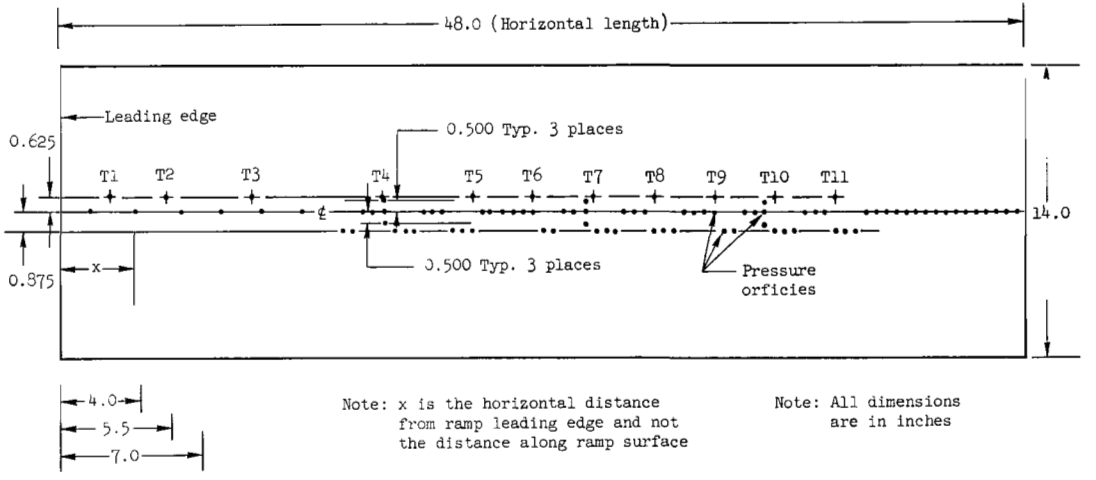

Figure 5.- Compression-surface model instrumentation locations.

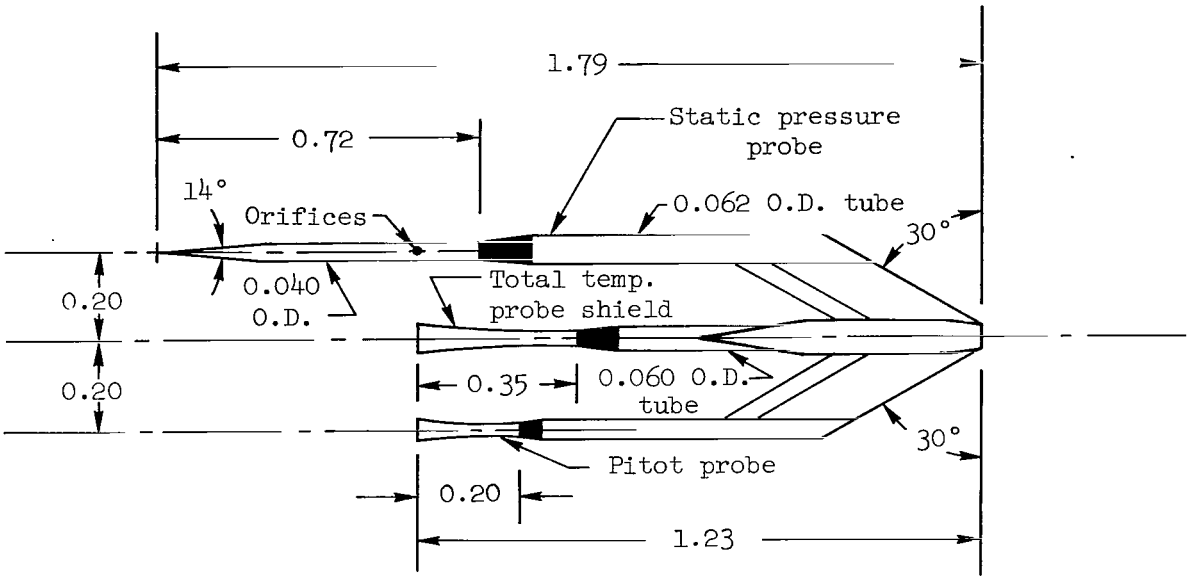

Note: All dimensions are in inches

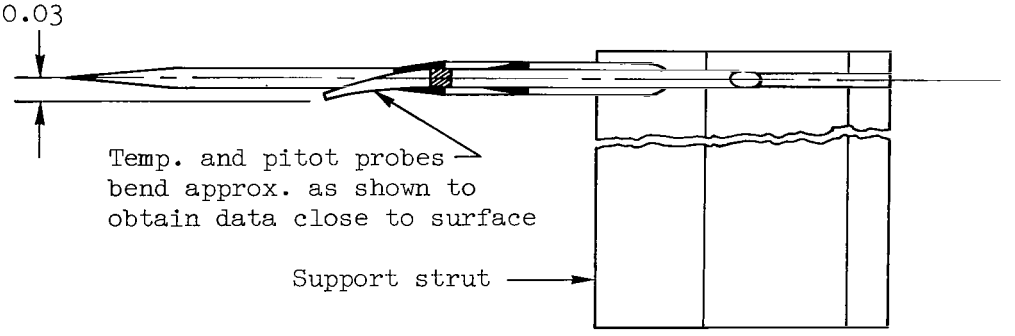

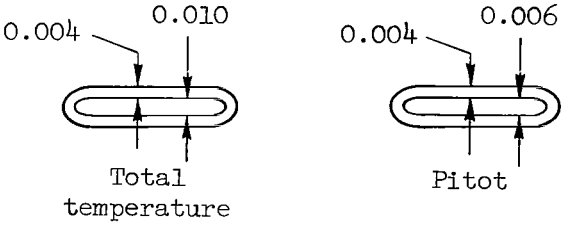

Detail of probe tips

Figure 6.- Boundary-layer probe assembly.

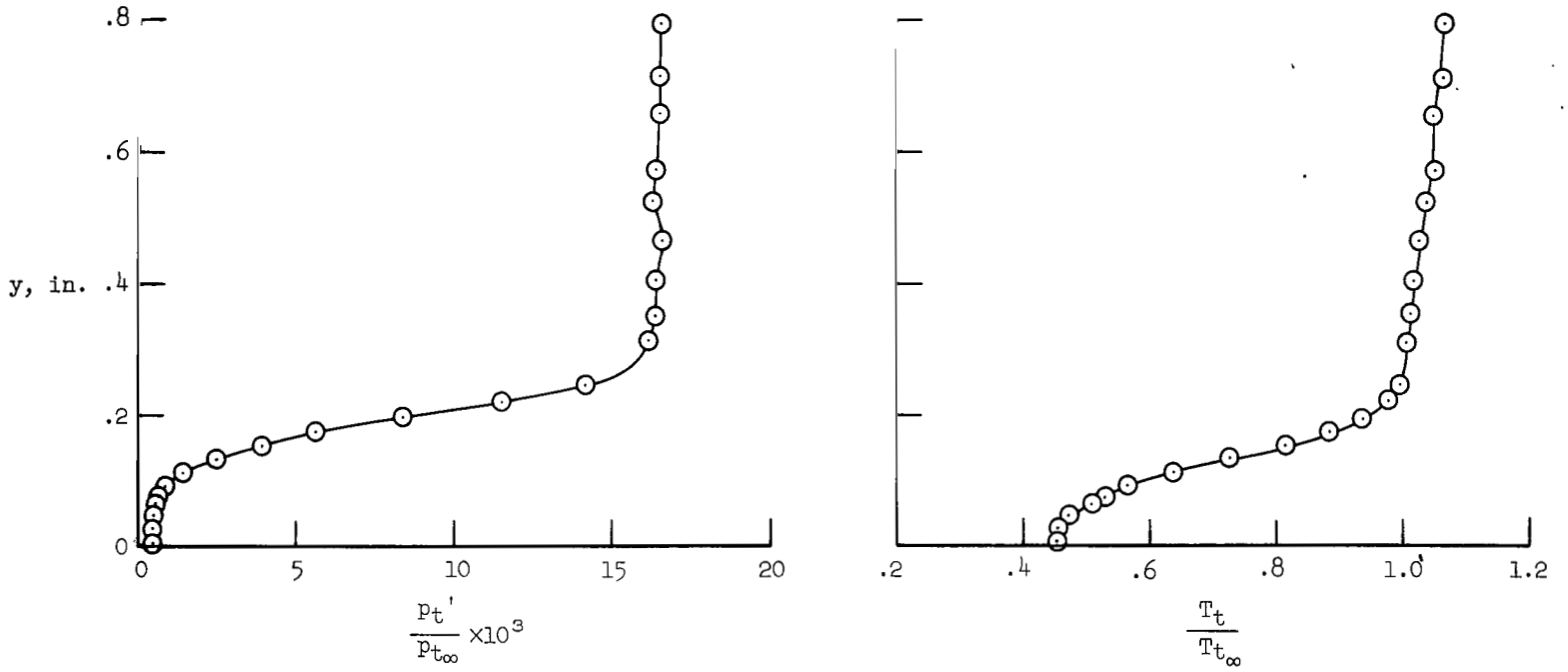

(a) Upstream of interaction; FP 64, $p_w/p_\infty = 2.2$, $T_w/T_{t_\infty} = 0.42$.

Figure 7.- Pitot pressure, static pressure, and total-temperature measurements at $M_\infty = 7.3$ for an initially laminar boundary layer on flat-plate model.

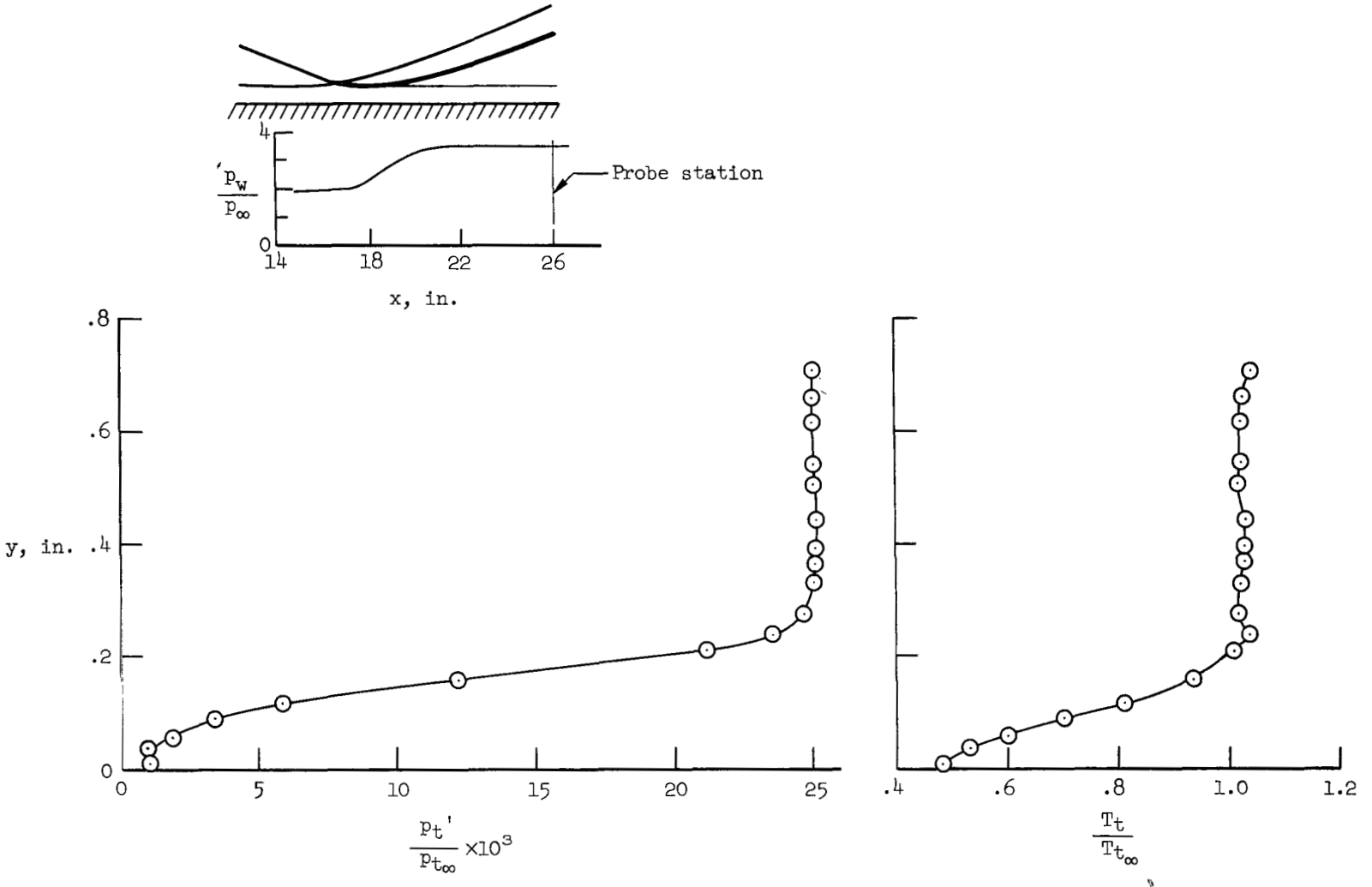

(b) Downstream of interaction, FP 61; $p_F/p_o = 1.85$; $p_w/p_\infty = 3.6$; $T_w/T_{t_\infty} = 0.40$.

Figure 7.- Continued.

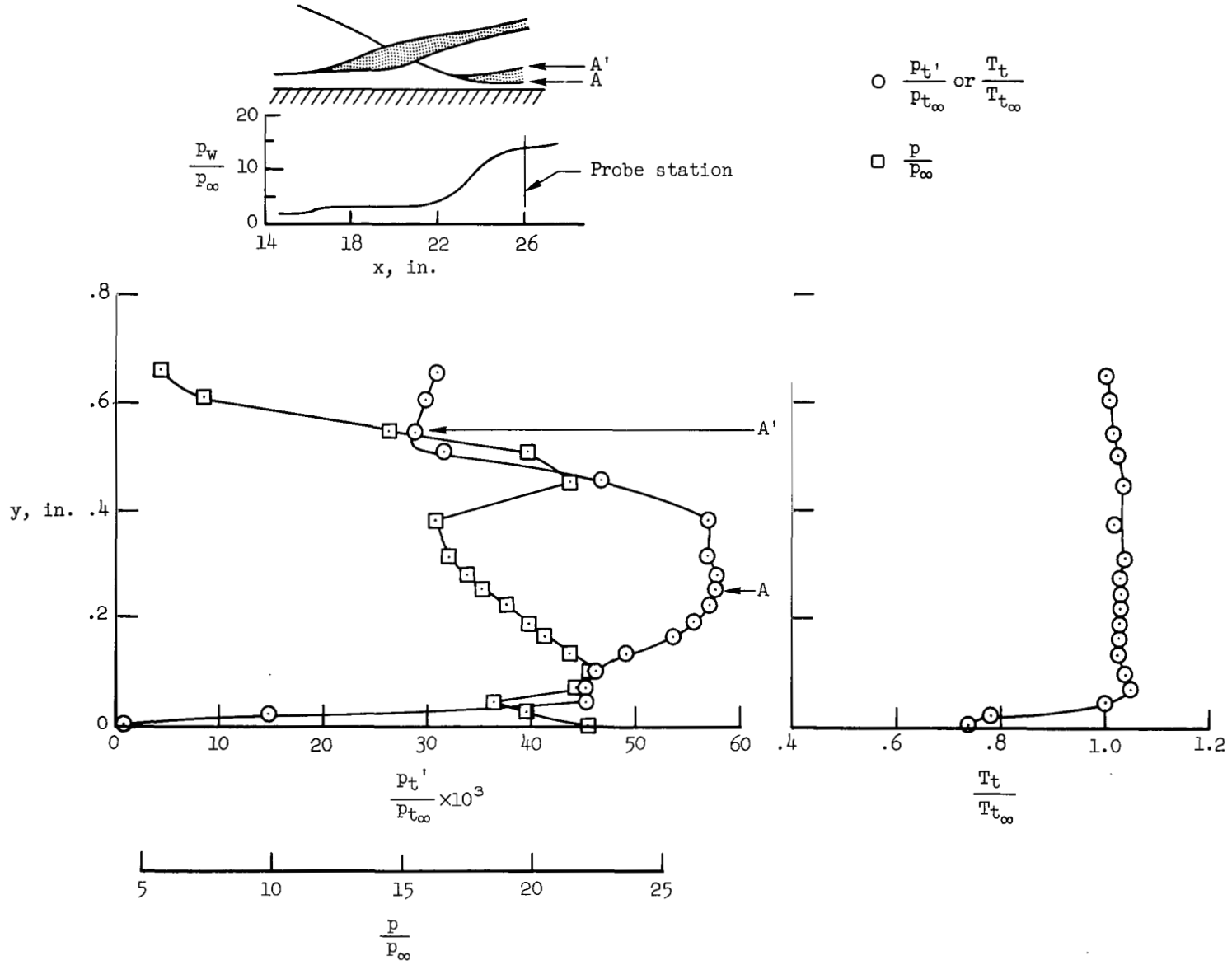

(c) Downstream of interaction, FP 62; $p_F/p_o = 7.0$; $p_w/p_\infty = 13.8$; $T_w/T_{t_\infty} = 0.42$.

Figure 7.- Concluded.

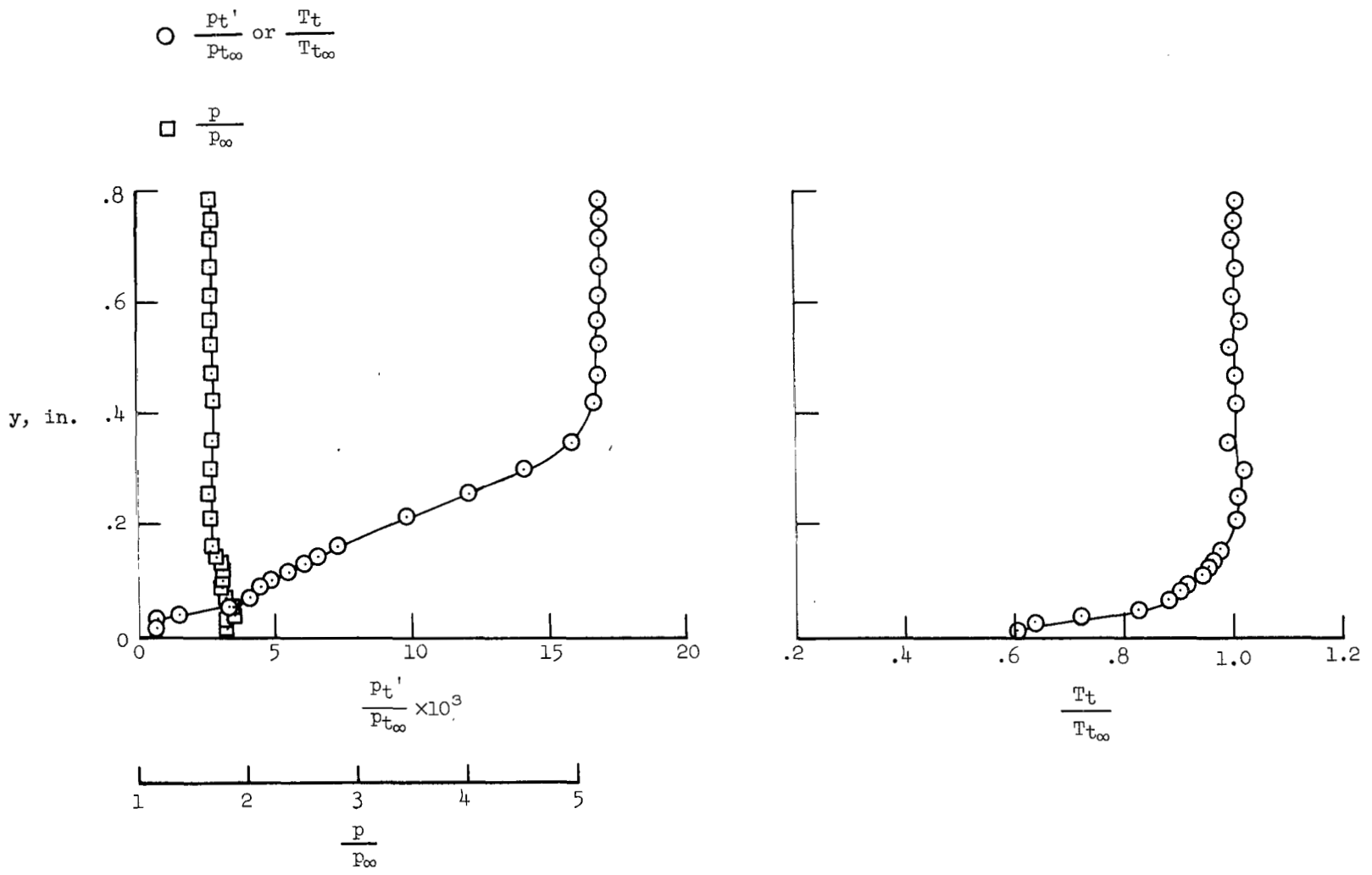

(a) Upstream of interaction, FP 69; $p_w/p_\infty = 1.8$; $T_w/T_{t_\infty} = 0.43$.

Figure 8.- Pitot pressure, static pressure, and total-temperature measurements at $M_\infty = 7.3$ for an entering turbulent boundary layer on flat-plate model.

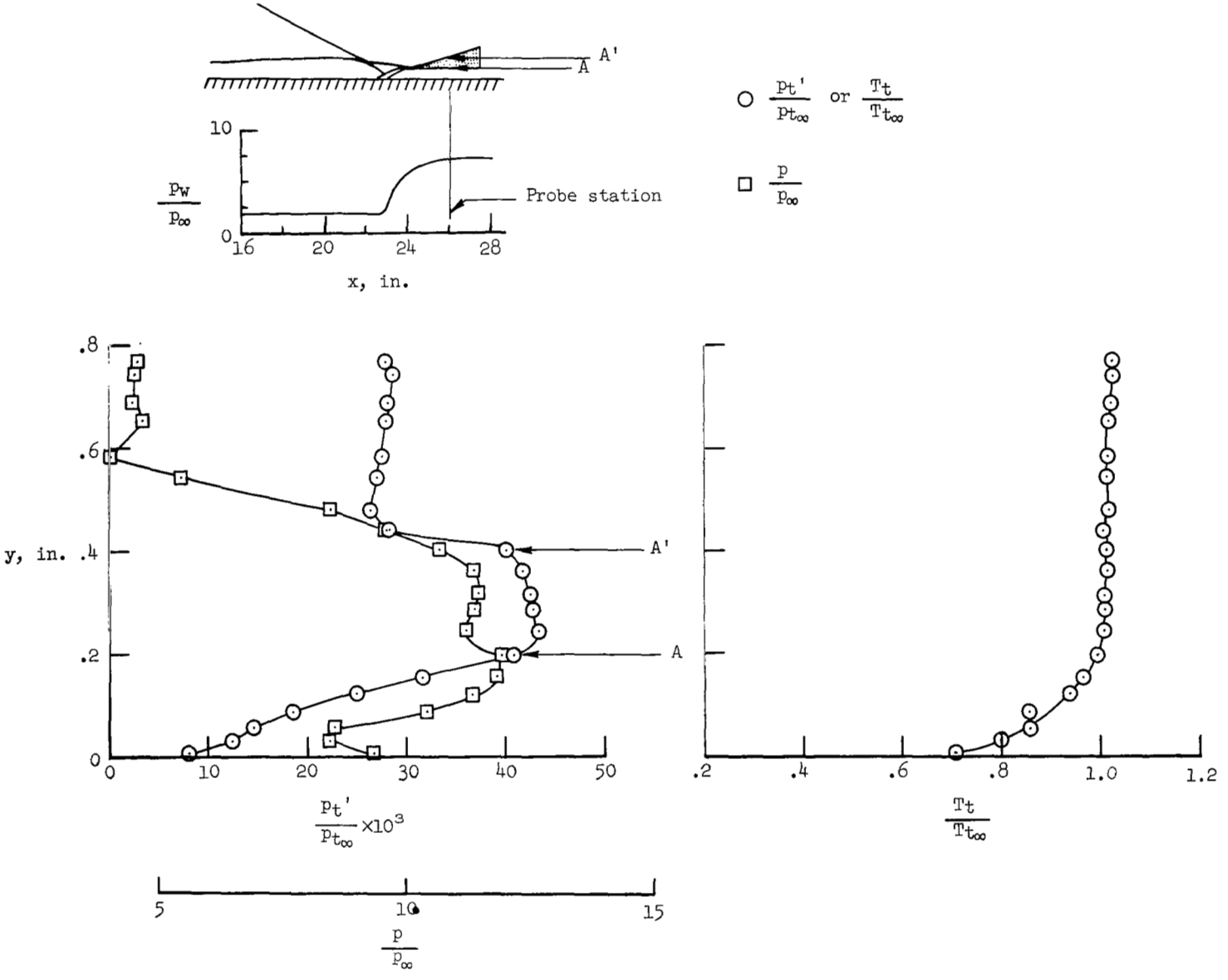

(b) Downstream of interaction, FP 66; $p_F/p_o = 4.3$; $p_w/p_\infty = 7.5$; $T_w/T_{t_\infty} = 0.46$.

Figure 8.- Concluded.

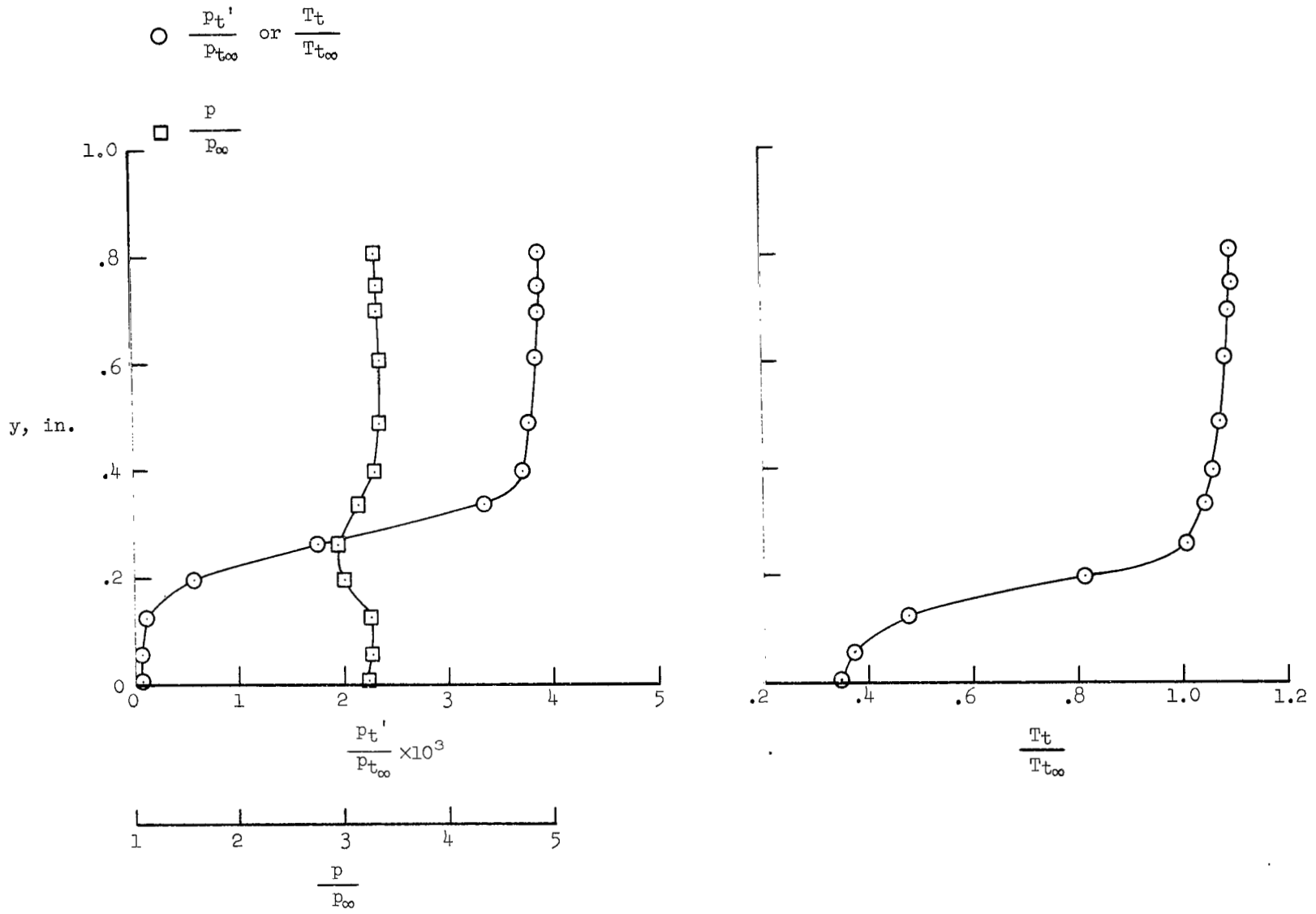

(a) Upstream of interaction, FP 41; $p_w/p_\infty = 3.0$; $T_w/T_{t\infty} = 0.32$.

Figure 9.- Pitot pressure, static pressure, and total-temperature measurements at $M_\infty = 10.4$ for an entering laminar boundary layer on flat-plate model.

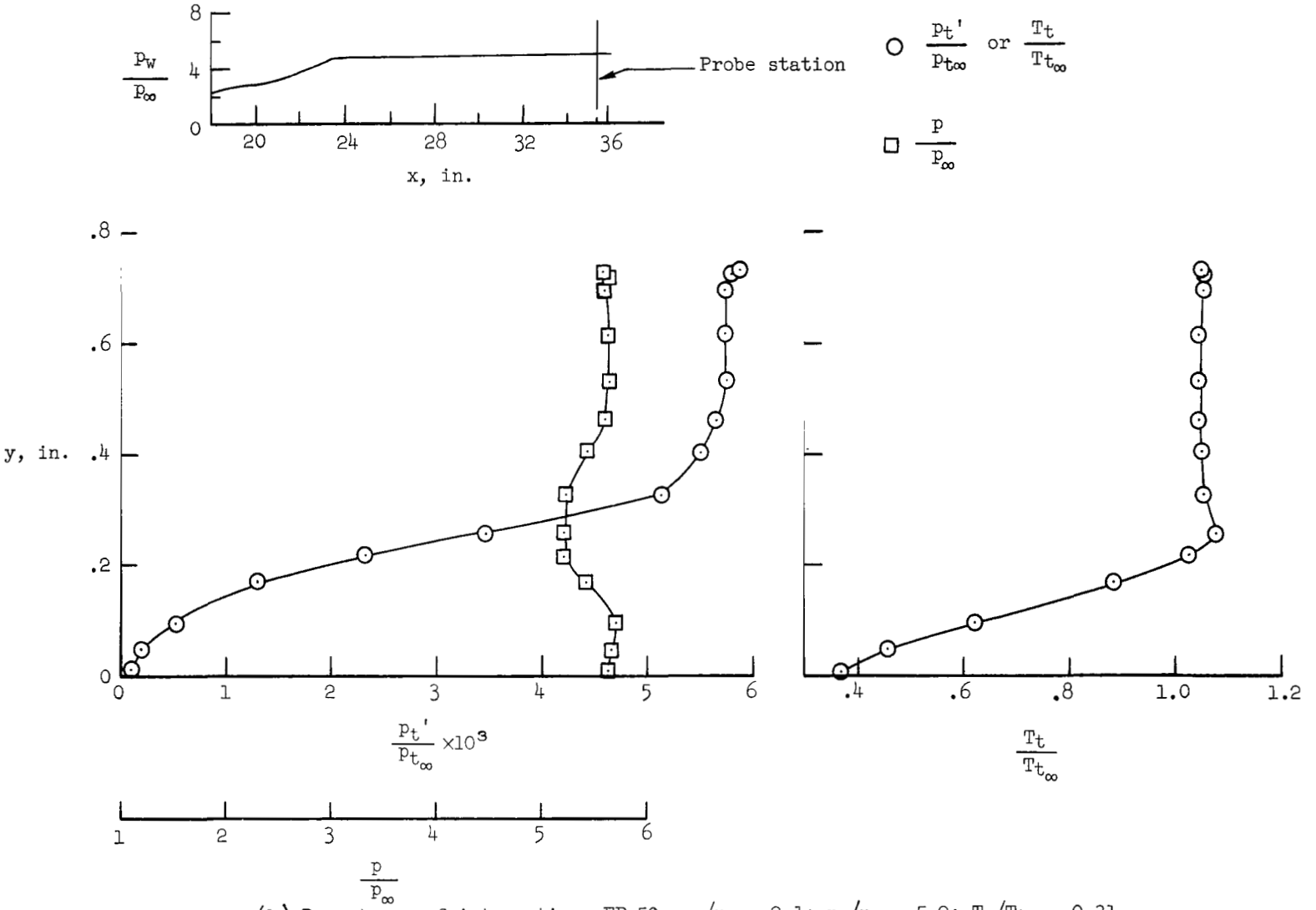

(b) Downstream of interaction, FP 50; $p_F/p_O = 2.1$; $p_w/p_\infty = 5.2$; $T_w/T_{t\infty} = 0.31$.

Figure 9.- Continued.

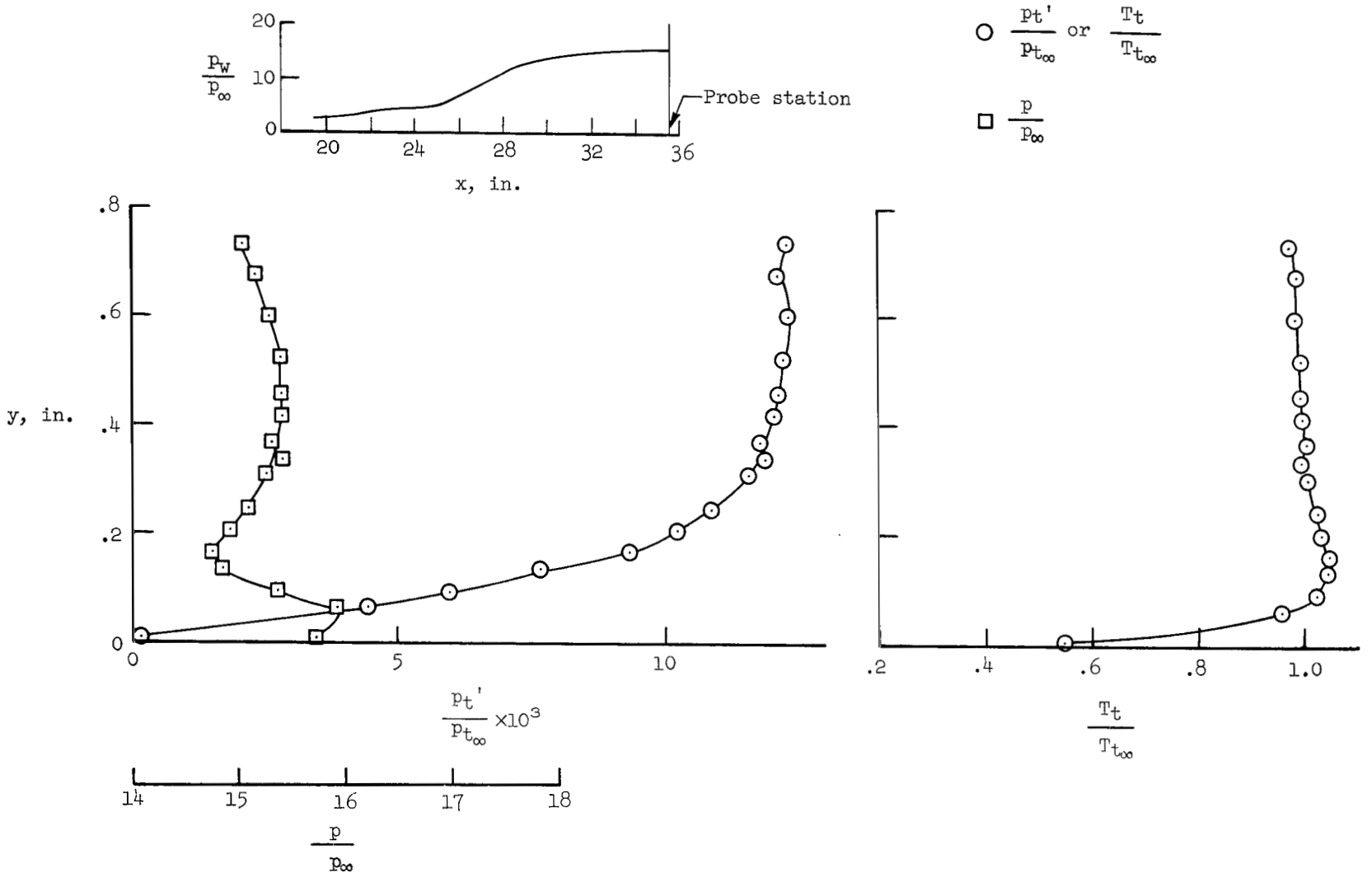

(c) Downstream of interaction, FP 51; $p_F/p_O = 7.0$; $p_w/p_\infty = 15.3$; $T_w/T_{t_\infty} = 0.31$.

Figure 9.- Concluded.

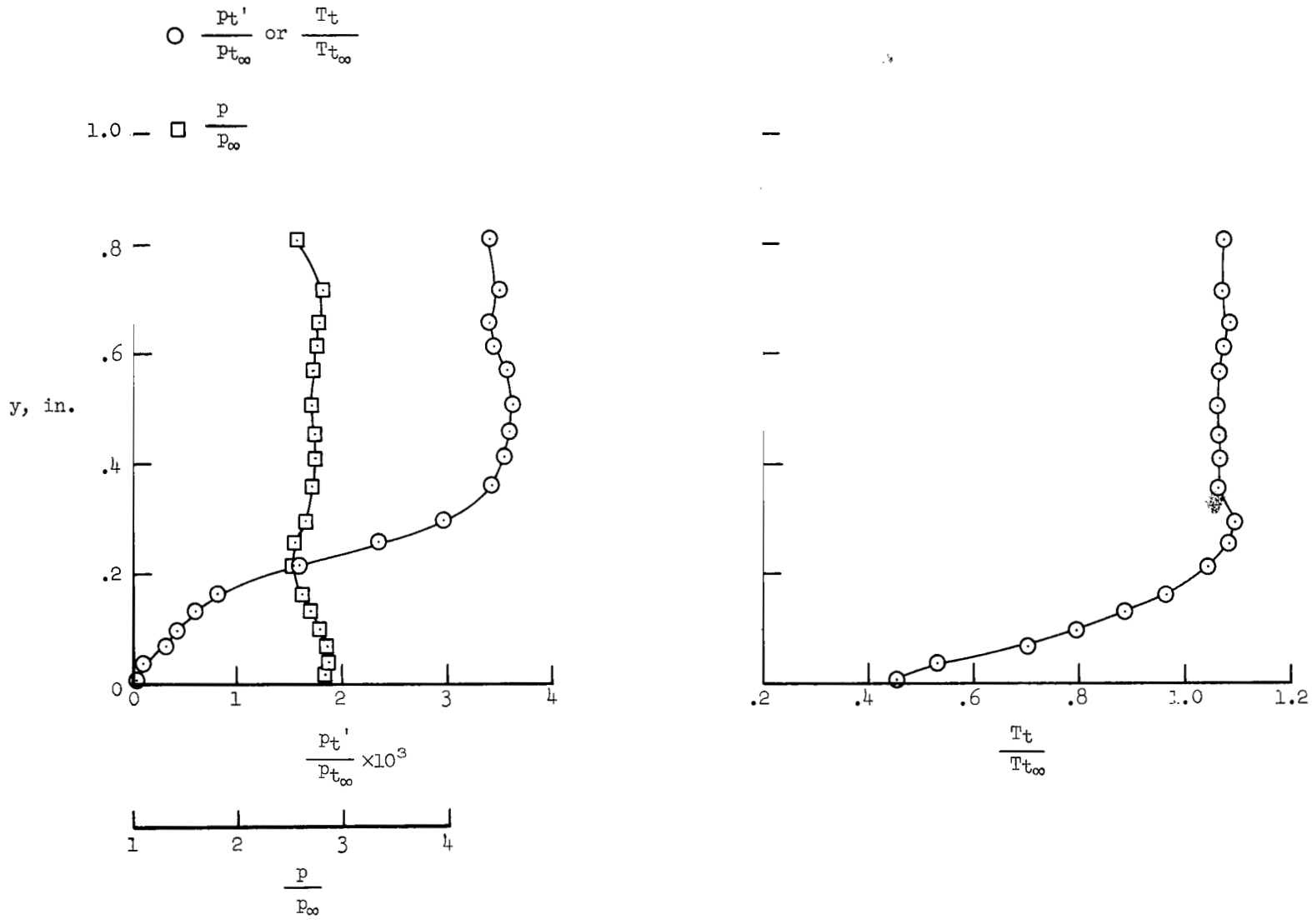

(a) Upstream of interaction, FP 40; $p_w/p_\infty = 2.7$; $T_w/T_{t_\infty} = 0.40$.

Figure 10.- Pitot pressure, static pressure, and total-temperature measurements at $M_\infty = 10.4$ for an entering turbulent boundary layer on flat-plate model.

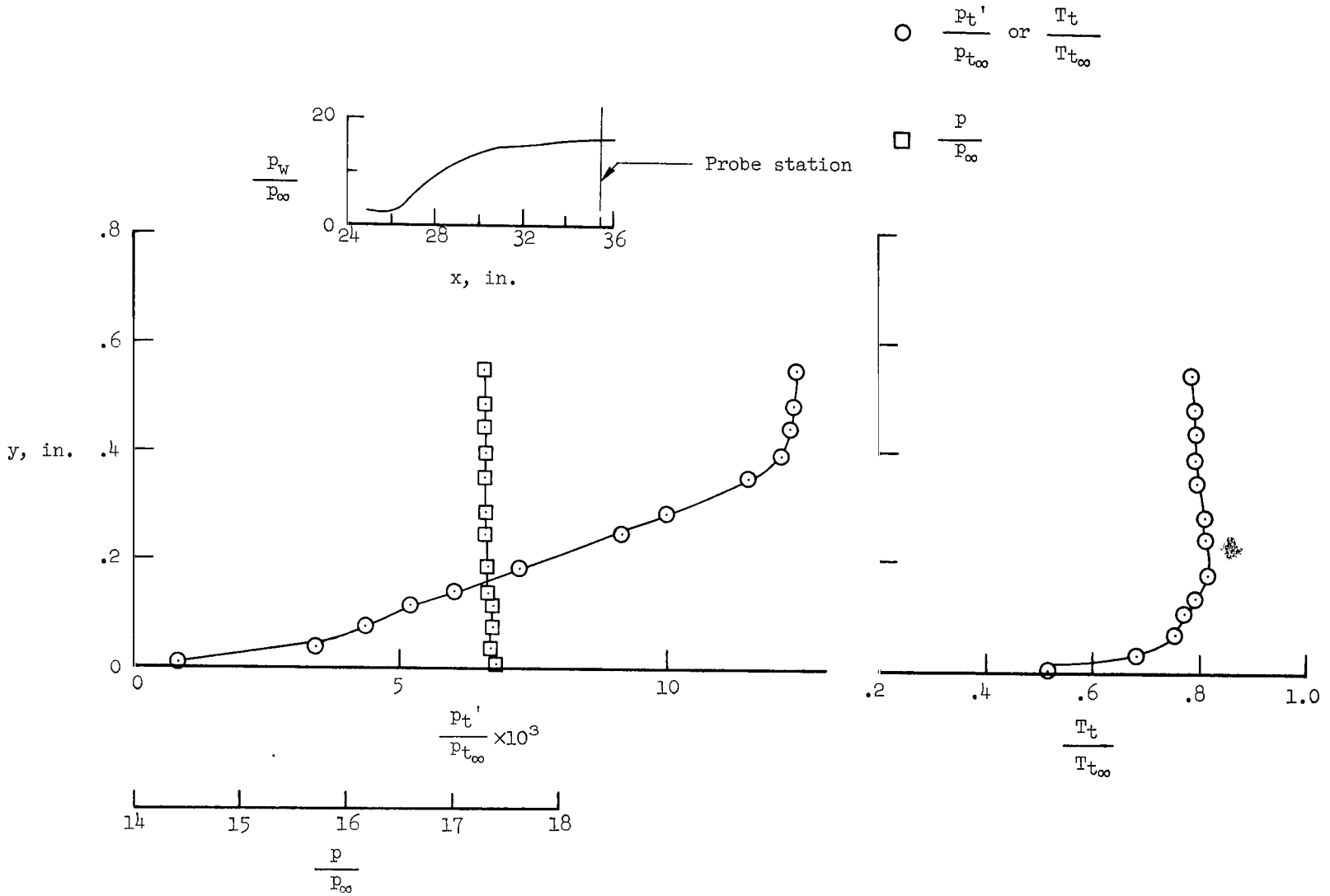

(b) Downstream of interaction, FP 48; $p_F/p_o = 5.8$; $p_w/p_\infty = 16.4$; $T_w/T_{t_\infty} = 0.35$.

Figure 10.- Continued.

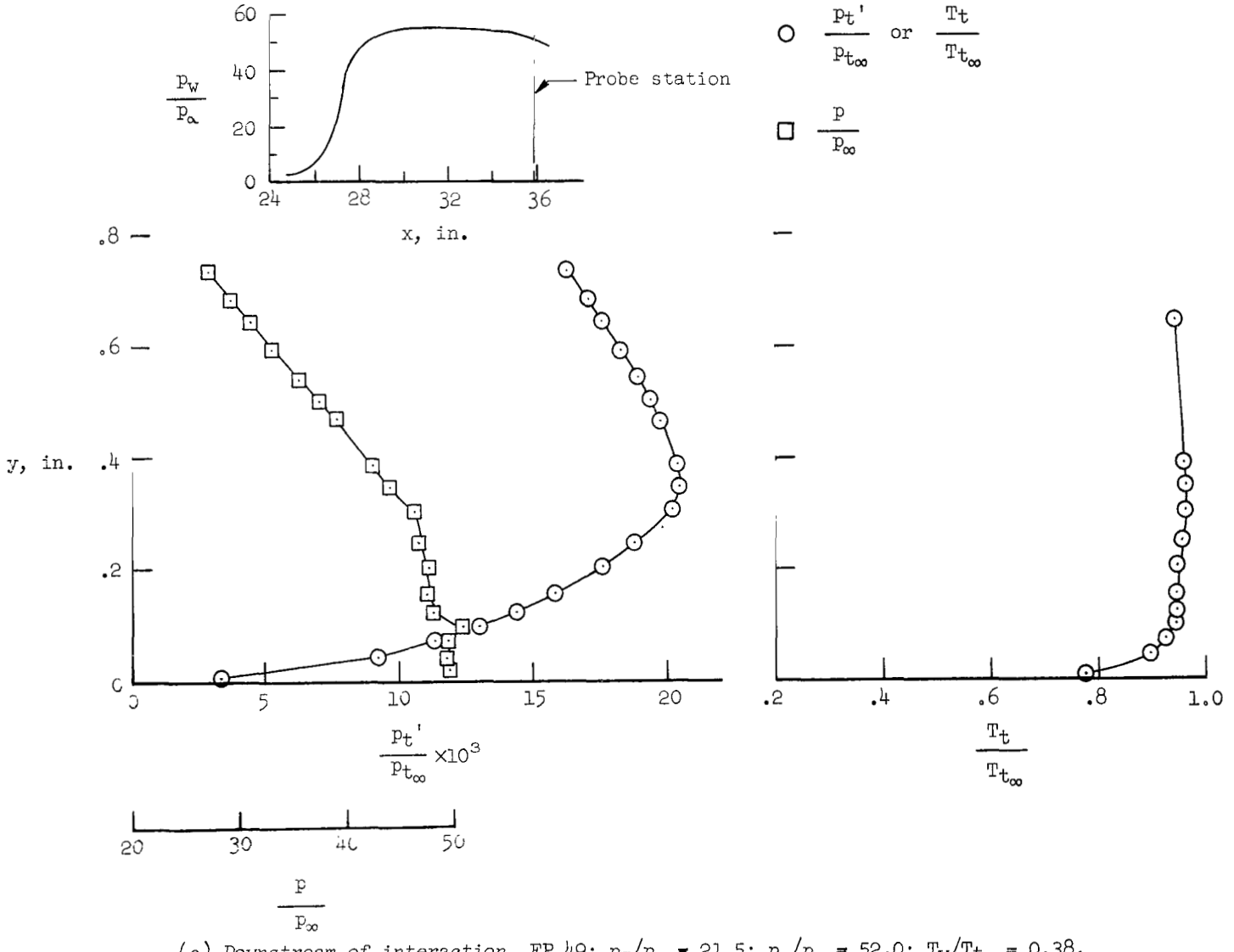

(c) Downstream of interaction, FP 49; $p_F/p_O = 21.5$; $p_w/p_\infty = 52.0$; $T_w/T_{t_\infty} = 0.38$.

Figure 10.- Concluded.

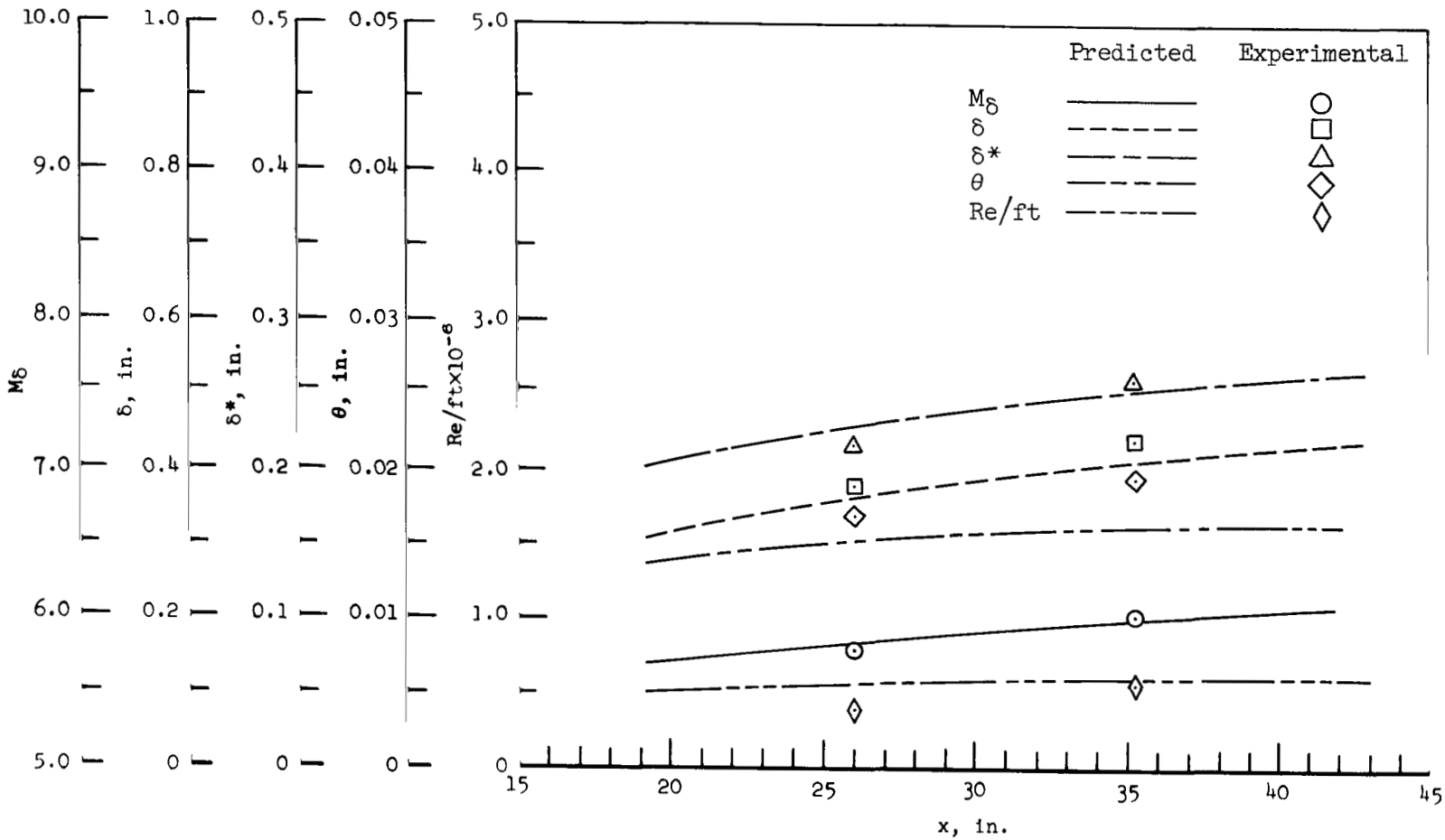

(a) Laminar flow.

Figure 11.- Boundary-layer-edge conditions and integral properties for flat plate at Mach number 7.3.

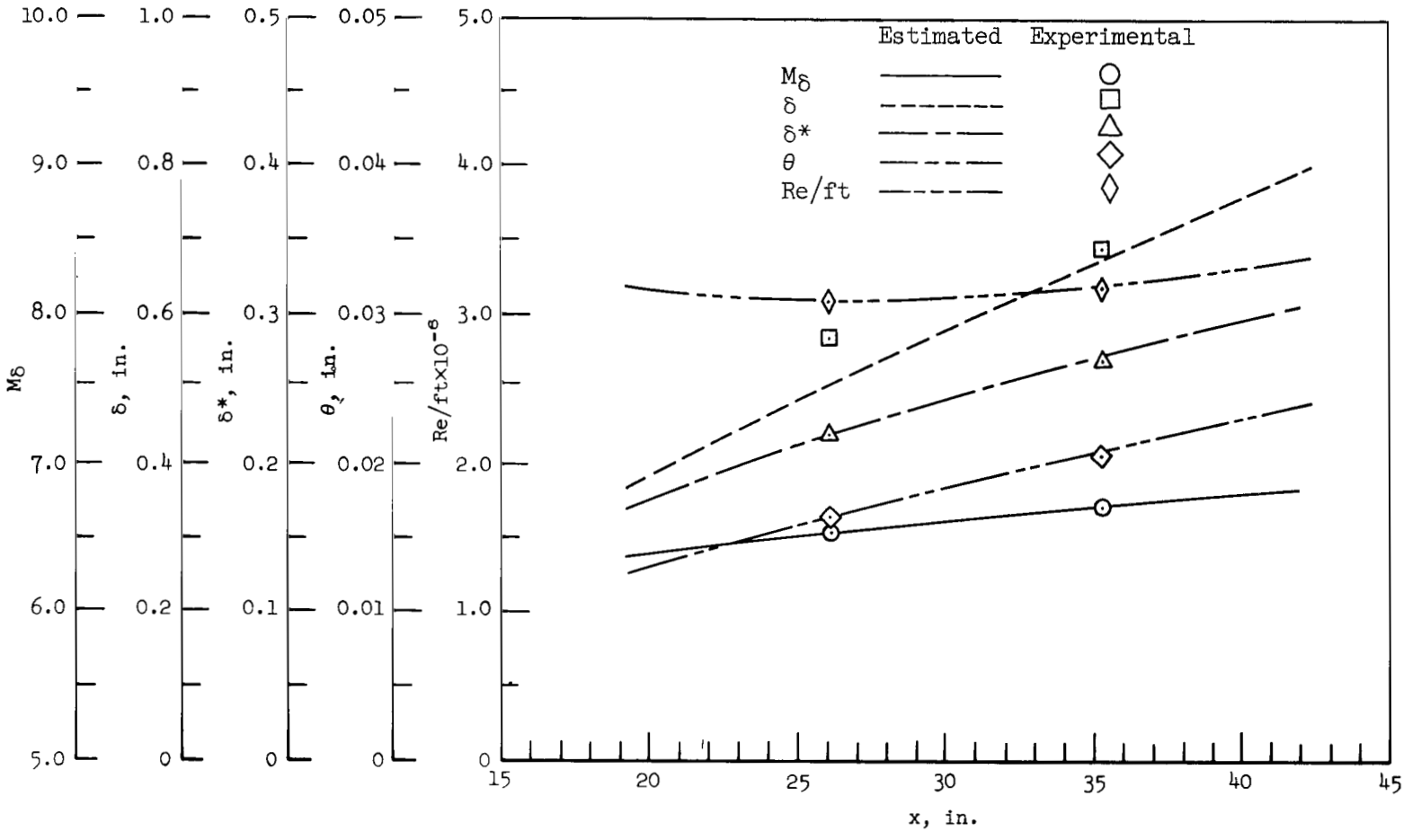

(b) Turbulent flow (1 row of trips).

Figure 11.- Concluded.

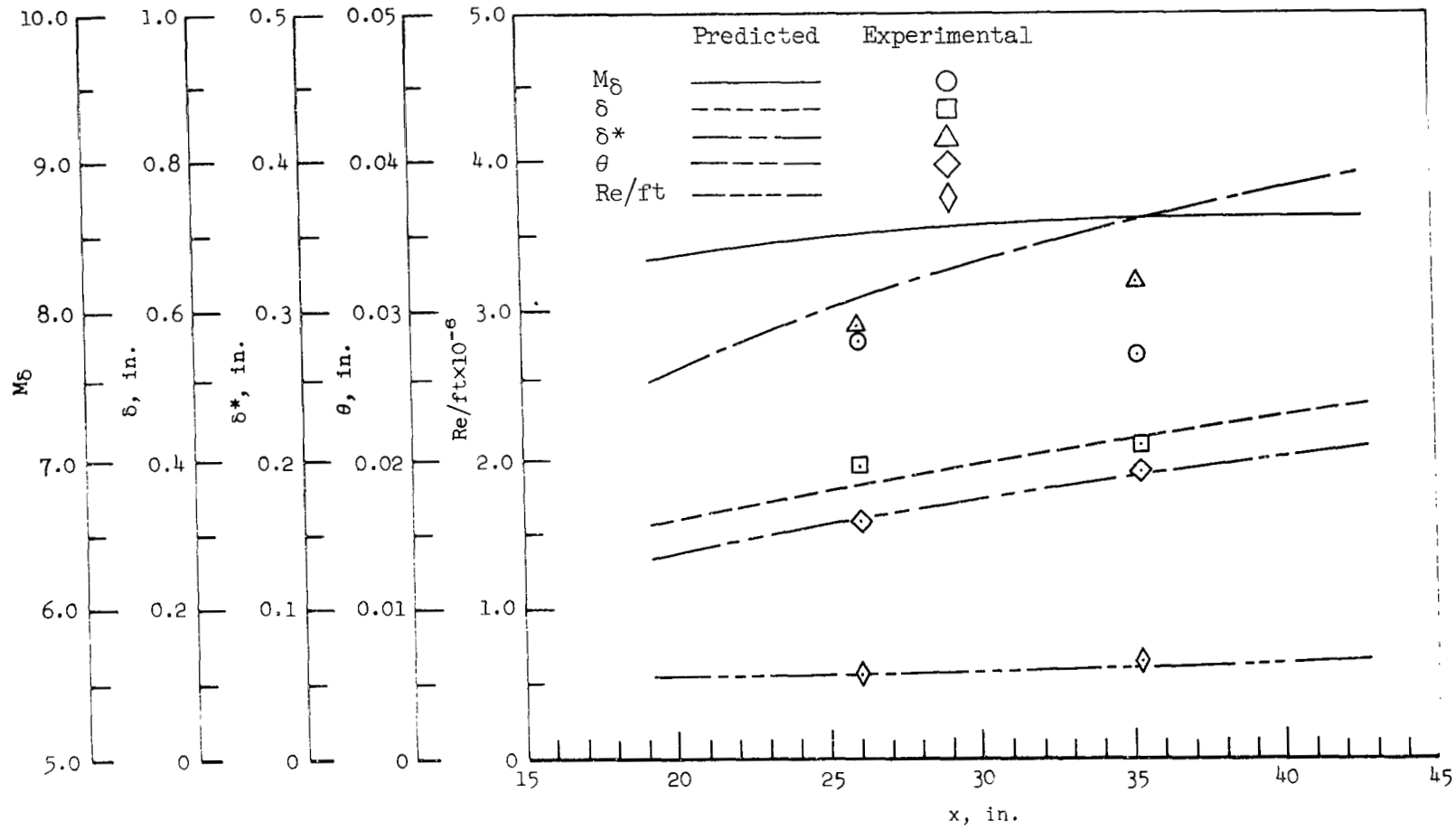

(a) Laminar flow.

Figure 12.- Boundary-layer-edge conditions and integral properties for flat-plate model at Mach number 10.4.

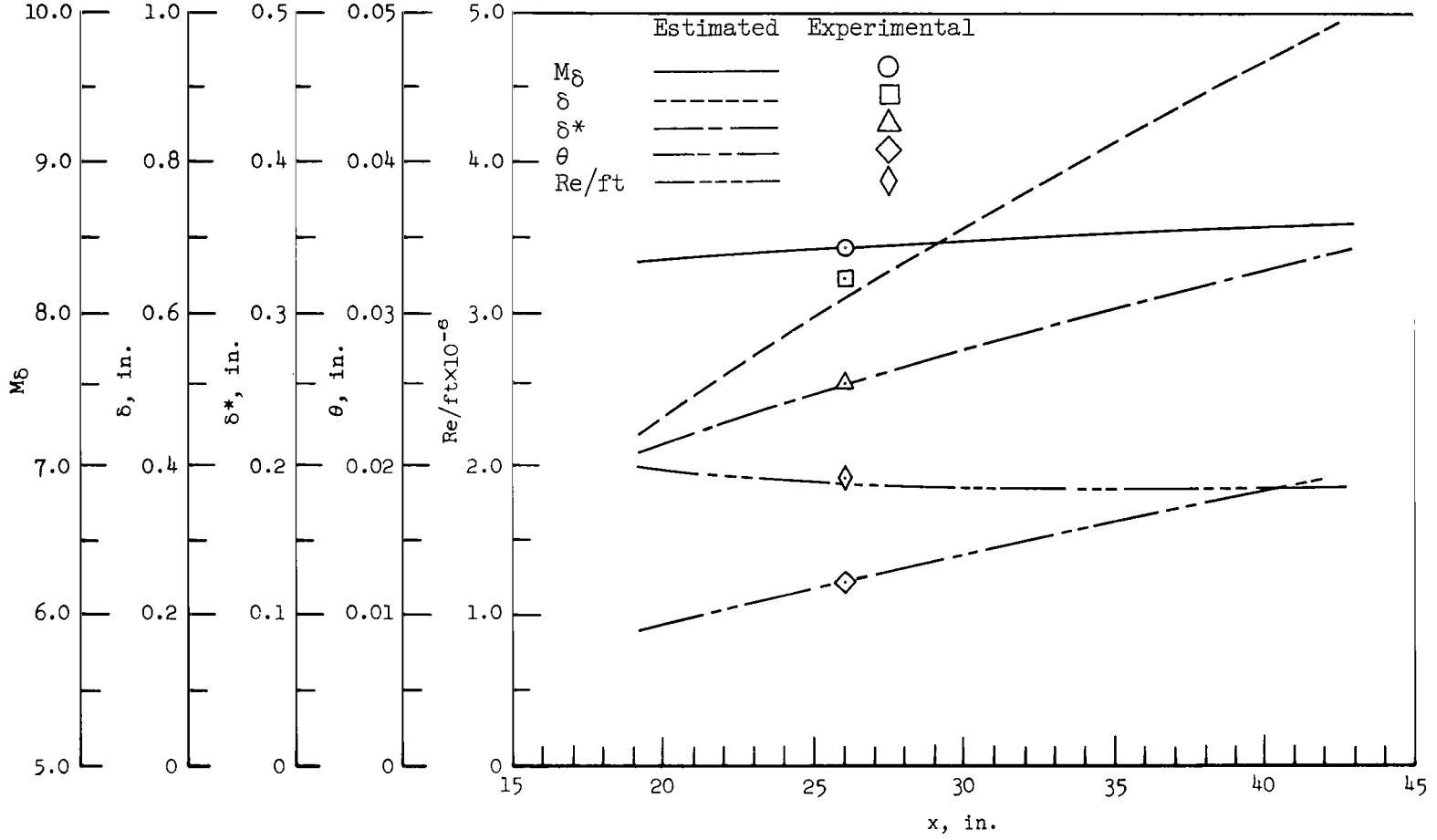

(b) Turbulent flow (3 rows of trips).

Figure 12.- Concluded.

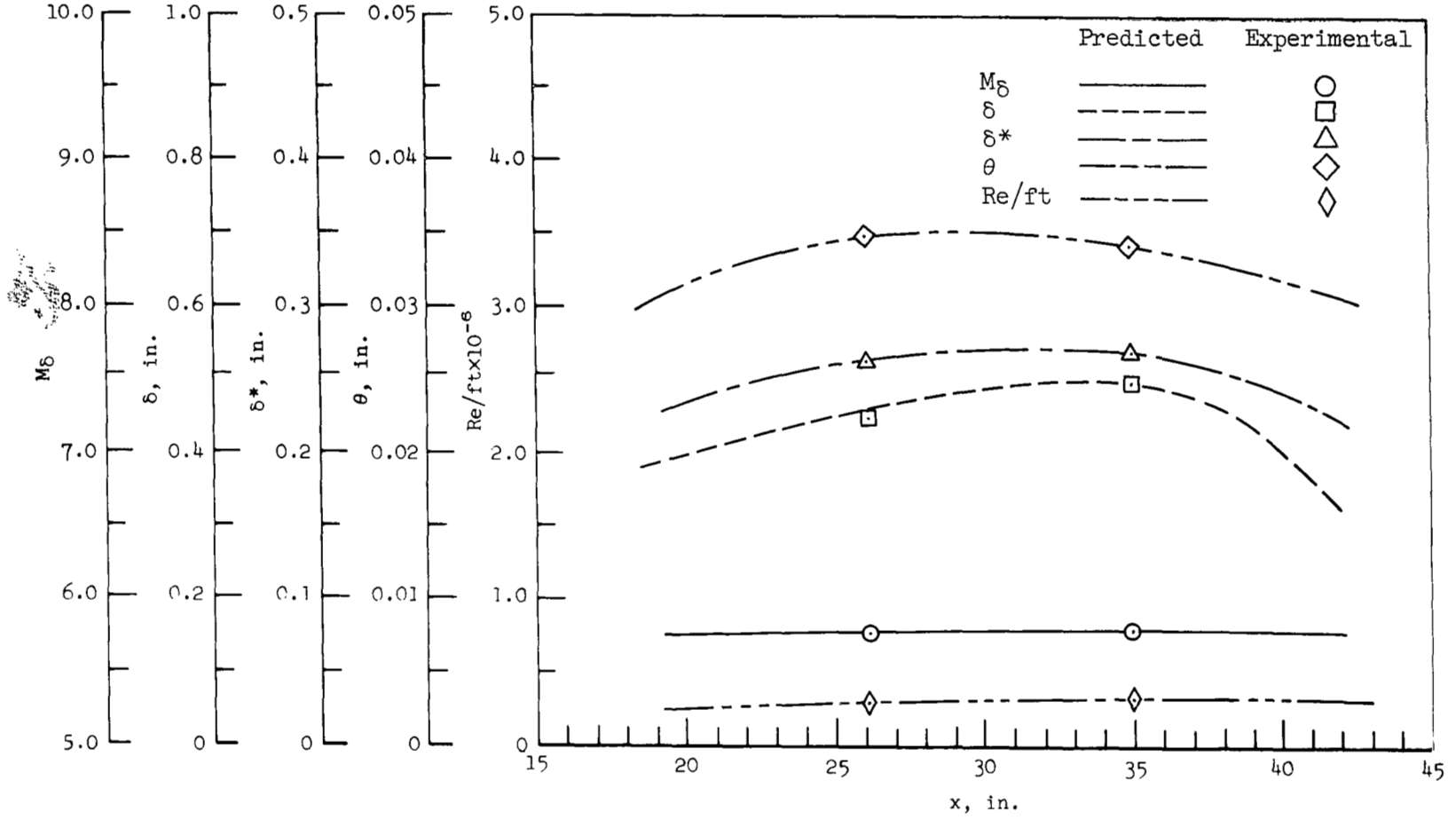

(a) Laminar flow.

Figure 13.- Boundary-layer-edge conditions and integral properties for compression-surface model at Mach number 7.3.

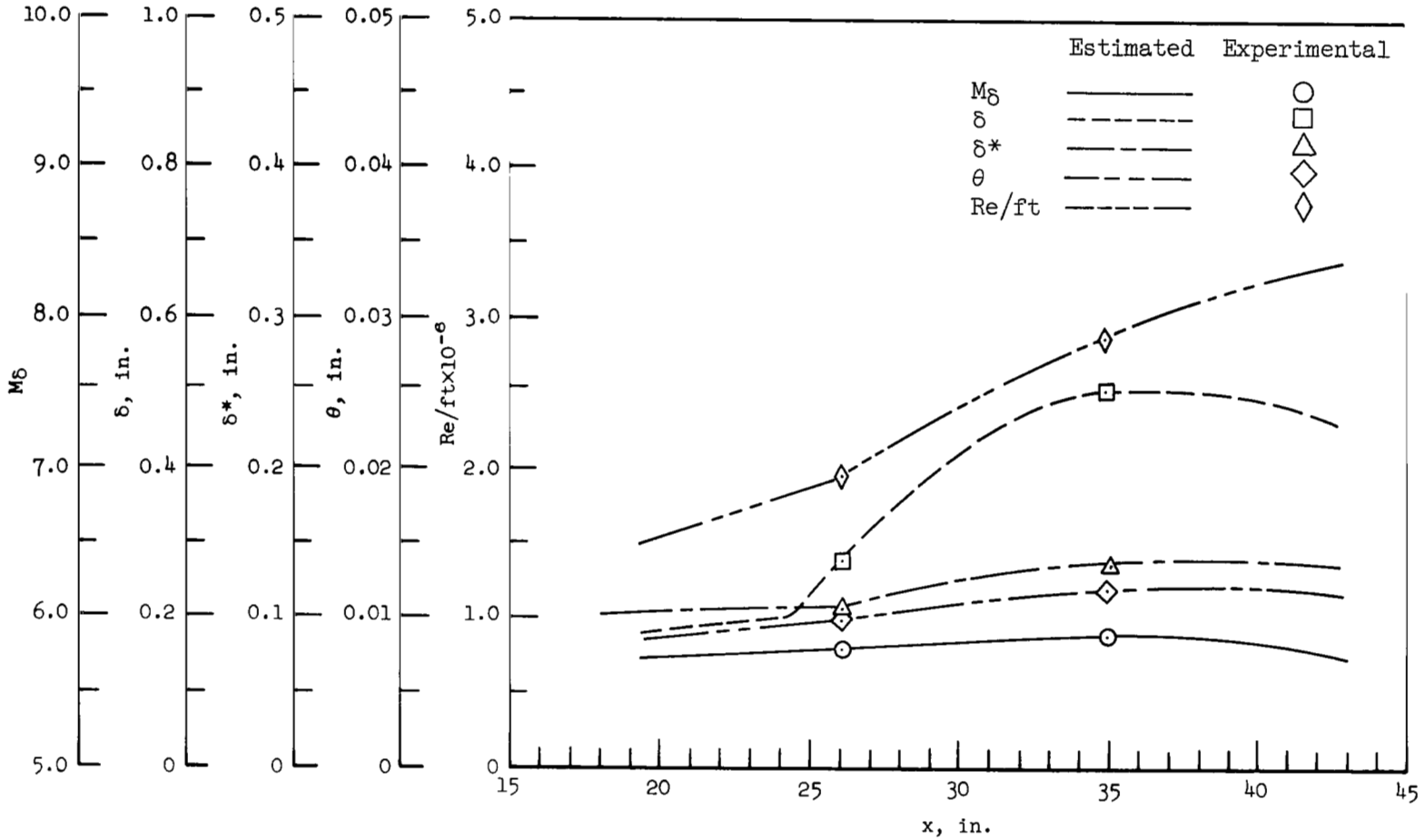

(b) Turbulent flow (natural transition).

Figure 13.- Concluded.

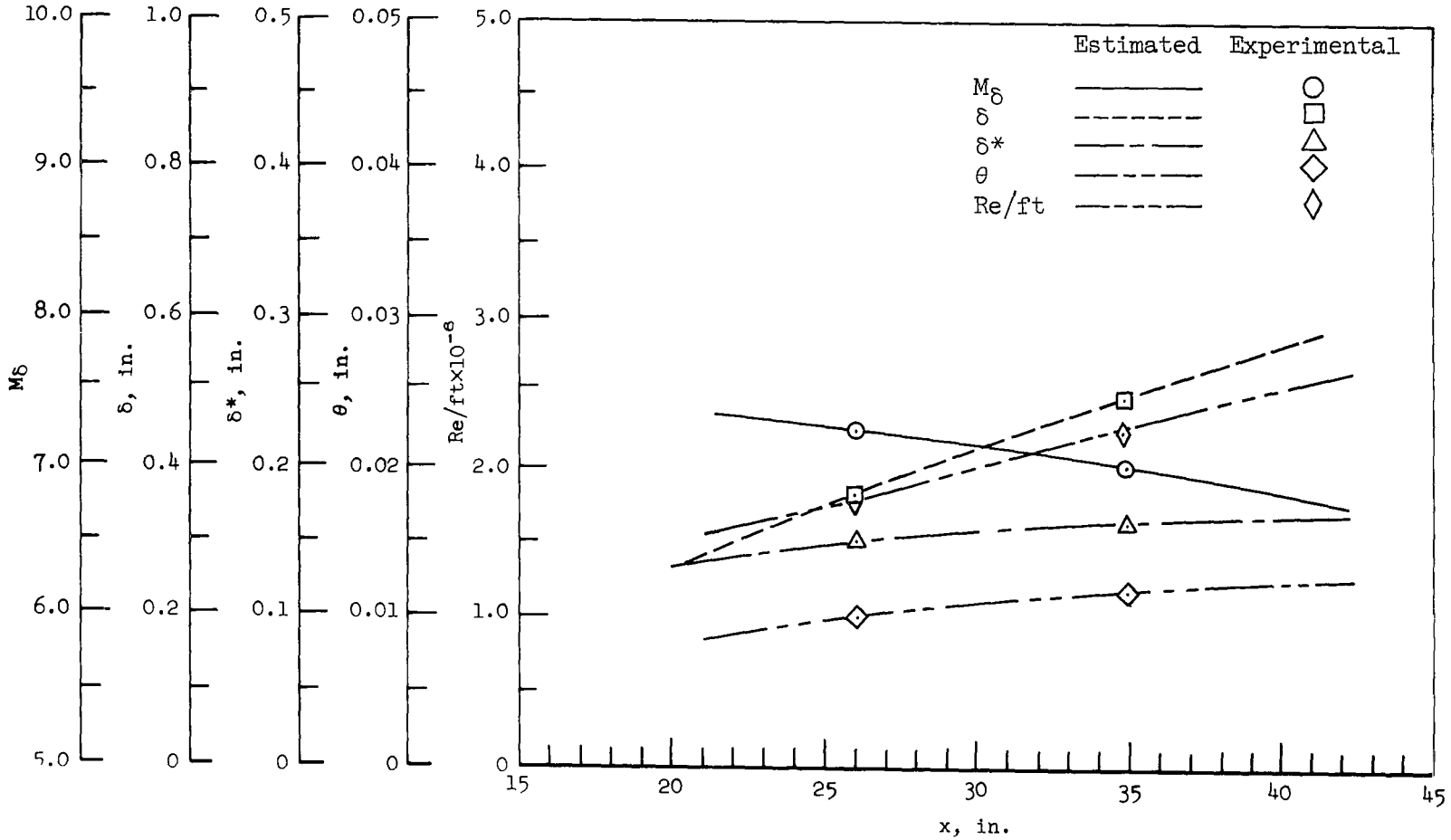

Figure 14.- Boundary-layer-edge conditions and integral properties for compression-surface model at Mach number 10.4; turbulent flow (2 rows of trips).

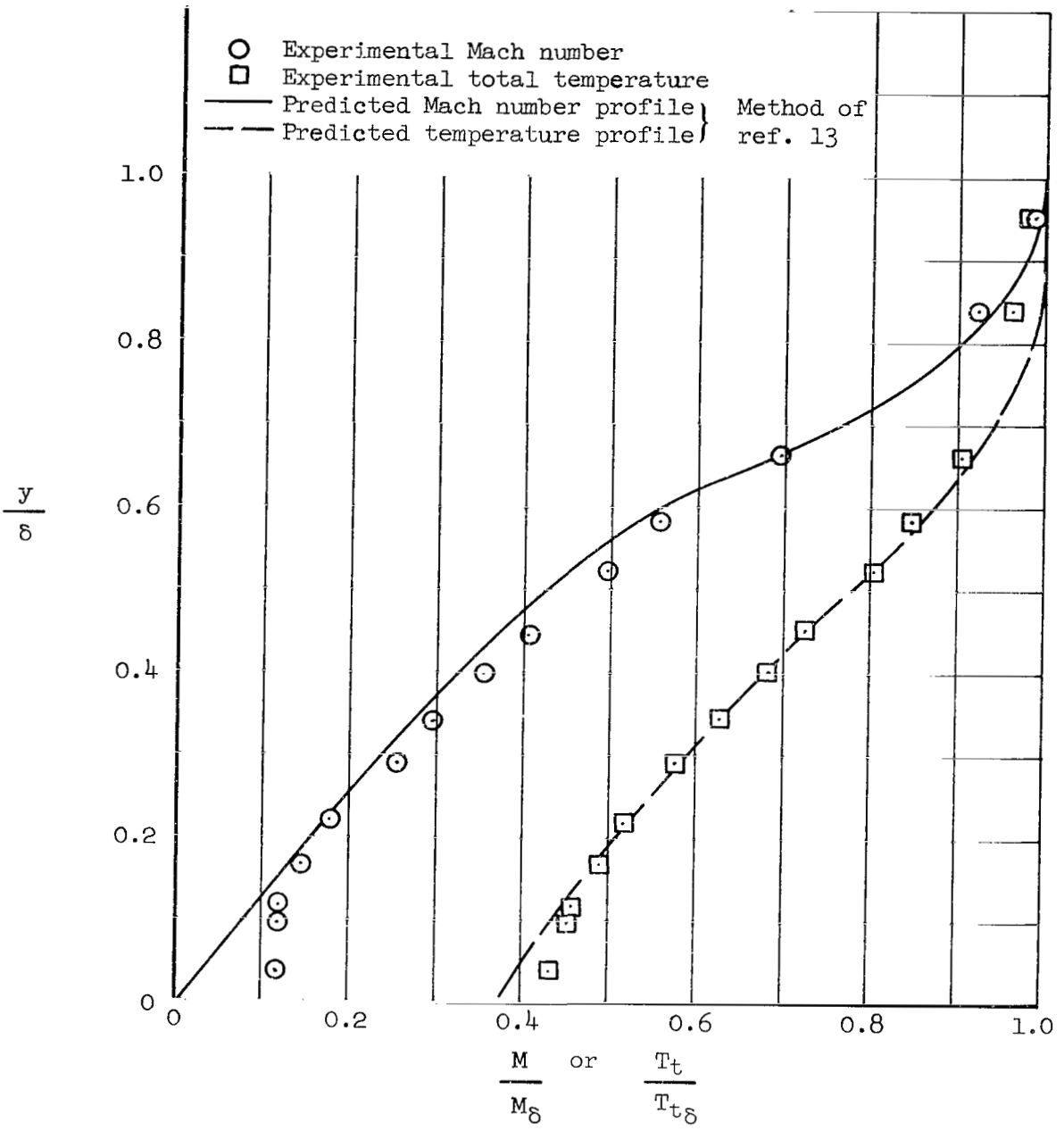

(a) Laminar boundary layer; FP 67.

Figure 15.- Typical Mach number and total-temperature profiles ahead of interactions on the flat-plate model; $M_\infty = 7.3$.

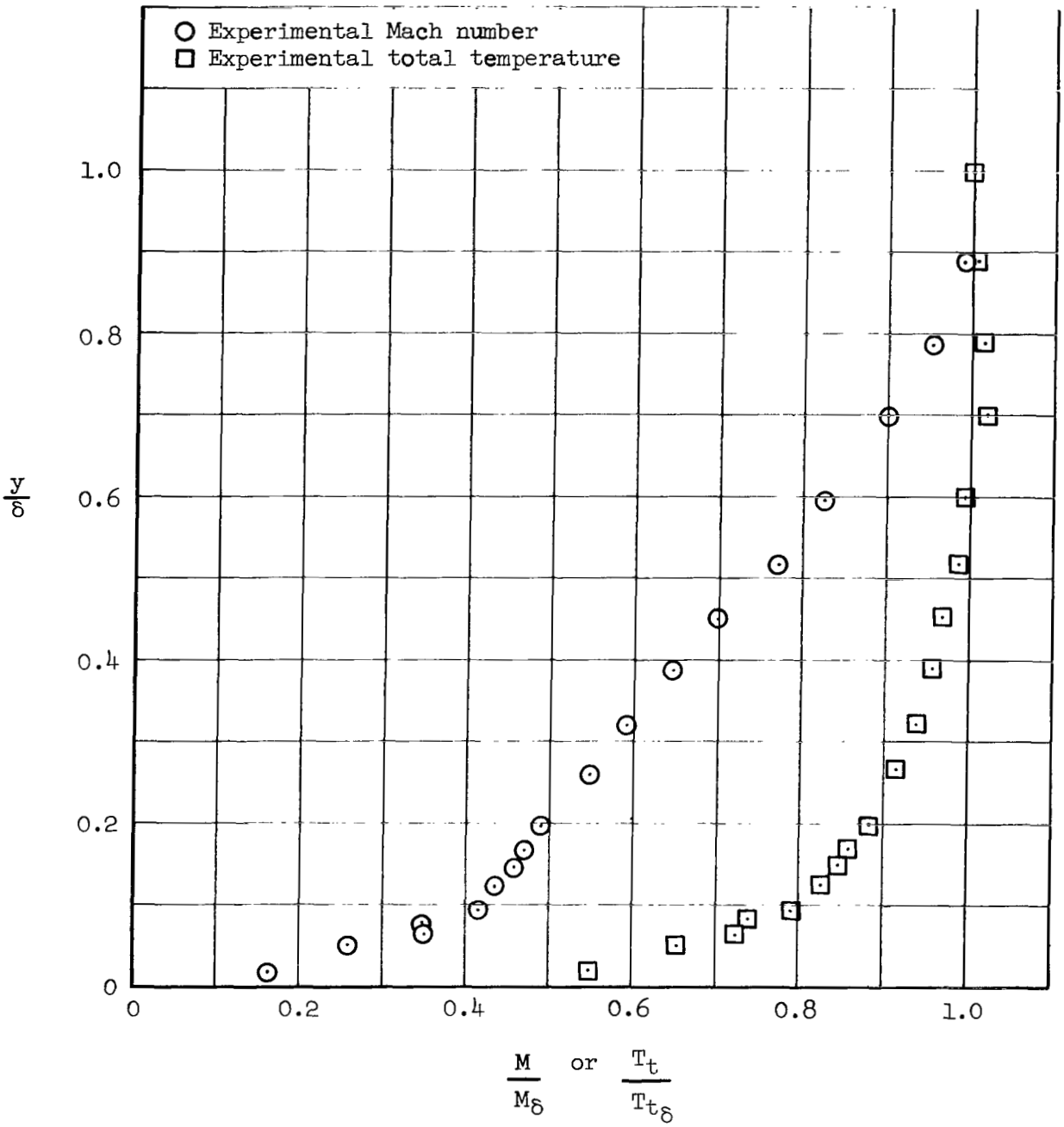

(b) Turbulent boundary layer; FP 68.

Figure 15.- Concluded.

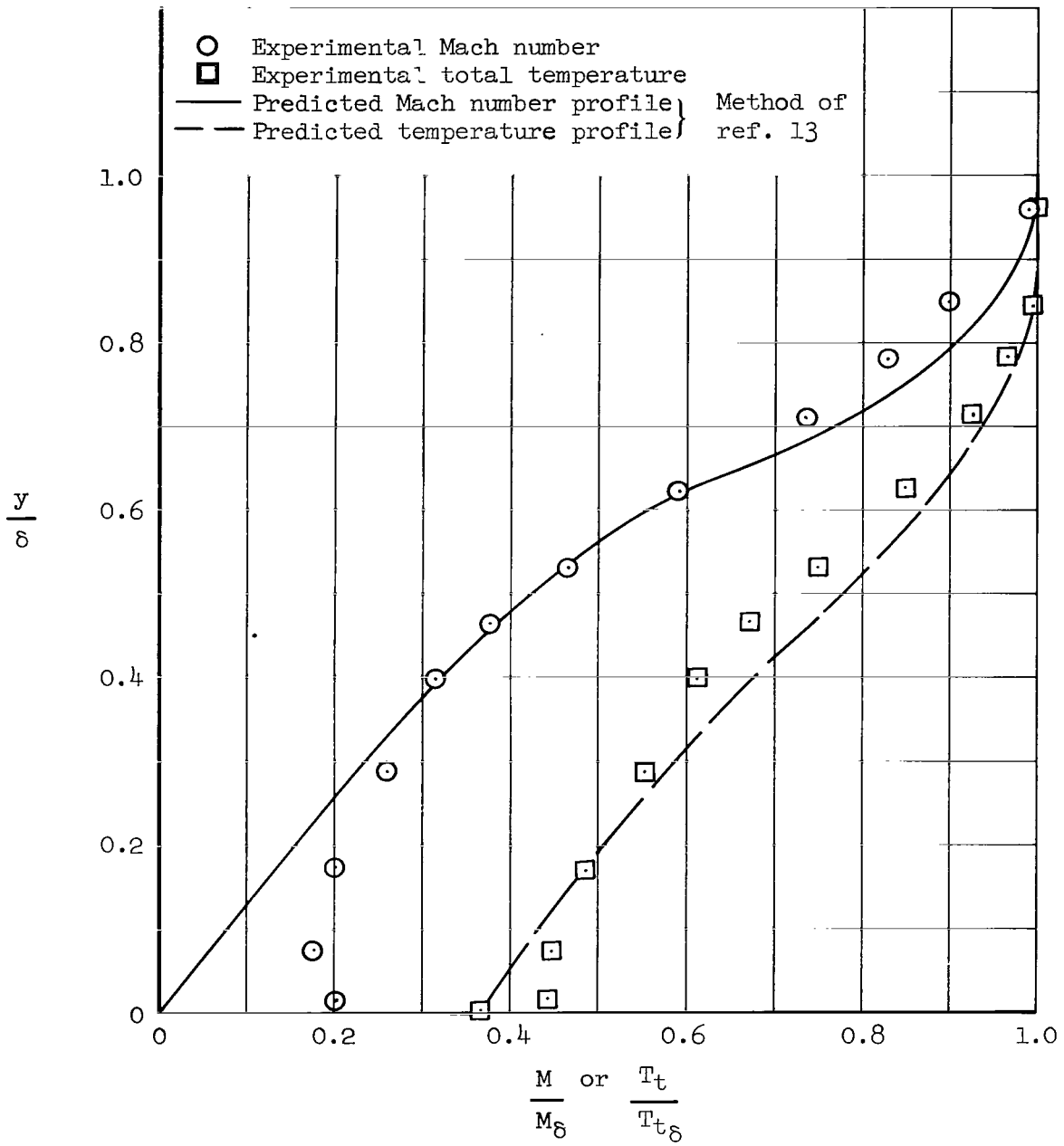

(a) Laminar boundary layer; CS 93.

Figure 16.- Typical Mach number and total-temperature profiles ahead of interactions on the compression-surface model; $M_\infty = 7.3$.

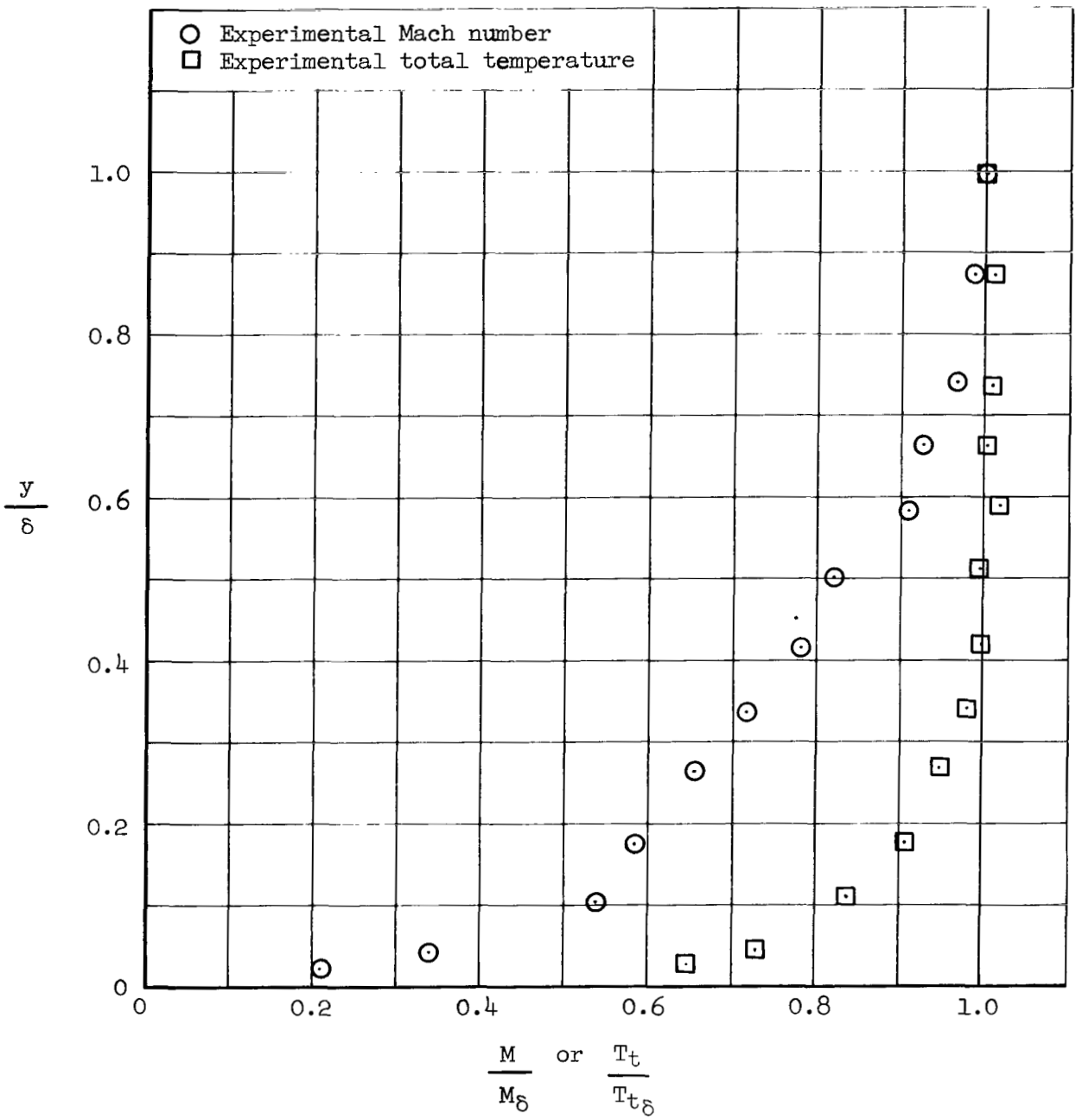

(b) Turbulent boundary layer; CS 54.

Figure 16.- Concluded.

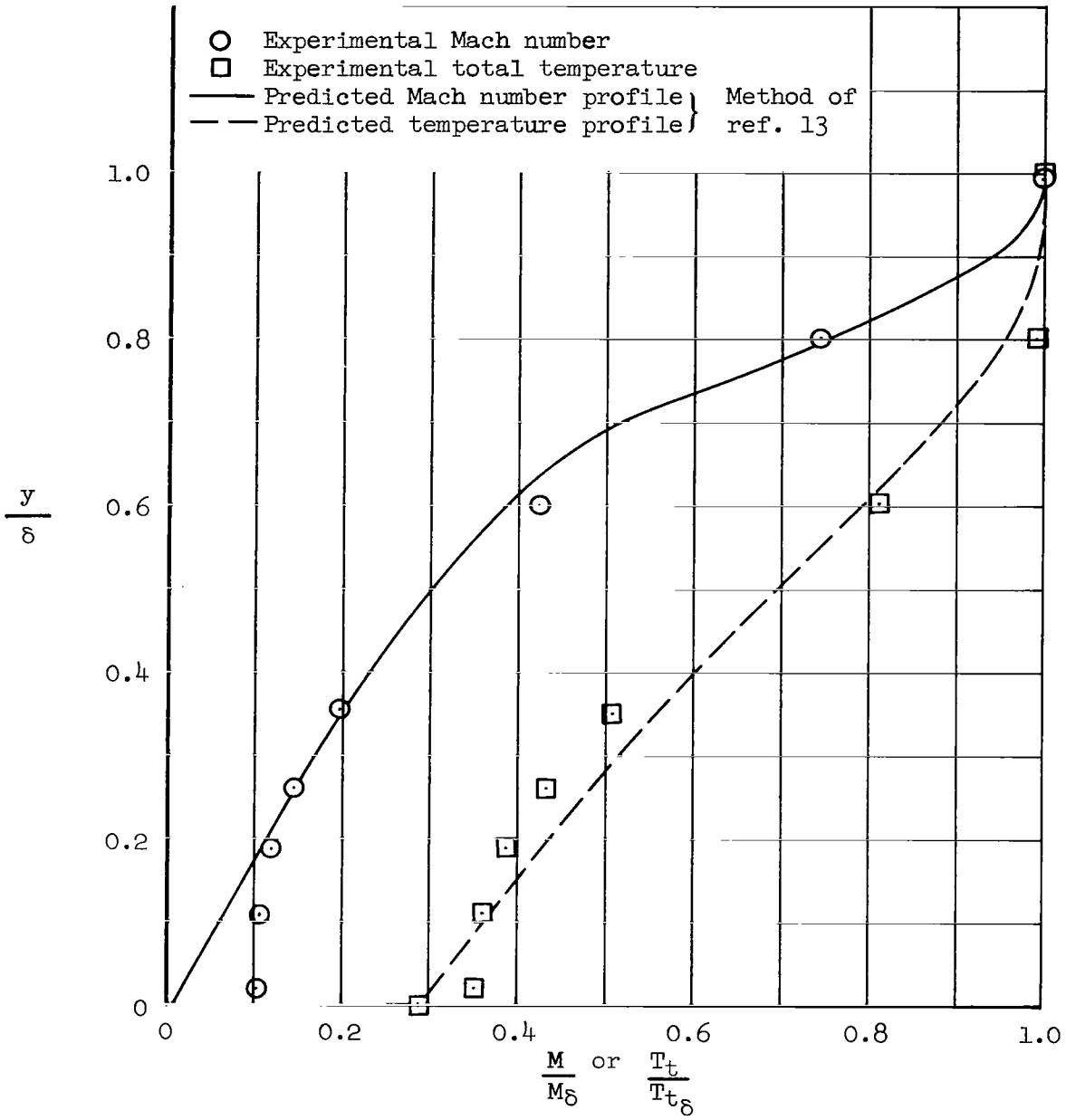

(a) Laminar boundary layer; FP 11.

Figure 17.- Typical Mach number and total-temperature profiles ahead of interactions on the flat-plate model; M_∞ = 10.4.

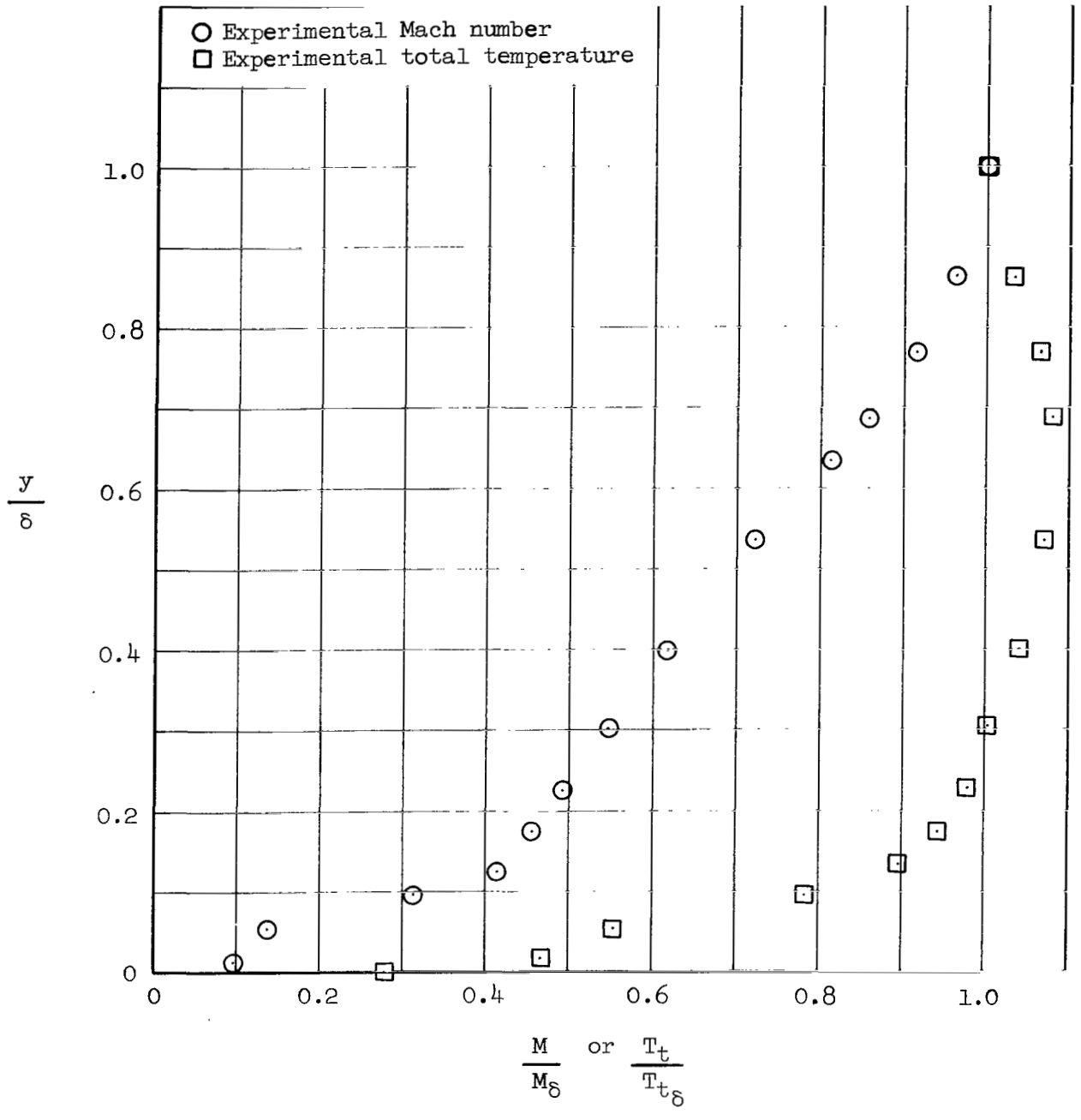

(b) Turbulent boundary layer; FP 19.

Figure 17.- Concluded.

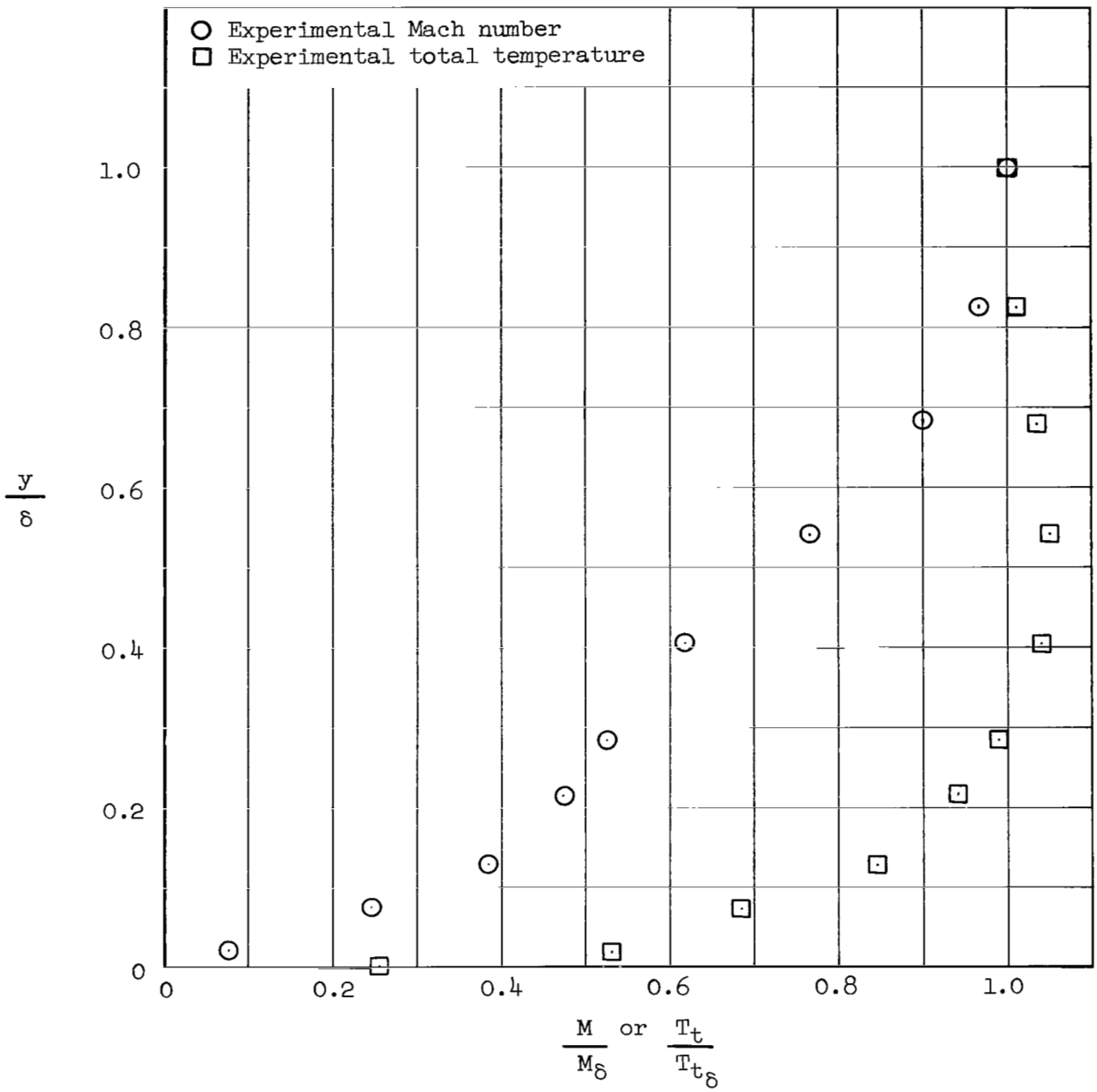

Figure 18.- Typical Mach number and total-temperature profiles ahead of interactions on the compression-surface model; CS 46, $M_\infty = 10.4$, turbulent boundary layer.

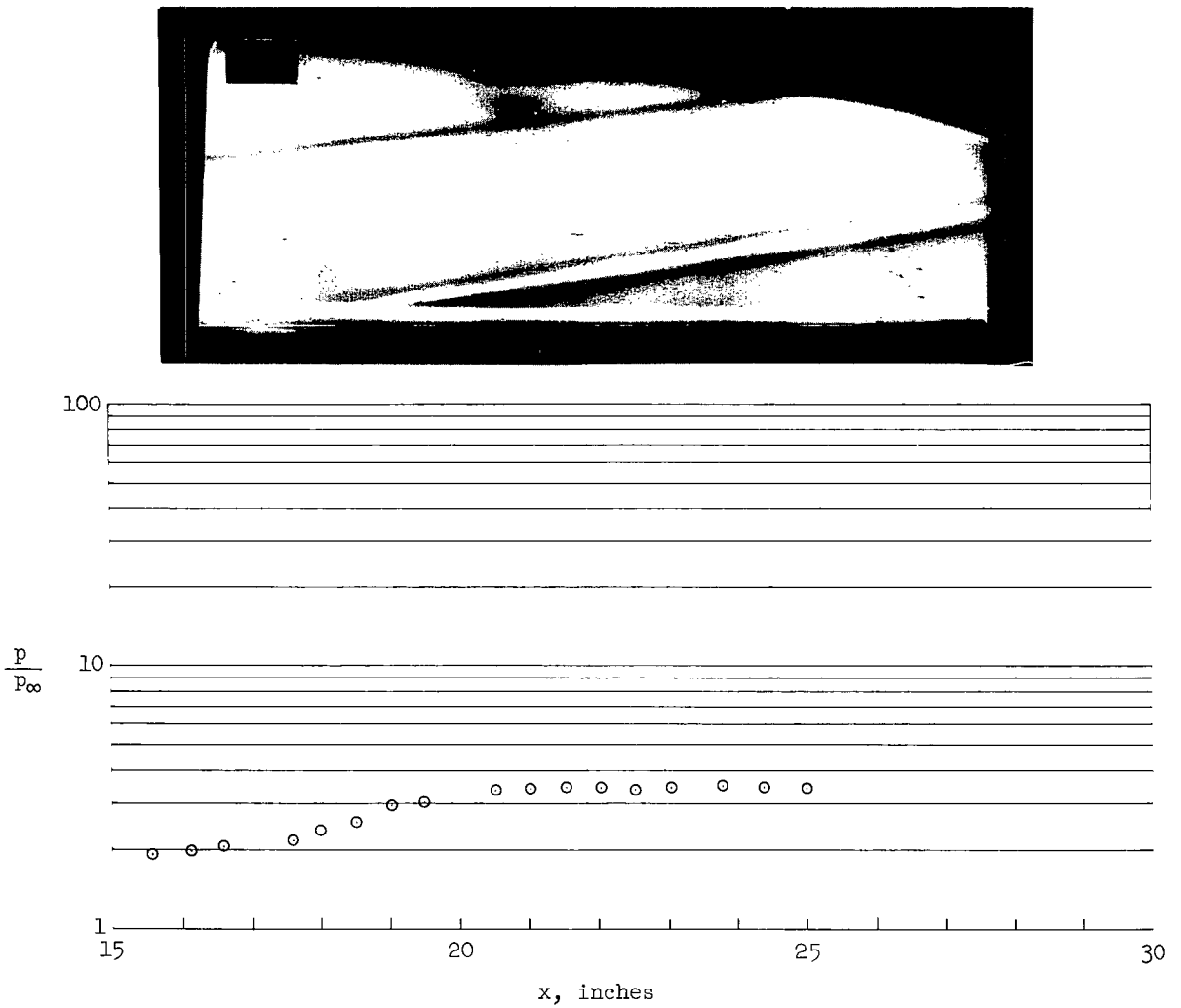

(a) Laminar boundary layer; FP 60, $\alpha_L = 2°$.

Figure 19.- Schlieren photograph and experimental surface pressure distribution for interaction on flat-plate model; $M_\infty = 7.3$.

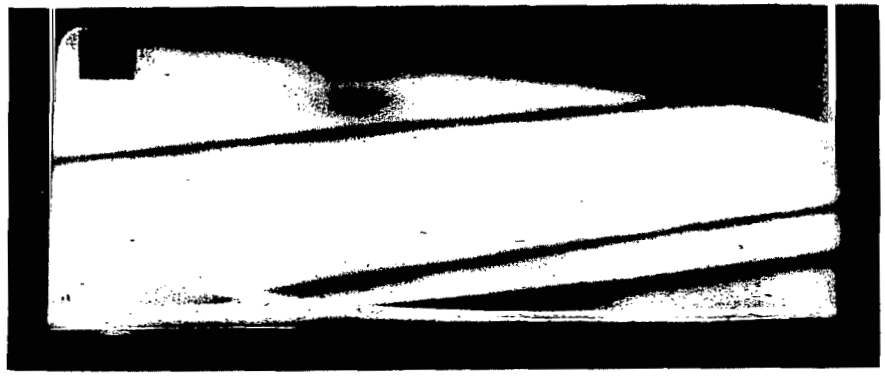

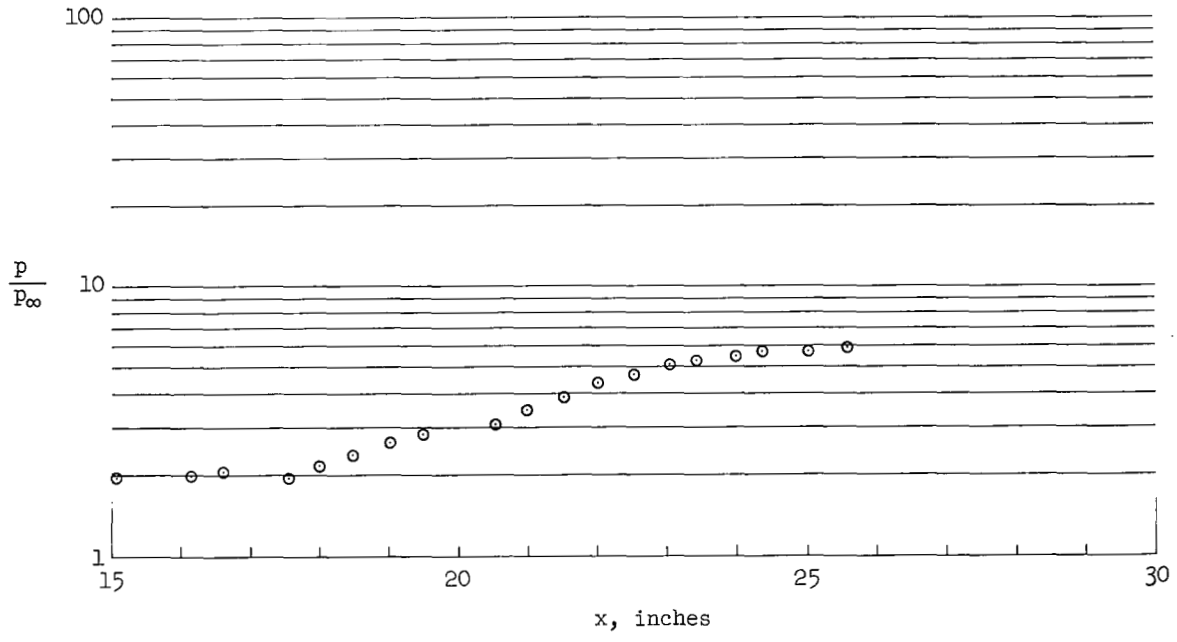

(b) Laminar boundary layer; FP 60, $\alpha_L = 4°$.

Figure 19.- Continued.

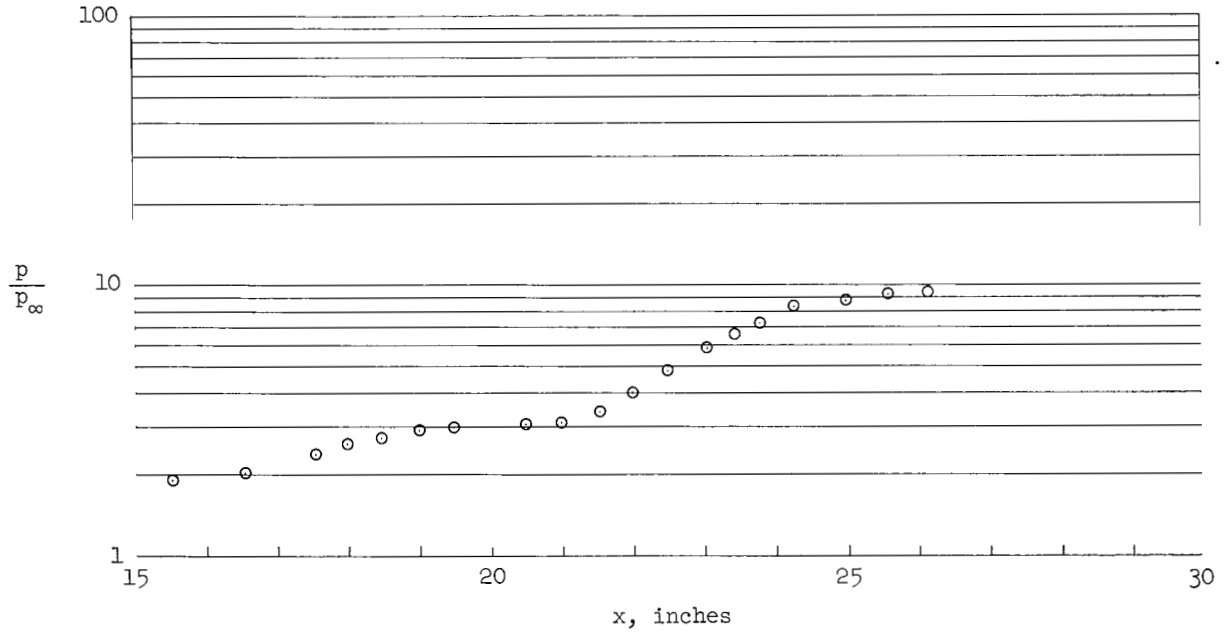

(c) Laminar boundary layer; FP 60, $\alpha_L = 6°$.

Figure 19.- Continued.

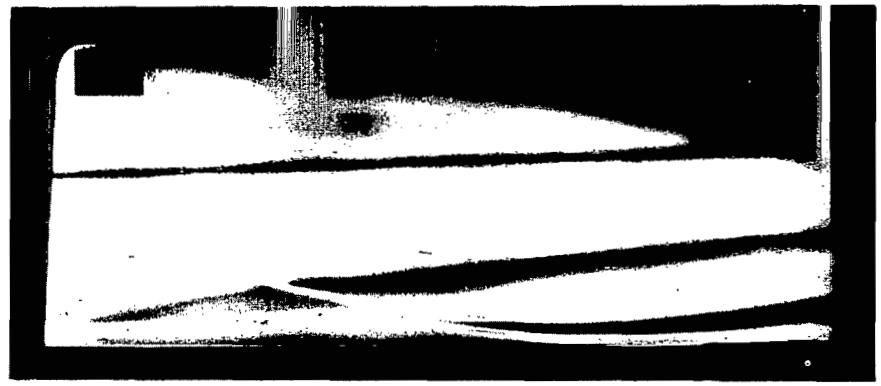

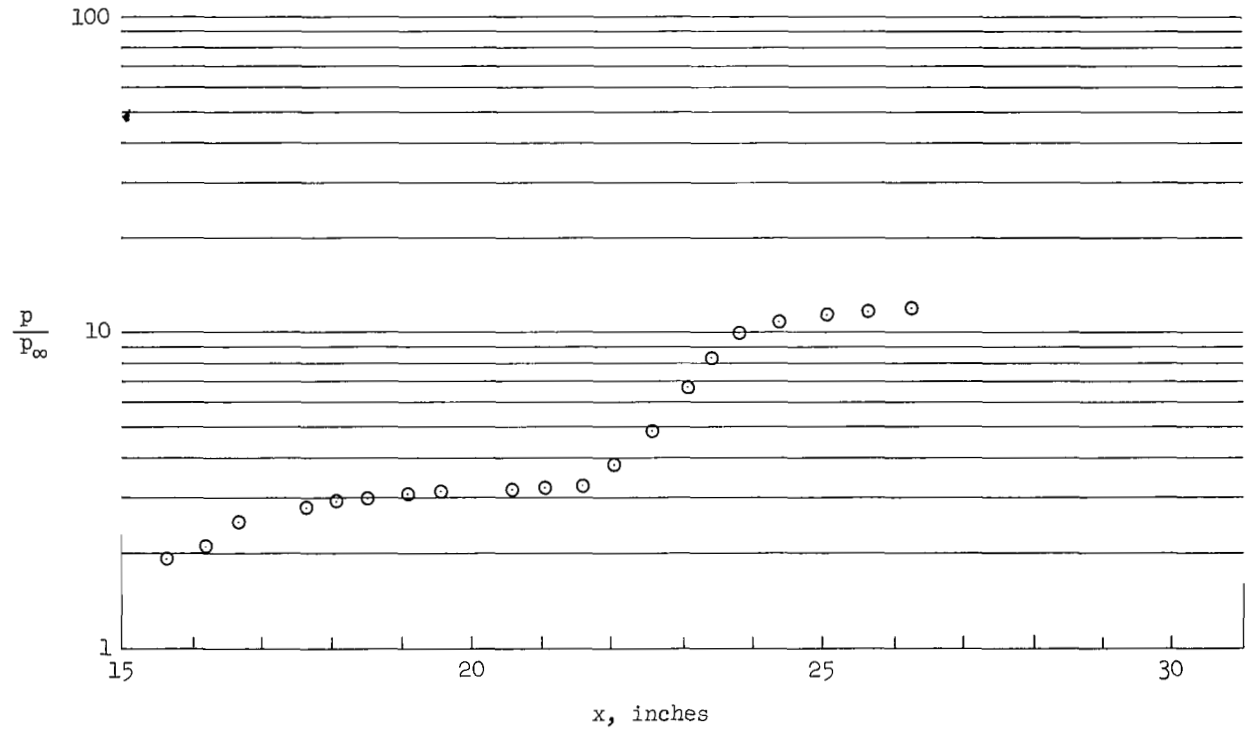

(d) Laminar boundary layer; FP 60, $\alpha_L = 8°$.

Figure 19.- Continued.

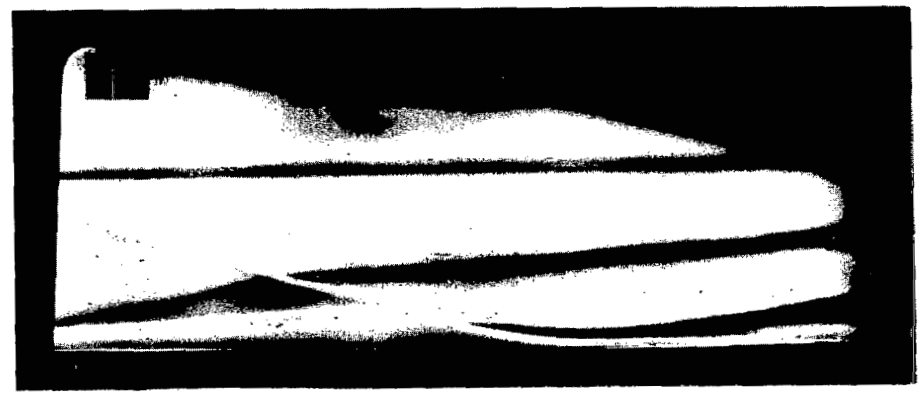

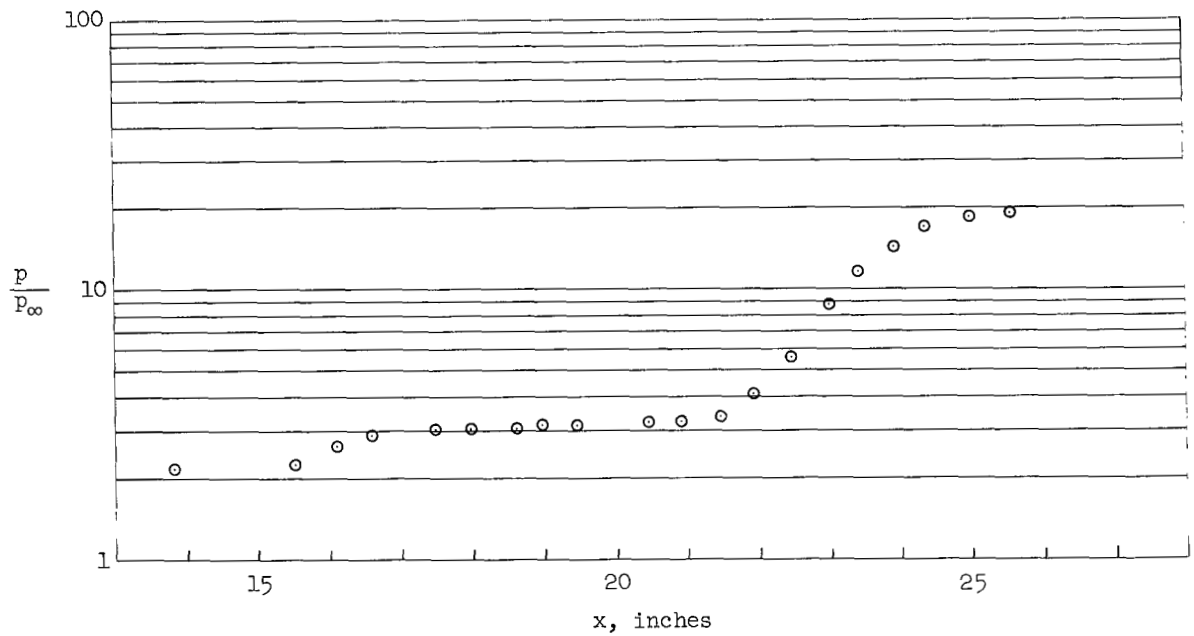

(e) Laminar boundary layer; FP 60, $\alpha_L = 10°$.

Figure 19.- Continued.

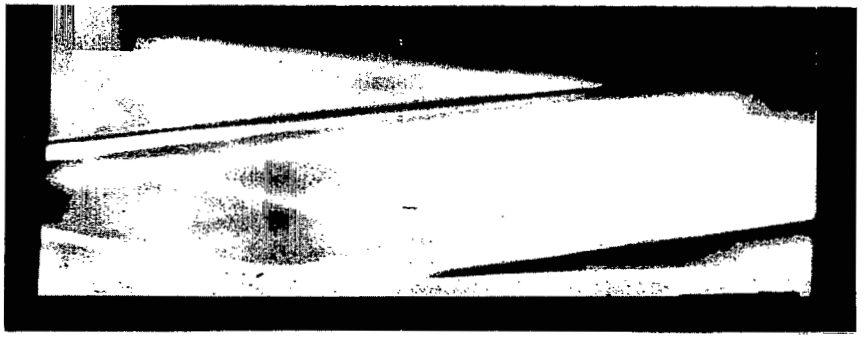

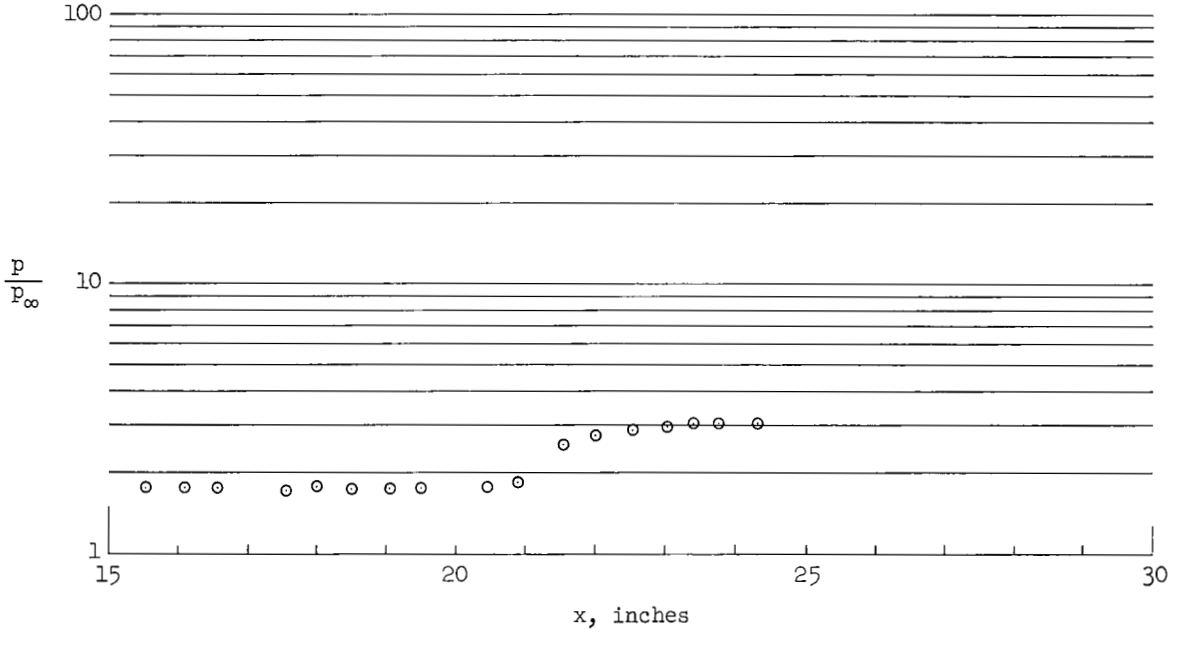

(f) Turbulent boundary layer; FP 59, $\alpha_L = 2°$.

Figure 19.- Continued.

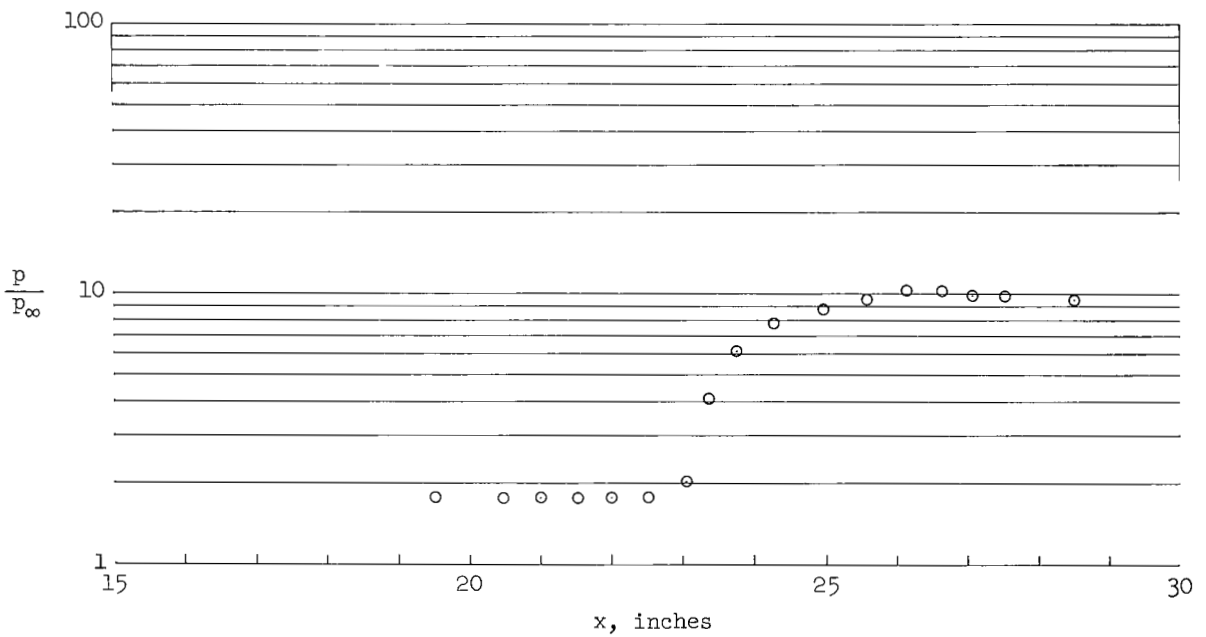

(g) Turbulent boundary layer; FP 59, $\alpha_L = 6°$.

Figure 19.- Continued.

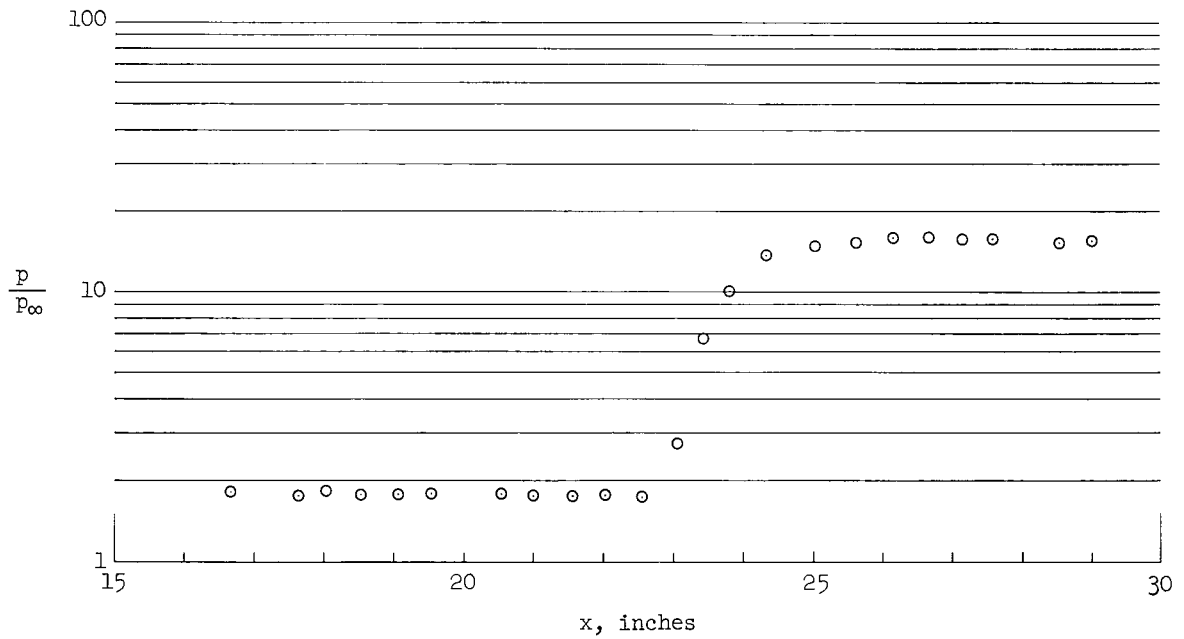

(h) Turbulent boundary layer; FP 59, $\alpha_L = 8°$.

Figure 19.- Continued.

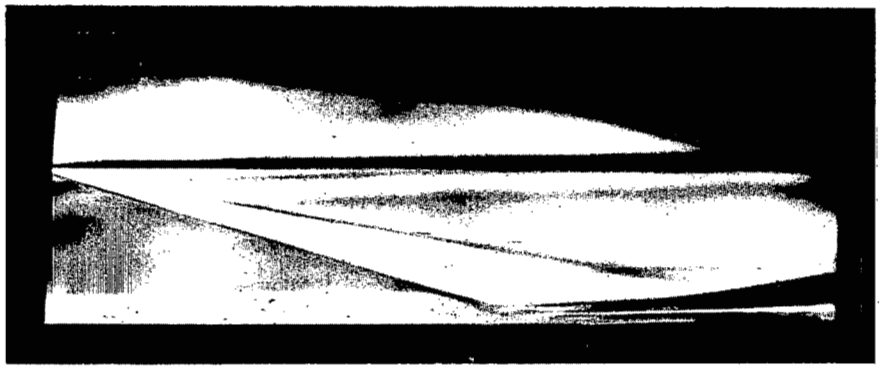

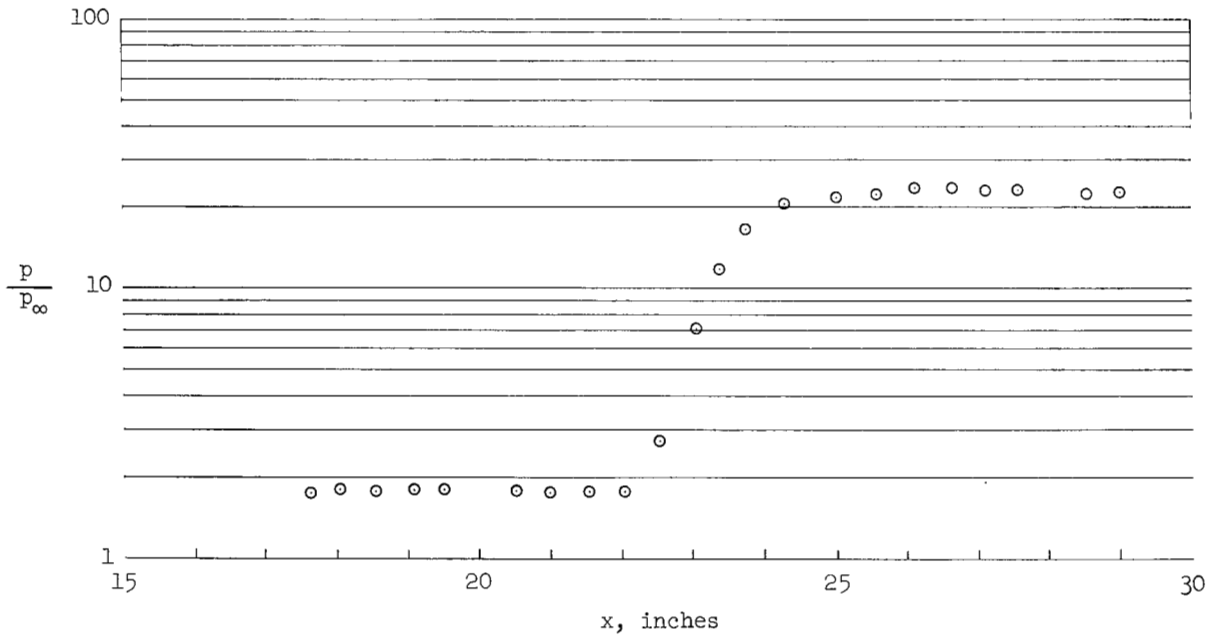

(i) Turbulent boundary layer; FP 59, $\alpha_L = 10°$.

Figure 19.- Concluded.

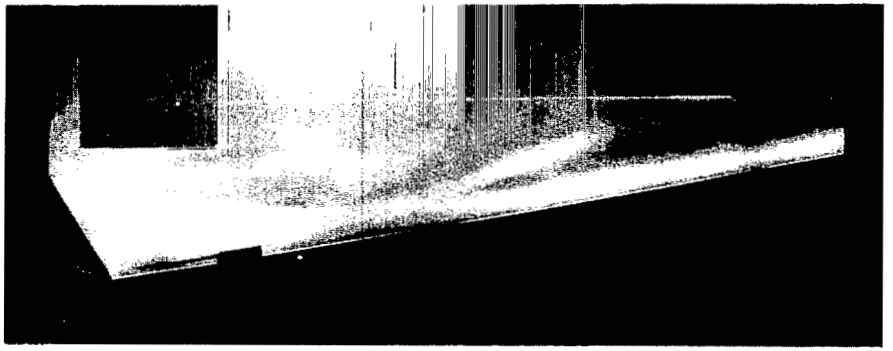

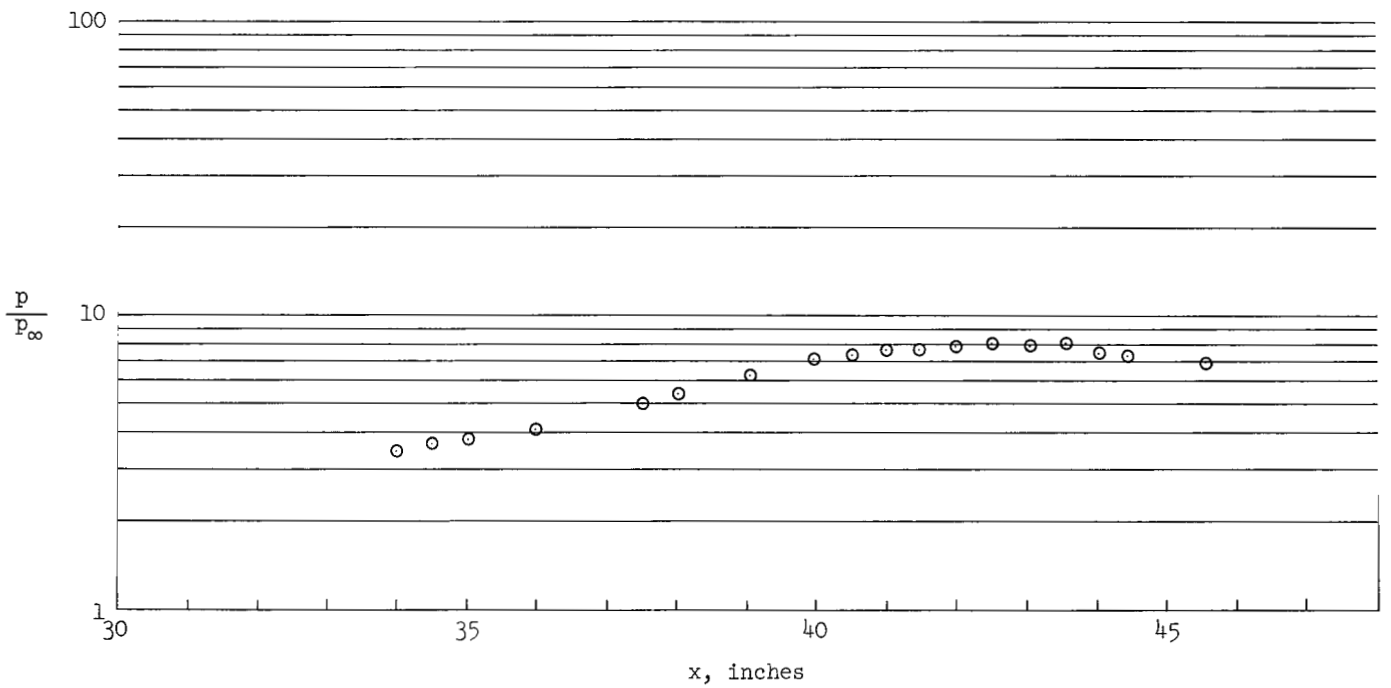

(a) Laminar boundary layer; CS 102, $\alpha_L = 3°$.

Figure 20.- Schlieren photograph and experimental surface pressure distribution for interaction on compression-surface model; $M_\infty = 7.3$.

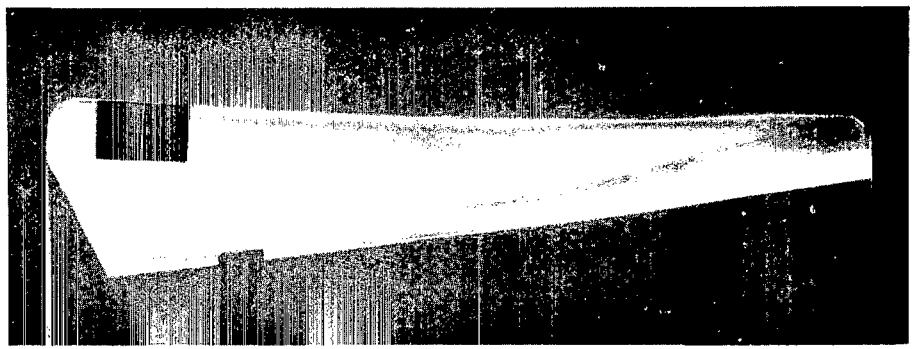

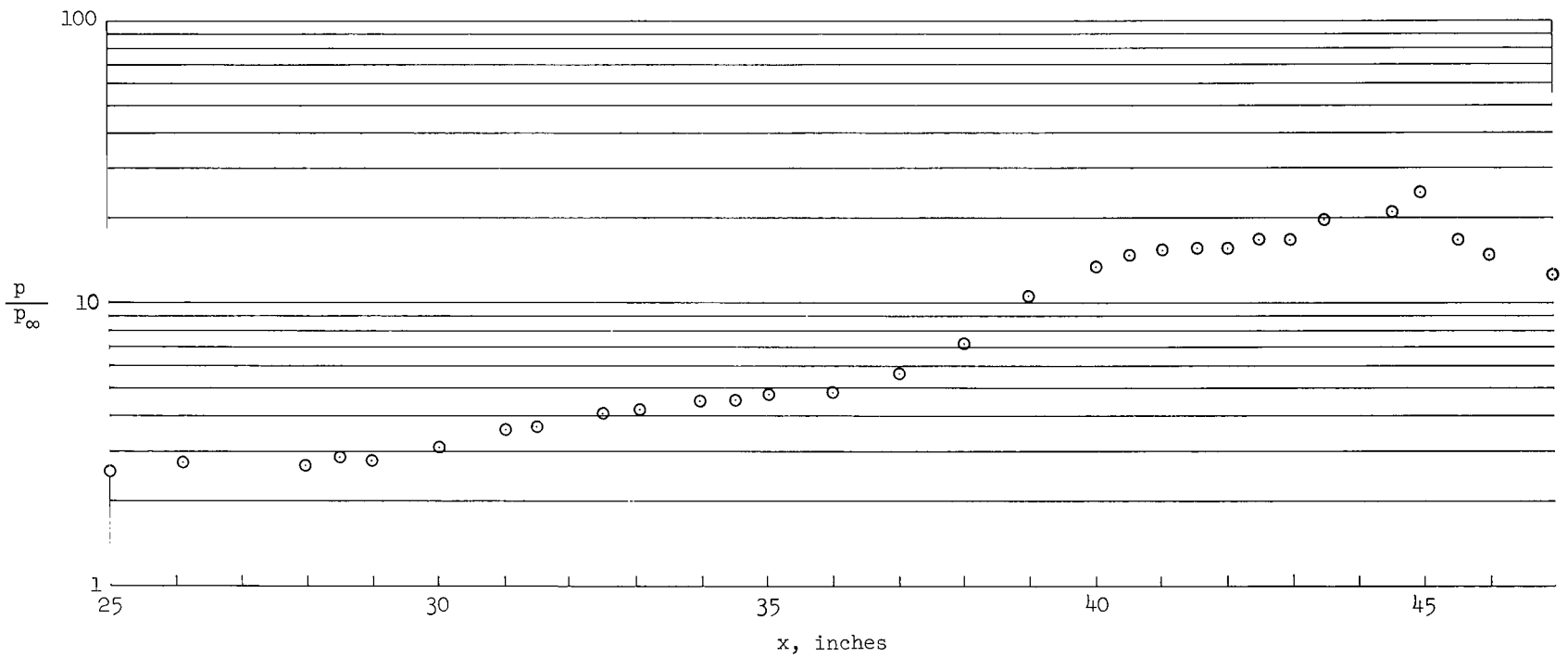

(b) Laminar boundary layer; CS 79, $\alpha_L = 7°$.

Figure 20.- Continued.

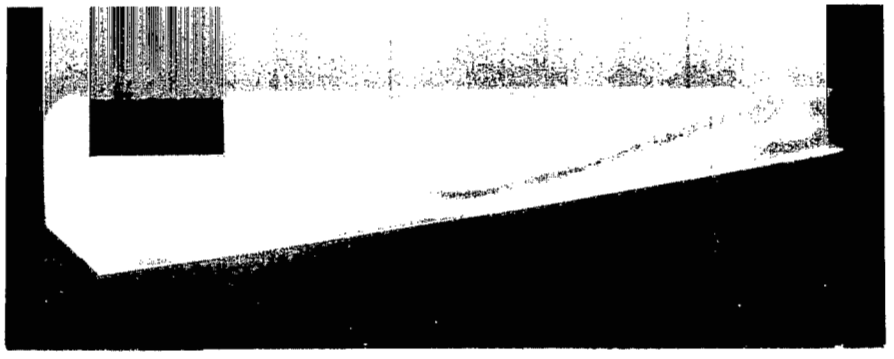

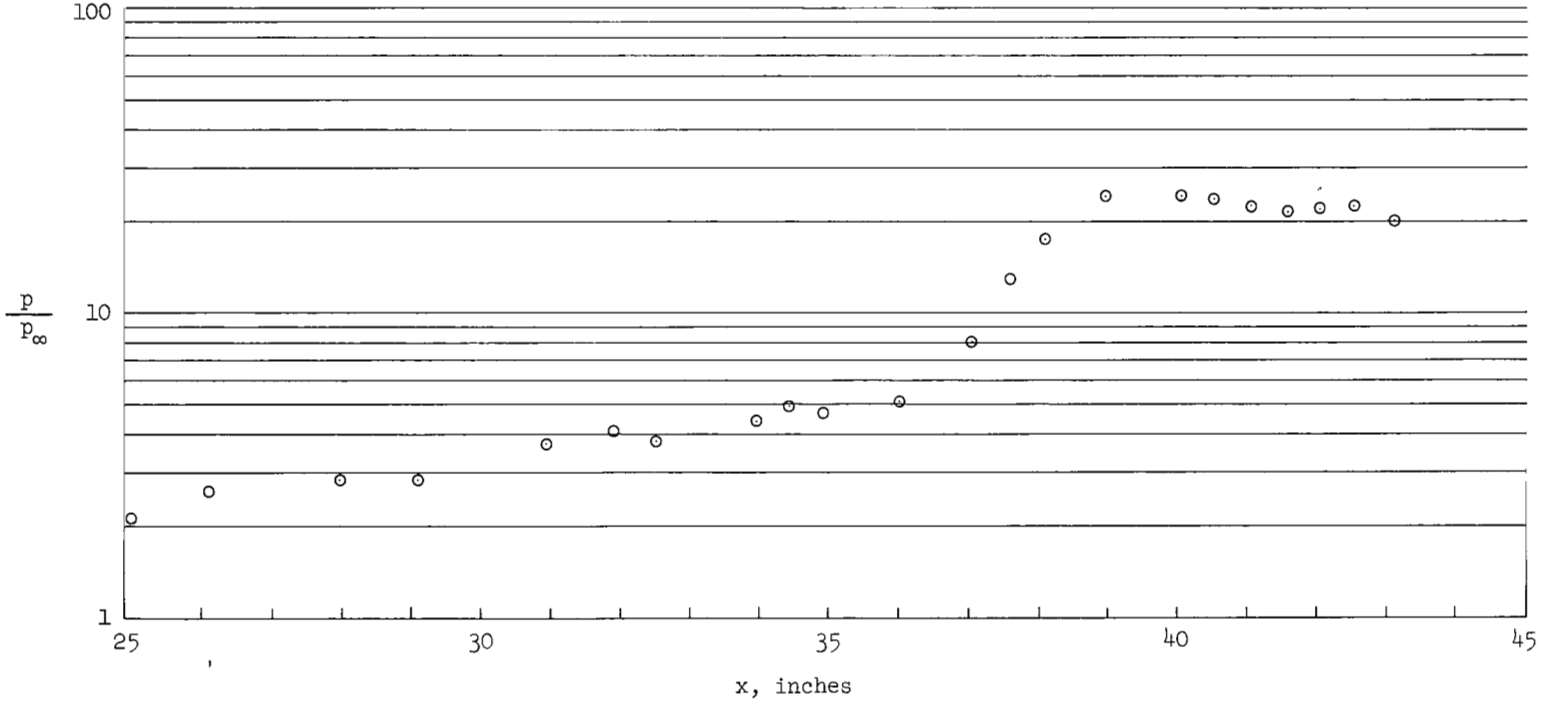

(c) Laminar boundary layer; CS 105, $\alpha_L = 10°$.

Figure 20.- Continued.

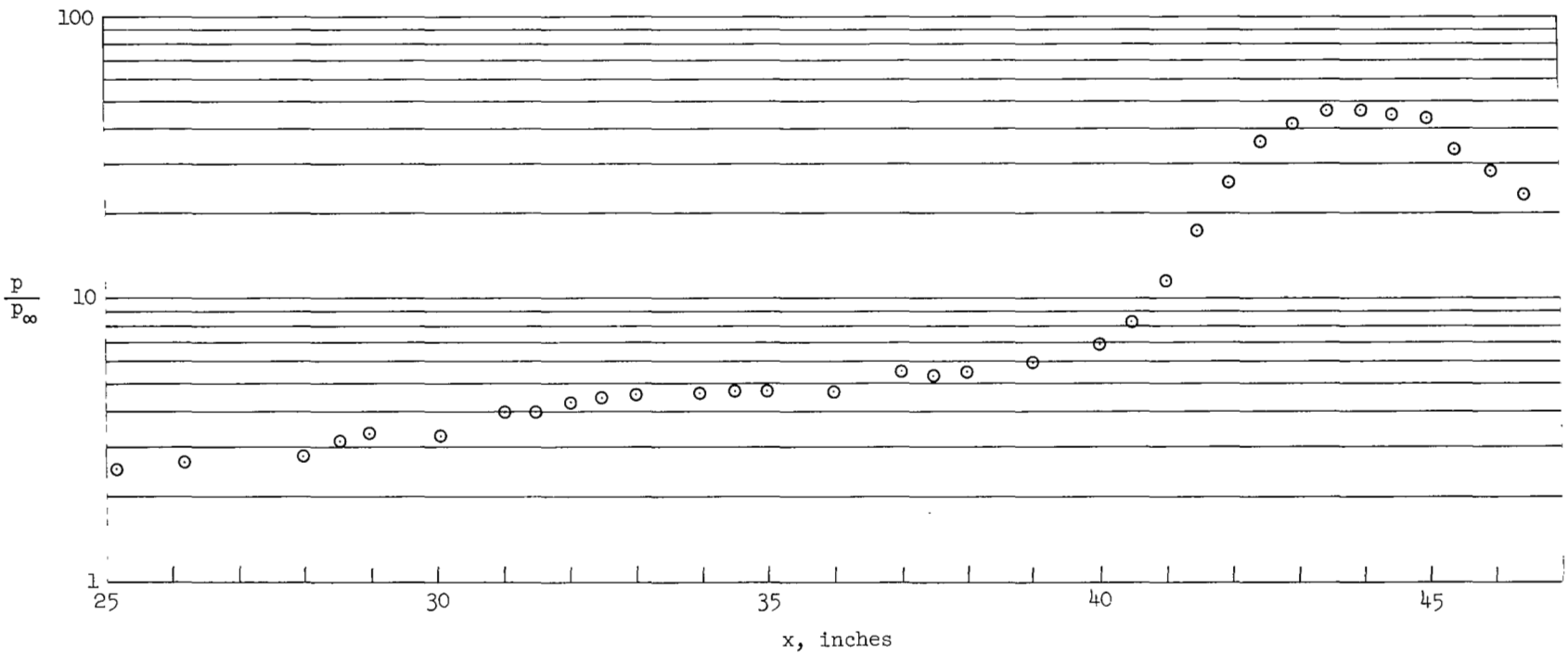

(d) Laminar boundary layer; CS 75, $\alpha_L = 14°$.

Figure 20.- Continued.

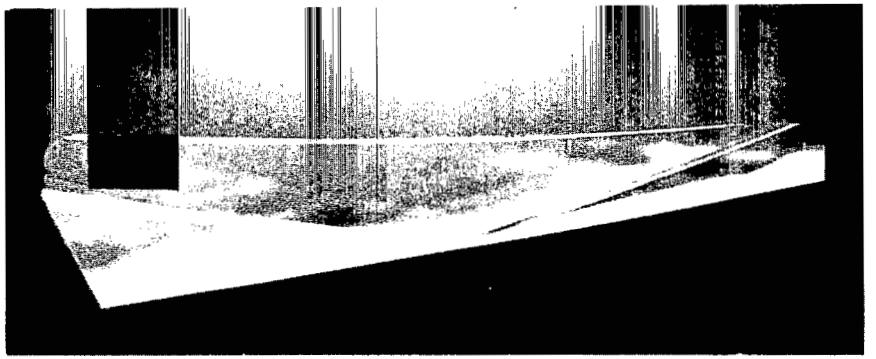

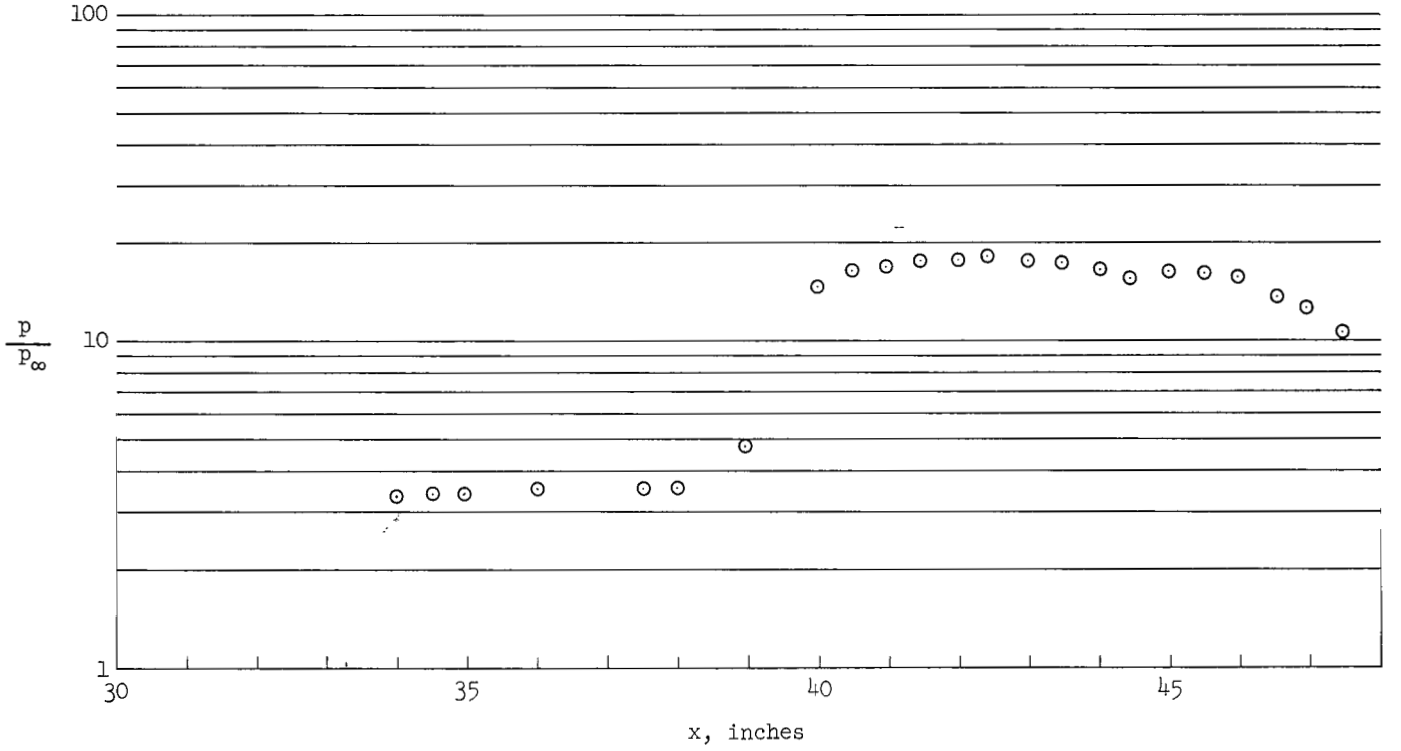

(e) Turbulent boundary layer; CS 62, $\alpha_L = 7°$.

Figure 20.- Continued.

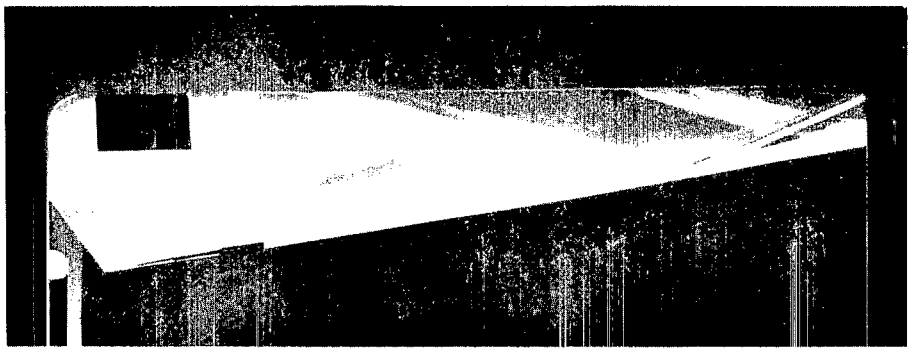

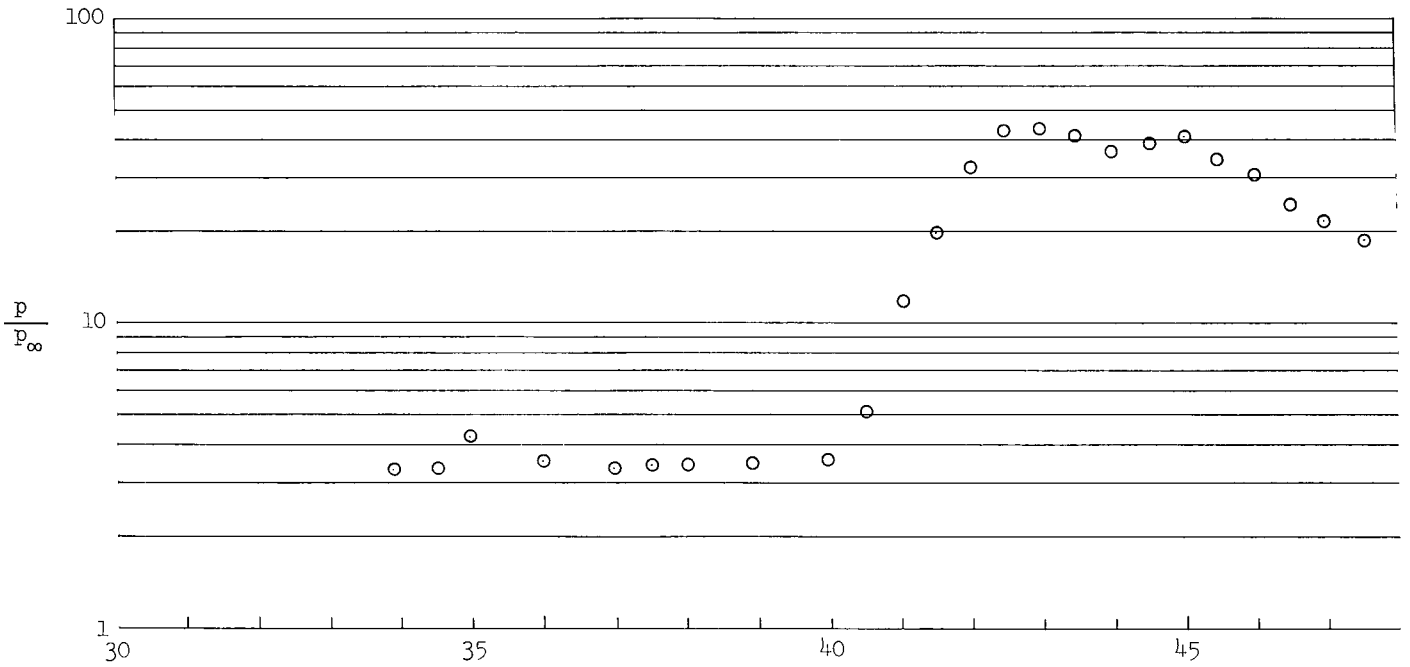

(f) Turbulent boundary layer; CS 76, $\alpha_L = 14°$.

Figure 20.- Continued.

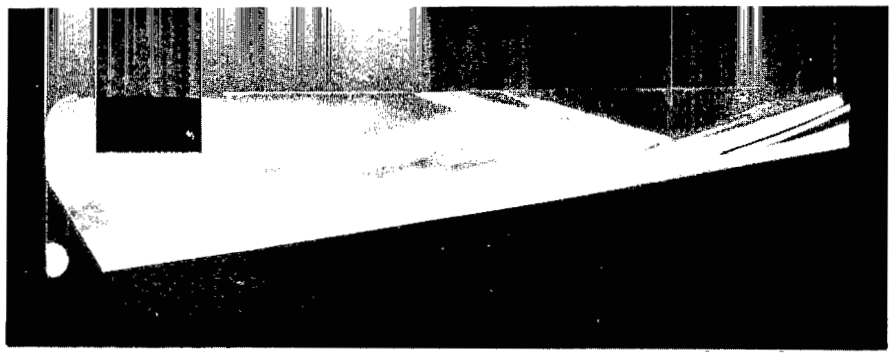

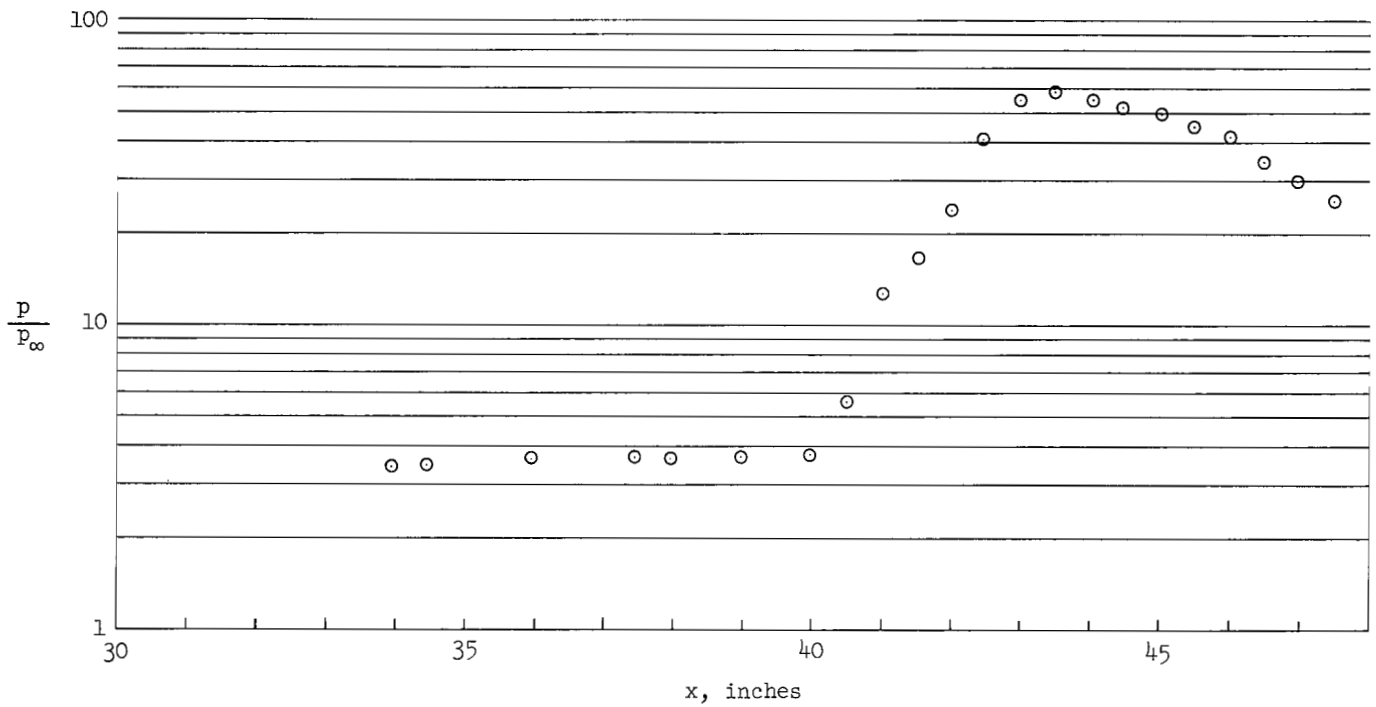

(g) Turbulent boundary layer; CS 69, $\alpha_L = 17°$.

Figure 20.- Concluded.

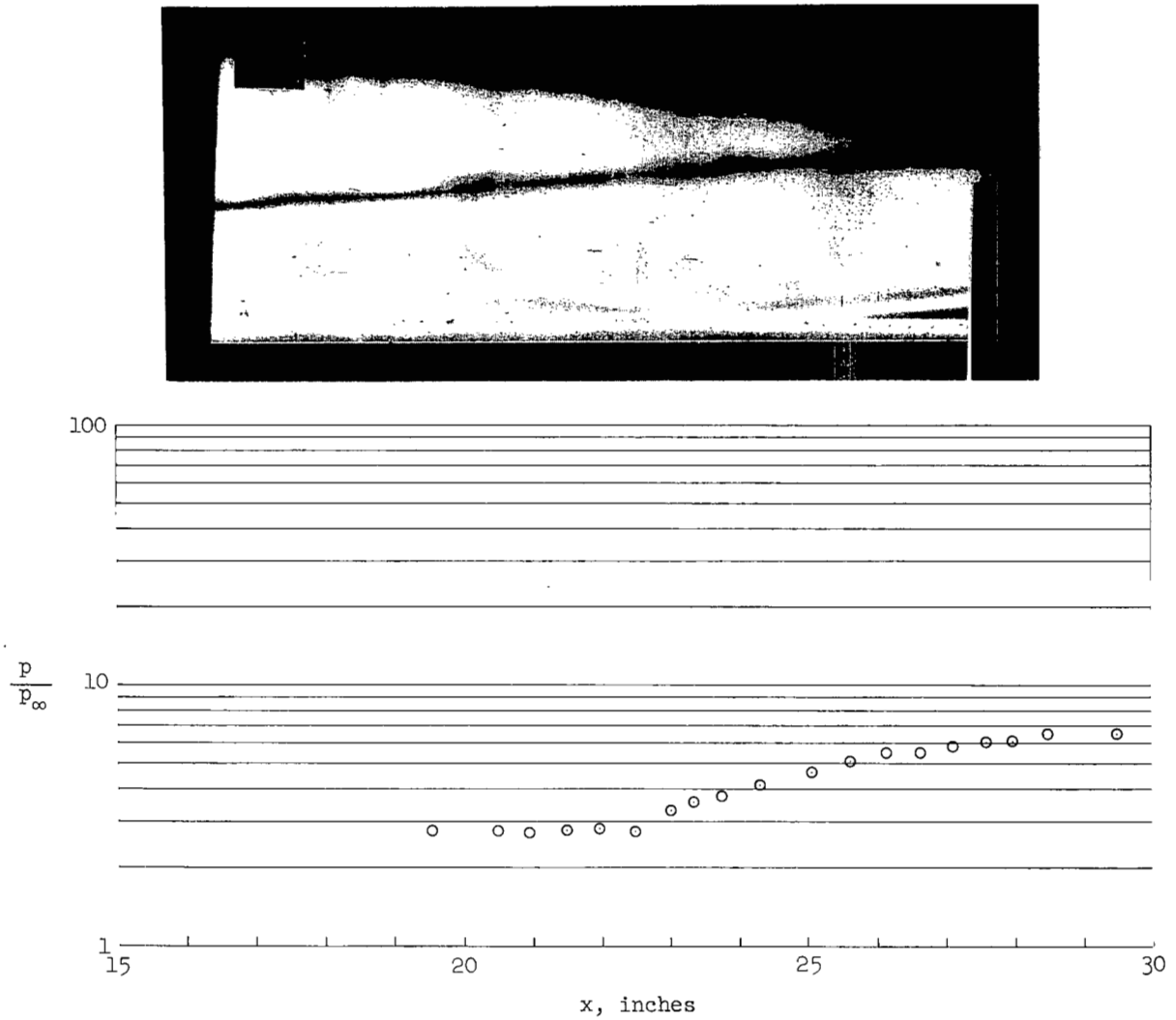

(a) Laminar boundary layer; FP 35, $\alpha_L = 3°$.

Figure 21.- Schlieren photograph and experimental surface pressure distribution for interaction on flat-plate model; $M_\infty = 10.4$.

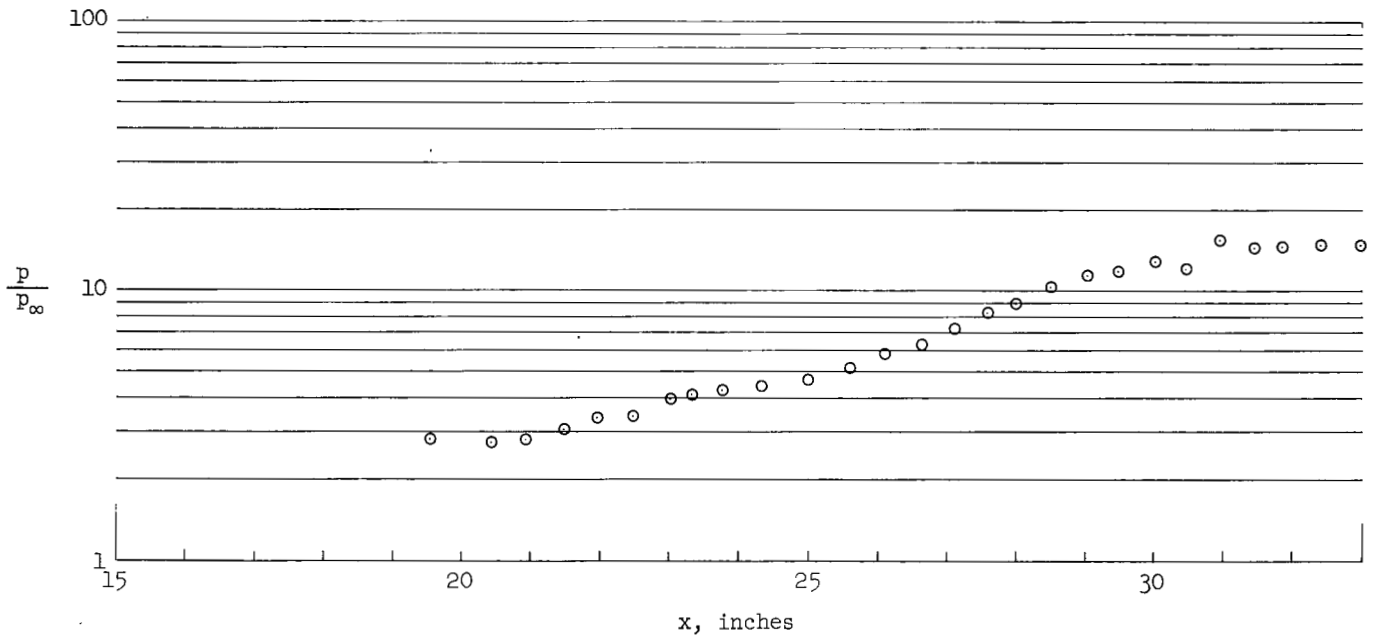

(b) Laminar boundary layer; FP 35, $\alpha_L = 5°$.

Figure 21.- Continued.

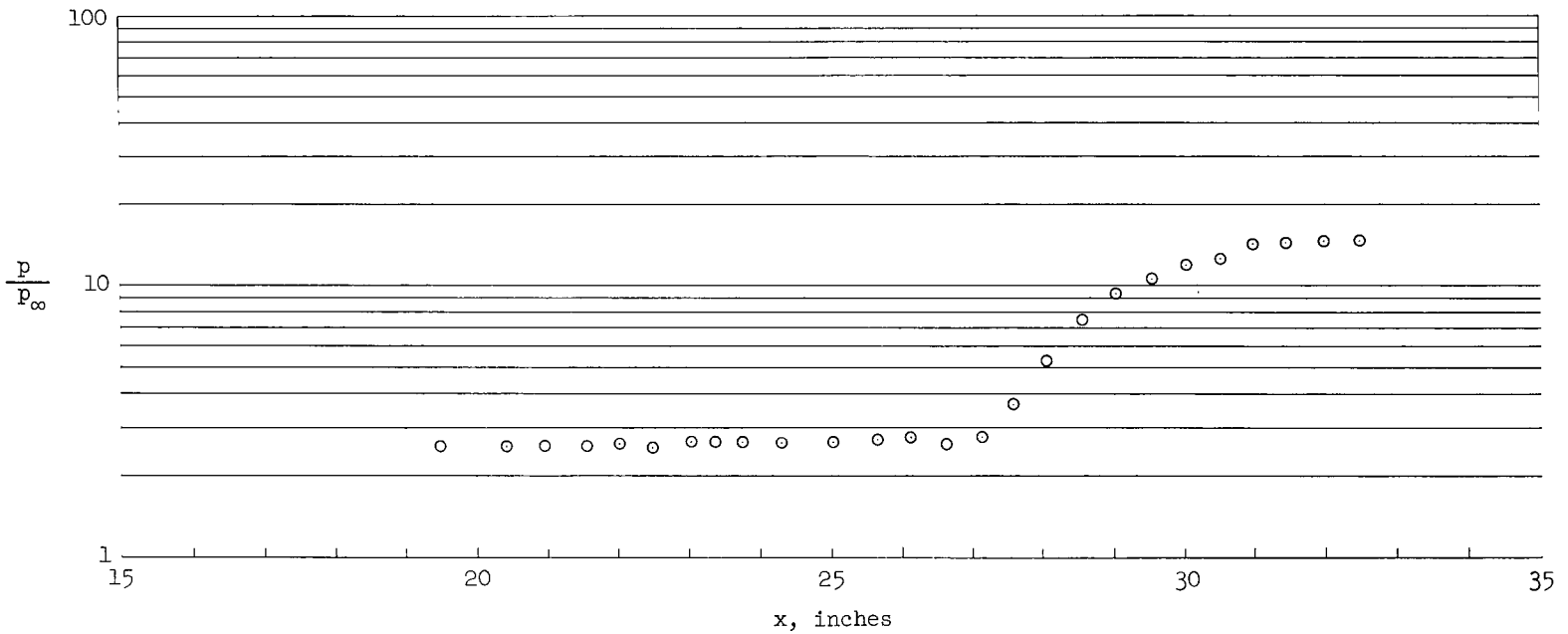

(c) Turbulent boundary layer; FP 37, $\alpha_L = 5°$.

Figure 21.- Continued.

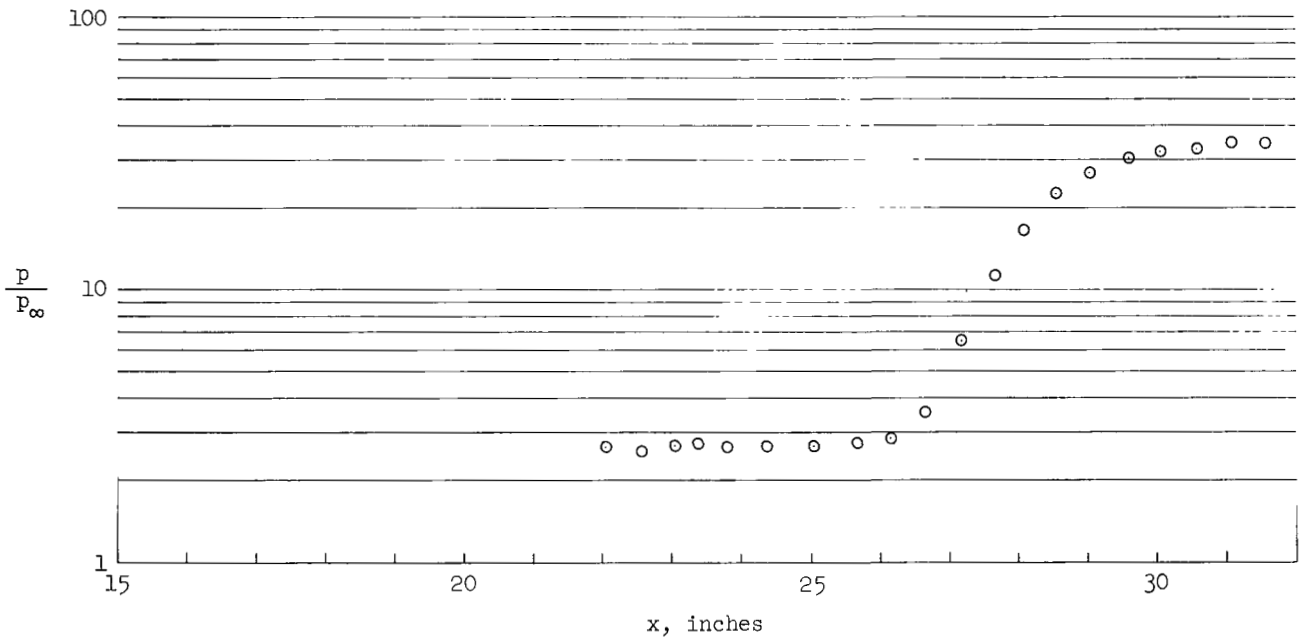

(d) Turbulent boundary layer; FP 37, $\alpha_L = 8°$.

Figure 21.- Continued.

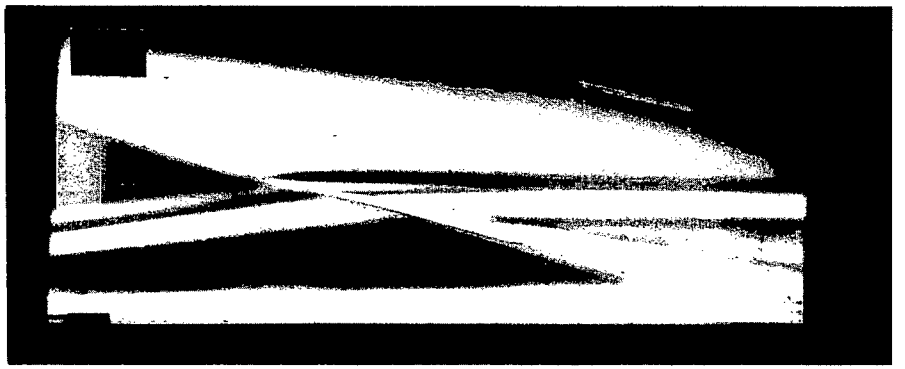

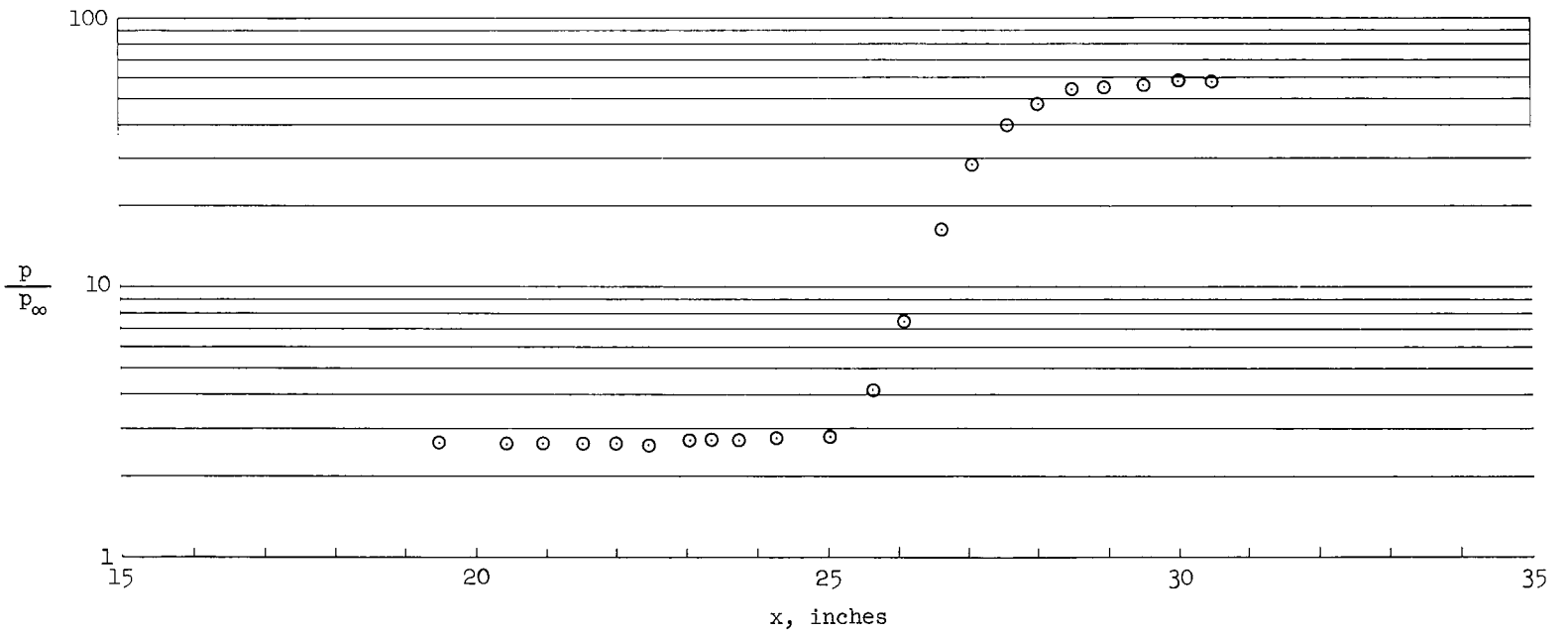

(e) Turbulent boundary layer; FP 37, $\alpha_L = 10°$.

Figure 21.- Concluded.

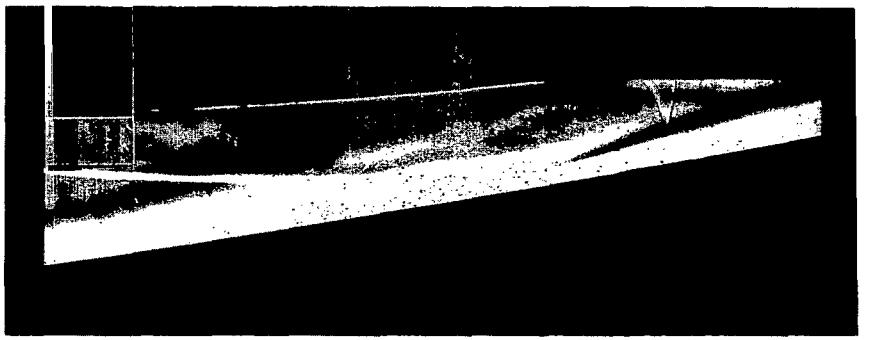

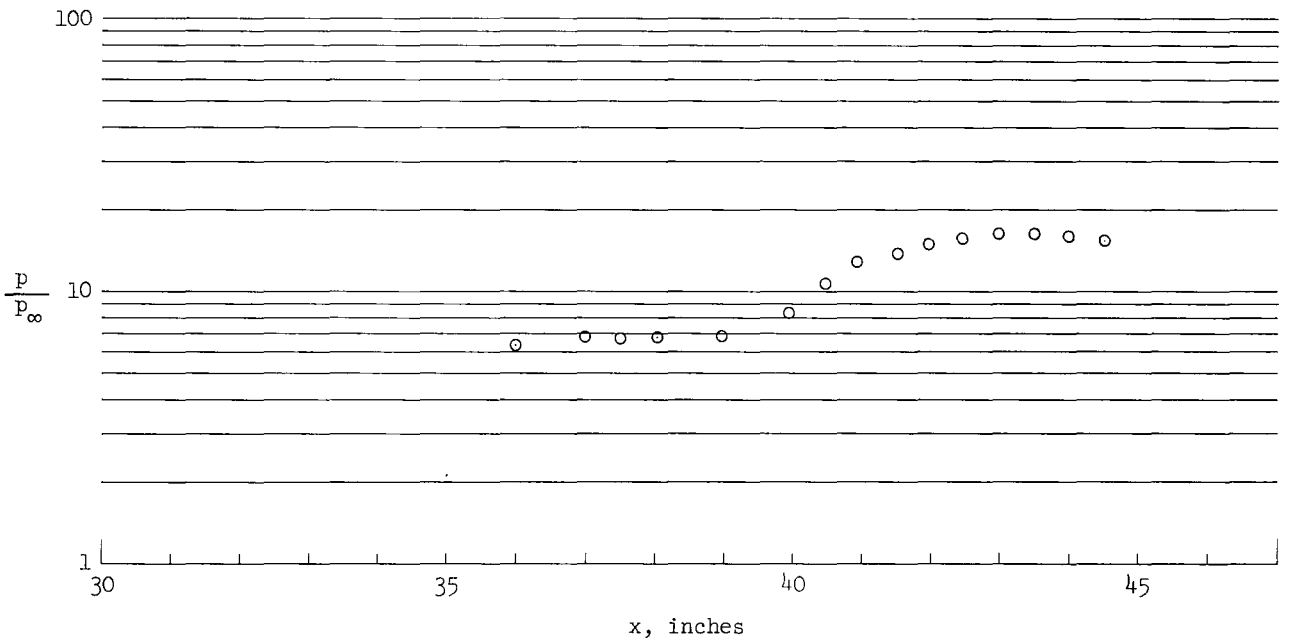

(a) Turbulent boundary layer; CS 18, $\alpha_L = 3°$.

Figure 22.- Schlieren photograph and experimental surface pressure distribution for interaction on compression-surface model; $M_\infty = 10.4$.

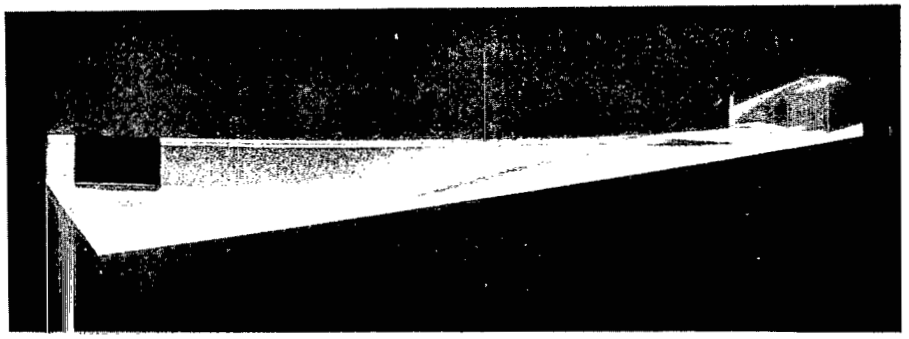

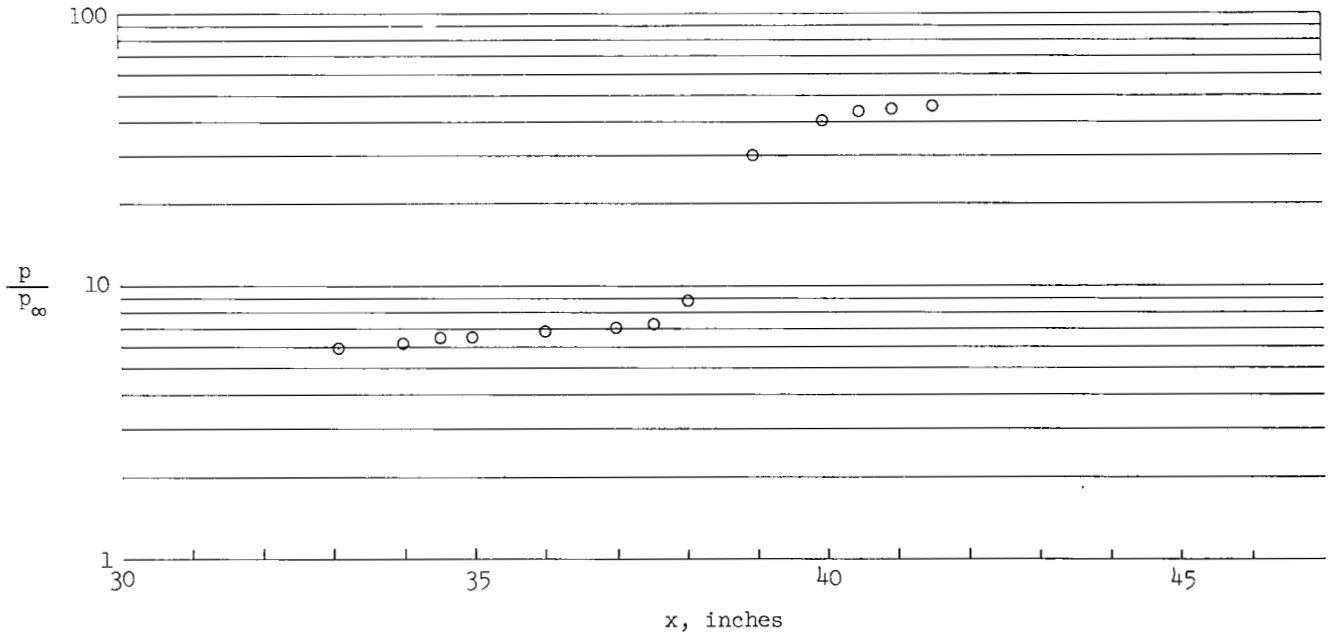

(b) Turbulent boundary layer; CS 25, $\alpha_L = 7°$.

Figure 22.- Continued.

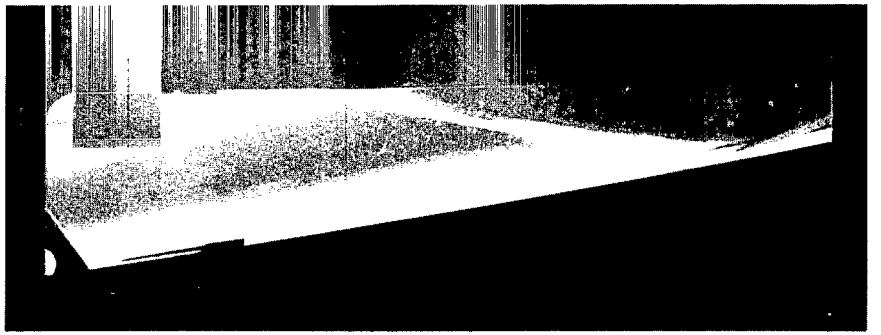

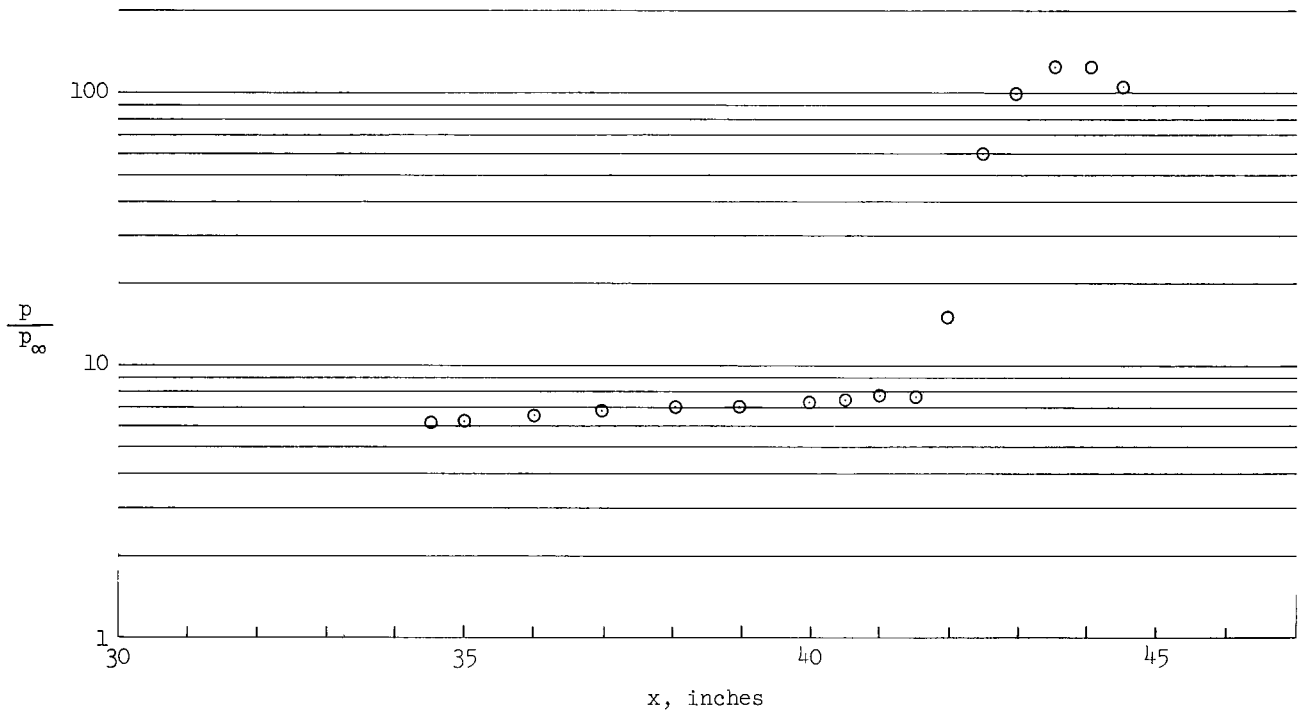

(c) Turbulent boundary layer; CS 38, α_L = 14°.

Figure 22.- Concluded.

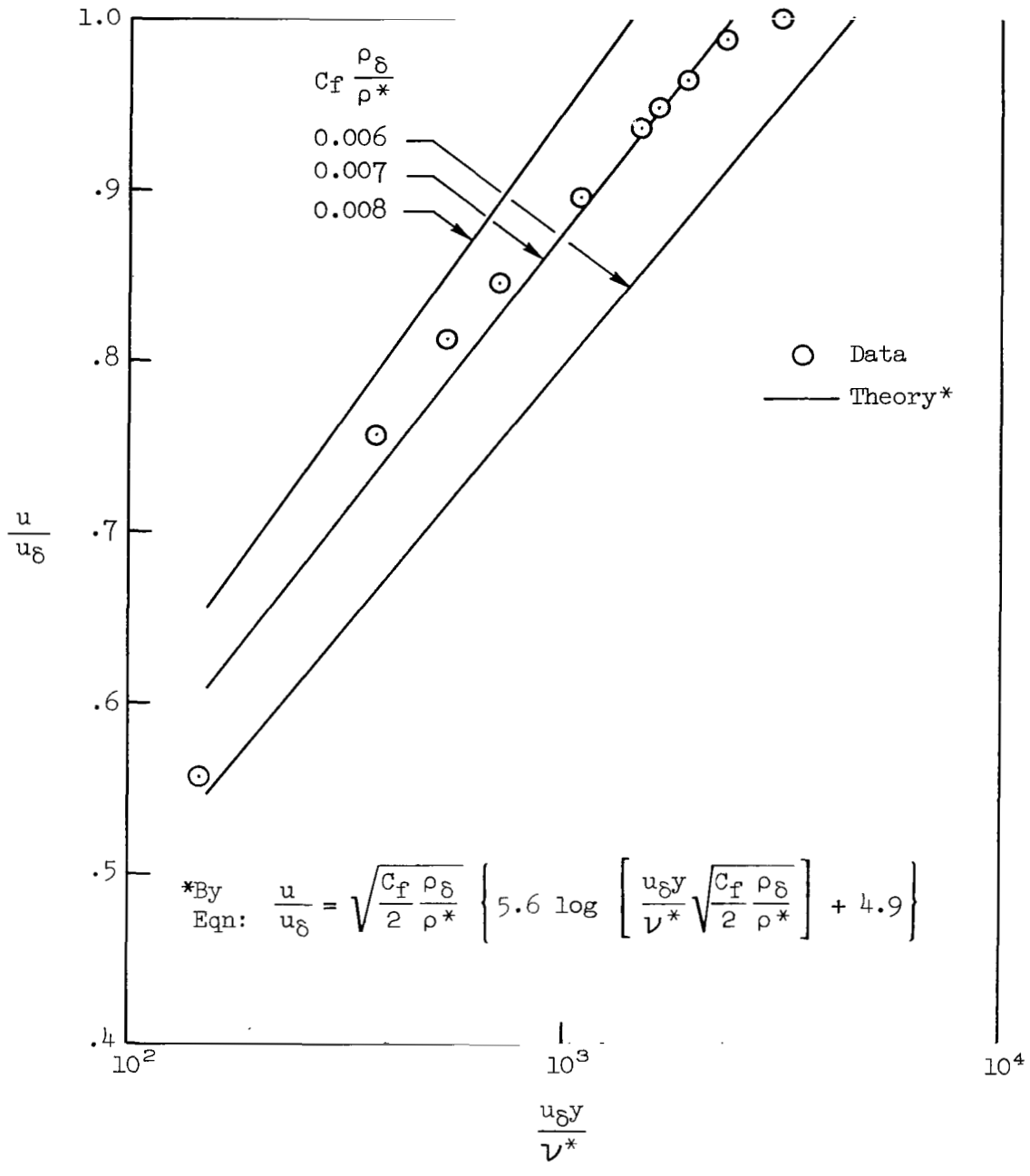

Figure 23.- Comparison of experimental velocity profile with "law-of-the-wall" profiles, FP 19; $M_\infty = 10.4$.

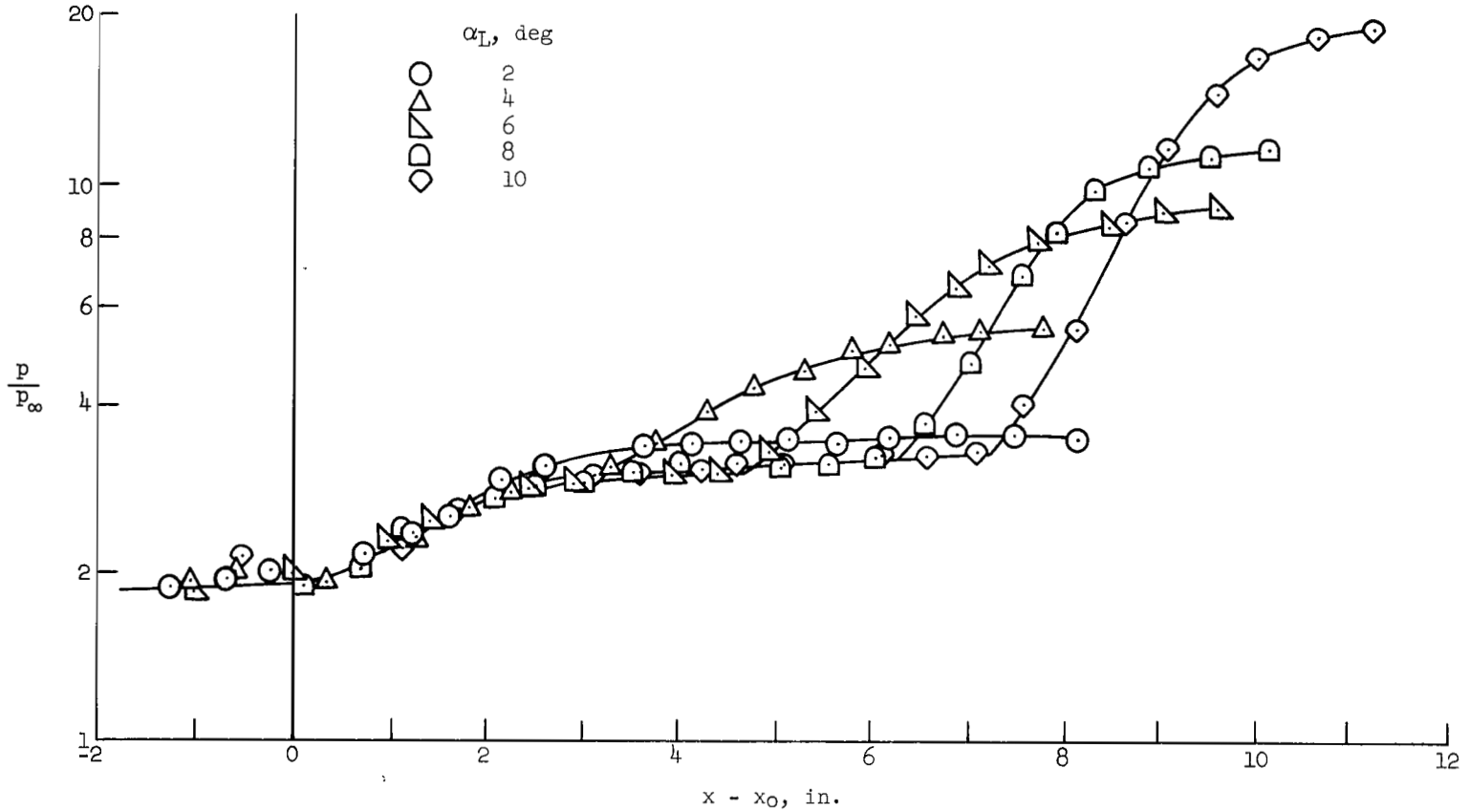

(a) Laminar boundary layer.

Figure 24.- Composite pressure distribution for flat-plate model; M_∞ = 7.3.

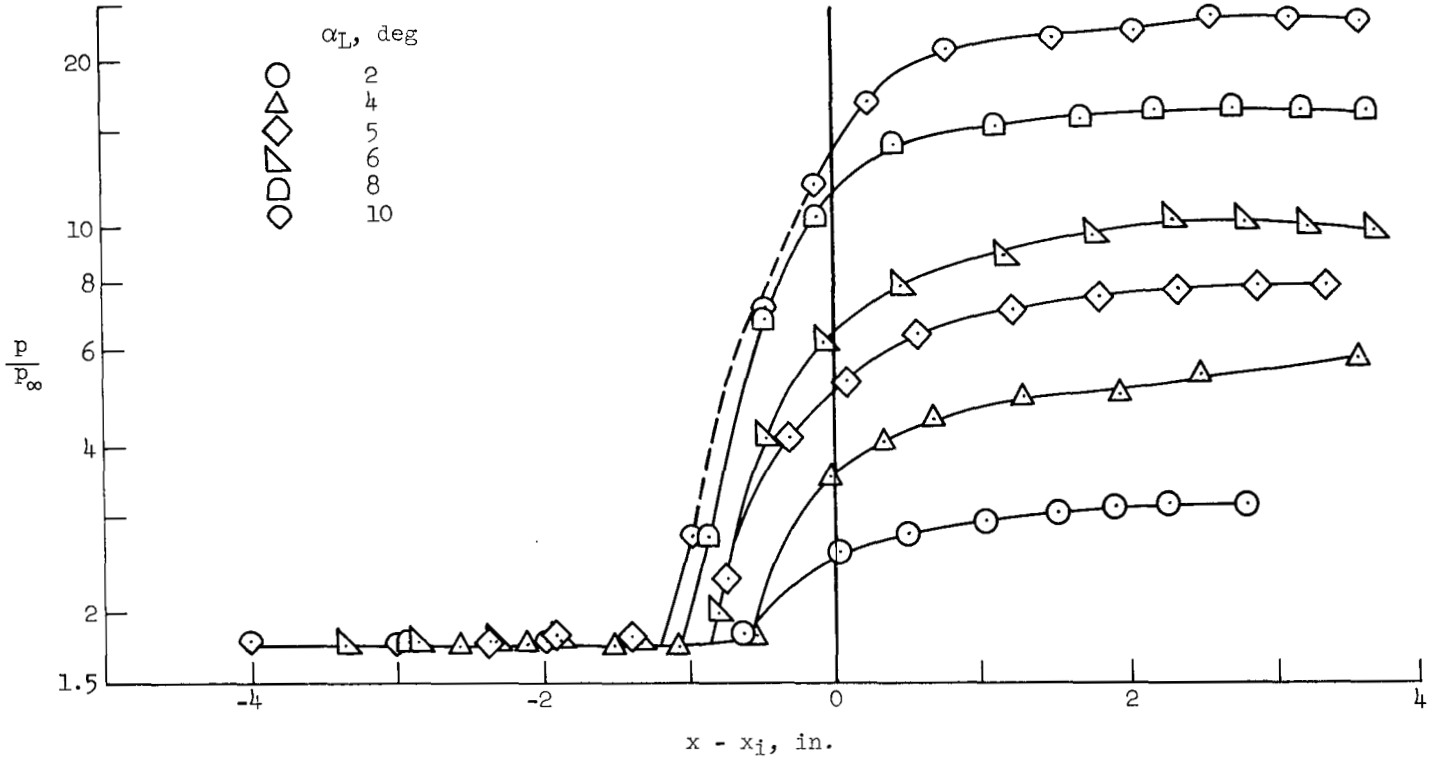

(b) Turbulent boundary layer.

Figure 24.- Concluded.

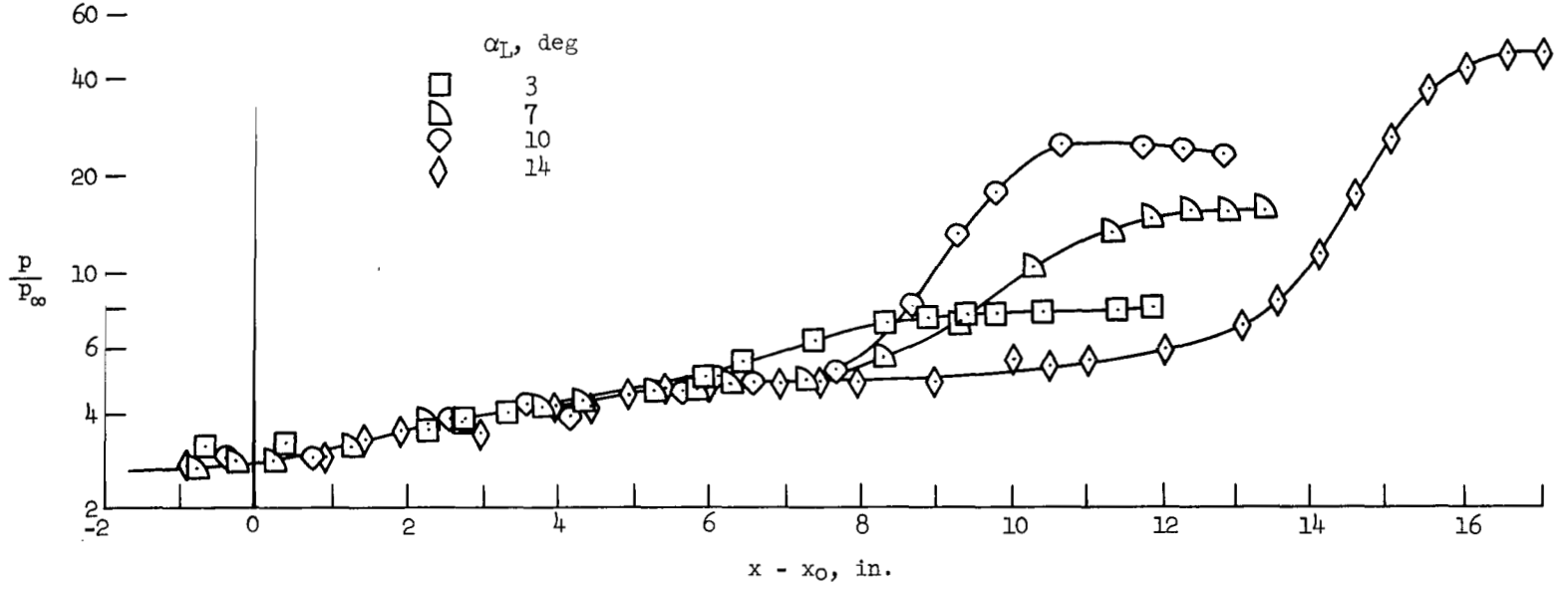

(a) Laminar boundary layer.

Figure 25.- Composite pressure distribution for compression-surface model; M_∞ = 7.3.

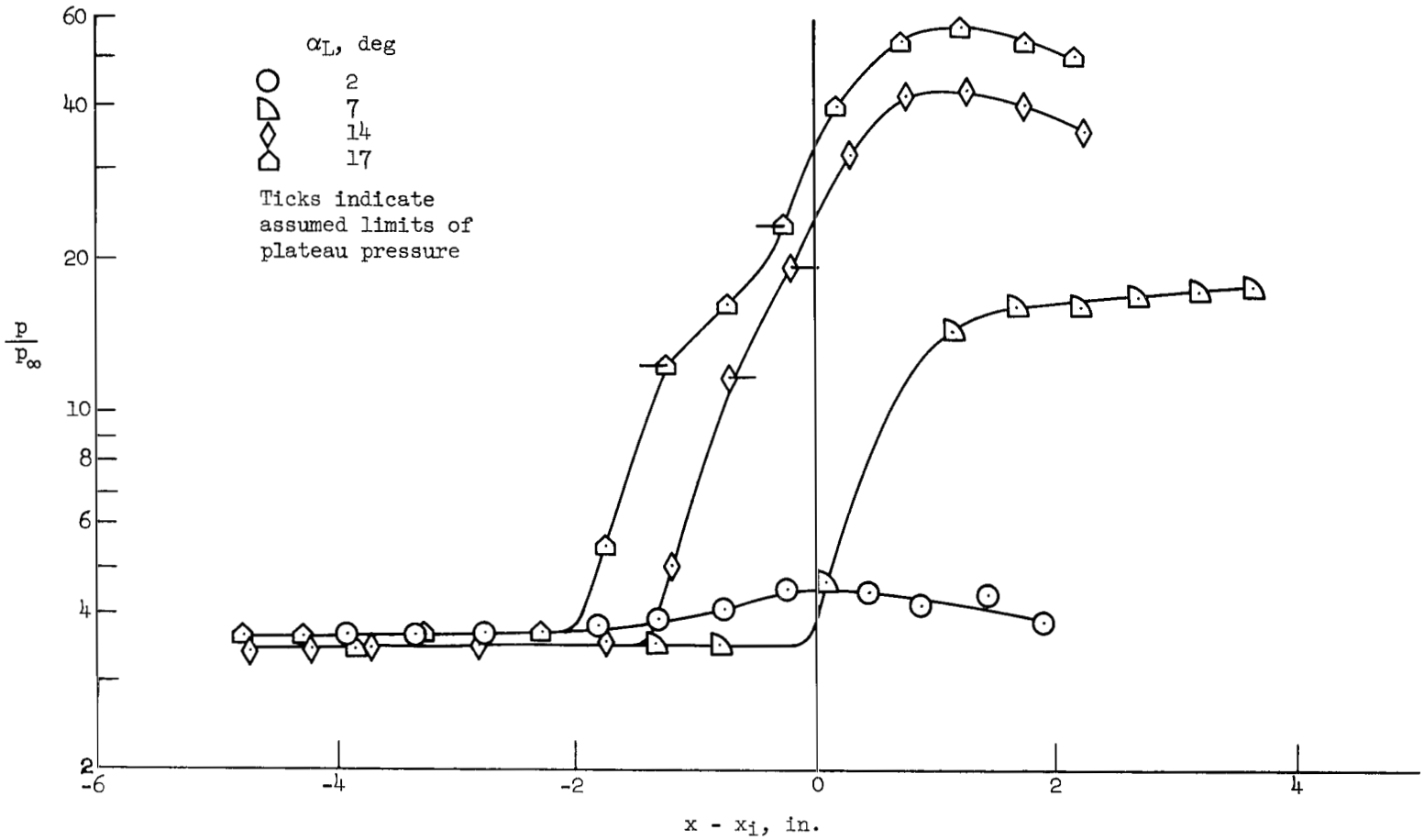

(b) Turbulent boundary layer.

Figure 25.- Concluded.

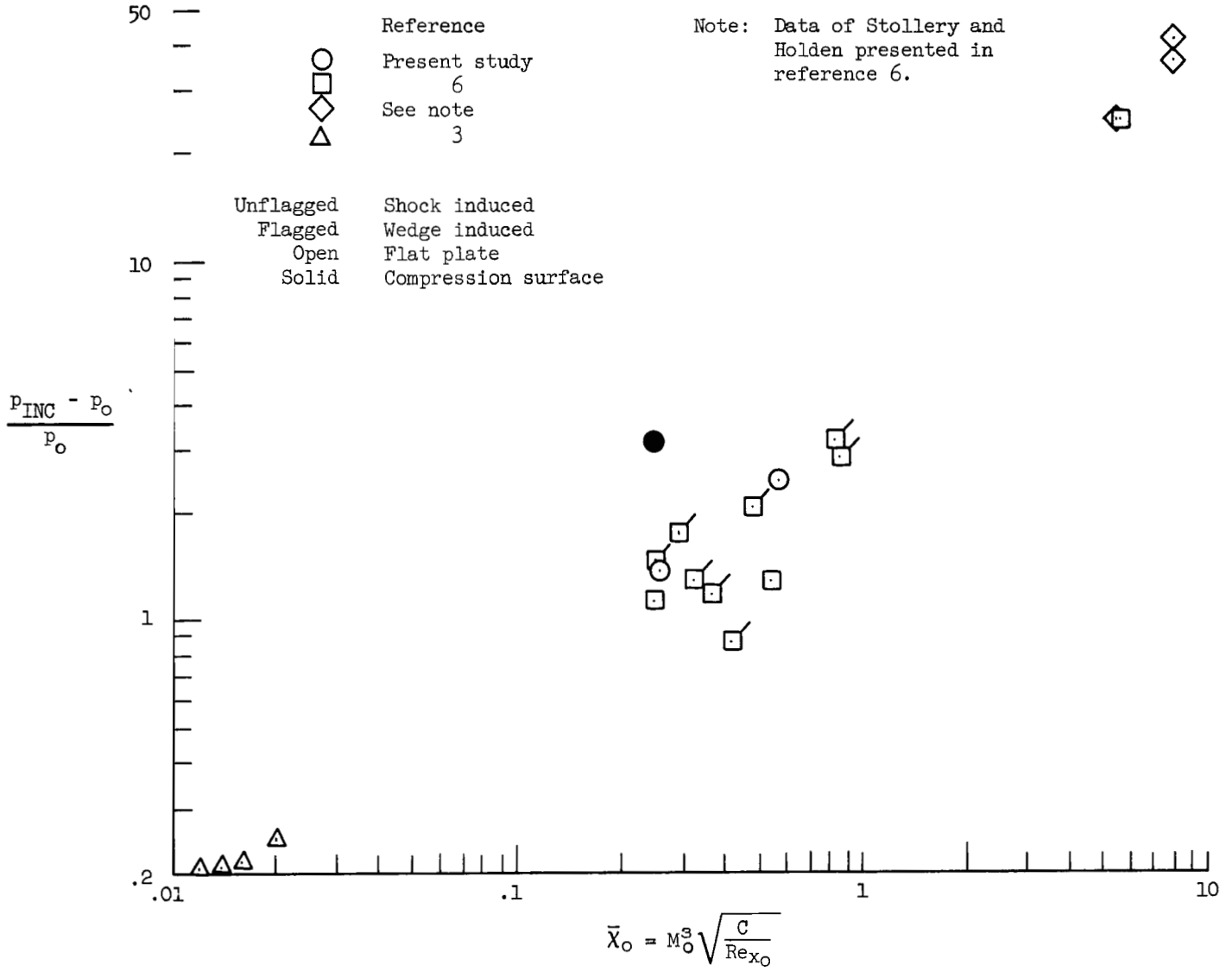

(a) Laminar boundary layer.

Figure 26.- Correlation of incipient separation pressures.

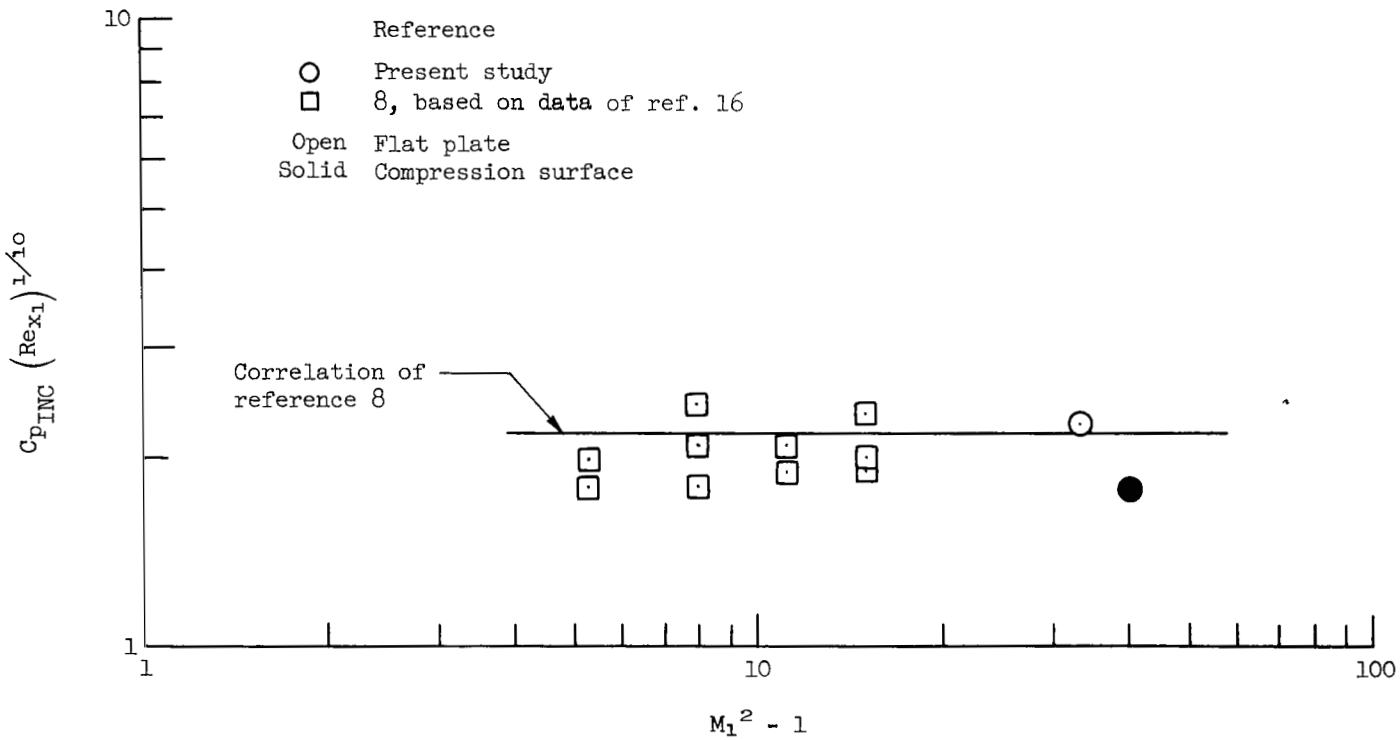

(b) Turbulent boundary layer.

Figure 26.- Concluded.

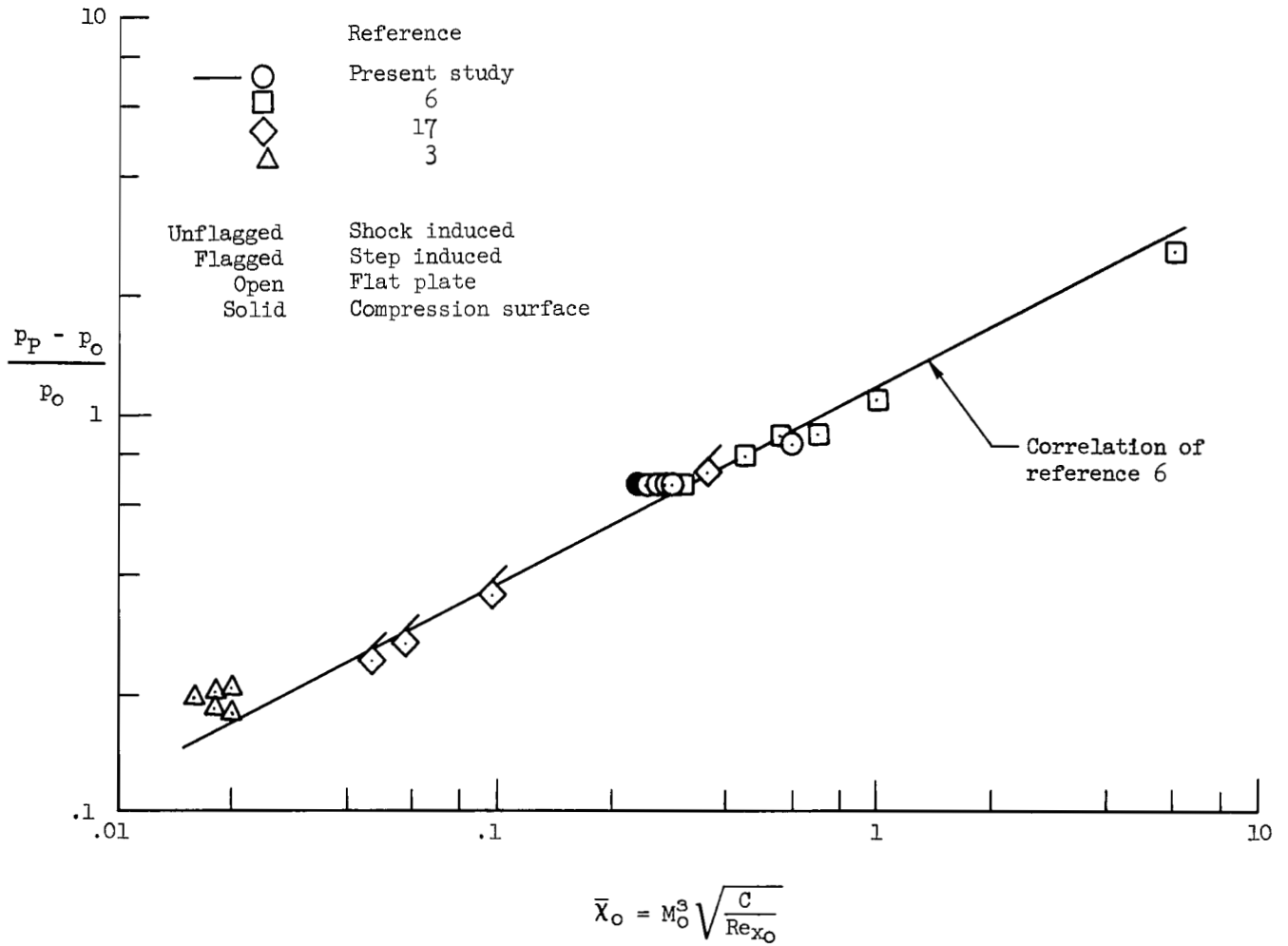

(a) Laminar boundary layer.

Figure 27.- Correlation of plateau pressures.

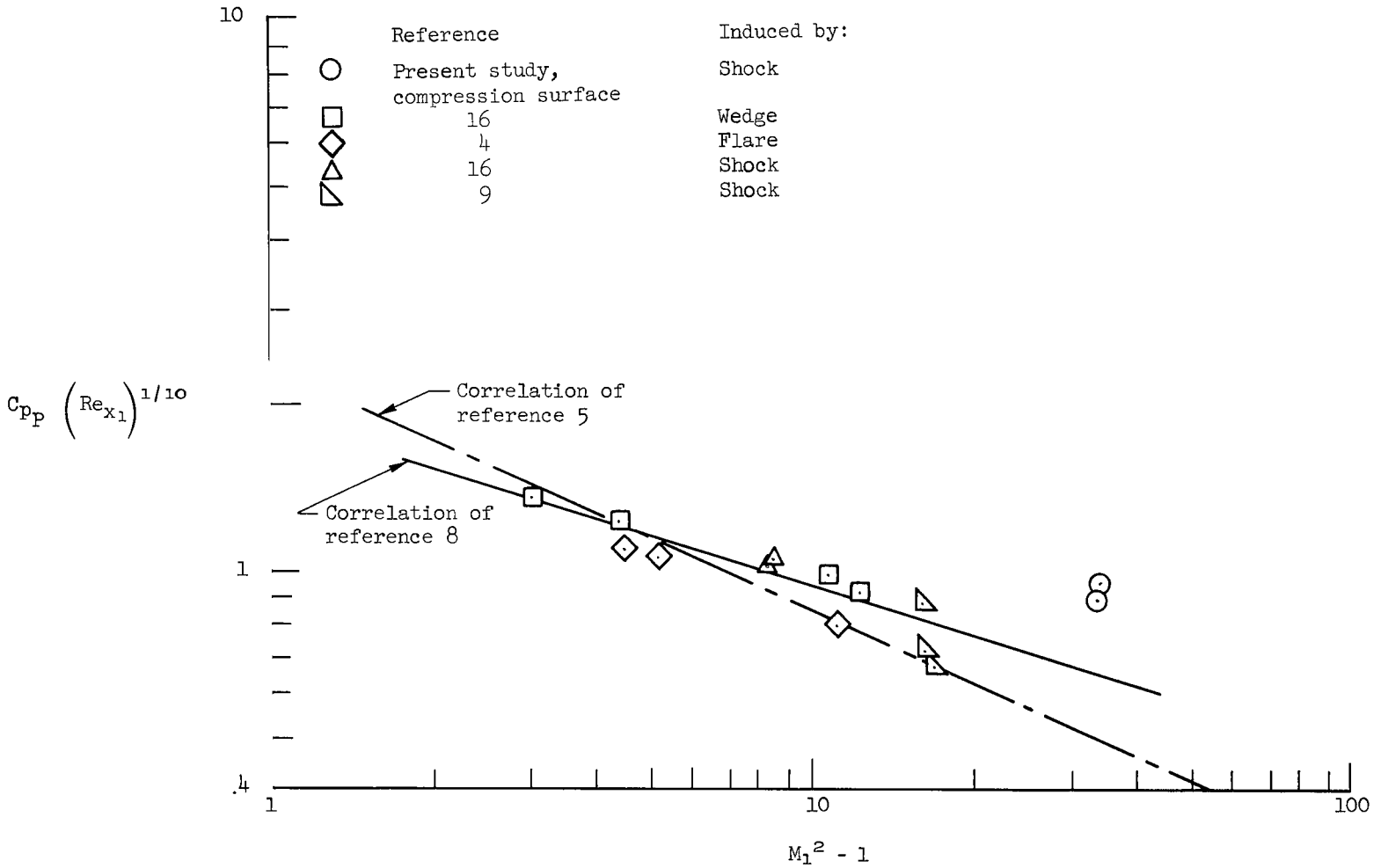

(b) Turbulent boundary layer.

Figure 27.- Concluded.

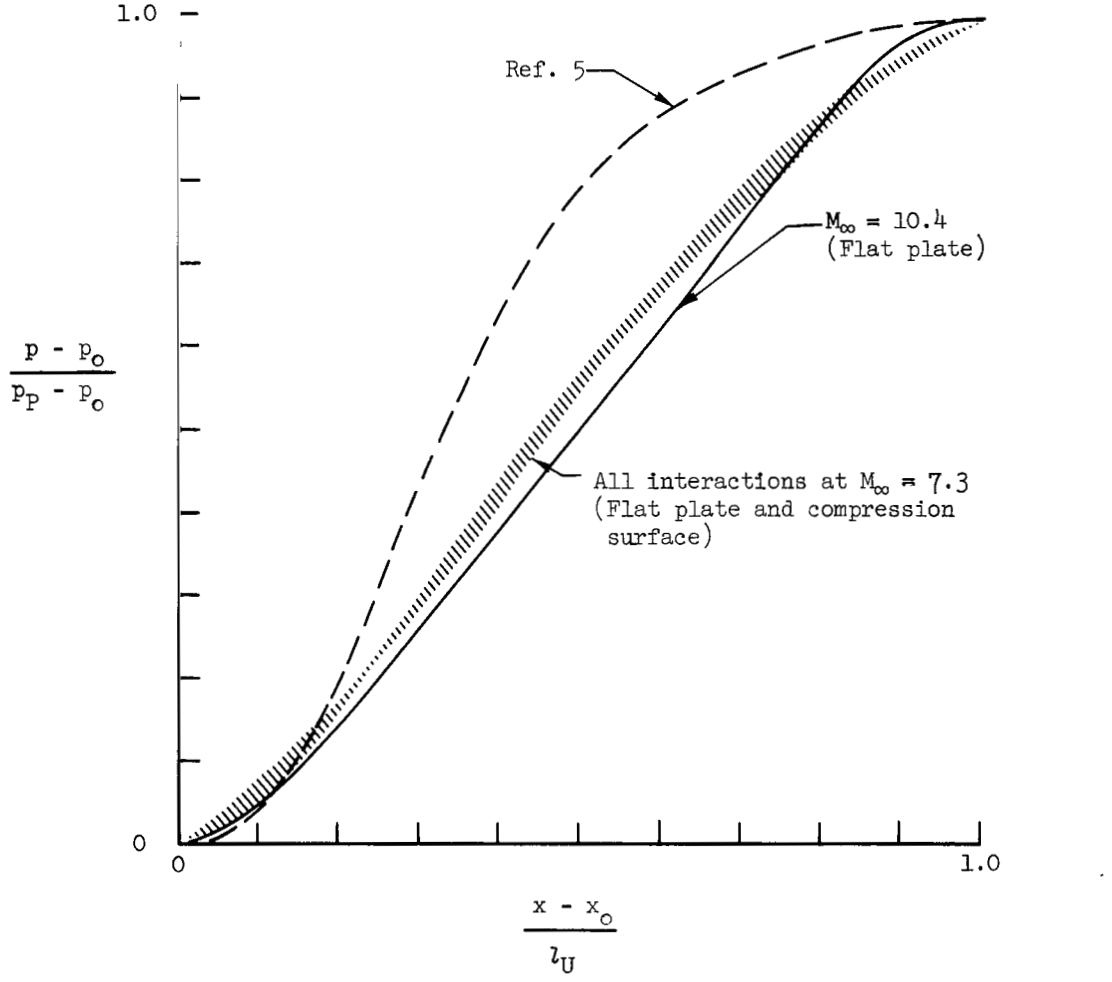

(a) Free interaction region.

Figure 28.- Dimensionless pressure distribution for separated laminar boundary layers.

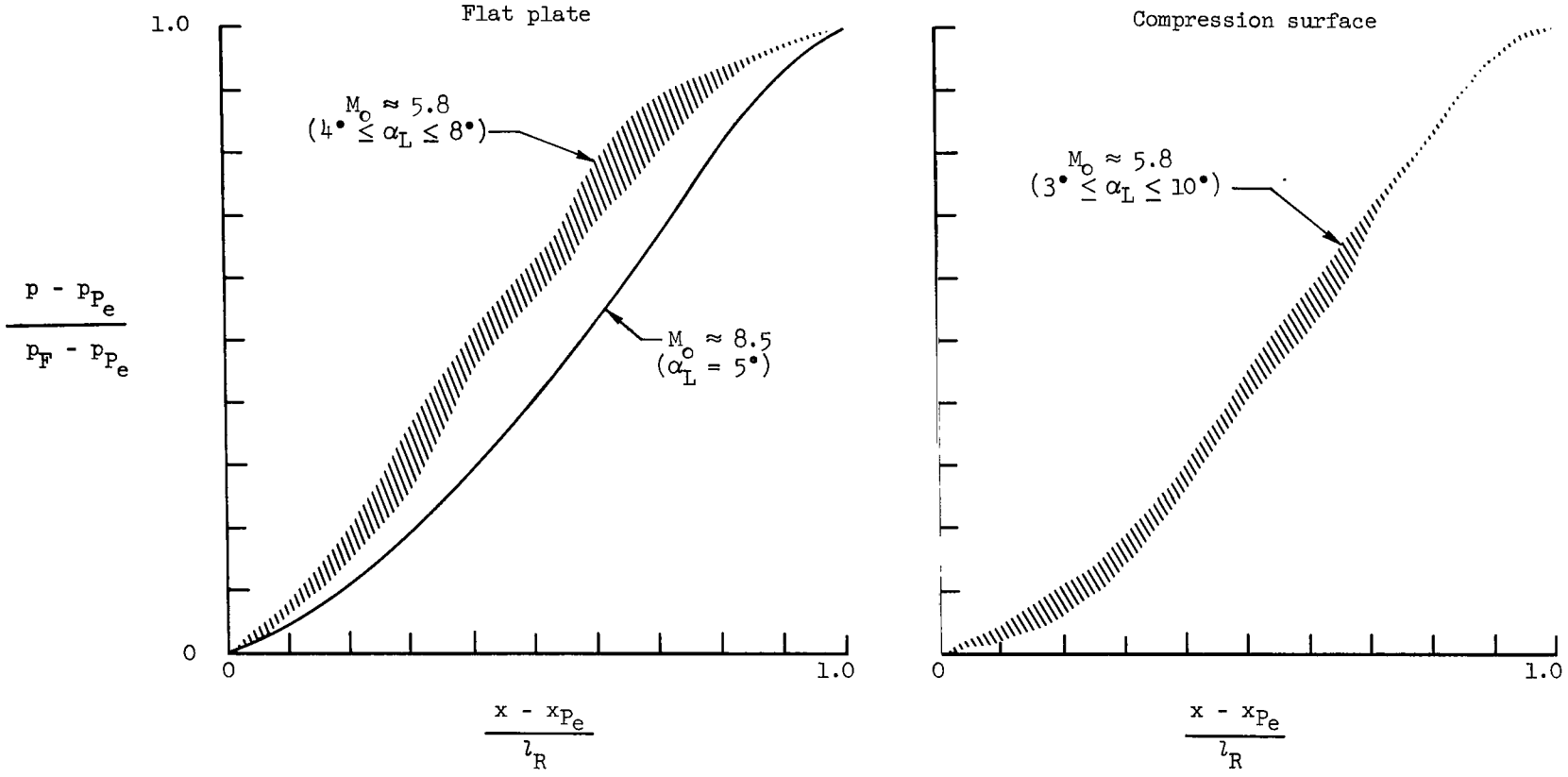

(b) Reattachment region.

Figure 28.- Concluded.

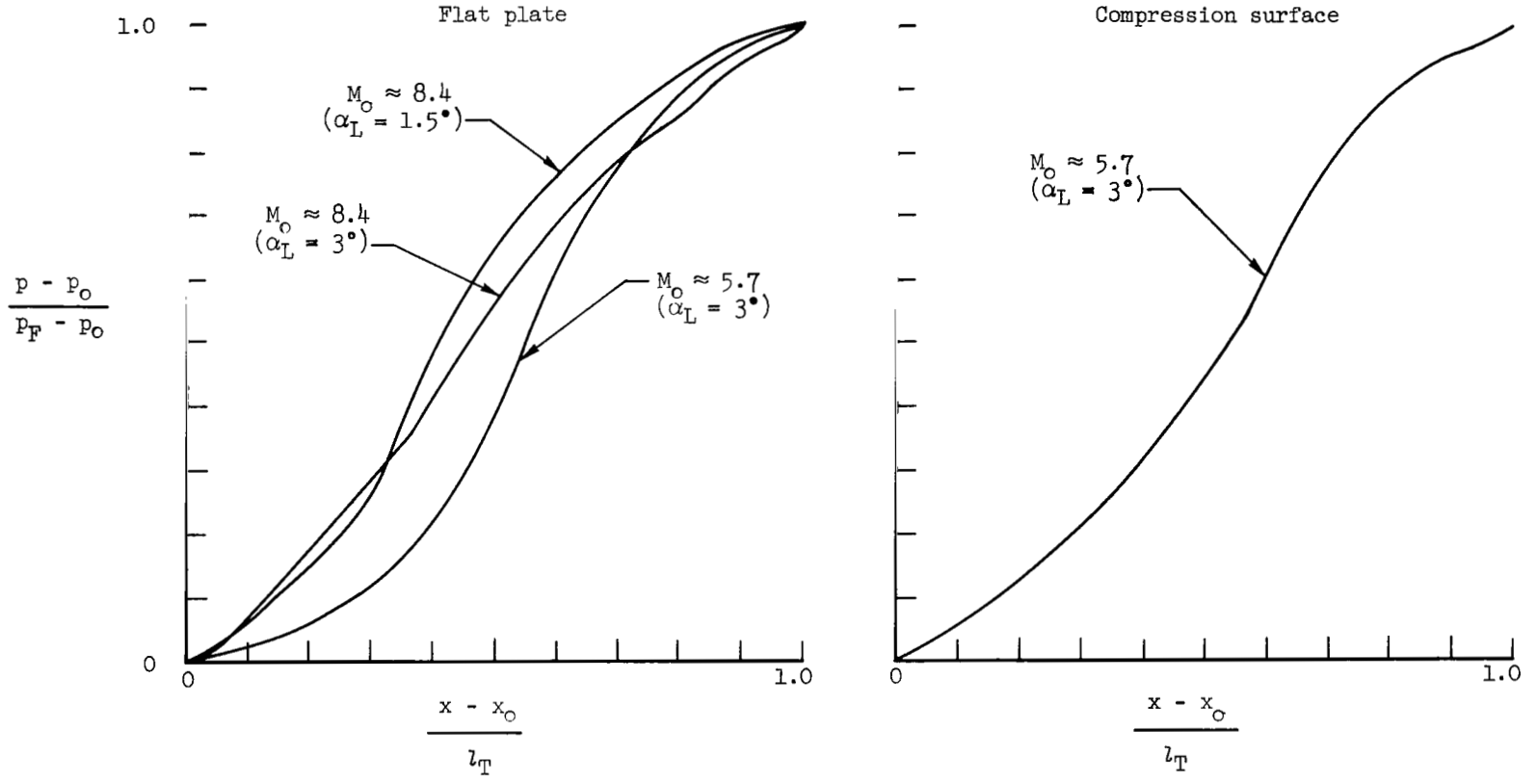

(a) Laminar boundary layer.

Figure 29.- Dimensionless pressure distribution for unseparated interactions.

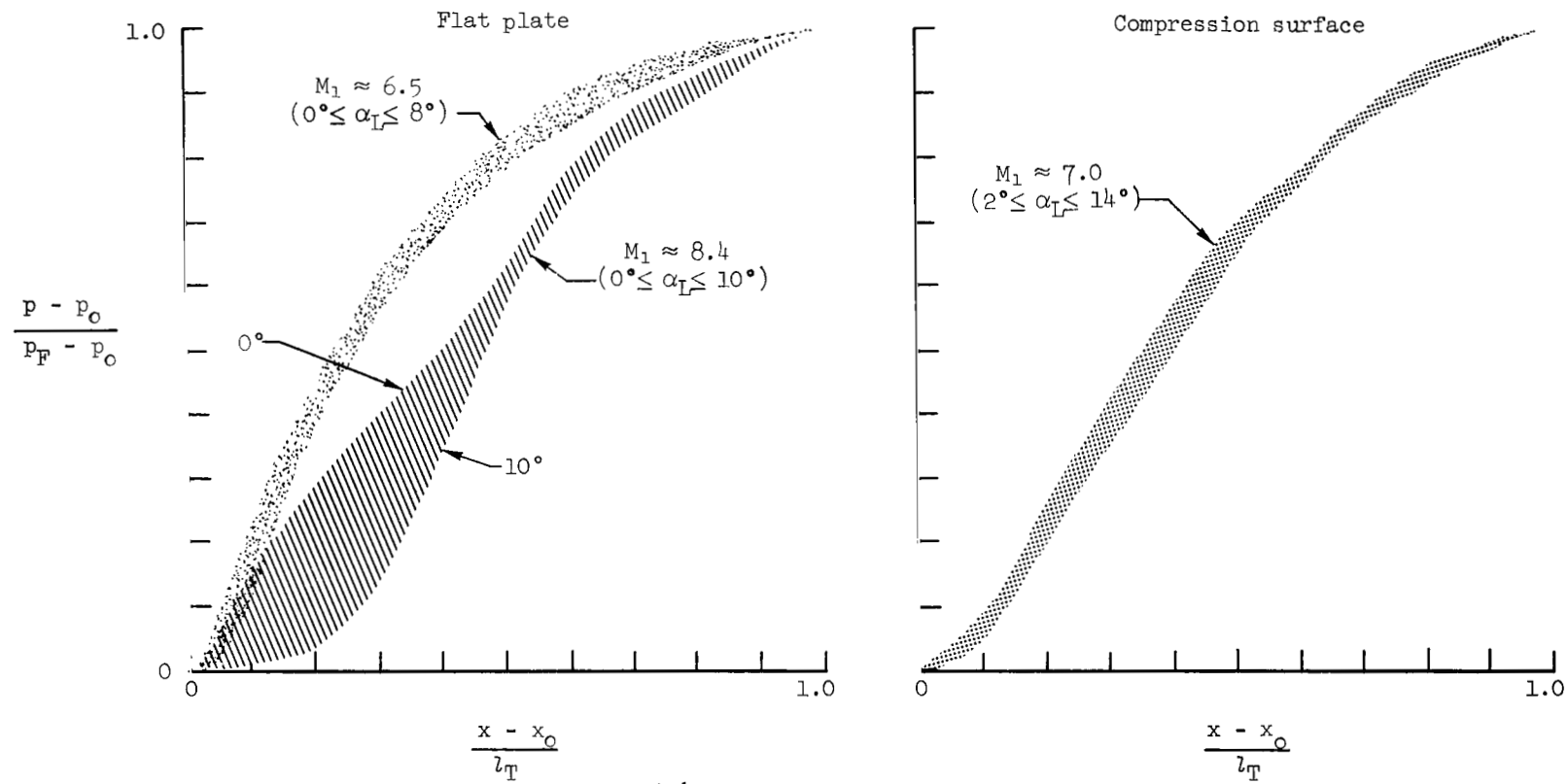

(b) Turbulent boundary layer.

Figure 29.- Concluded.

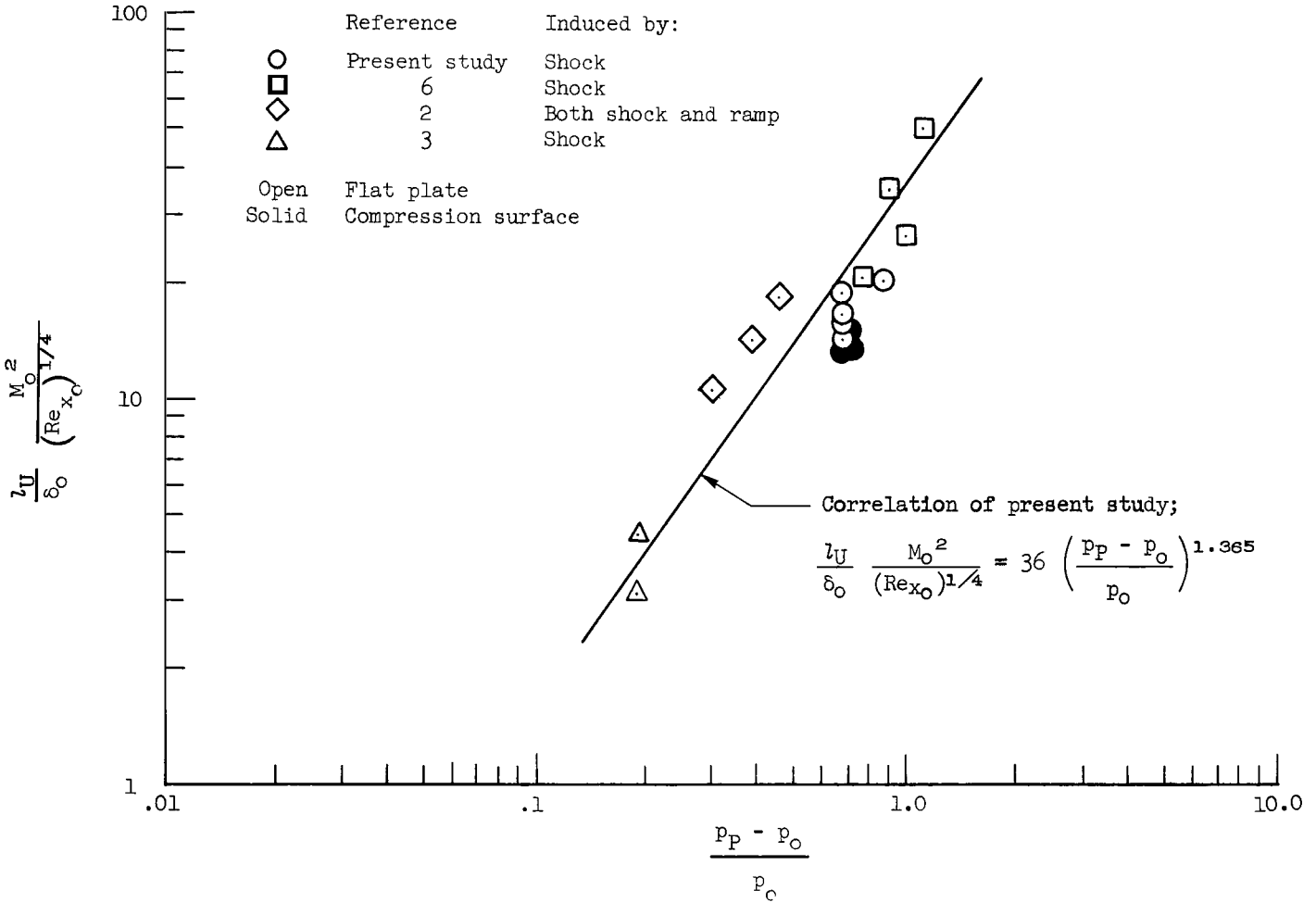

(a) Laminar boundary layer.

Figure 30.- Correlation of free interaction length.

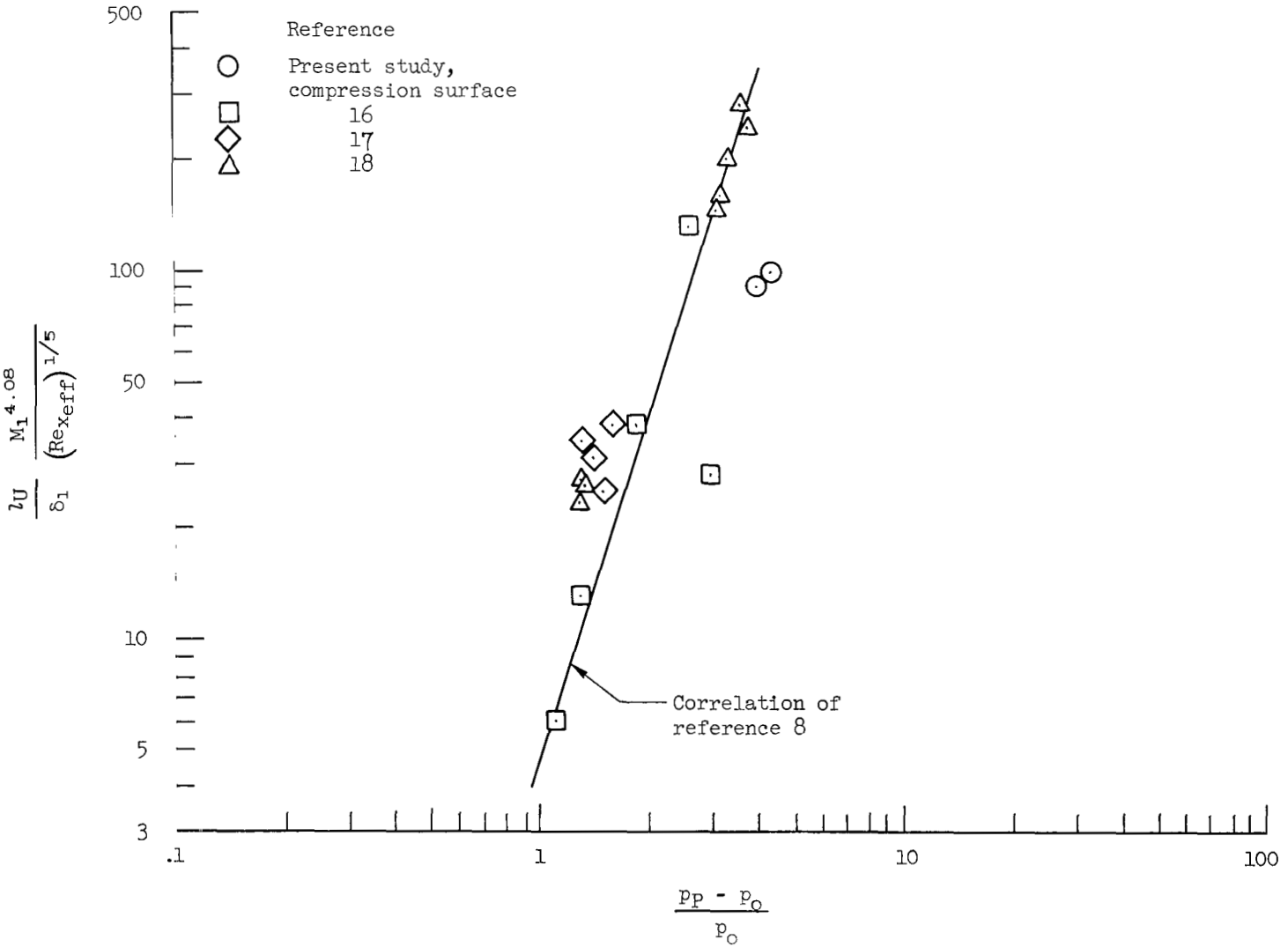

(b) Turbulent boundary layer.

Figure 30.- Concluded.

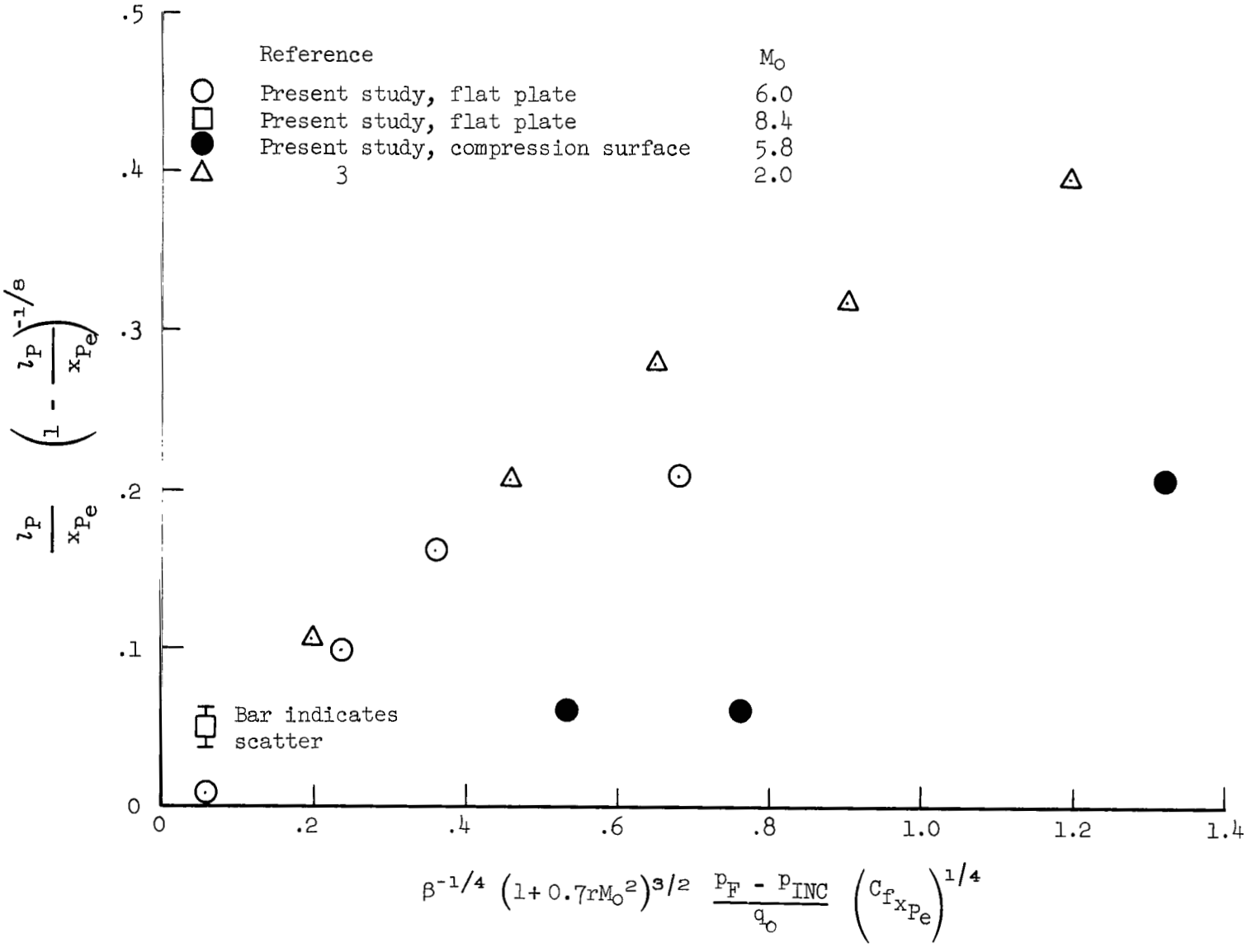

Figure 31.- Comparison of plateau length data using parameters of Hakkinen; laminar boundary layer.

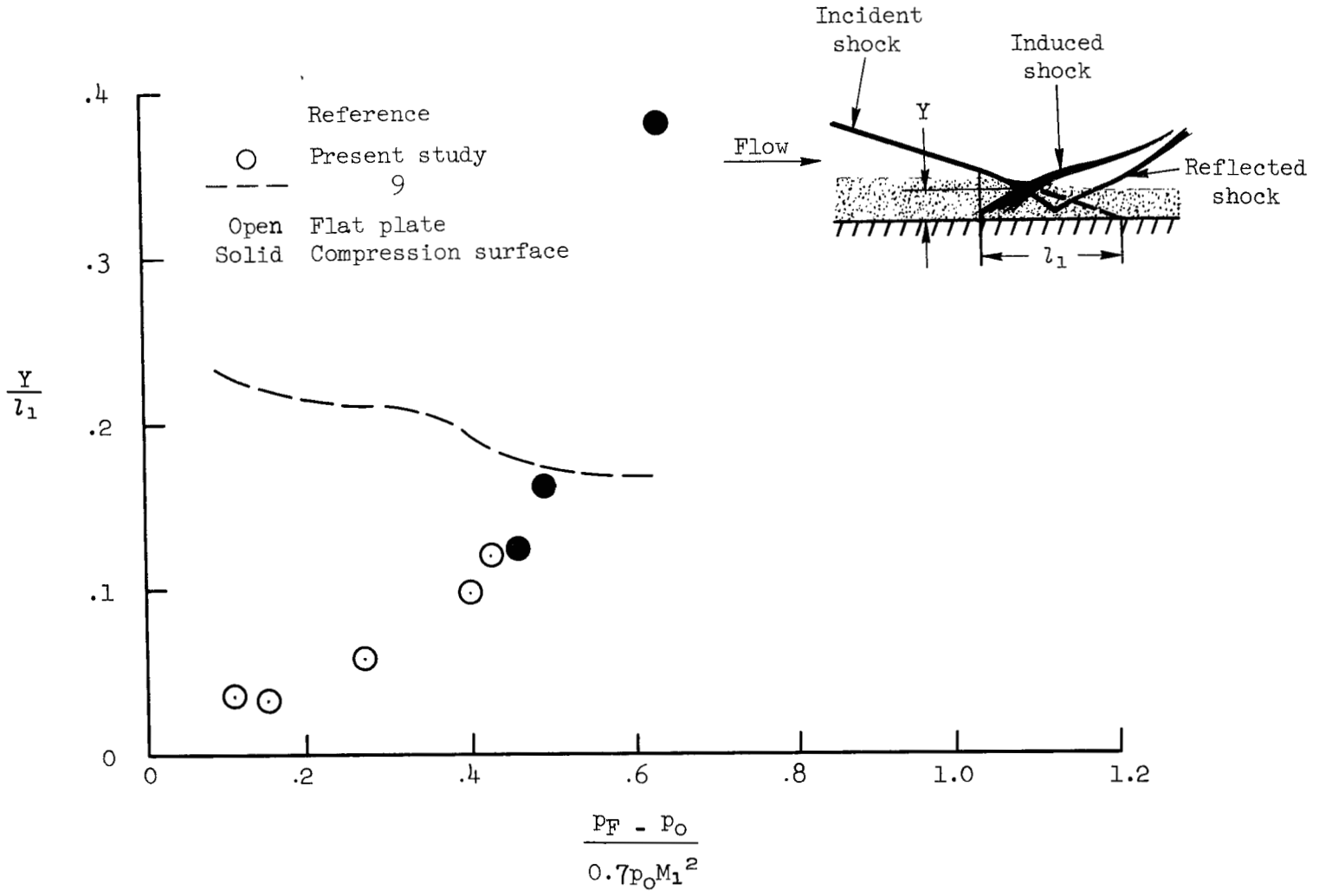

Figure 32.- Variation of Pinckney parameter, Y/l_1 with the pressure coefficient across the interaction; turbulent boundary layer.

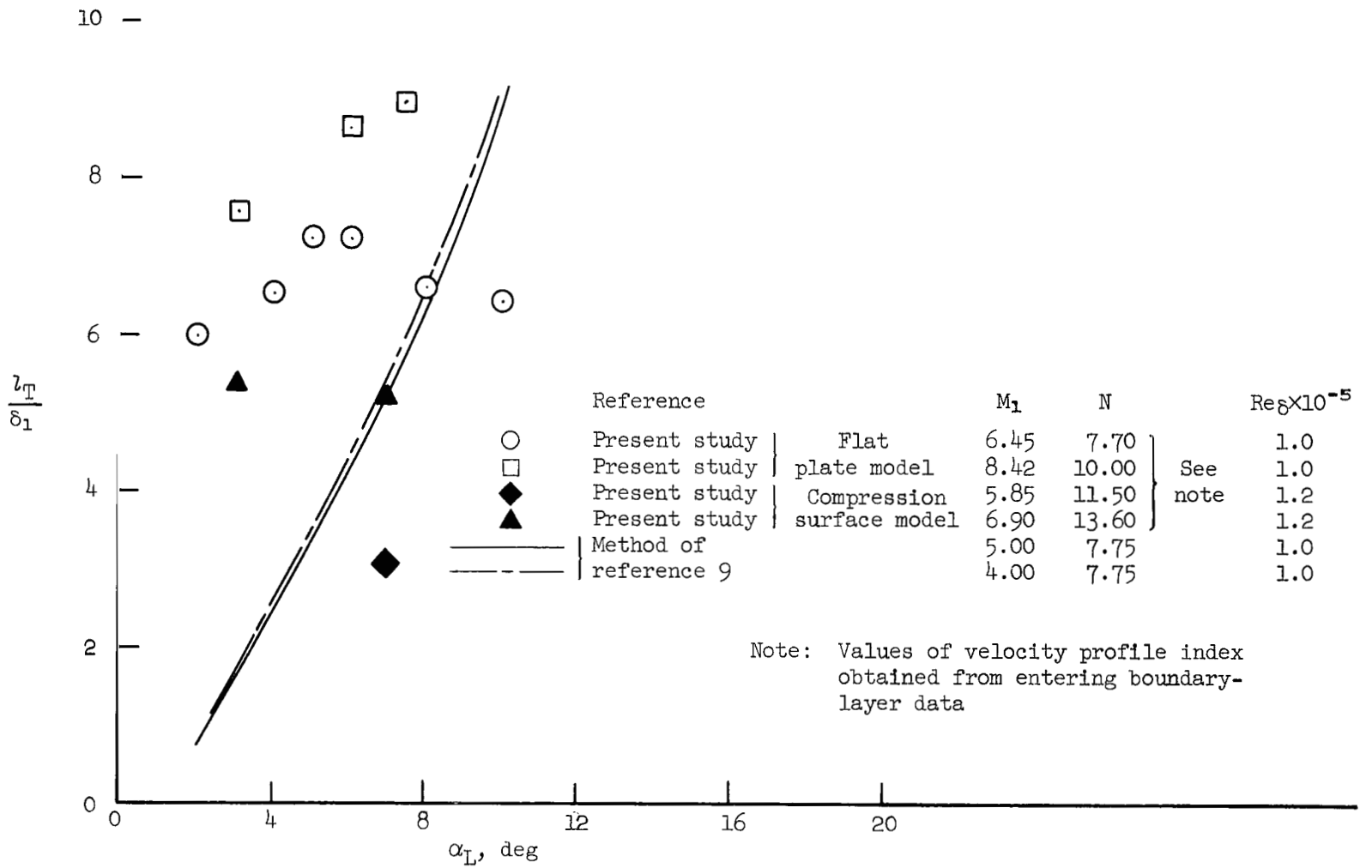

Figure 33.- Variation of total interaction length with impinging shock strength; turbulent boundary layer.

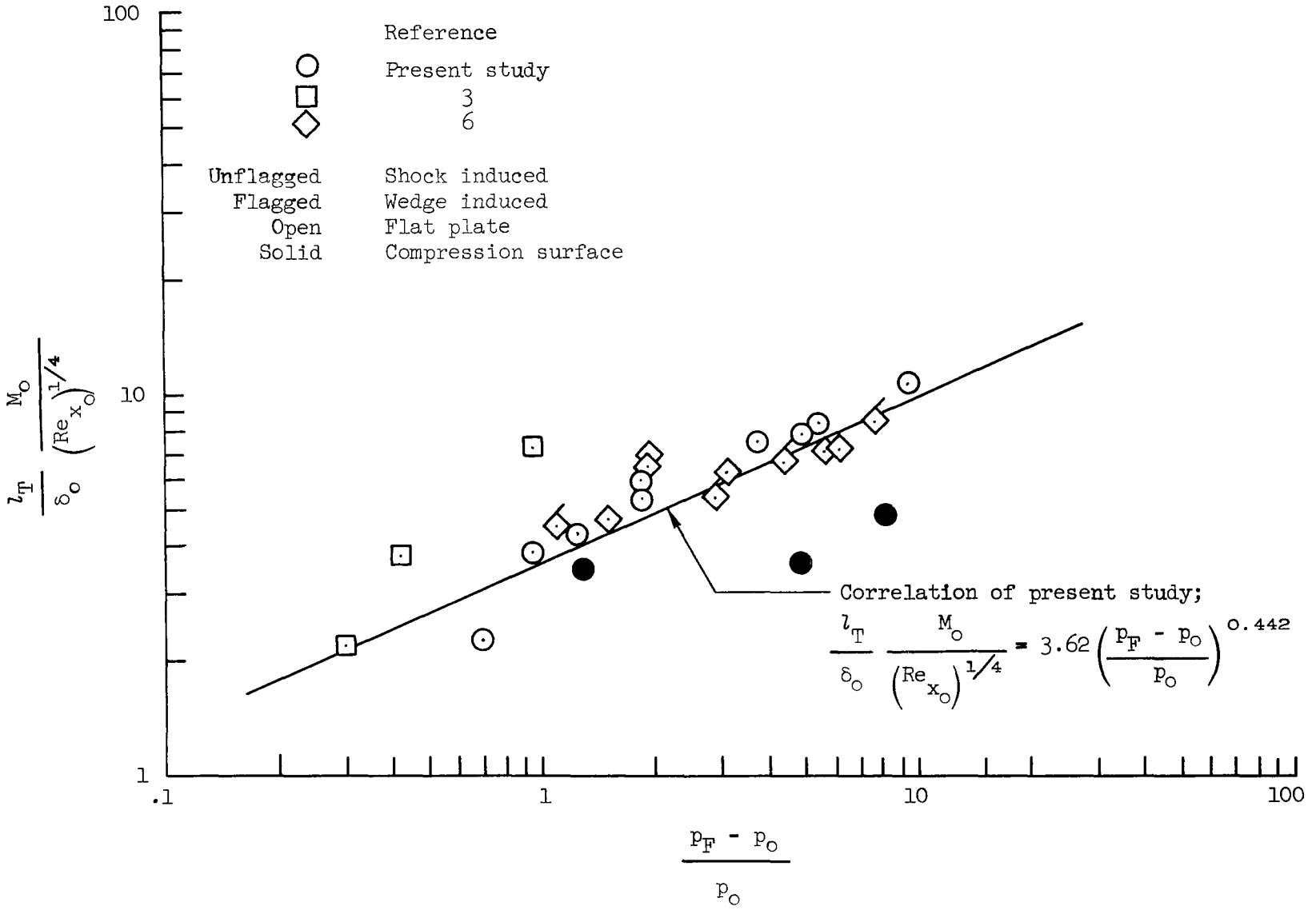

Figure 34.- Correlation of total interaction length; laminar boundary layer.

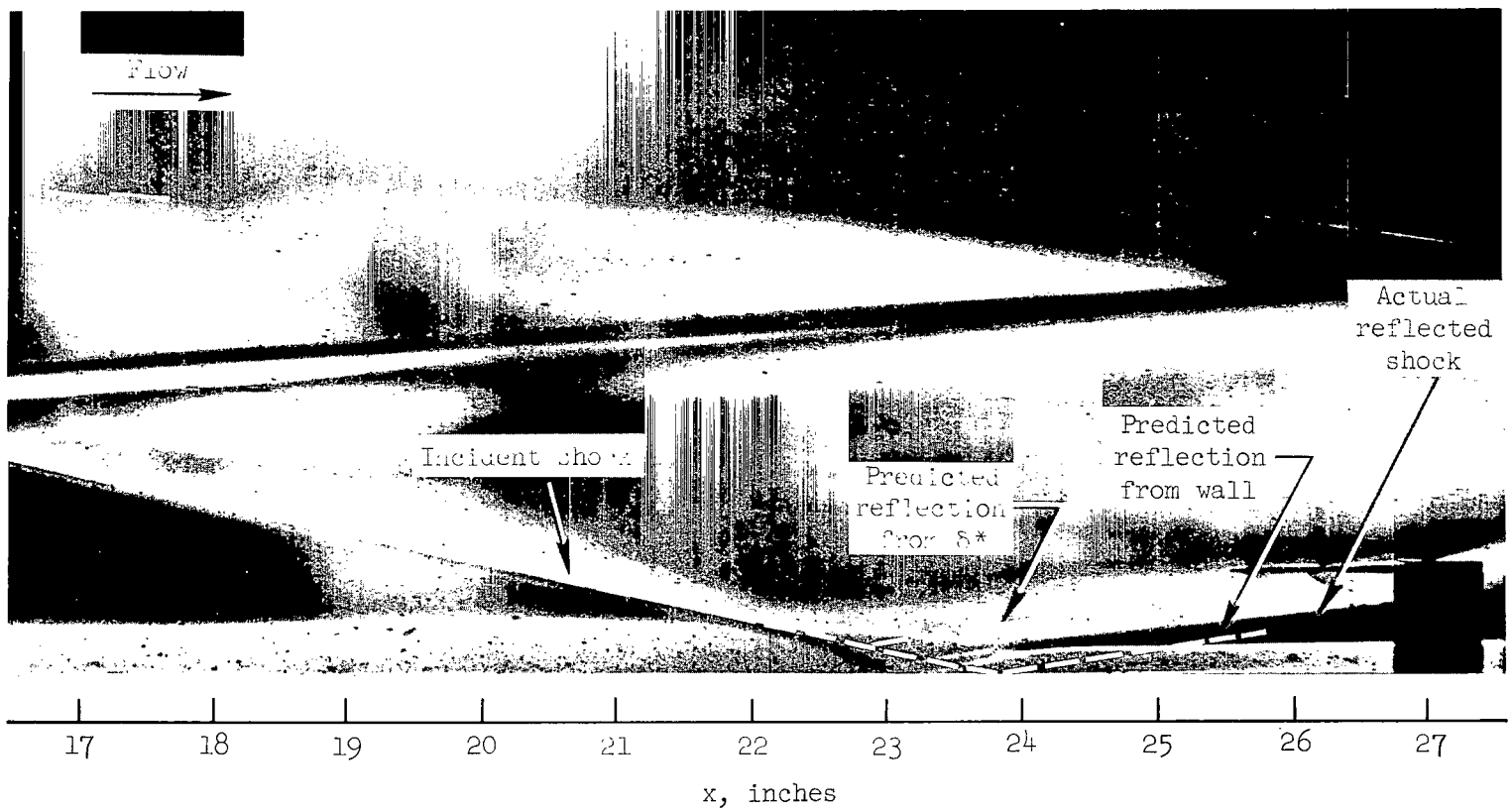

Figure 35.- Example of two simple interaction models superimposed on schlieren photograph; FP 66, $M_\infty = 7.3$, $\alpha_L = 5°$, turbulent boundary layer.

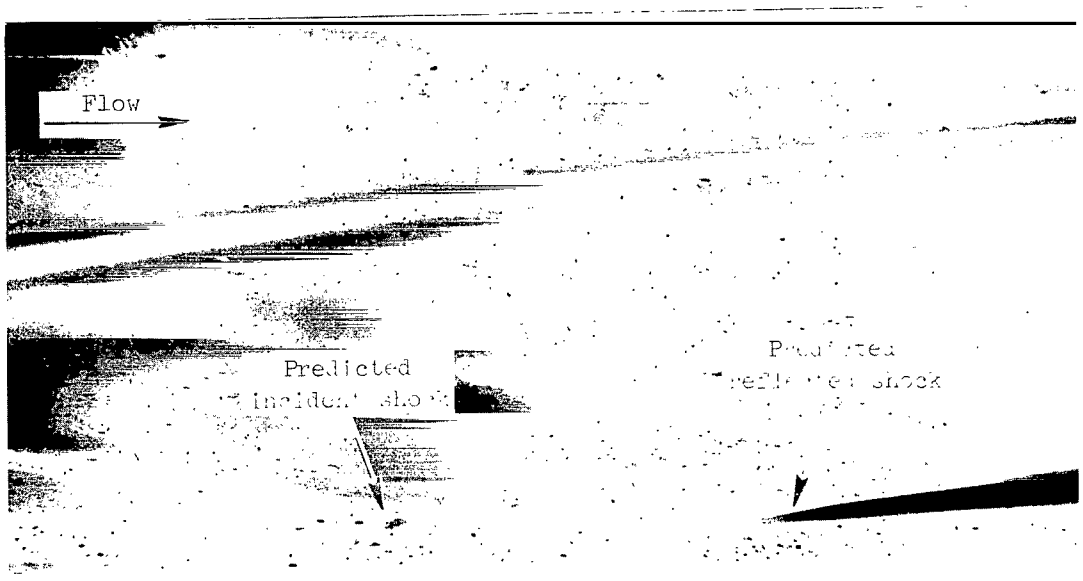

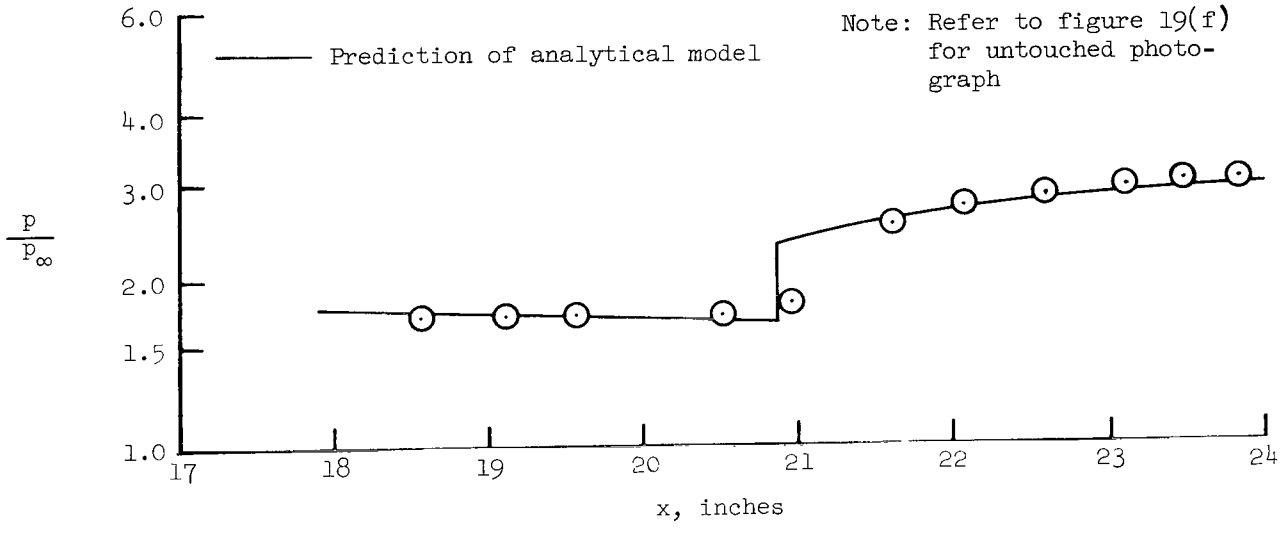

(a) $\alpha_L = 2°$

Figure 36.- Comparison of predicted and experimental shock-wave configuration and surface pressure distribution, FP 59; $M_\infty = 7.4$, turbulent boundary layer.

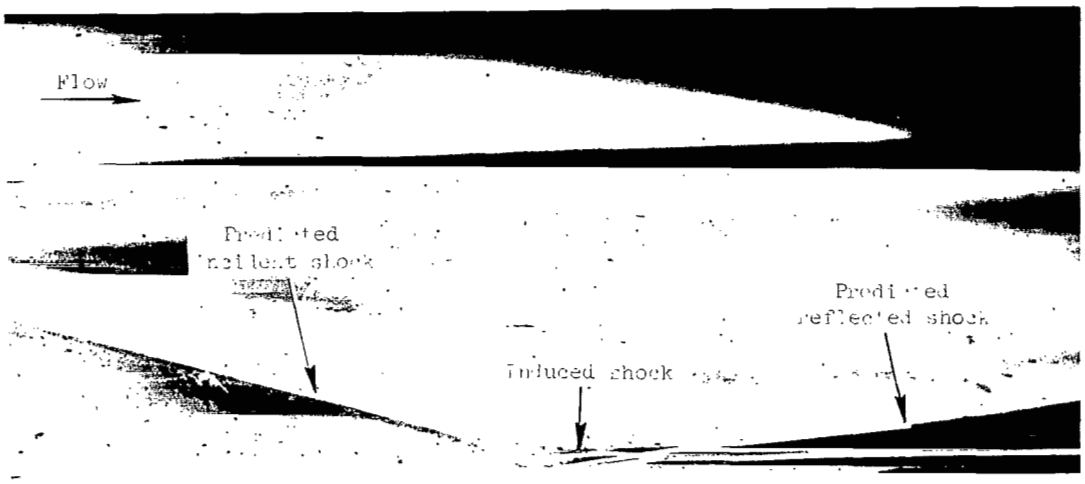

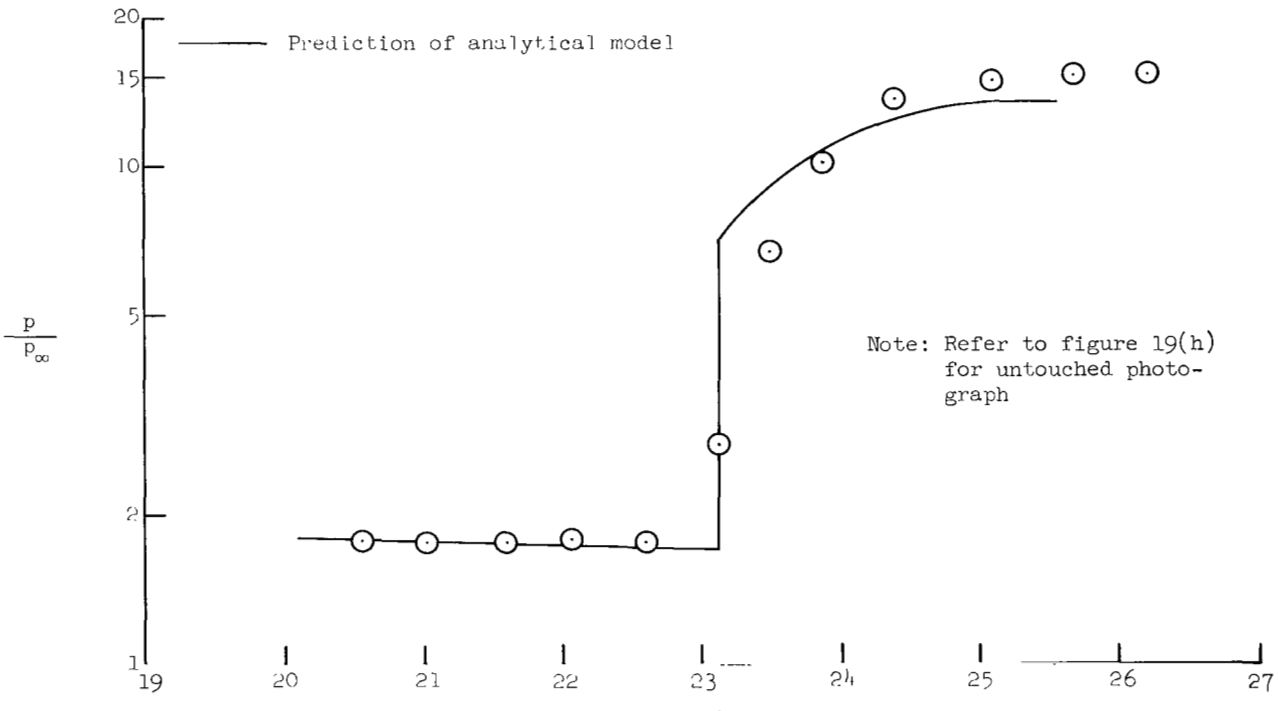

(b) $\alpha_L = 8°$

Figure 36.- Concluded.

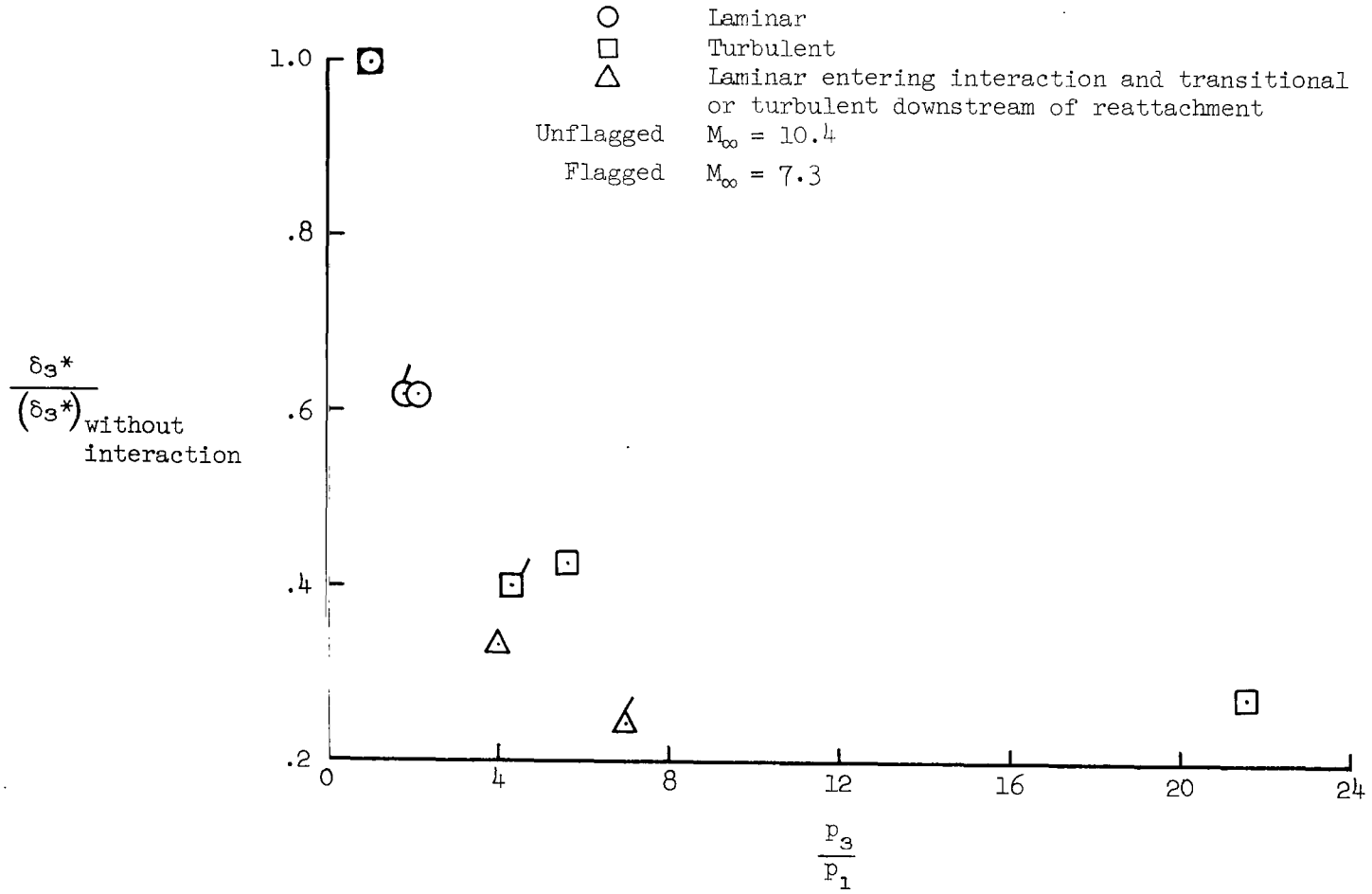

(a) Displacement thickness.

Figure 37.- Variation of downstream integral parameters with pressure rise.

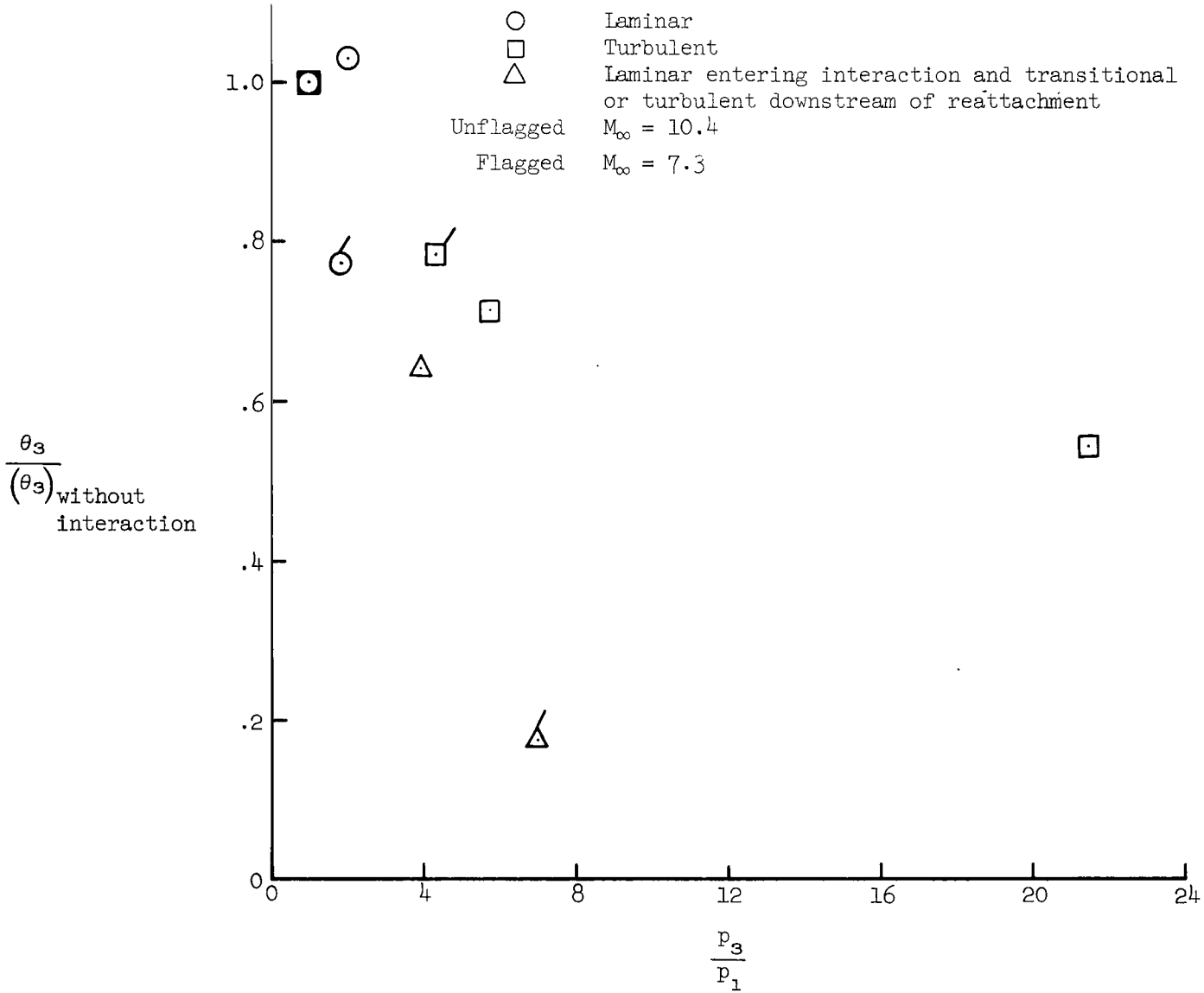

(b) Momentum thickness.

Figure 37.- Concluded.

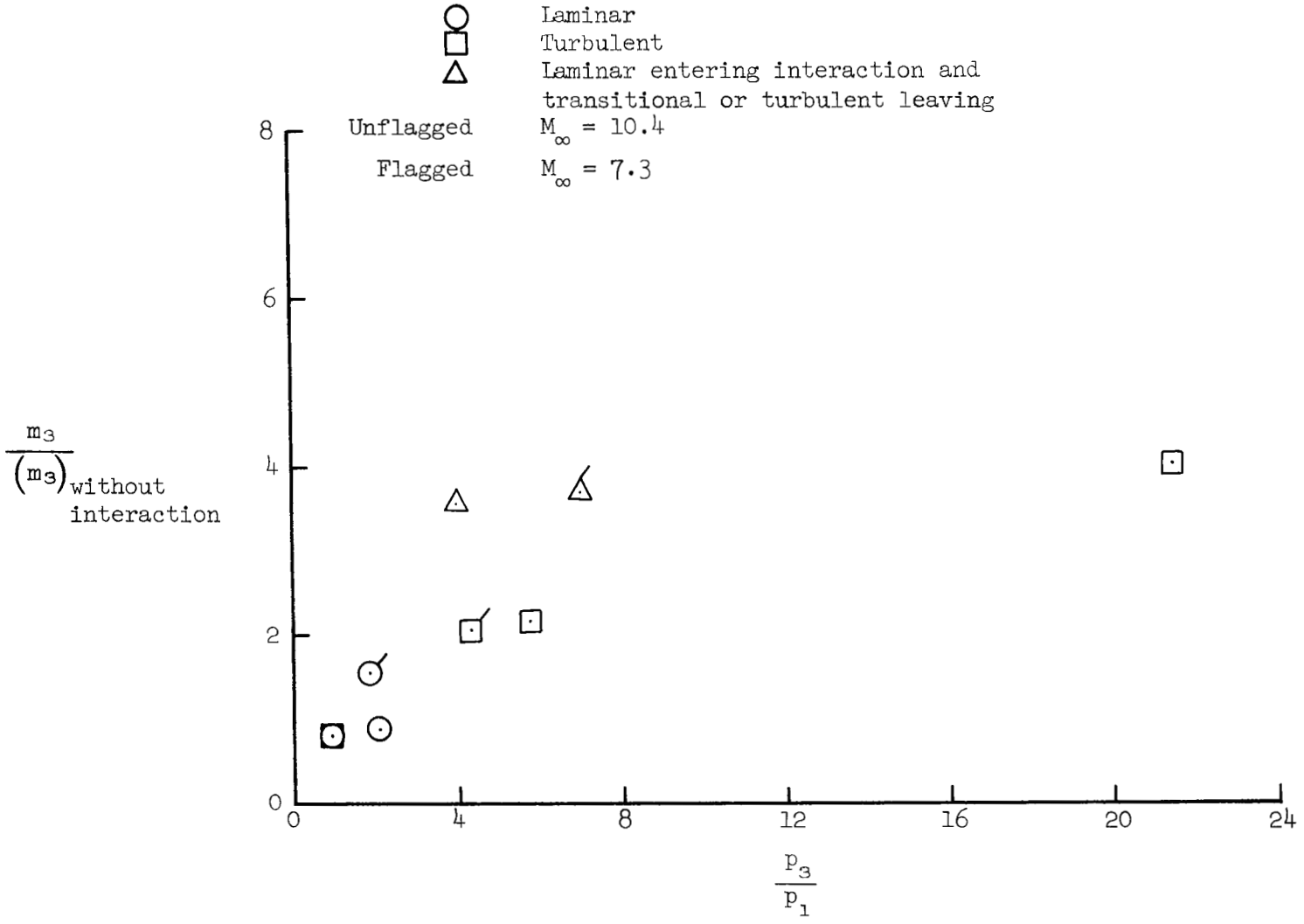

Figure 38.- Variation of downstream boundary-layer mass flow with pressure rise.

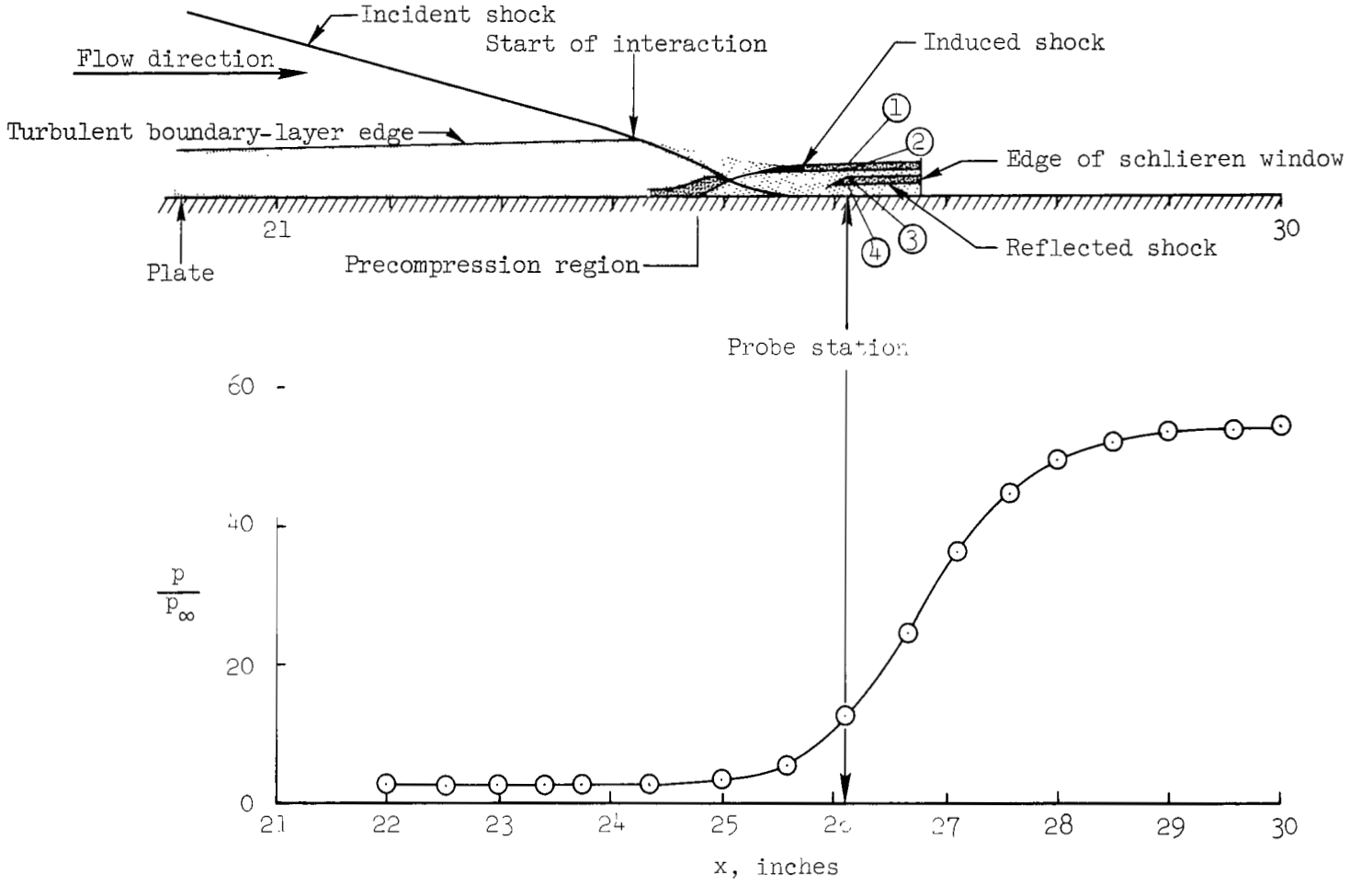

(a) Surface pressure and shock configuration, FP 49.

Figure 39.- Details of a turbulent boundary-layer shock-wave interaction; $M_\infty = 10.4$, $\alpha_L = 10°$.

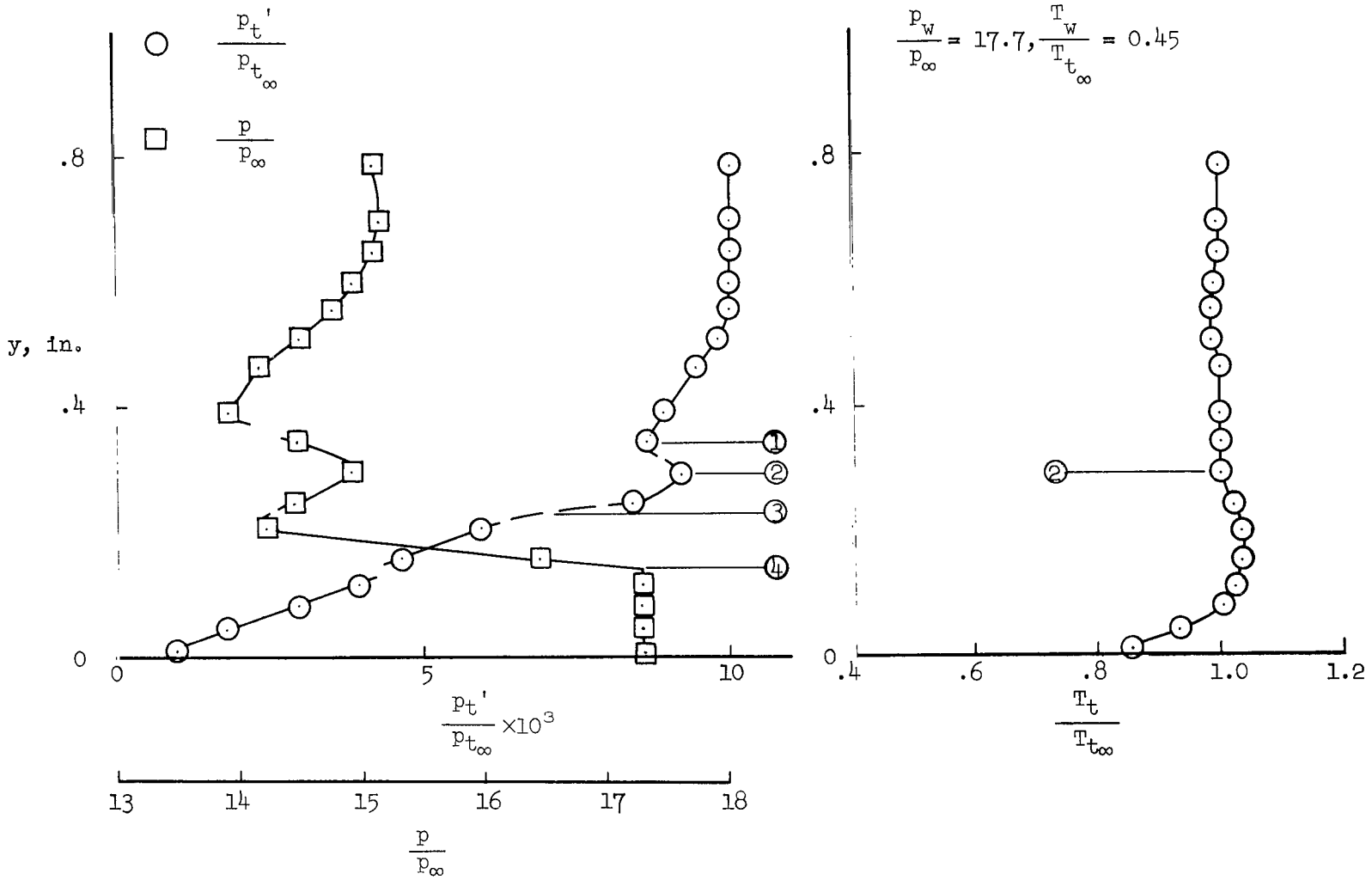

(b) Probe surveys, FP 46.

Figure 39.- Continued.

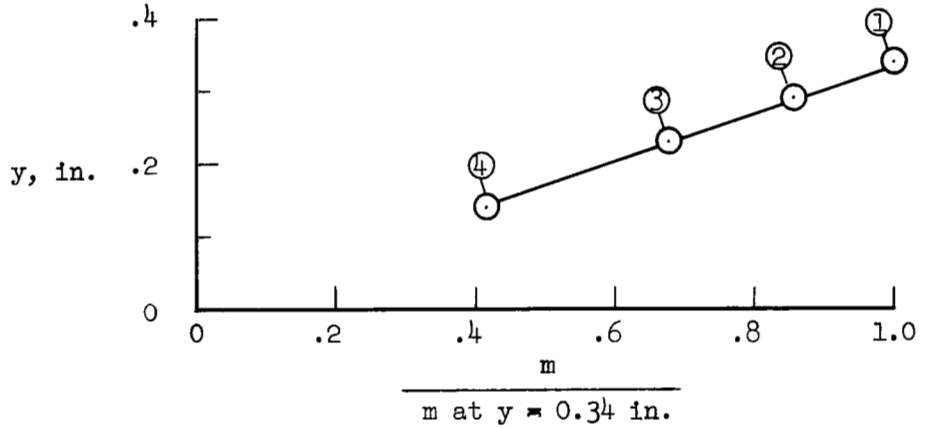

(c) Normalized mass-flow variation, FP 46 and FP 49.

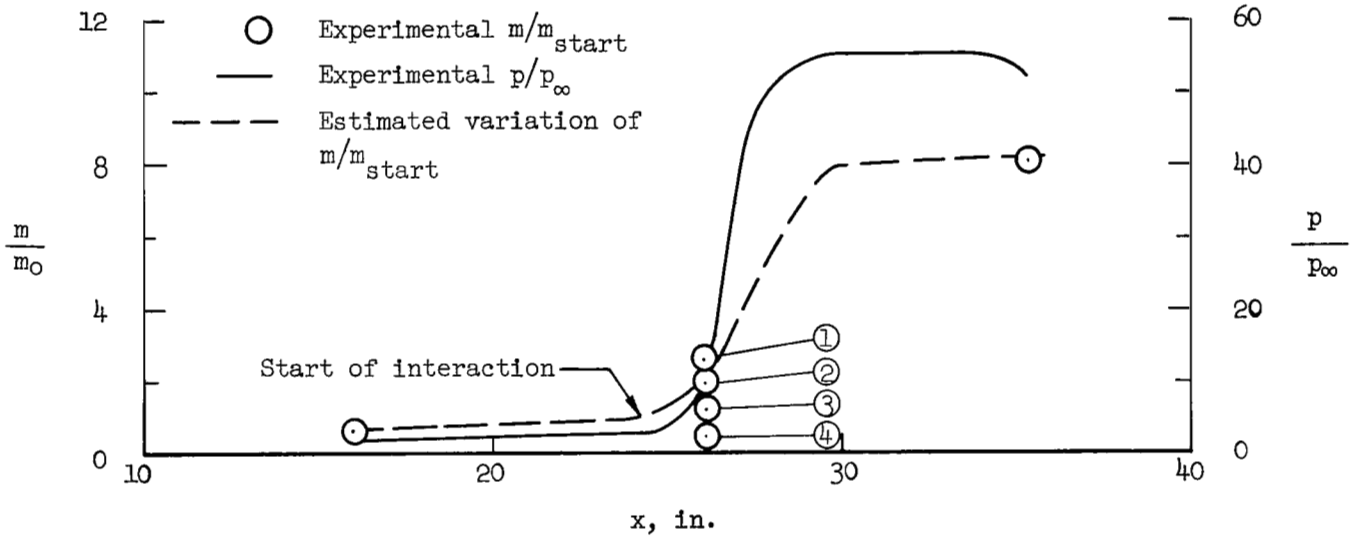

(d) Longitudinal distribution of mass flow and surface pressure, FP 46 and FP 49.

Figure 39.- Concluded.

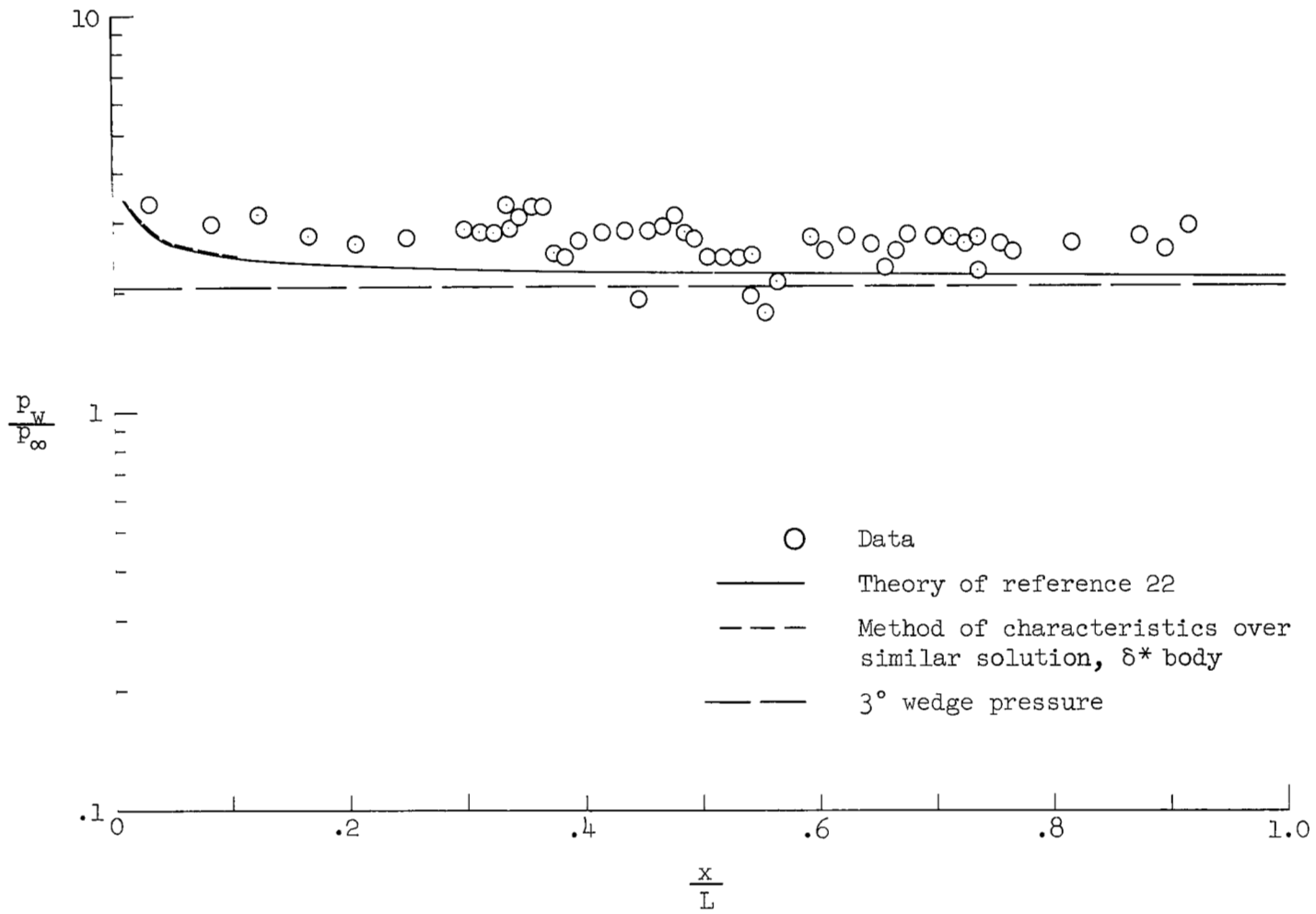

Figure 40.- Comparison of pressure data for a typical low-pressure test condition with results obtained from weak interaction theory (ref. 22) and the method of characteristics, FP 23; $M_\infty = 10.4$.

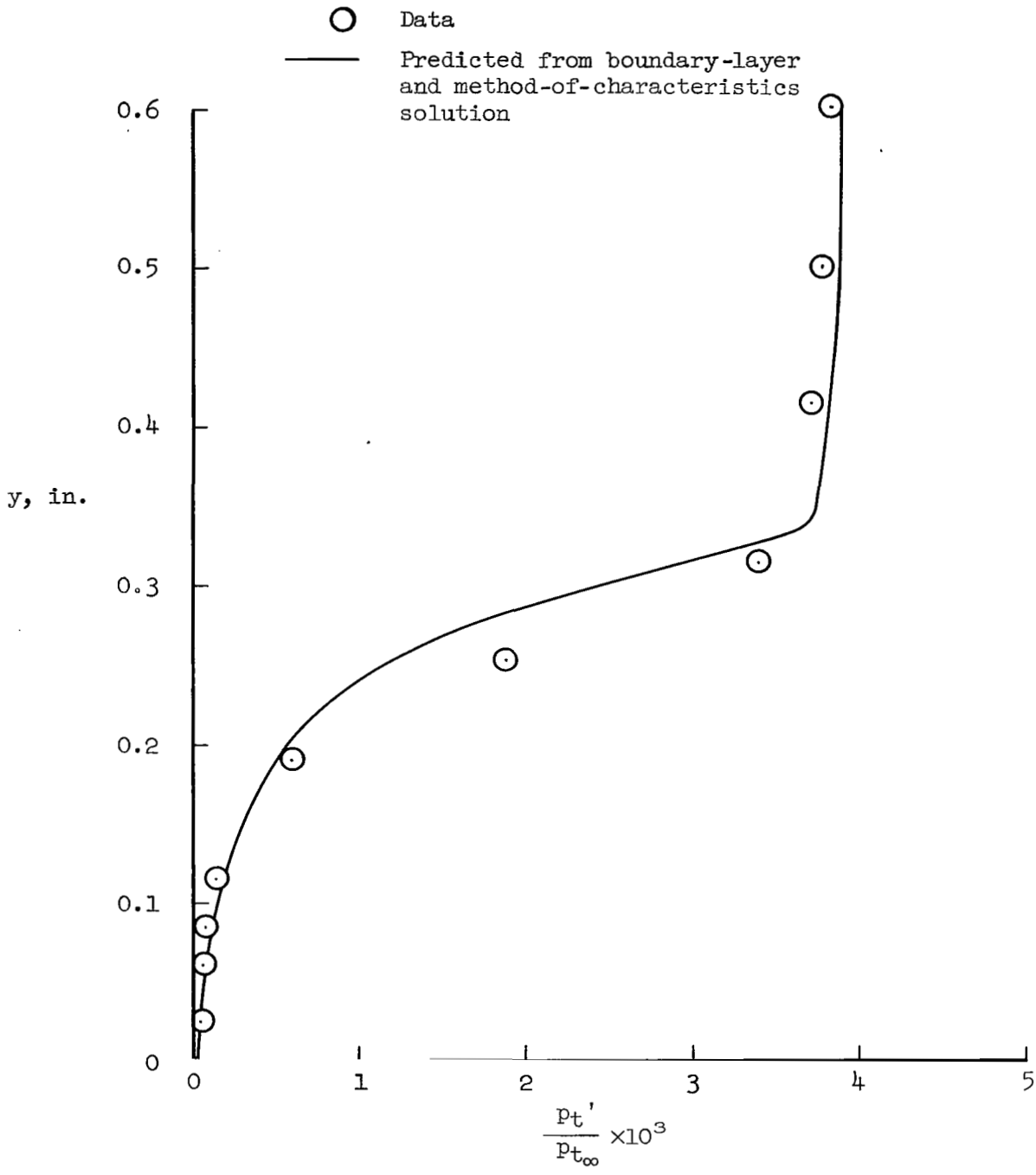

Figure 41.- Comparison of measured and predicted pitot pressure at probe station 1; FP 23, $M_\infty = 10.4$, laminar boundary layer.

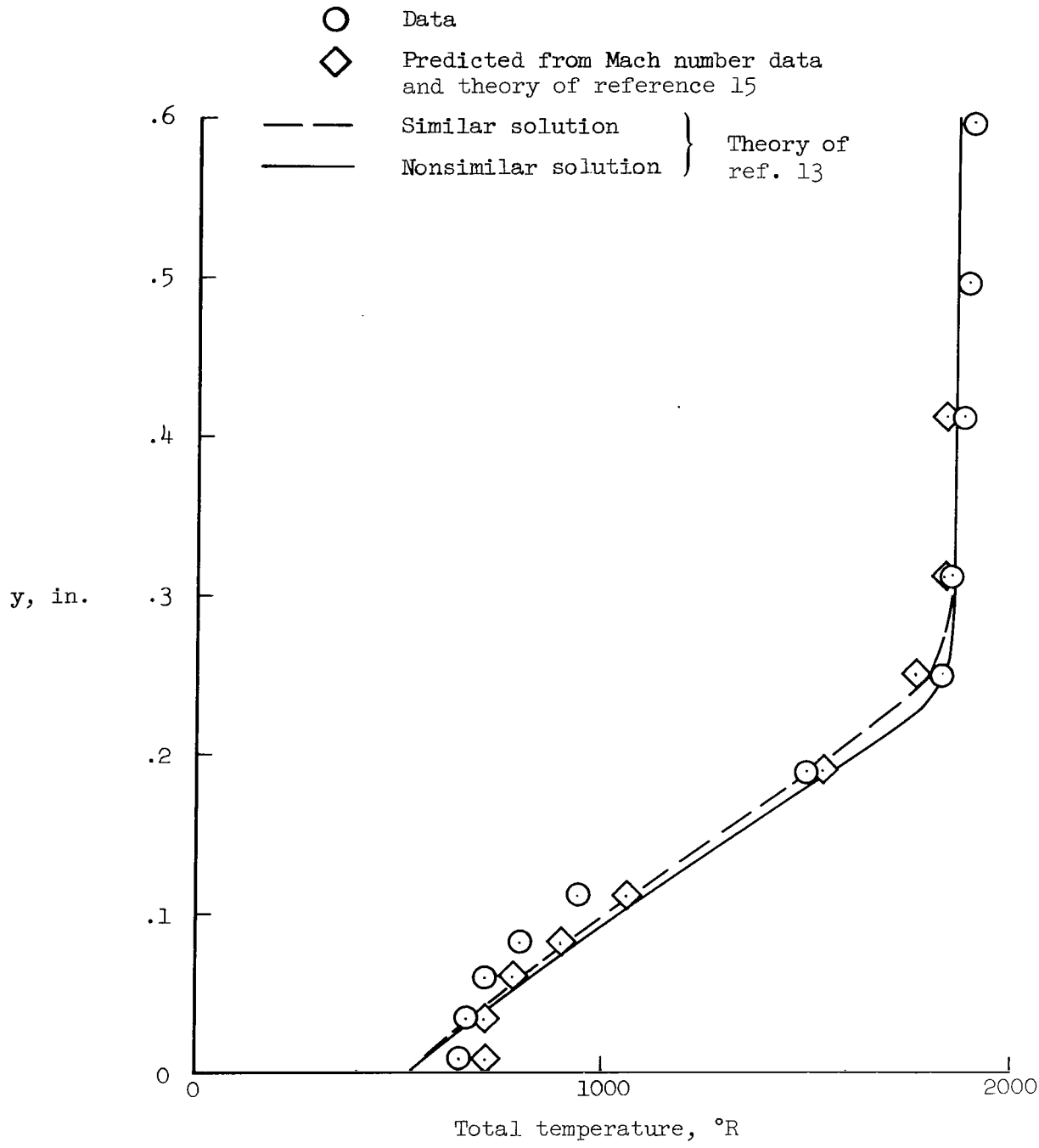

Figure 42.- Comparison of experimental and predicted total-temperature profiles; FP 23, M_∞ = 10.4, laminar boundary layer.

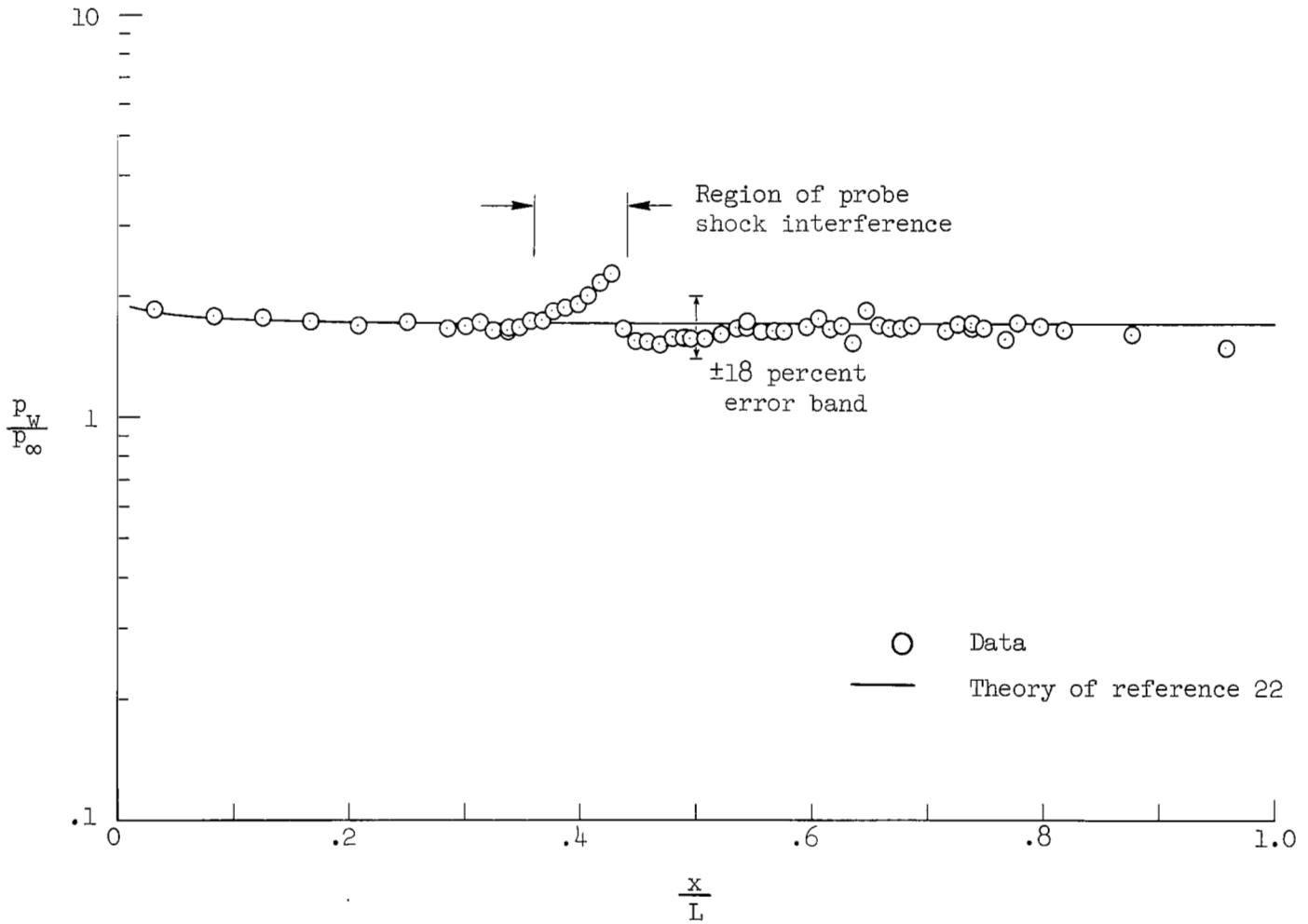

Figure 43.- Comparison of pressure data for a typical high-pressure test condition with results obtained from weak interaction theory (ref. 22), FP 71; $M_\infty = 7.3$.

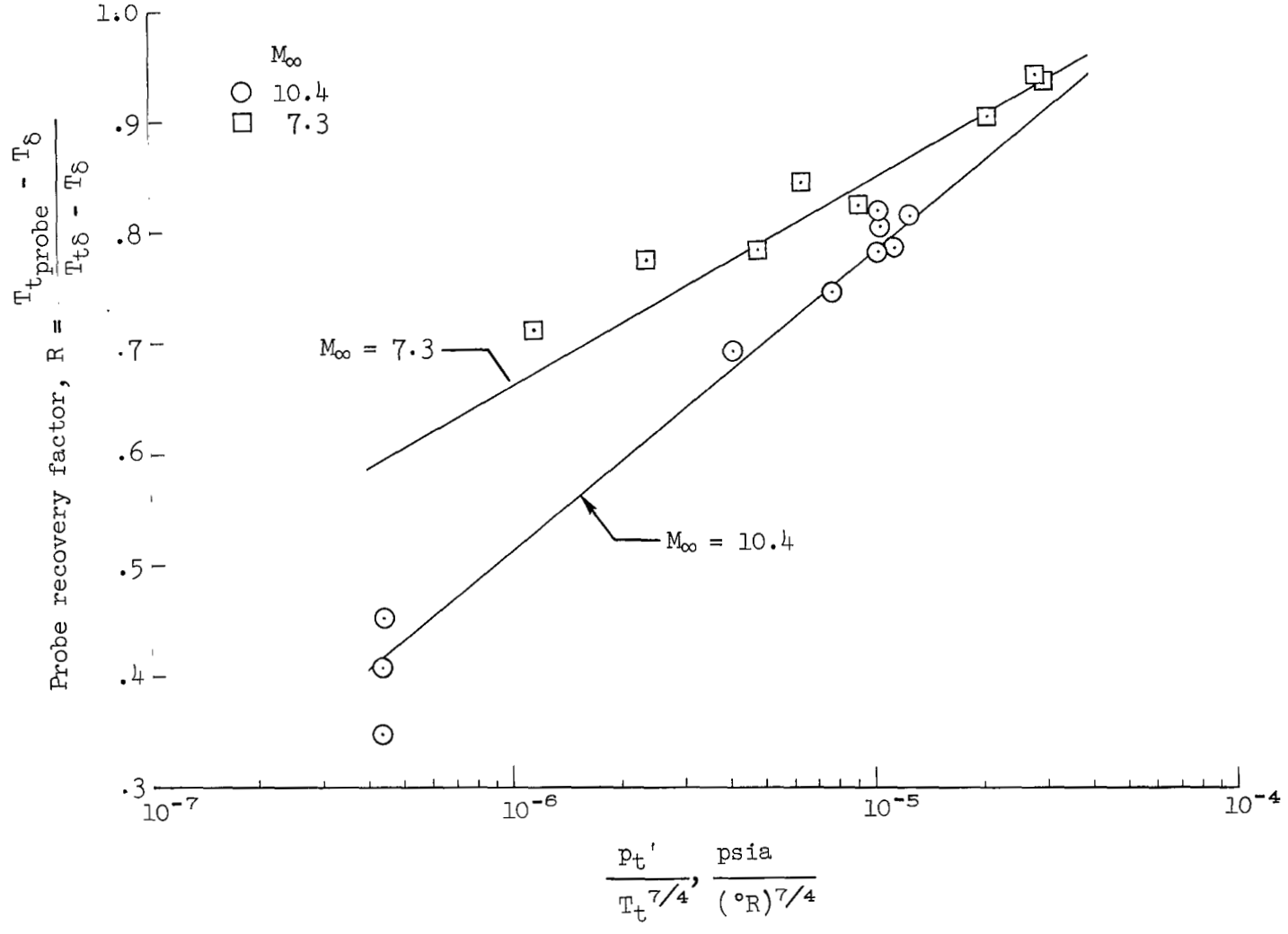

Figure 44.- Typical total-temperature calibration curves for the probe temperature recovery factor.

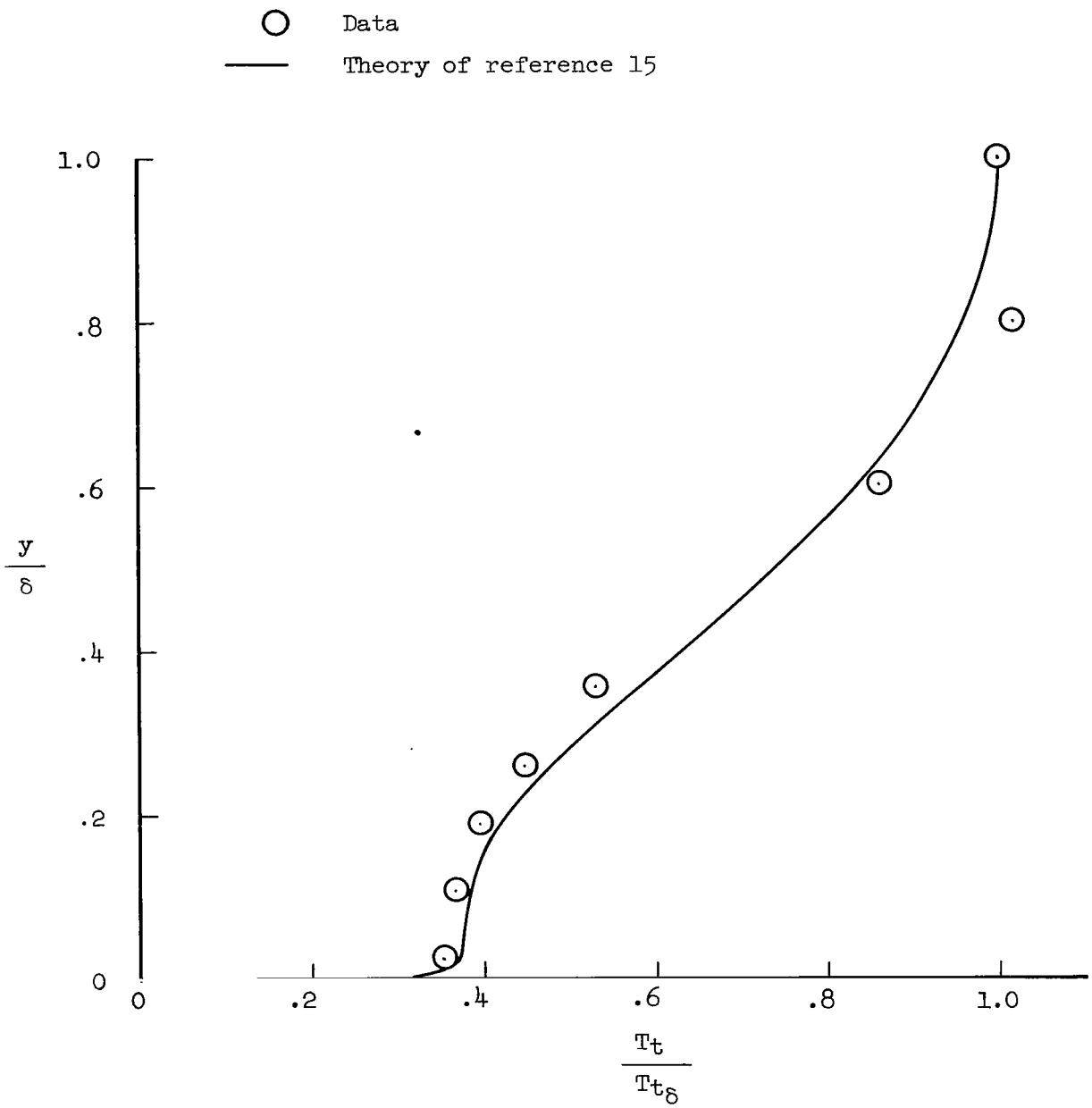

Figure 45.- Comparison of experimental total-temperature profile with results obtained by using the experimental Mach number distribution and the Crocco relationship (Prandtl number = 1.0), FP 23; M_∞ = 10.4, laminar boundary layer.

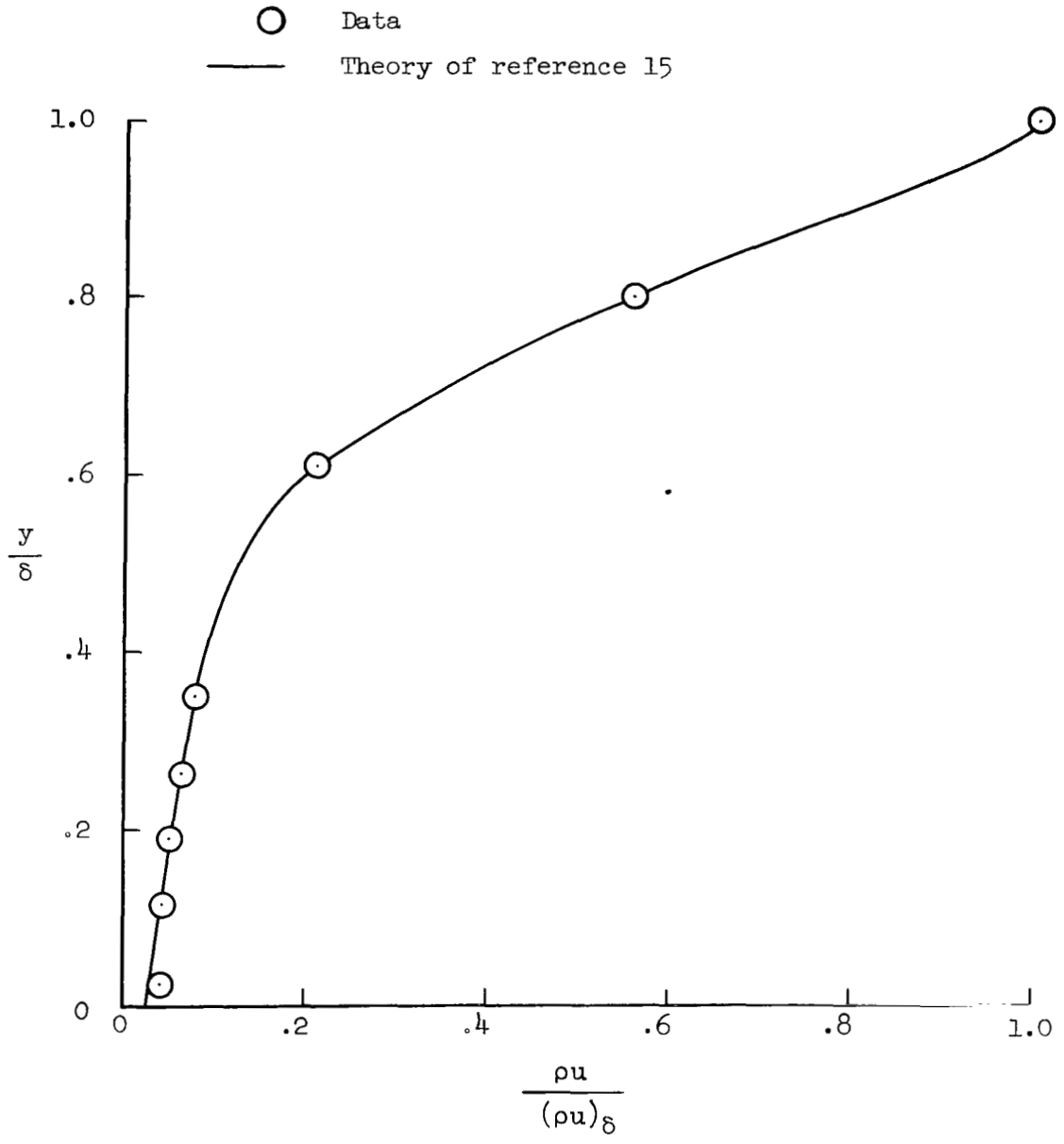

Figure 46.- Mass-flux profile in the boundary layer computed using experimental and Crocco temperature distributions; FP 23, M_∞ = 10.4, laminar boundary layer.

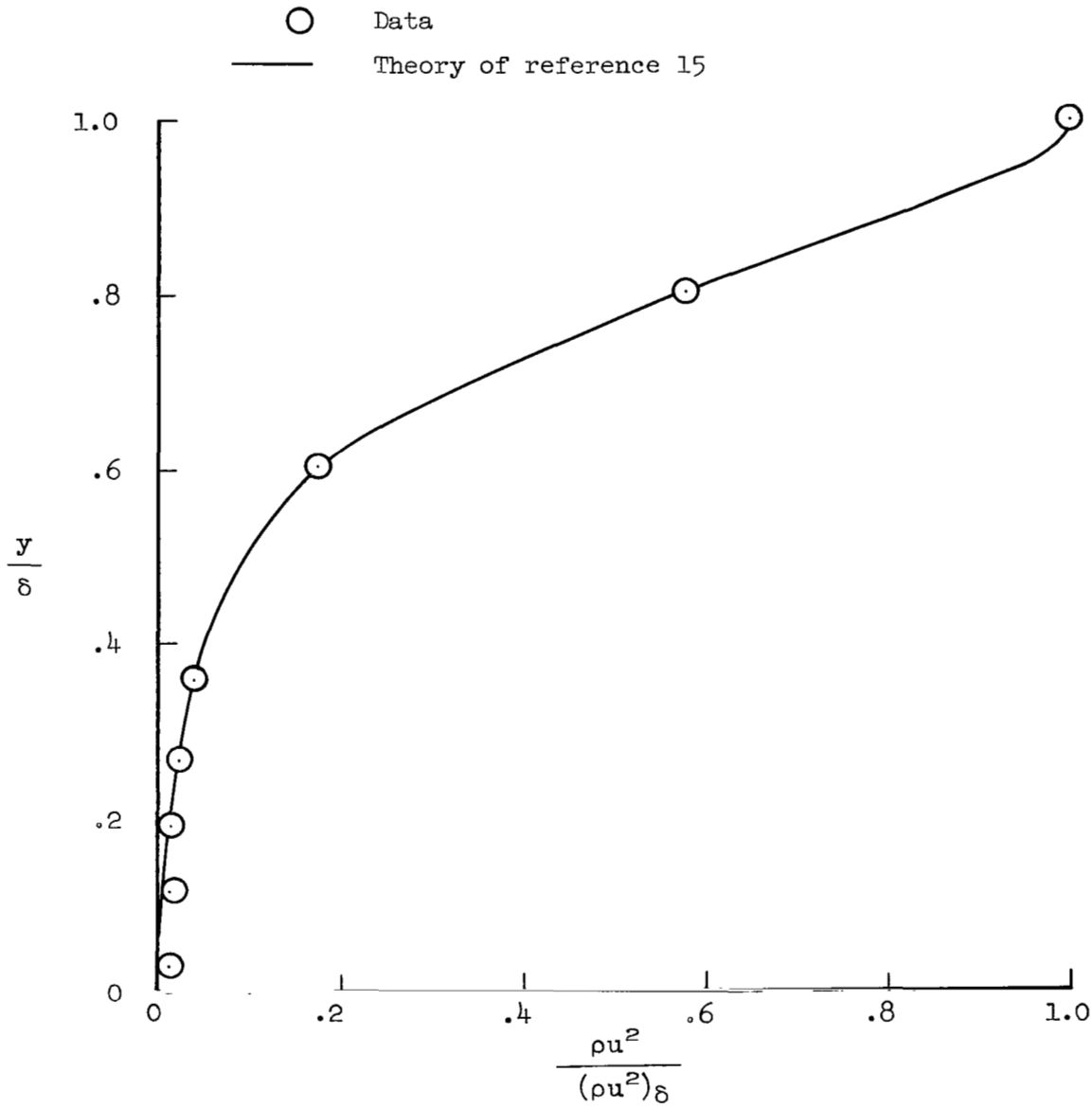

Figure 47.- Momentum-flux profile in the boundary layer computed using experimental and Crocco temperature distributions; FP 23, $M_\infty = 10.4$, laminar boundary layer.

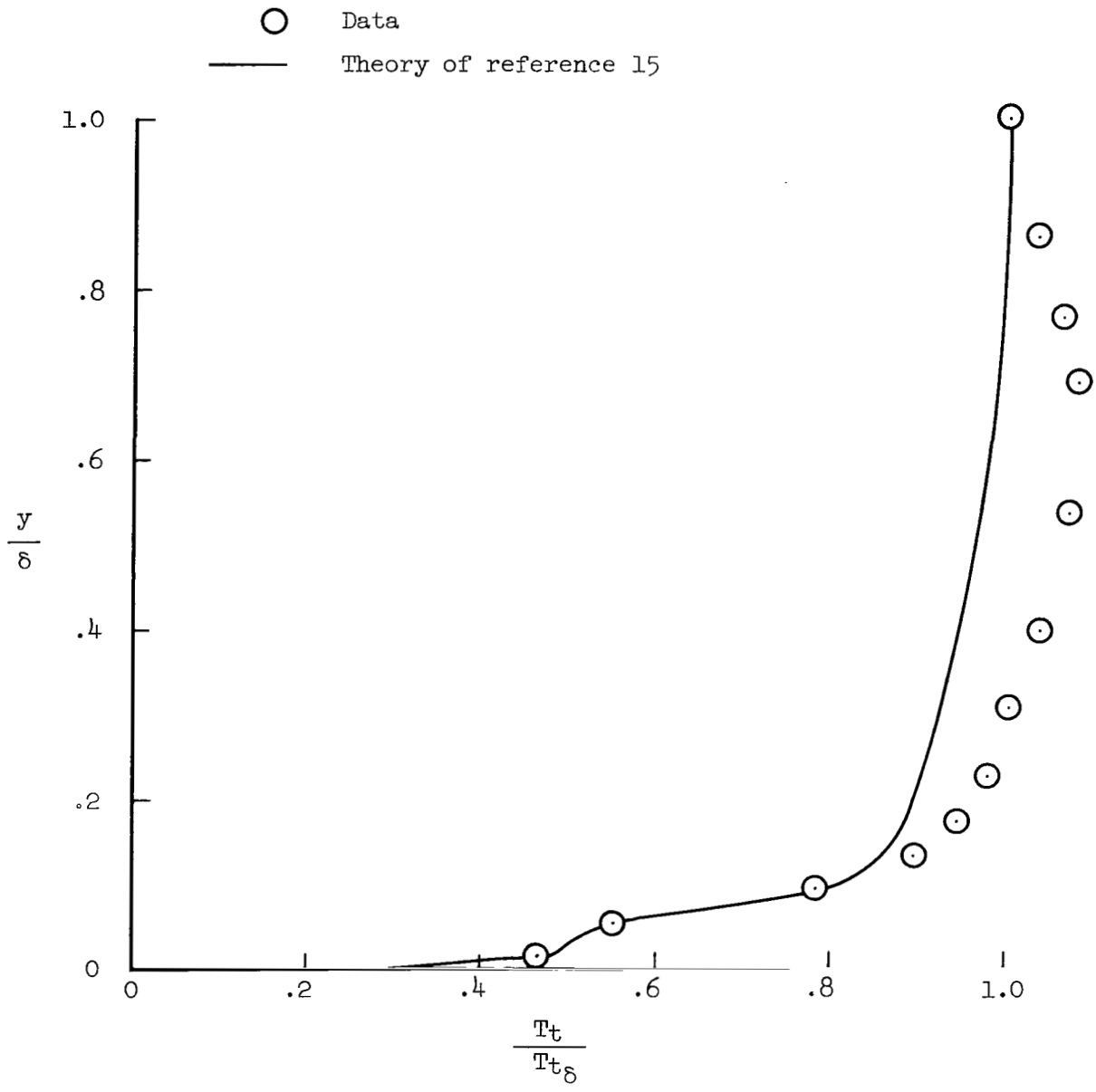

Figure 48.- Comparison of experimental total-temperature profile with results obtained by using the experimental Mach number distribution and the Crocco relationship (Prandtl number = 1.0), FP 19; $M_\infty = 10.4$, turbulent boundary layer.

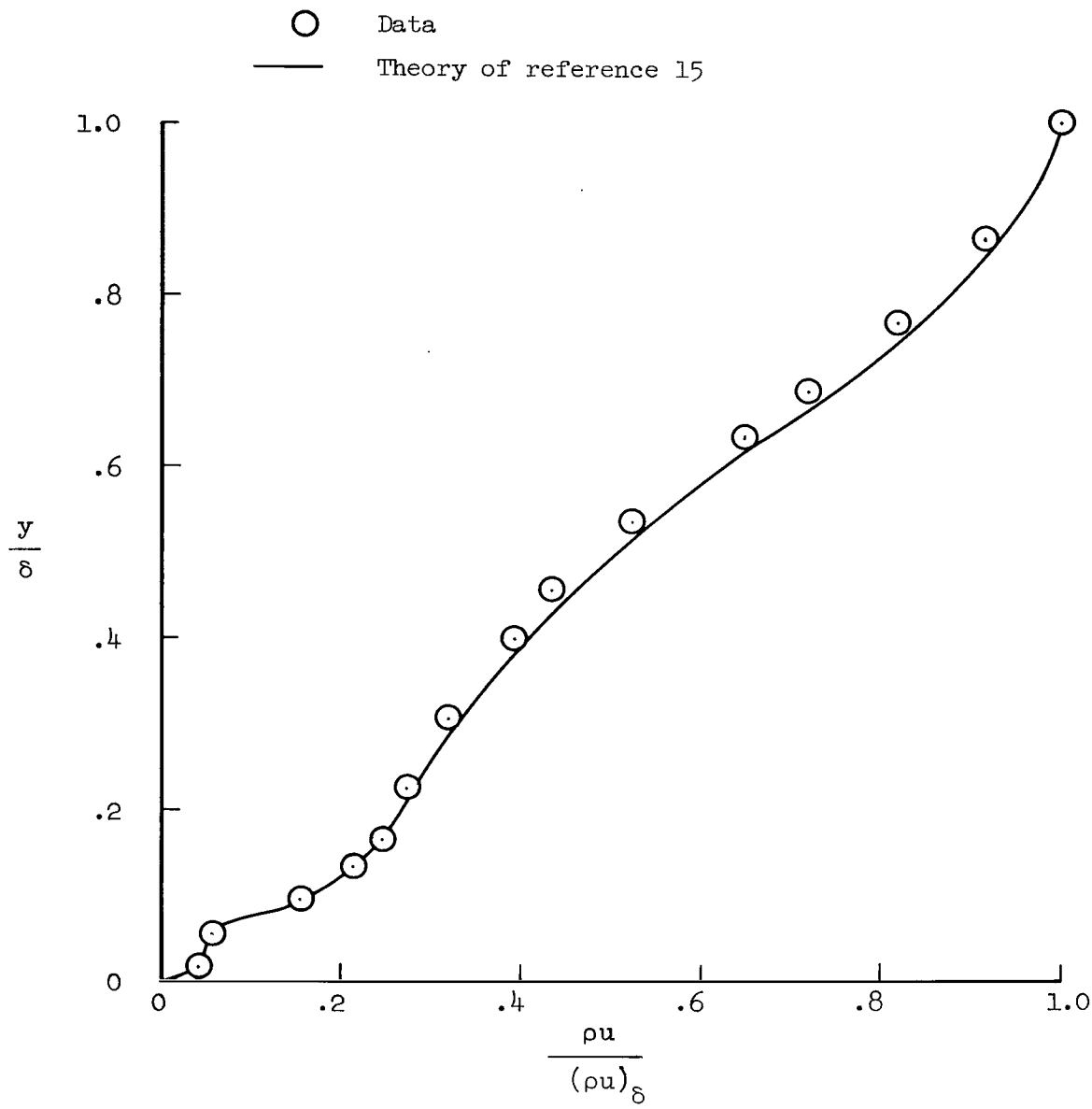

Figure 49.- Mass-flux profile in the boundary layer computed using experimental and Crocco temperature distributions; FP 19, $M_\infty = 10.4$, turbulent boundary layer.

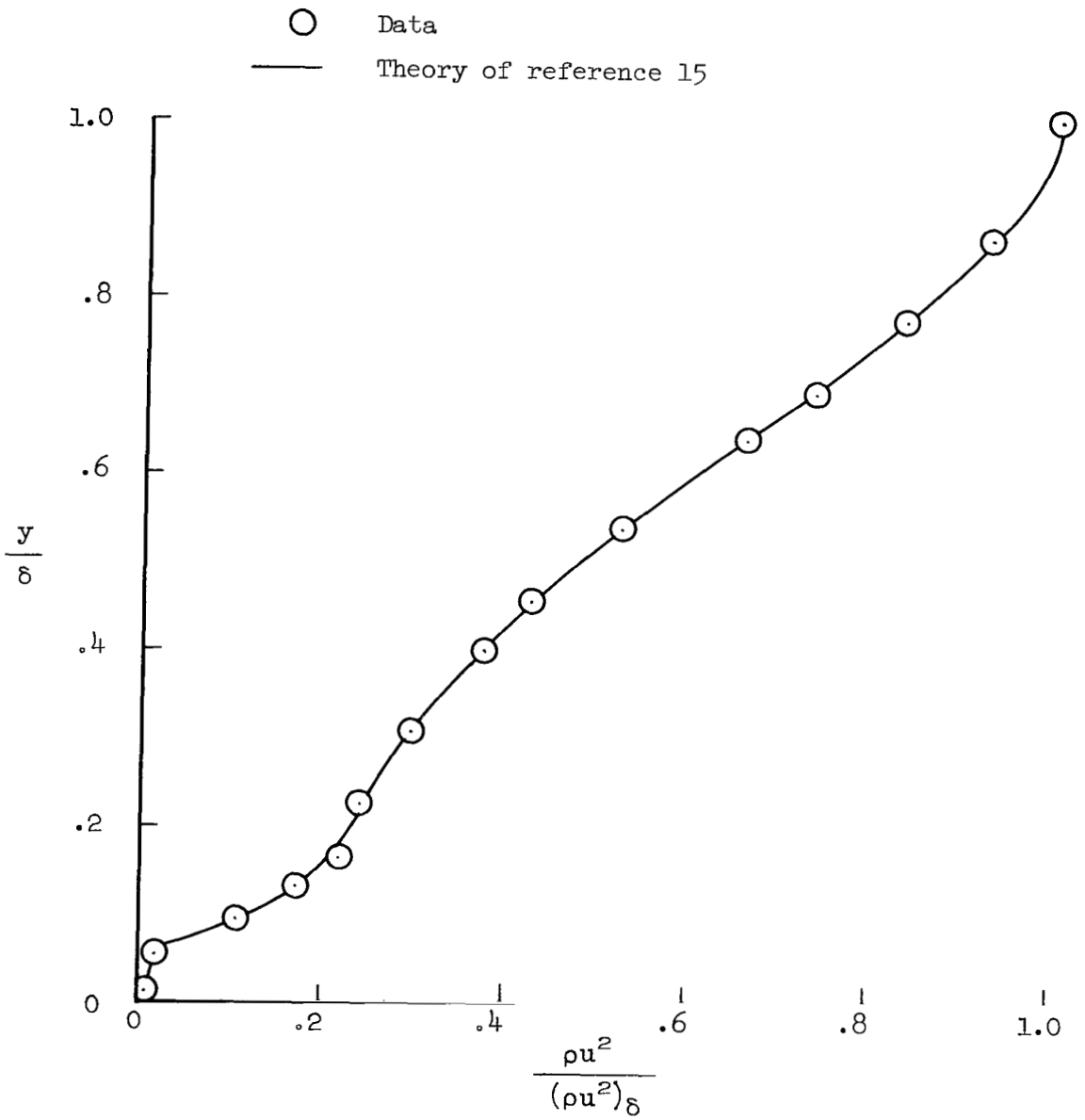

Figure 50.- Momentum-flux profile in the boundary layer computed using experimental and Crocco temperature distributions; FP 19, $M_\infty = 10.4$, turbulent boundary layer.

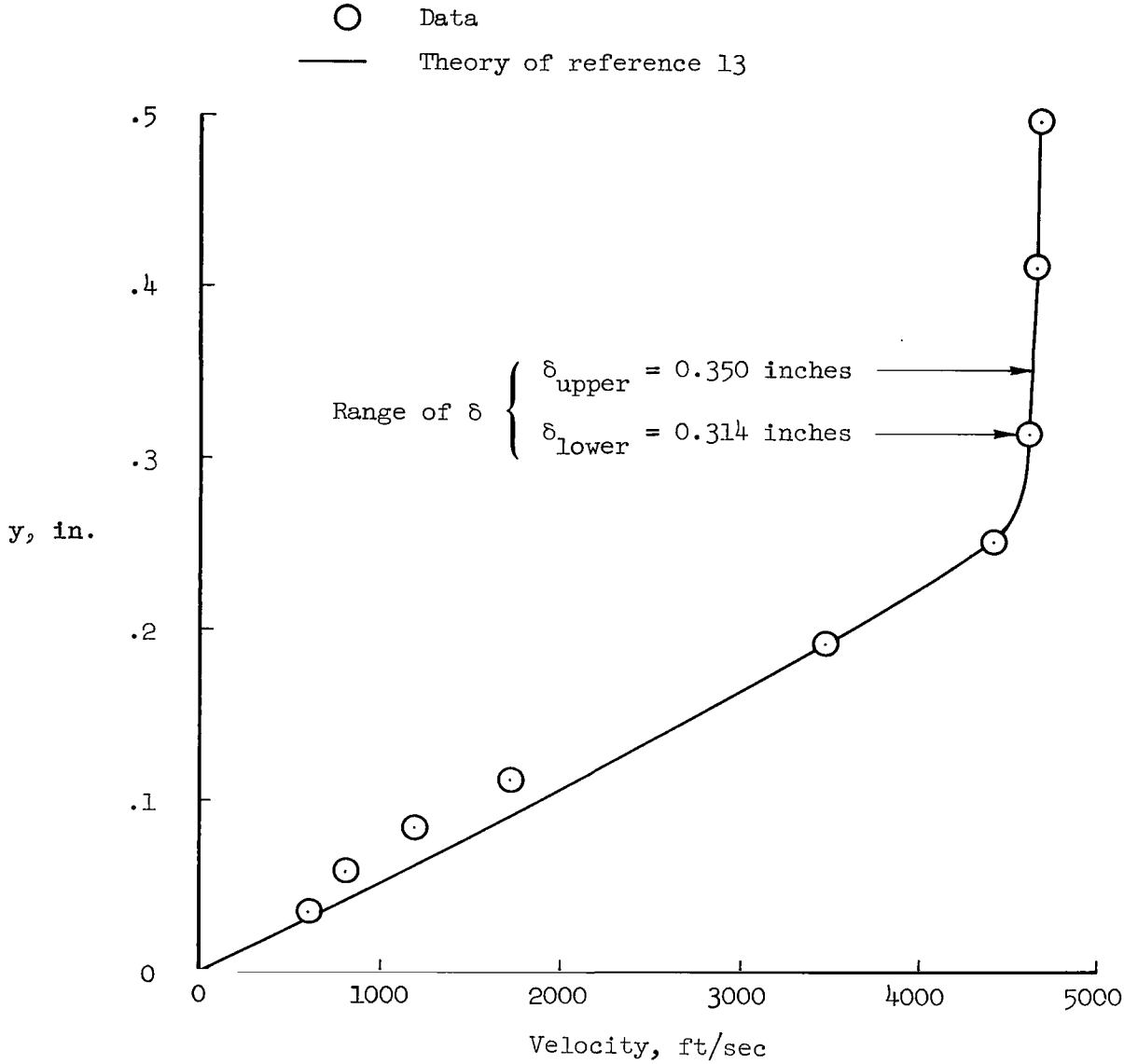

Figure 51.- Typical velocity distribution showing uncertainty in boundary-layer thickness; FP 23, M_∞ = 10.4, laminar boundary layer.

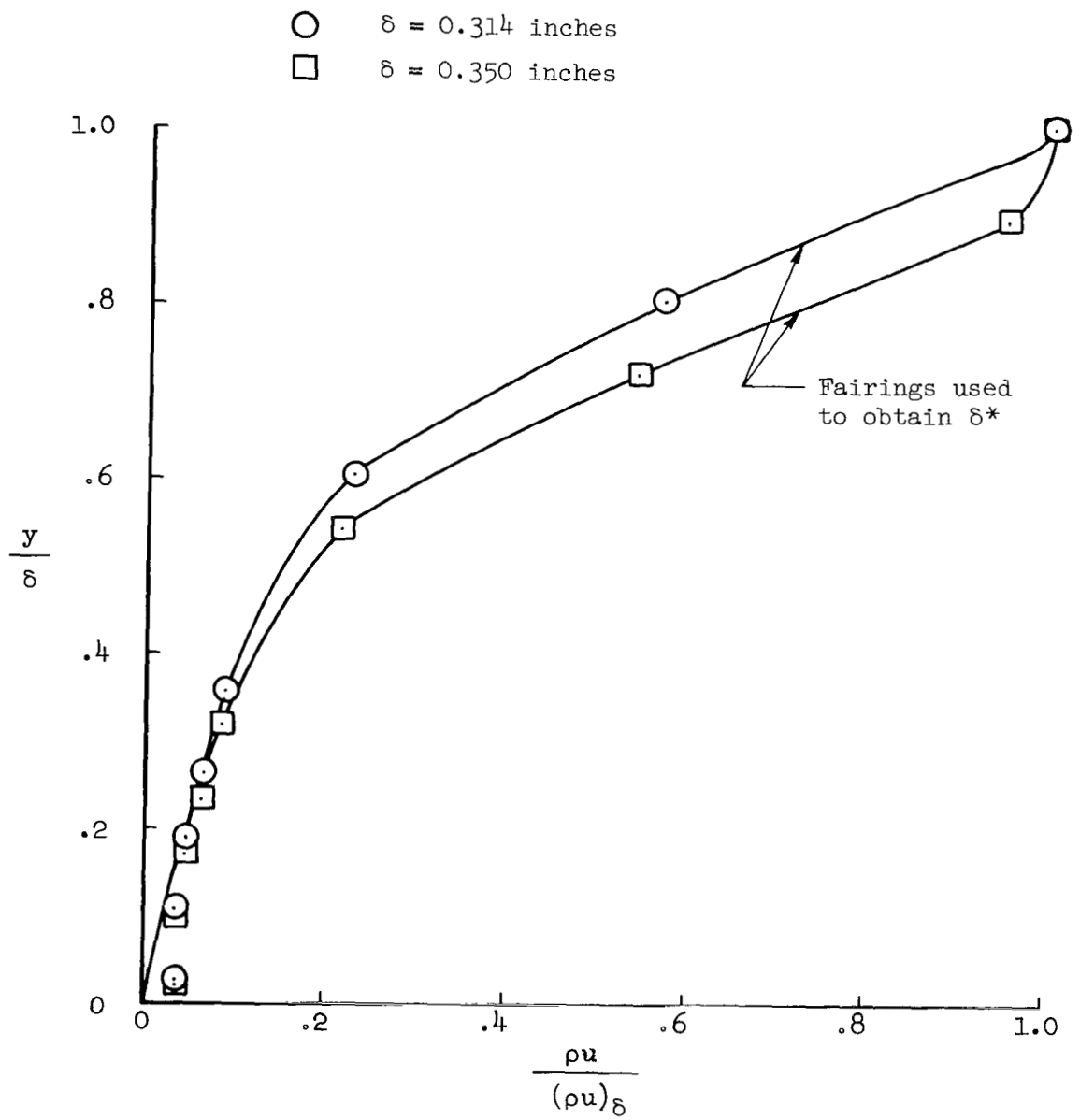

Figure 52.- The effect of the choice of boundary-layer thickness on the mass-flux profile, FP 23, $M_\infty = 10.4$, laminar boundary layer.

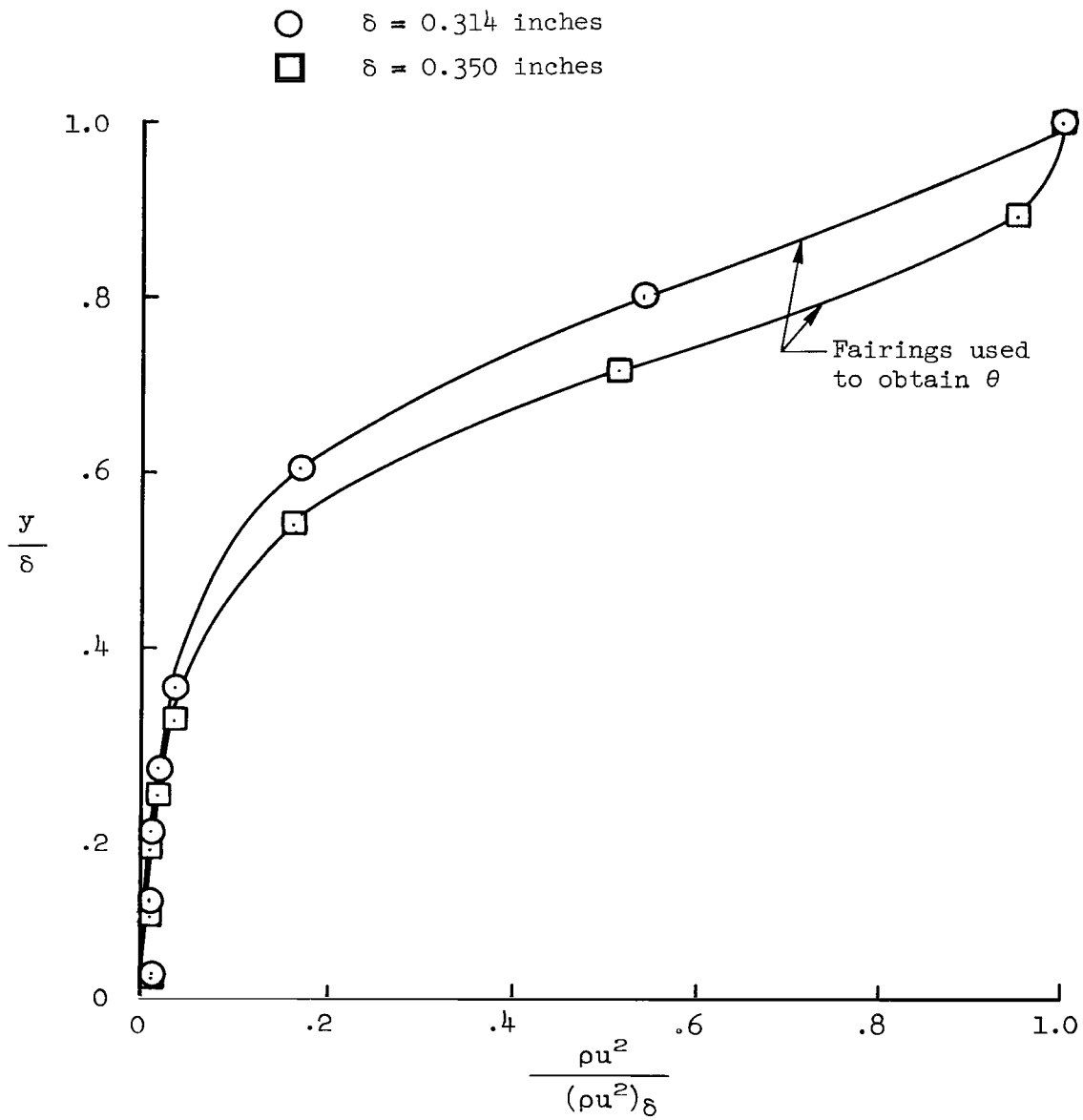

Figure 53.- The effect of the choice of boundary-layer thickness on the momentum-flux profile, FP 23, $M_\infty = 10.4$, laminar boundary layer.

"The aeronautical and space activities of the United States shall be conducted so as to contribute . . . to the expansion of human knowledge of phenomena in the atmosphere and space. The Administration shall provide for the widest practicable and appropriate dissemination of information concerning its activities and the results thereof."

—NATIONAL AERONAUTICS AND SPACE ACT OF 1958

NASA SCIENTIFIC AND TECHNICAL PUBLICATIONS

TECHNICAL REPORTS: Scientific and technical information considered important, complete, and a lasting contribution to existing knowledge.

TECHNICAL NOTES: Information less broad in scope but nevertheless of importance as a contribution to existing knowledge.

TECHNICAL MEMORANDUMS: Information receiving limited distribution because of preliminary data, security classification, or other reasons.

CONTRACTOR REPORTS: Scientific and technical information generated under a NASA contract or grant and considered an important contribution to existing knowledge.

TECHNICAL TRANSLATIONS: Information published in a foreign language considered to merit NASA distribution in English.

SPECIAL PUBLICATIONS: Information derived from or of value to NASA activities. Publications include conference proceedings, monographs, data compilations, handbooks, sourcebooks, and special bibliographies.

TECHNOLOGY UTILIZATION PUBLICATIONS: Information on technology used by NASA that may be of particular interest in commercial and other non-aerospace applications. Publications include Tech Briefs, Technology Utilization Reports and Notes, and Technology Surveys.

Details on the availability of these publications may be obtained from:

SCIENTIFIC AND TECHNICAL INFORMATION DIVISION

NATIONAL AERONAUTICS AND SPACE ADMINISTRATION

Washington, D.C. 20546